6-1-2014

Nitroxide Radicals for Low Frequency Electron Paramagnetic Resonance Imaging (EPRI)

Joshua R. Biller
University of Denver

NITROXIDE RADICALS FOR LOW FREQUENCY ELECTRON PARAMAGNETIC RESONANCE IMAGING (EPRI)

A Dissertation

Presented to

the Faculty of Natural Sciences and Mathematics

University of Denver

In Partial Fulfillment

of the Requirements for the Degree

Doctor of Philosophy

by

Joshua R. Biller

June 2014

Advisor: Gareth R. Eaton

Author: Joshua R. Biller
Title: NITROXIDE RADICALS FOR LOW FREQUENCY ELECTRON PARAMAGNETIC RESONANCE IMAGING (EPRI)
Advisor: Gareth R. Eaton
Degree Date: June 2014

ABSTRACT

Optimization of nitroxides as probes for EPR imaging requires detailed understanding of spectral properties such as spin lattice relaxation times, spin packet linewidths, and nuclear hyperfine splitting. Initial measurements of relaxation times for six low molecular weight nitroxides at X-band stimulated further measurement at frequencies between 250 MHz and 34 GHz. The impact of tumbling was studied with perdeuterated 2,2,6,6-tetramethyl-4-piperidinyl-1-oxyl (PDT) in five solvents with viscosities resulting in tumbling correlation times, τ_R, between 4 and 50 ps. A set of three $^{14}N/^{15}N$ pairs of nitroxides in water was selected such that τ_R varied between 9 and 19 ps. To test the impact of structure on relaxation, three additional nitroxides with τ_R between 10 and 26 ps were studied.

In the fast tumbling regime $1/T_2 \sim 1/T_1$ and relaxation is dominated by spin rotation, modulation of A-anisotropy and a thermally activated process. The contribution to $1/T_1$ from spin rotation is independent of frequency and decreases as τ_R increases. The modulation of nitrogen hyperfine anisotropy increases as frequency decreases and as τ_R increases, dominating at low frequencies for $\tau_R > \sim 15$ ps. The modulation of g anisotropy is significant only at 34 GHz. Inclusion of a thermally activated process was required to account for the observation that for most of the radicals, $1/T_1$ was smaller at 250 MHz than at 1-2 GHz. The thermally activated process likely arises from intramolecular motions of the nitroxide ring that modulate the isotropic A values.

A phantom of three 4 mm tubes containing different $^{15}N,^{2}H$-substituted nitroxides was constructed for use at 250 MHz. Projections for 2D spectral-spatial images were obtained by continuous wave (CW) and rapid scan (RS) EPR using a bimodal cross-loop resonator. Relative to CW projections obtained for the same data acquisition time (5 min), RS projections had significantly improved image quality. All experiments were facilitated by advancements in resonator design and testing, which are also described.

ACKNOWLEDGMENTS

I thank Megan Biller for her love and support, and for reminding me that being "content" with what you are doing is entirely different from being "happy" about it. I'm grateful for my son, Conrad, who is always ready with a wide smile when I come home.

I am indebted to Dr. George Rinard, Richard Quine and Dr. Mark Tseitlin for enabling my tendency to break things in the name of science (research). Work together with Dr. Rinard furthered resonator development in the lab. Richard Quine was invaluable for questions relating to low-frequency pulse EPR experiments. Dr. Tseitlin guided me through the rapid-scan imaging experiments, and after decrying my request for full spectrum imaging as ludicrous, invented a way to do it. Virginia Meyer and Hanan Elajaili helped with replicates for the measurements in Chapter 3. Virginia Meyer made measurements of about half the radicals at Q-band detailed in Chapter 5. Hanan had the unenviable job of collecting saturation recovery data as a secondary confirmation of my inversion recovery data. My work also would not have been possible without Dr. Gerald Rosen at the University of Maryland, who synthesized and provided a large number of the nitroxide radicals I worked with.

The work in this dissertation was supported by grants from the NIH/NIBIB (EB002034 and EB000557), hard won by Dr. Gareth and Dr. Sandra Eaton. I am thankful for their guidance, pertaining to the practice of science, as well as how to conduct one's self as a scientist. I'm grateful for many hours spent discussing theory and modeling with Dr. Sandra, and experimental design with Dr. Gareth.

TABLE OF CONTENTS

LIST OF TABLES

LIST OF FIGURES

LIST OF ABBREVIATIONS AND COMMON NAMES

BPP	Bloemburgen, Pound and Purcell spectral density function
CD	Cole-Davidson spectral density function
CLR	Cross Loop Resonator
CTPO	3-carbamoyl-2,2,5,5-tetramethyl-3-pyrrolinyl-1-oxyl
CW	Continuous Wave
ELDOR	Electron-electron double resonance
END	Electron-Nuclear-Dipole
ENDOR	Electron nuclear double resonance
EPR	Electron Paramagnetic Resonance
EPRI	Electron Paramagnetic Resonance Imaging
FPT	Freeze-pump-thaw
Fremy's Salt	Disodium nitrosodisulfonate or potassium nitrosodisulfonate
GSD	Generalized Spin Diffusion
ITU	International Telecommunication Union
LGR	Loop Gap Resonator
mHCTPO	4-protio-3-carbamoyl-2,2,5,5-tetraperdeuteromethyl-3-pyrrolinyl-1-oxyl
PDT	4-oxo-2,2,6,6-tetramethyl-piperidinyl-(d_{16})-oxyl
Proxyl	3-carboxy-2,2,5,5-tetramethyl-1-pyrrolidinyl-1-oxyl
RS	Rapid scan
SNR	Signal-to-noise ratio
SR	Spin rotation
TD	Time domain, also Pulse EPR
TEMPONE	4-oxo-2,2,6,6-tetramethyl-piperidinyl-oxyl

THERM Thermally Activated Process

TOMCO RF Amplifier Producer, http://www.tomcorf.com/

VHF Very High Frequency, ITU designated range of 30-300 MHz

CHAPTER 1

INTRODUCTION

1.1 Where Is The Oxygen?

Tomlinson and Gray first reported a diverse partial pressure of oxygen (pO_2) in tumors in 1955 [1]. Since then hypoxic fractions have been shown to make up to 25% of uterine, cervix, head/neck and breast cancers [2], whereas no such areas exist in normal tissue. Tumor hypoxic regions are associated with resistance to radiation [3] and poor patient prognosis. X-ray irradiation alone does not produce radicals of sufficient strength to damage tumor DNA. Instead the radicals induced by irradiation produce the more powerful superoxide radical, and superoxide confers the lethal damage. Knowledge of the spatial distribution of O_2 in tumors can be used for localization and improvement of the efficiency of radiation treatment.

Oxygen is ubiquitous in the body, and multiple techniques have been developed to measure oxygen concentration (oxymetry) in tumors or after ischemic events [4]. The first considerations for any method are whether the method is quantitative or qualitative, and in what location the oxygen can be measured. Blood Oxygen Level-Dependent (BOLD) imaging can measure changes in blood oxygenation by detecting changes in T_2 weighted nuclear magnetic resonance images (MRI), but does not provide quantitative information and cannot access the oxygen level in tissue [5]. The current “gold standard”

in quantitative oxymetry are microelectrodes which measure the electric current from reduction of oxygen at the cathode. Since oxygen is consumed during the measurement, repeated measurements cannot be taken. Oxymetry by electrodes is also highly invasive. Some methods, such as positron emission tomography (PET) imaging, and ^{19}F MRI require infusion of exogenous probes. For PET imaging, these are short-lived radionuclides based off ^{19}F-containing imidazoles [5], and costly cyclotrons are required to produce the radionuclides. ^{19}F-MRI monitors the spin-lattice relaxation rate of injected per-fluorocarbon (PFC). Since the rate of relaxation varies linearly with oxygen concentration, this is a quantitative technique applicable to both the vasculature and organs. The limiting factors for ^{19}F-MRI are the unknown toxicity PFC's, the lack of ^{19}F channels in most clinical scanners, and sensitivity limitations at low (1.5 T) fields [6].

In 1994 Dr. Howard Halpern at the University of Chicago reported the measurement of oxygen *in* vivo using murine fibrosarcomas implanted in mouse leg using electron paramagnetic resonance (EPR) at 250 MHz [7]. This stimulated other work on murine sarcomas [8, 9]. EPR imaging (EPRI) has developed as an alternative quantitative technique for measuring oxygen concentration [10-15]. The quantitative nature of EPRI is derived from the interaction of an exogenously delivered EPR sensitive probe with oxygen in the tumor or target site. Collision with O_2 causes a broadening of line width and decrease in the characteristic relaxation time of the probe which may be calibrated so that a change in line width or relaxation time in vivo reports on a change in $[O_2]$. EPR probes are also sensitive to temperature, microviscosity [16] and pH [17-21].

All of these features may be monitored in the heterogeneous tumor environment with the spatial resolution of an image.

1.2 Development Of EPRI

For the purposes of this dissertation, the term "low-frequency" for *in vivo* work will span the region between 250 MHz and 1.2 GHz. In this span of frequencies the penetration depth of RF energy ranges from 1 cm at 1 GHz to ca. 7 cm at 250 MHz, offering a wide range for imaging biological targets deep within an organism or near the surface. The development effort behind EPRI over the last twenty years is weighted heavily towards the continuous wave (CW) method [8, 9] [22-41] (Fig. 1.1) as this is the most well characterized and familiar EPR method.

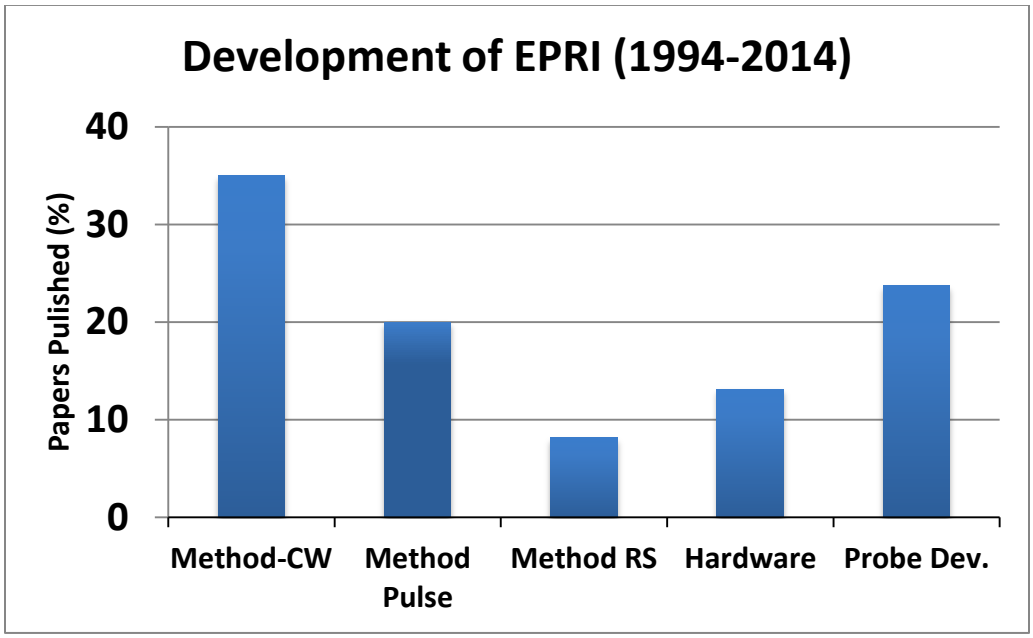

Figure 1.1 Development of EPRI has occurred through many paths. A sampling of over 160 papers from 1994 to 2014 paint a picture of where development effort has been focused.

Most commercial EPR spectrometers operate at frequencies of 9.5 GHz and higher, so new instruments had to be constructed to operate at lower frequencies [42-45]. New means of data acquisition and post-processing were explored [46-51], and comparisons were made to optimize image reconstruction methods [52-57]. Resonators, devices which focus the radiofrequency energy and then collect the signal after excitation, had to be re-designed for larger samples, and samples that move [58-68]. The continuous wave (CW) method used for imaging non-living objects at higher frequencies suffers under *in vivo* conditions. For CW methods the highest EPR signal is observed under high efficiency (high Q-value) resonator conditions. Animals are comprised to a large extent of water, which is lossy (absorbs radio- or microwave energy), and represent a very low resonator Q condition. Techniques better suited for low-Q condition, like time domain (pulse) EPR were developed [69-87]. The sensitivity of pulsed EPR is constrained by the rapid decay of the transient response from the spins after application of the pulse. The electron relaxation times for soluble exogenous probes range from 0.5 to 12 microseconds at 250 MHz [88, 89]. The resonator response, or "ringing" after the pulse can be from 2 to 4 microseconds, and is large relative to the response of the spins, making pulse EPR feasible for only a small selection of the radicals available for *in vivo* EPR. Low frequency pulse EPR requires switching of RF power on the order of tens of nanoseconds, leading to development of new RF amplifiers [90-92]. Recent comparisons between CW and Pulse methods have shown the strengths and weakness of each technique [93, 94].

The rapid scan (RS) technique developed at the University of Denver [95-101] is "middle ground" between pulse and CW EPR for *in vivo* applications. As in the CW experiment, the field is swept with low RF power applied continuously, but the field is swept orders of magnitude faster than in CW, allowing fast signal averaging to amplify weak signals. This is similar to fast averaging of the transient response in pulse EPR. Rapid scan is not hindered by resonator ringing, because the RF is not pulsed, and so probes with short relaxation times can be used. The similarities and differences for the three techniques are the focus of more discussion in Chapter 2.

1.3 The Best Probe For EPRI

The growth of EPRI has driven synthetic development of the exogenous probe molecules that are monitored. Fig. 1.2 shows the structure of several stable radicals, which can be used as EPRI probes and categorized into either soluble molecular probes [102] (Fig. 1.2 A, B) or particulate probes (Fig. 1.2 C). The most common molecular probes are the nitroxide [103] [104] [105] and trityl [106-110] molecules which are directly dissolved in the examined systems and can travel to other biological compartments. Particulate probes are insoluble materials that are implanted and used to report on their immediate environment including carbonaceous materials or crystalline forms of lithium phthalocyanine (LiPc) [111-114]. The particulate probes can be much more sensitive to oxygen than molecular probes, but implantation is highly invasive and the probes cannot move to other sites once injected.

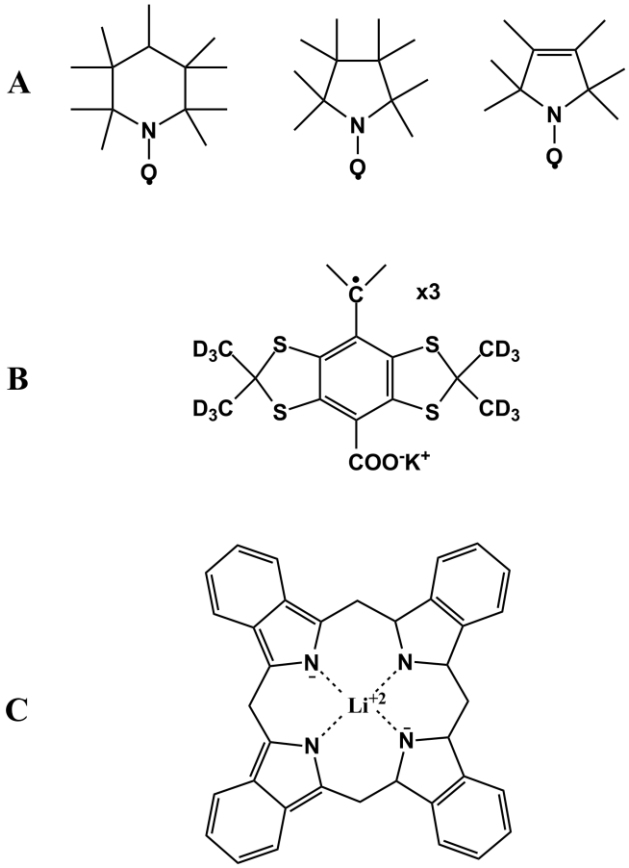

Figure 1.2. **Structures of common probes used for EPRI.** The radicals discussed in the text. Nitroxides (A) and trityls (B) are water soluble while lithium phthalocyanine (LiPc, C) probes are surgically implanted.

Subramanian and Krishna have point out six requirements for an "optimal paramagnetic spin probe"

i. "*A spin probe should have a single EPR line, as multiple lines would be redundant and suffer a decrease in intensity when the signal is distributed to other lines*. [74]"

The trityl probes are often referred to as "single line" probes, since they do not contain large nuclear hyperfine splittings like that of the nitrogen atoms in

nitroxides. Though trityl lines are very narrow, they do have some small unresolved hyperfine, either deuterium in the case of the symmetric trityl (Trityl-CD_3) [106], or very small proton hyperfine in the case of Ox63 which broaden the spin packet T_2 determined linewidth from ca. 6 mG to 30 mG or 160 mG, respectively. In addition trityl have fully resolved coupling to ^{13}C and the resulting lines account for ~30% of the radical signal. Compare this with the 16 G splittings of a nitroxide spectrum, giving a total spectrum width of ca. 32 G. A pulse short enough to excite the entire nitroxide spectrum is not possible, and it is not feasible to scan the entire spectrum for CW experiments, which lead Subramanian and Krishna to specify the narrow line trityl probes as ideal for imaging.

ii. "*The line width should be as narrow as possible so that some signal remains after the long characteristic dead times which dominate at the lower frequencies of EPRI*. [74]"

For a purely Lorentzian line, the width of the spectrum is inversely proportional to T_2. For a given resonator Q, the characteristic ringdown (dead time) will increase as operating frequency is decreased. A simple analysis would then be that the most narrow line probe would be the best. In practice, no linewidth of an EPRI probe is strictly relaxation determined. Hyperfine broadening can cause a large variation in measured linewidth that is not reflective of large changes in T_2 [115]. This is illustrated with a series of nitroxide radicals in Chapter 3. The relaxation time constant which described the decay of the signal

after a pulse is designated T_2^* and is shorter than the spin-packet determined T_2 if there is unresolved hyperfine coupling. The point would be better made by saying the relaxation times (T_1 and T_2) should be as long as possible, to facilitate imaging at low frequencies. Relaxation times of the trityl radicals from 1 GHz to 250 MHz range from 6-16 microseconds [89]. Relaxation times for the nitroxide probes currently used for *in vivo* imaging are on the order of 500 ns to 1 microsecond [88]. Chapters 4 and 5 address why the relaxation times for nitroxides are so short, and suggests how this class of radicals could be synthesized differently to achieve relaxation times 4-10 time longer.

iii. "*The in vivo half-life of the probe must be at least 10 minutes to permit collection of 3D images*. [74]"

A major drawback for the six-member ring nitroxide structure shown in Fig. 1.2 is easy reduction *in vivo*, with a half life on the order of 30-60 s post injection. The five-member ring structures are less susceptible to reduction. Synthetic modifications to the nitroxide base structure can result in longer intracellular lifetime [116]. The trityl radicals are 5-6 times larger than the nitroxide structures and carry three negative charges (carboxy groups) and have *in vivo* half lives between 17 and 21 minutes [117]. The trityl radical can accumulate to a high concentration in the bladder and obscure imaging of the tumor in mouse studies. Placement of a catheter in the mouse for *in vivo* studies allows recovery of trityl radical cleared by the renal system [118].

iv. "*The spin probe should be water soluble for administration either intravenously or intraperitonially* [74]."

The trityl probes typically used for *in vivo* imaging have been made water soluble with the addition of a carboxylic acid group on each of the three phenyl rings attached to the central carbon. The most commonly used nitroxide probe structures (see Fig. 1.2) are made water soluble simply by addition of a single carboxy group.

v. "*The probe should be able to cross cell membranes or the blood brain barrier*. [74]"

Some nitroxide probes can be designed to cross the blood-brain-barrier (BBB) [119-121]. Their smaller size (ca. 200 g/mol) in relation to trityl radicals allow packing into lysozomes or other vesicles for transport across the cell membrane [122]. Trityl radicals, which are large and negatively charged, do not cross the BBB. This is perhaps the largest drawback for trityl radicals, keeping the application of the radical to imaging of tumors with good access to the blood stream. An alternative would be direct injection of the trityl radical into the tumor body. Esterification of the molecule has become a successful strategy for the intracellular accumulation of both nitroxides [123, 124] and trityls [125]. Intracellular esterases convert the ester to a carboxylic acid which is then trapped in the cell and can accumulate.

vi. "*Probe toxicity should be small at the doses required for EPRI* [74]."

Probe toxicity is in general lower for nitroxides than trityls, based on cell culture assays [126]. A major impediment to imaging with either radical in human subjects is a lack (currently) of FDA study and clearance.

1.4 Challenges To The Implementation Of EPRI In The Clinical Setting

There has been great progress in the last twenty years in the development of EPRI. The effort now turns to implementation in the clinical setting. Three major challenges remain. The first is the development of robust and straightforward instrumentation which can be mass produced and commercialized. A Ph.D. in magnetic resonance should not be a requirement for operating an EPRI machine in the hospital. The second challenge is designing EPRI probes that are stable and non-toxic to humans, and have the longest possible relaxation times to give the very best signal for clinical diagnosis. Larger signal (i.e. the longest relaxation time, or narrowest line) leads to lower dosage and faster completion of the procedure. There are currently no EPRI probes approved by the Food and Drug Administration (FDA), representing the third major hurdle, but there is still much to learn from EPR pre-clinical imaging.

1.5 Dissertation Structure

This dissertation addresses three of the development avenues identified in Fig. 1.1. Chapter 2 introduces the reader to the theory of EPR, and gives an overview of pulse, rapid scan and continuous wave methods. Chapters 3, 4 and 5 focus on the characteristic linewidths and relaxation times of many different nitroxide radicals. Relaxation times are related to the observed CW signal and the structure of the individual molecule. The work

in these chapters explains why relaxation times are shorter for nitroxide spin probes (compared to trityls) and identifies synthetic routes for making nitroxide relaxation times longer. The rapid scan technique is expanded at 250 MHz in Chapter 6 as a series of nitroxide phantoms are imaged. The imaging encompasses the traditional method of a single line out of three (^{14}N) or two (^{15}N) total lines, and makes a comparison with the continuous wave technique. Chapter 7 address advancements in hardware, most notable resonator design for pulse and rapid scan EPR. Chapter 8 brings the work to a close, with a discussion of the future of EPRI, with a focus on the use of nitroxide radicals and the rapid-scan technique.

It is my sincere hope that the work in this dissertation may one day help to overcome the challenges to implementation of EPRI in the clinical setting (Sec. 1.4). EPRI is a powerful biophysical technique, though few in the medical research community are acquainted with it. When that changes (and I think it will sooner than later), low-frequency EPR and EPRI have much to teach cancer researchers. Combined with directed X-ray irradiation, or heavy ion irradiation this benefit will in turn be passed onto patients in the clinical setting. The following quote is from a fictional doctor, but conveys my sentiment on the power of magnetic resonance, and EPRI especially.

"My God man, drilling holes in his head is not the answer! Now, put away your butcher's knives and let me save this patient before it's too late!"

Dr. Leonard H. "Bones" McCoy

1.6 References

Most of the references in this list are cited in the chapter. Some are not, but were part of the ~160 papers collected to create Fig. 1.1. These papers do not represent a comprehensive survey by any stretch, but are meant to give interested parties a solid base for understanding EPRI. Papers relating to relaxation times of nitroxide or trityl probes have been left out in some cases. Those papers are cited in subsequent chapters in this dissertation.

[1] R. H. Tomlinson and L. H. Gray, "The histological structure of some human lung cancers and the possible implications for radiotherapy," *British Journal of Cancer*, vol. 9, pp. 539-849, 1955.

[2] P. Vaupel, M. Hockel and A. Mayer, "Detection and characterization of tumor hypoxia using pO2 histography," *Anitoxidant and Redox Signaling*, vol. 9, pp. 1221-1235, 2007.

[3] J. M. Brown and W. R. Wilson, "Exploiting tumor hypoxia in cancer treatment," *Nat. Rev*., vol. 4, pp. 437-447, 2004.

[4] P. Kuppusamy and J. L. Zweier, "Cardiac applications of EPR imaging," *NMR in Biomedicine*, vol. 17, no. 5, pp. 226-239, 2004.

[5] R. Ahmad and P. Kuppusamy, "Theory, Instrumentation and Applications of Electron Paramagnetic Resonance Oximetry," *Chem. Rev*., vol. 110, pp. 3212-3236, 2010.

[6] R. Avni, B. Cohen and M. Neeman, "Hypoxic stress and cancer: imaging the axis of evil in tumor metastasis," *NMR in Biomedicine*, vol. 24, pp. 569-581, 2010.

[7] H. J. Halpern, C. Yu, M. Peric, E. D. Barth, D. J. Grdina and B. A. Teicher, "Oxymetry deep in tissues with low-frequency electron paramagnetic resonance," *Proc. Natl. Acad. Sci. U.S.A*., vol. 91, pp. 13047-13051, 1994.

[8] H. J. Halpern, Y. Cheng, M. Peric, E. D. Barth, G. S. Karczmar, J. N. River, D. J. Grdina and B. A. Teicher, "Measurement of Differences in pO2 in Response to Perfuorocarbon/Carbogen in FSa and NFSa Murine Fibrosarcomas with Low-Frequency Electron Paramagnetic Resonance Oximetry," *Radiation Research*, vol. 145, no. 5, pp. 610-618, 1996.

[9] P. Kuppusamy, M. Afeworki, R. A. Shankar, D. Coffin, M. C. Krishna, S. M. Hahn, J.

B. Mitchell and J. L. Zweier, "In vivo Electron Paramagnetic Resonance Imaging of Tumor Heterogeneity and oxygenation in a murine model," *Cancer Research*, vol. 58, no. 7, pp. 15662-1568, 1998.

[10] B. Gallez, C. Baudelet and B. F. Jordan, "Assessment of tumor oxygenation by electron paramagnetic resonance: principles and applications," *NMR in Biomedicine*, vol. 17, no. 5, pp. 240-262, 2004.

[11] H. J. Halpern, "Applications of In Vivo EPR Spectroscopy and Imaging in Cancer Research," in In Vivo EPR (ESR): Biological Magnetic Resonance vol. 18, L. Berliner, Ed., Springer, 2003, pp. 469-482.

[12] H. M. Swartz and R. B. Clarkson, "The measurement of oxygen in vivo using EPR techniques," *Phys. Med. Biol.* , vol. 43, p. 1957, 1998.

[13] D. J. Greenslade, A. V. Koptyug and M. R. Symons, "Aspects of low-frequency low-field electron spin resonance," *Annu. Rep. Prog. Chem., Sect. C: Phys. Chem.*, vol. 92, pp. 3-21, 1995.

[14] M. C. Krishna, N. Devasahayam, J. A. Cook, S. Subramanian, P. Kuppusamy and J. B. Mitchell, "Electron Paramagnetic Resonance for Small Animal Imaging Applications," *ILAR J*, vol. 42, no. 3, pp. 209-218, 2001.

[15] H. M. Swartz and J. F. Dunn, "Measurements of Oxygen in Tissues: Overview and Perspectives on Methods," *Oxygen Transport to Tissue XXIV: Advances in Experimental Medicine and Biology*, vol. 530, pp. 1-12, 2003.

[16] H. J. Halpern, G. R. Chandramouli, E. D. Barth, C. Yu, M. Peric, D. J. Grdina and B. A. Teicher, "Diminished Aqueous Microviscosity of Tumors in Murine Models Measured with in Vivo Radiofrequency Electron Paramagnetic Resonance," *Cancer Research*, vol. 15, pp. 5836-5841, 1999.

[17] V. V. Khramtsov, L. M. Weiner, I. A. Grigoriev and L. B. Volodarsky, "Proton Exchange in stable nitroxide radicals. EPR study of the pH of aqueous solutions.," *Chem. Phys. Lett.*, vol. 91, pp. 69-72, 1982.

[18] V. V. Khramtsov, I. A. Grigor'ev, M. A. Foster, D. J. Lurie and I. Nicholson, "Biological Applications of spin pH probes," *Cell. Mol. Biol.*, vol. 46, pp. 1361-1374, 2000.

[19] B. Gallez, K. Mader and H. M. Swartz, "Noninvasive measurements of the pH inside the gut by using pH-sensitive nitroxides. An in vivo ESR study.," *Magn. Reson. Med.*, vol. 36, pp. 694-697, 1996.

[20] A. A. Bobko, I. Dhimitruka, J. L. Zweier and V. V. Khramtsov, "Trityl Radicals as

Persistent Dual Function pH and Oxygen Probes for in Vivo Electron Paramagnetic Resonance Spectroscopy and Imaging: Concept and Experiment," *J. Am. Chem. Soc*., vol. 129, no. 23, pp. 7240-7241, 2007.

[21] I. Dhimitruka, A. A. Bobko, C. M. Hadad, J. L. Zweier and V. V. Khramtsov, "Synthesis and Characterization of Amino Derivatives of Persistent Trityl Radicals as Dual Function pH and Oxygen Paramagnetic Probes," *J. Am. Chem. Soc*., vol. 130, no. 32, pp. 10780-10787, 2008.

[22] M. Elas, B. B. Williams, A. Parasca, C. Mailer, C. A. Pelizzari, M. A. Lewis, J. N. River, G. S. Karczmar, E. D. Barth and H. J. Halpern, "Quantitative tumor oxymetric images from 4D electron paramagnetic resonance imaging (EPRI): Methodology and comparison with bood oxygen level-dependent (BOLD) MRI," *Magn. Reson. Med.* , vol. 49, no. 4, pp. 682-691, 2003.

[23] Y. Deng, R. P. Pandian, R. Ahmad, P. Kuppusamy and J. L. Zweier, "Application of magnetic field over-modulation for improved EPR linewidth measurements using probes with Lorentzian lineshape," *J. Magn. Reson.*, vol. 181, no. 2, pp. 254-261, 2006.

[24] M. Elas, K. H. Ahn, A. Parasca, E. D. Barth, D. Lee, C. Haney and H. J. Halpern, "Electron paramagnetic resonance oxygen images correlate spatially and quantitatively with Oxylite oxygen measurements," *Clinical Cancer Research*, vol. 12, no. 14 (Pt. 1), pp. 4209-4217, 2006.

[25] M. Elas, J. M. Magwood, B. Butler, C. Li, R. Wardak, R. DeVries, E. D. Barth, B. Epel, S. Rubinstein, C. A. Pelizzari, R. R. Weichselbaum and H. J. Halpern, "EPR Oxygen Images Predict Tumor Control by a 50% Tumor Control Radiation Dose," *Cancer Research.*, vol. 73, pp. 5328-5335, 2013.

[26] Y. Hama, K. Matsumoto, R. Murugesan, S. Subramanian, N. Devasahayam, J. W. Koscielniak, F. Hyodo, J. A. Cook, J. B. Mitchell and M. C. Krishna, "Continuous Wave EPR Oximetric Imaging at 300 MHz Using Radiofrequency Power Saturation Effects," *Antioxidants and Redox Signaling*, vol. 9, no. 10, pp. 1709-1716, 2007.

[27] G. Redler, E. D. Barth, K. S. Bauer, J. Y. Kao, G. M. Rosen and H. J. Halpern, "In vivo electron paramagnetic resonance imaging of differential tumor targeting using cis-3,4-di(acetoxymethoxycarbonyl)-2,2,5,5-tetramethyl-1-pyrrolidinyloxyl," *Magn. Reson. Med.*, vol. 71, no. 4, pp. 1650-1656, 2013.

[28] M. Elas, K. Ichikawa and H. J. Halpern, "Oxidative Stress Imaging in Live Animals with Techniques Based on Electron Paramagnetic Resonance," *Radiation Research*, vol. 177, no. 4, pp. 514-523, 2012.

[29] A. A. Bobko, T. D. Eubank, J. L. Voorhees, O. V. Efimova, J. L. Zweier, I. A.

Grigor'ev, A. Samouilov and V. V. Khramtsov, "In vivo monitoring of pH, redox status, and glutathione using L-band EPR of assessment for therapeutic effectiveness in solid tumors," *Magn. Reson. Med.*, vol. 67, no. 6, pp. 1827-1836, 2012.

[30] M. Elas, D. Hleihel, E. D. Barth, C. R. Haney, K. H. Ahn, C. A. Pelizzari, B. Epel, R. R. Weichselbaum and H. J. Halpern, "Where it's at really matters: in situ in vivo vascular *endothelial* growth factor spatially correlates with electron paramagnetic resonance pO2 images in tumors of living mice.," *Mol .Imag. Biol.*, vol. 13, no. 6, pp. 1107-1113, 2011.

[31] G. He, "Electron Paramagnetic Resonance Oximetry and Redoximetry," *Advanced Protocols in Oxidative Stresss II: Methods in Molecular Biology*, vol. 594, pp. 85-105, 2010.

[32] J. Shen, R. Sood, J. Weaver, G. S. Timmins, A. Schnell, M. Miyake, J. P. Kao, G. M. Rosen and K. J. Liu, "Direct visualization of mouse brain oxygen distribution by electron paramagnetic resonance imaging: application to focal cerebral ischemia.," *J. Cereb. Blood Flow Metab.*, vol. 29, no. 10, pp. 1695-1703, 2009.

[33] P. Tsai, G. L. Cao, T. J. Merkel and G. M. Rosen, "Spin labelling of Bacillus anthracis endospores: a model for in vivo tracking by EPR imaging.," *Free Rad. Res.*, vol. 42, no. 1, pp. 49-56, 2008.

[34] R. Ahmad, D. S. Vikram, L. C. Potter and P. Kuppusamy, "Estimation of mean and median pO2 values for a composite EPR spectrum," *J. Magn. Reson.*, vol. 192, no. 2, pp. 269-275, 2008.

[35] S. Som, L. C. Potter, R. Ahmad, D. Vikram and P. Kuppusamy, "EPR oximetry in three spatial dimensions using sparse spin distribution," *J. Magn. Reson.*, vol. 193, no. 2, pp. 210-217, 2008.

[36] M. Elas, R. Bell, D. Hleihel, E. D. Barth, C. McFaul, C. R. Haney , J. Bielanska, K. Pustelny, K. Ahn, C. A. Pelizzari, M. Kocherginsky and H. J. Halpern, "Electron Paramagnetic Resonance Oxygen Image Hypoxic Fraction Plus Radiation Dose Strongly Correlates With Tumor Cure in FSa Fibrosarcomas," *International Journal of Radiation Oncology Biology Physics*, vol. 71, no. 2, pp. 542-549, 2008.

[37] C. R. Haney, A. D. Parasca, X. Fan, R. M. Bell, M. A. Zamora, G. S. Karczmar, H. J. Maucen, H. J. Halpern, R. R. Weichselbaum and C. A. Pelizzari, "Characterization of response to radiation mediated gene therapy by means of multimodality imaging," *Magn. Reson. Med.*, vol. 62, no. 2, pp. 348-356, 2009.

[38] X. Pan, D. Xia and H. J. Halpern, "Targeted-ROI imaging in electron paramagnetic resonance imaging," *J. Magn. Reson.*, vol. 187, no. 1, pp. 66-77, 2007.

[39] X. Zhu, L. Zuo, A. J. Cardounel, J. L. Zweier and G. He, "Characterization of In Vivo Tissue Redox Status, Oxygenation, and Formation of Reactive Oxygen Species in Postichemic Myocardium," *Antioxidants and Redox Signaling*, vol. 9, no. 4, pp. 447-455, 2007.

[40] B. B. Williams, X. Pan and H. J. Halpern, "EPR Imaging: The relationship between CW spectra acquired from an extended sample subjected to fixed stepped gradients and the Radon transform of the resonance density," *J. Magn. Reson.*, vol. 174, no. 1, pp. 88-96, 2005.

[41] G. Ilangovan, H. Li, J. L. Zweier, M. C. Krishna, J. B. Mitchell and P. Kuppusamy, "In vivo measurement of regional oxygenation and imaging of redox status in RIF-1 murine tumor: Effect of carbogen breathing," *Magn. Reson. Med.*, vol. 48, no. 4, pp. 723-730, 2002.

[42] B. Epel, S. V. Sundramoorthy, C. Mailer and H. J. Halpern, "A versatile high speed 250-MHz pulse imager for biomedical applications," *Concepts Magn. Reson.*, vol. 33B, pp. 163-176, 2008.

[43] R. Murugesan, M. Afeworki, J. A. Cook, N. Devasahayam, R. Tschudin, J. B. Mitchell, S. Subramanian and M. C. Krishna, "A broadband pulsed radio frequency electron paramagnetic resonance spectrometer for biological applications," *Rev. Sci. Instrum.*, vol. 59, p. 1869, 1998.

[44] R. W. Quine, G. A. Rinard, S. S. Eaton and G. R. Eaton, "A pulsed and continuous wave 250 MHz electron paramagnetic resonance spectrometer," *Concepts Magn. Reson.*, vol. 15, no. 1, pp. 59-91, 2002.

[45] G. A. Rinard, R. W. Quine, G. R. Eaton, S. S. Eaton, E. D. Barth, C. A. Pelizzari and H. J. Halpern, "Magnet and gradient coil system for low-field EPR imaging," *Concepts Magn. Reson.*, vol. 15, pp. 51-58, 2002.

[46] C. Mailer, B. H. Robinson, B. B. Williams and H. J. Halpern, "Spectral fitting: The extraction of crucial information from a spectrum and a spectral image," *Magn. Reson. Med.*, vol. 49, no. 6, pp. 1175-1180, 2003.

[47] S. Subramanian, R. Murugesan, N. Devasahayam, J. A. Cook, M. Afeworki, T. Pohida, R. G. Tschudin, J. B. Mitchell and M. C. Krishna, "High-Speed Data Acquisition System and Receiver Configurations for Time-Domain Radiofrequency Electron Paramagnetic Resonance Spectroscopy and Imaging," *J. Magn. Reson.*, vol. 137, no. 2, pp. 379-388, 1999.

[48] A. G. Taube, S. Subramanian, R. Murugesan, N. Devasahayam, J. B. Mitchell, M. C. Krishna and J. A. Cook, "An application system for automation of constant-time radio frequency electron paramagnetic resonance imaging," *Computer Methods and*

Programs in Biomedicine, vol. 72, no. 2, pp. 127-138, 2003.

[49] M. Tseitlin, R. W. Quine, S. S. Eaton and G. R. Eaton, "Use of polyphase continuous excitation based on the Frank sequence in EPR," *J. Magn. Reson*. , vol. 211, no. 2, pp. 221-227, 2011.

[50] R. H. Pursley, G. Salem, N. Devasahayam, S. Subramanian, J. Koscielniak, M. C. Krishna and T. J. Pohida, "Integration of digital signal processing technologies with pulsed electron paramagnetic resonance imaging," *J. Mag. Reson.* , vol. 178, no. 2, pp. 220-227, 2006.

[51] R. H. Pursley, G. Salem, T. J. Pohida, N. Devashayam, S. Subramanian and M. C. Krishna, "Direct detection and time-locked subsampling applied to pulsed electron paramagnetic resonance imaging," *Rev. Sci. Instrum.*, vol. 76, no. 5, 2005.

[52] M. Tseitlin, T. Czechowski, S. S. Eaton and G. R. Eaton, "Regularized Optimization (RO) Reconstruction for Oximetric EPR Imaging," *J. Magn. Reson.*, vol. 194, no. 2, pp. 212-221, 2008.

[53] M. Tseitlin, A. Dhami, S. S. Eaton and G. R. Eaton, "Comparison of maximum entropy and filtered back-projection methods to reconstruct rapid-scan EPR images," *J. Magn. Reson.*, vol. 184, no. 1, pp. 157-168, 2007.

[54] K. H. Ahn and H. J. Halpern, "Comparison of local and global angular interpolation applied to spectral-spatial EPR image reconstruction," *Med. Phys.*, vol. 34, no. 3, pp. 1047-1052, 2007.

[55] K. H. Ahn and H. J. Halpern, "Spatially Uniform Sampling in 4-D EPR spectral-spatial imaging," *J. Magn. Reson.*, vol. 185, no. 1, pp. 152-158, 2007.

[56] K. H. Ahn and H. J. Halpern, "Object dependent sweep width reduction with spectral-spatial EPR imaging," *J. Magn. Reson.*, vol. 186, no. 1, pp. 105-111, 2007.

[57] S. Som, L. C. Potter, R. Ahmad and P. Kuppusamy, "A parametric approach to spectral-spatial EPR imaging," J. Magn. Reson., vol. 186, no. 1, pp. 1-10, 2007.

[58] V. S. Sundramoorthy, B. Epel and H. J. Halpern, "Orthogonal resonators for pulse in vivo electron paramagnetic imaging at 250 MHz," *J. Magn. Reson.*, vol. 240, pp. 45-51, 2014.

[59] J. R. Biller, M. Tseitlin, R. Q. Quine, G. A. Rinard, H. A. Weismiller, H. Elajaili, G. M. Rosen, J. Y. Kao, S. S. Eaton and G. R. Eaton, "Imaging of Nitroxides at 250 MHz using Rapid-Scan Electron Paramagnetic Resonance," *J. Magn. Reson.*, vol. 242, pp. 162-168, 2014.

[60] N. Devasahayam, S. Subramanian, R. Murugesan, J. Cook, M. Afeworki, R. G. Tschudin, J. B. Mitchell and M. C. Krishna, "Parallel Coil Resonators for Time-Domain Radiofrequency Electron Paramagnetic Resonance Imaging of Biological Objects," *J. Magn. Reson.*, vol. 142, no. 1, pp. 168-176, 2000.

[61] Y. Kawada, H. Hirata and H. Fujii, "Use of multi-coil parallel-gap resonators for co-registration EPR/NMR imaging," *J. Magn. Reson.*, vol. 184, no. 1, pp. 29-38, 2007.

[62] G. A. Rinard, R. W. Quine, J. R. Biller and G. R. Eaton, "A Wire-Crossed-Loop Resonator for Rapid Scan EPR," *Concepts Magn. Reson.*, vol. 37B, no. 2, pp. 86-91, 2010.

[63] G. A. Rinard, R. W. Quine, G. R. Eaton and S. S. Eaton, "250 MHz Crossed-Loop Resonator for Pulsed Electron Paramagnetic Resonance," *Concepts Magn. Reson.*, vol. 15, no. 1, pp. 37-46, 2002.

[64] H. Jang, S. Subramanian, N. Devasahayam, K. Saito, S. Matsumoto, M. C. Krishna and A. B. McMillan, "Single Acquisition Quantitative Single-Point Electron Paramagnetic Resonance Imaging," *Magn. Reson. Med.*, vol. 70, no. 4, pp. 1173-1181, 2013.

[65] M. Tseitlin, R. W. Quine, S. S. Eaton, G. R. Eaton, H. J. Halpern and J. H. Ardenkjaer-Larsen, "Use of the Frank sequence in pulsed EPR.," *J. Magn. Reson.*, vol. 209, no. 2, pp. 306-309, 2011.

[66] V. S. Subramanian, B. Epel, C. Mailer and H. J. Halpern, "A passive dual-circulator based transmit/receive switch for use with reflection resonators in pulse EPR," *Concepts Magn. Reson.*, vol. 35B, no. 3, pp. 133-138, 2009.

[67] G. A. Rinard, R. W. Quine and G. R. Eaton, "An L-band Crossed Loop (Bimodal) EPR Resonator," *J. Magn. Reson.*, vol. 144, pp. 85-88, 2000.

[68] B. Epel, S. V. Sundramoorthy and H. J. Halpern, "Retractable loop-gap resonators for electron paramagnetic resonance imaging with in situ irradiation capabilities," *Concepts Magn. Reson.*, vol. 39B, pp. 167-172, 2011.

[69] S. Subramanian, J. B. Mitchell and M. C. Krishna, "Time-Domain Radio Frequency EPR Imaging," in In Vivo EPR (ESR) Biological Magnetic Resonance, vol. 18, 2003, pp. 153-197.

[70] M. Afeworki, G. M. van Dam, N. Devasahayam, R. Murugesan, J. Cook, D. Coffin, J. H. A-Larsen, J. B. Mitchell, S. Subramanian and M. C. Krishna, "Three-dimensional whole body imaging of spin probes in mice by time-domain radiofrequency electron paramagnetic resonance," *Magn. Reson. Med.*, vol. 43, no.

3, pp. 375-382, 2000.

[71] B. Epel and H. J. Halpern, "Comparison of transverse and spin-lattice relaxation based electron paramagnetic resonance oxygen images," in Biomedical Imaging: From Nano to Macro, 2011 IEEE International Symposium on, Chicago, 2011.

[72] C. Mailer, S. V. Sundramoorthy, C. P. Pelizzari and H. J. Halpern, "Spin echo spectroscopic electron paramagnetic resonance imaging," *Magn. Reson. Med.,* vol. 55, no. 4, pp. 904-912, 2006.

[73] P. Seifi, B. Epel, S. V. Sundramoorthy, C. Mailer and H. J. Halpern, "Frequency bandwidth extension by use of multiple Zeeman field offsets for electron spin-echo EPR oxygen imaging of large objects," *Med. Phys.*, vol. 38, p. 3062, 2011.

[74] S. Subramanian and M. C. Krishna, "Time-Domain Radio Frequency EPR Imaging," in Biological Magnetic Resonance: Biomedical EPR- Part A: Free Radicals, Metals, Medicine and Physiology, vol. 23, 2005, pp. 321-382.

[75] B. Epel, M. K. Bowman, C. Mailer and H. J. Halpern, "Absolute oxygen R1e imaging in vivo with pulse electron paramagnetic resonance," *Magn. Reson. Med.*, p. DOI: 10.1002/mrm.24926, 2013.

[76] M. C. Krishna, S. Matsumoto, H. Yasui, K. Saito, N. Devasahayam, S. Subramanian and J. B. Mitchell, "Electron Paramagnetic Resonance Imaging of Tumor pO2," *Radiation Research*, vol. 177, no. 4, pp. 376-386, 2012.

[77] V. V. Khramtsov, G. L. Caia, K. Shet, E. Kesselring, S. Petryakov, J. L. Zweier and A. Samouilov, "Variable Field Proton–Electron Double-Resonance Imaging: Application to pH mapping of aqueous samples," *J. Magn. Reson.*, vol. 202, no. 2, pp. 267-273, 2010.

[78] P. Seifi, B. Epel, C. Mailer and H. J. Halpern, "Multiple-stepped Zeeman field offset method applied in acquiring enhanced resolution spin-echo electron paramagnetic resonance images," *Med. Phys.*, vol. 37, pp. 5412-5420, 2010.

[79] F. Hyodo, R. Murugesan, K. Matsumoto, E. Hyodo, S. Subramanian, J. B. Mitchell and M. C. Krishna, "Monitoring redox-sensitive paramagnetic contrast agent by EPRI, OMRI and MRI," *J. Magn. Reson.*, vol. 190, no. 1, pp. 105-112, 2008.

[80] S. Matsumoto, F. Hyodo, S. Subramanian, N. Devasahayam, J. Munasinghe, E. Hyodo, C. Gadisetti, J. A. Cook, J. B. Mitchell and M. C. Krishna, "Low-field paramagnetic resonance imaging of tumor oxygenation and glycolytic activity in mice," *J. Clin. Invest.*, vol. 118, pp. 1965-1973, 2008.

[81] N. Devasahayam, S. Subramanian and M. C. Krishna, "A novel programmable pulse

generator with nanosecond resolution for pulsed electron paramagnetic resonance applications," *Rev. Sci. Instrum.*, vol. 79, no. 2, pp. 026106-1 to 026106-4, 2008.

[82] K. Matsumoto, S. Subramanian, R. Murugesan, J. B. Mitchell and M. C. Krishna, "Spatially Resolved Biologic Information from In Vivo EPRI, OMRI, and MRI," *Antioxidant and Redox Signaling*, vol. 9, no. 8, pp. 1125-1142, 2007.

[83] K. Matsumoto, S. Subramanian, N. Devasahayam, T. Aravalluvan, R. Murugesan, J. A. Cook, J. B. Mitchell and M. C. Krishna, "Electron paramagnetic resonance imaging of tumor hypoxia: Enhanced spatial and temporal resolution for in vivo pO2 determination," *Mag. Reson. Med.* , vol. 55, no. 5, pp. 1157-1163, 2006.

[84] M. C. Krishna, S. English, K. Yamada, J. Yoo, R. Murugesan, N. Devasahayam, J. A. Cook, K. Golman, J. H. Ardenkjaer-Larsen, S. Subramanian and J. B. Mitchell, "Overhauser enhanced magnetic resonance imaging for tumor oximetry: Coregistration of tumor anatomy and tissue oxygen concentration," *Proc. Natl. Acad. Sci. U.S.A.*, vol. 99, no. 4, pp. 2216-2221, 2002.

[85] S. Subramanian, N. Devasahayam, R. Murugesan, K. Yamada, J. Cook, A. Taube, J. B. Mitchell, J. B. Lohman and M. C. Krishna, "Single-point (constant-time) imaging in radiofrequency Fourier transform electron paramagnetic resonance," *Magn. Reson. Med.*, vol. 48, no. 2, pp. 370-379, 2002.

[86] S. Subramanian, K. Yamada, A. Irie, R. Murugesan, J. A. Cook, N. Devasahayam, G. M. Van Dam, J. B. Mitchell and M. C. Krishna, "Noninvasive in vivo oximetric imaging by radiofrequency FT EPR," *Magn. Reson. Med.*, vol. 47, no. 5, pp. 1001-1008, 2002.

[87] R. Murugesan, J. A. Cook, N. Devasahayam, M. Afeworki, S. Subramanian, R. Tschudin, J. A. Larsen, J. B. Mitchell, A. Russo and M. C. Krishna, "In vivo imaging of a stable paramagnetic probe by pulsed-radiofrequency electron paramagnetic resonance spectroscopy," *Magn. Reson. Med.*, vol. 38, no. 3, pp. 409-414, 1997.

[88] J. R. Biller, H. Elajaili, V. Meyer, G. M. Rosen, S. S. Eaton and G. R. Eaton, "Electron spin-lattice relaxation mechanisms of rapidly tumbling nitroxide radicals," *J. Magn. Reson.*, vol. 236, pp. 47-56, 2013.

[89] R. Owenius, G. R. Eaton and S. S. Eaton, "Frequency (250 MHz to 9.2 GHz) and viscosity dependence of electron spin relaxation of triarylmethyl radicals at room temperature.," *J. Magn. Reson.*, vol. 172, no. 1, pp. 168-175, 2005.

[90] R. W. Quine, G. R. Eaton, S. Dillon and D. Myer, "Fast-response VHF-band pulsed power amplifiers," *Concepts Magn. Reson.*, vol. 27B, pp. 1-7, 2005.

[91] R. W. Quine, G. R. Eaton and S. Dillon, "Fast-response VHF pulsed 2 kW power amplifiers," *Concepts Magn. Reson.*, vol. 29B, no. 4, pp. 185-190, 2006.

[92] R. W. Quine, M. Tseytlin, S. S. Eaton and G. R. Eaton, "A very fast switched-attenuator circuit for microwave and RF applications," *Concepts Magn. Reson.*, vol. 37B, pp. 39-44, 2010.

[93] B. Epel, S. V. Sundramoorthy, E. D. Barth, C. Mailer and H. J. Halpern, "Comparison of 250 MHz electron spin echo and continuous wave oxygen EPR imaging methods for in vivo applications," *Med. Phys.*, vol. 38, pp. 2045-2052, 2011.

[94] S. Subramanian, K. Matsumoto, J. B. Mitchell and M. C. Krishna, "Radio frequency continuous-wave and time-domain EPR imaging and Overhauser-enhanced magnetic resonance imaging of small animals: instrumental developments and comparison of relative merits for functional imaging," *NMR in Biomedicine*, vol. 17, no. 5, pp. 263-297, 2004.

[95] J. W. Stoner, D. Szymanski, S. S. Eaton, R. W. Quine, G. A. Rinard and G. R. Eaton , "Direct-detected rapid-scan EPR at 250 MHz," *J. Magn. Reson.*, vol. 170, pp. 127-135, 2004.

[96] J. P. Joshi, J. R. Ballard, G. A. Rinard, R. W. Quine, S. S. Eaton and G. R. Eaton, "Rapid-scan EPR with triangular scans and Fourier deconvolution to recover the slow scan spectrum," *J. Magn. Reson.*, vol. 175, pp. 44-51, 2005.

[97] M. Tseitlin, A. Dhami, R. W. Quine, G. A. Rinard, S. S. Eaton and G. R. Eaton, "Electron spin T2 of a nitroxyl radical at 250 MHz measured by rapid scan EPR," *Appl. Magn. Reson.*, vol. 30, pp. 651-656, 2006.

[98] M. Tseitlin, G. A. Rinard, R. W. Quine, S. S. Eaton and G. R. Eaton, "Deconvolution of Sinusoidal Rapid EPR Scans," *J. Magn. Reson.*, vol. 208, no. 2, pp. 279-283, 2011.

[99] M. Tseitlin, T. Czechowski, R. W. Quine, S. S. Eaton and G. R. Eaton, "Background Removal Procedure for Rapid Scan EPR," *J. Magn. Reson.*, vol. 196, no. 1, pp. 48-53, 2009.

[100] M. Tseitlin, R. W. Quine, G. A. Rinard, S. S. Eaton and G. R. Eaton, "Combining Absorption and Dispersion Signals to Improve Signal-to-noise for Rapid Scan EPR Imaging," *J. Magn. Reson.*, vol. 203, no. 2, pp. 305-310, 2010.

[101] R. W. Quine, G. A. Rinard, S. S. Eaton and G. R. Eaton, "Quantitative rapid scan EPR spectroscopy at 258 MHz," *J. Magn. Reson.*, vol. 205, no. 1, pp. 23-27, 2010.

[102] H. J. Halpern, "Stable Soluble Paramagnetic Compounds," in Biological Magnetic Resonance (18) In Vivo EPR (ESR), vol. 18, Springer, 2003, pp. 201-232.

[103] H. Utsumi, K. I. Yamada, K. Ichikawa, K. Sakai, Y. Kinoshita and S. Matsumoto, "Simultaneous molecular imaging of redox reactions monitored by Overhauser-enhanced MRI with 14N and 15N labeled nitroxyl radicals," *Proc. Nat. Acad. Sci. U.S.A.*, vol. 103, pp. 1463-1468, 2006.

[104] V. Khramtsov, "Functional EPR Spectroscopy and Imaging of Nitroxides," in Supramolecular Structure and Function 9, 2007, pp. 181-208.

[105] S. R. Burks, L. F. Macedo, E. D. Barth, K. H. Tkaczuk, S. S. Martin, G. M. Rosen, H. J. Halpern, A. M. Brodie and J. P. Kao, "Anti-HER2 immunoliposomes for selective delivery of electron paramagnetic resonance imaging probes to HER2-overexpressing breast tumor cells.," *Breast Cancer Res. Treat.*, vol. 124, no. 1, pp. 121-131, 2010.

[106] J. H. Ardenkjaer-Larsen, I. Laursen, I. Leunback, G. Ehnhom, L. G. Wistrand, J. S. Petersson and K. Golman, "EPR and DNP properties of certain novel single electron contrast agents intended for oximetric imaging," *J. Magn. Reson.*, vol. 133, no. 1, pp. 1-12, 1998.

[107] T. J. Reddy, T. Iwama, H. J. Halpern and V. H. Rawal, "General Synthesis of Persistent Trityl Radicals for EPR Imaging of Biological Systems," *J. Org. Chem.*, vol. 67, no. 14, pp. 4635-4639, 2002.

[108] M. K. Bowman, C. Mailer and H. J. Halpern, "The solution conformation of triarylmethyl radicals," *J. Magn. Reson.*, vol. 172, no. 2, pp. 254-267, 2005.

[109] I. Dhimitruka, O. Grigorieva, J. L. Zweier and V. V. Khramtsov, "Synthesis, structure, and EPR characterization of deuterated derivatives of Finland trityl radical," *Bioorg. Med. Chem. Let.*, vol. 20, no. 13, pp. 3946-3949, 2010.

[110] A. A. Bobko, I. Dhimitruka, T. D. Eubank, C. B. Marsh, J. L. Zweier and V. V. Khramtsov, "Trityl-based EPR probe with enhanced sensitivity to oxygen," *Free Rad. Biol. Med.*, vol. 47, no. 5, pp. 654-658, 2009.

[111] H. M. Swartz, J. Dunn, O. Grinberg, J. O'Hara and T. Walczak, "What Does EPR Oximetry with Solid Particles Measure- and How Does this Relate to Other Measures of PO?," Oxygen Transport to Tissue XIX, vol. 428, pp. 663-670, 1997.

[112] G. Ilangovan, H. Li, J. L. Zweier and P. Kuppusamy, "Electrochemical Preparation and EPR Studies of Lithium Phthalocyanine. 3. Measurements of Oxygen Concentration in Tissues and Biochemical Reactions," *J. Phys. Chem. B*, vol. 105,

no. 22, pp. 5323-5330, 2001.

[113] G. Ilangovan, A. Bratasz, H. Li, P. Schmalbrock, J. L. Zweier and P. Kuppusamy, "In vivo measurement and imaging of tumor oxygenation using coembedded paramagnetic particulates," *Magn. Reson. Med.*, vol. 52, no. 3, pp. 650-657, 2004.

[114] M. Afeworki, N. R. Miller, N. Devasahayam, J. Cook, J. B. Mitchell, S. Subramanian and M. C. Krishna, "Preparation and EPR Studies of Lithium Phthalocyanine Radical as an Oxymetric Probe," *Free Rad. Bio. Med.*, vol. 25, no. 1, pp. 72-78, 1998.

[115] J. R. Biller, V. Meyer, H. Elajaili, G. M. Rosen, J. P. Kao, S. S. Eaton and G. R. Eaton, "Relaxation times and line widths of isotopically-substituted nitroxides in aqueous solution at X-band," *J. Magn. Reson.*, vol. 212, no. 2, pp. 370-377, 2011.

[116] G. M. Rosen, S. R. Burks, M. J. Kohr and J. P. Kao, "Synthesis and biological testing of aminoxyls designed for long-term retention by living cells," *Org. Biomol. Chem.*, vol. 3, no. 4, pp. 645-648, 2005.

[117] K. Matsumoto, S. English, J. Yoo, K. Yamada, N. Devasahayam, J. A. Cook, J. B. Mitchell, S. Subramanian and M. C. Krishna, "Pharmacokinetics of a triarylmethyl-type paramagnetic spin probe used in EPR oximetry," *Magn. Reson. Med.*, vol. 52, pp. 885-892, 2004.

[118] C. R. Haney, A. D. Parasca, K. Ichikawa, B. B. Williams, M. Elas, C. A. Pelizzari and H. J. Halpern, "Reduction of Image Artifacts in Mice by Bladder Flushing with a Novel Double-Lumen Urethral Catheter," *Mol. Imaging*, vol. 5, no. 3, pp. 175-179, 2006.

[119] M. Miyake, S. R. Burks, J. Weaver , P. Tsai, W. Liu, D. Bigio, K. S. Bauer, K. J. Liu, G. M. Rosen and J. P. Kao, "Comparison of two nitroxide labile esters for delivering electron paramagnetic resonance probes into mouse brain.," *J. Pharm. Sci.*, vol. 99, no. 8, pp. 3594-3600, 2010.

[120] J. Shen, S. Liu, M. Miyake, W. Liu, A. Pritchard, J. P. Kao, G. M. Rosen, Y. Tong and K. J. Liu, "Use of 3-acetoxymethoxycarbonyl-2,2,5,5-tetramethyl-1-pyrrolidinyloxyl as an EPR oximetry probe: potential for in vivo measurement of tissue oxygenation in mouse brain," *Magn. Reson. Med.*, vol. 55, no. 6, pp. 1433-1440, 2006.

[121] M. Miyake, J. Shen, S. Liu, H. Shi, W. Liu, Z. Yuan, A. Pritchard, J. P. Kao, K. J. Liu and G. M. Rosen, "Acetoxymethoxycarbonyl nitroxides as electron paramagnetic resonance proimaging agents to measure O2 levels in mouse brain: a pharmacokinetic and pharmacodynamic study.," *J. Pharmacol. Exp. Ther.*, vol. 318,

no. 3, pp. 1187-1193, 2006.

[122] S. R. Burks, E. D. Barth, H. J. Halpern, G. M. Rosen and J. Y. Kao, "Cellular Uptake of Electron Paramagnetic Resonance Imaging Probes Through Endocytosis of Liposomes," *Biochim. Biophys. Acta*, vol. 1788, no. 10, pp. 2301-2308, 2009.

[123] J. P. Kao and G. M. Rosen, "Esterase-assisted accumulation of 3-carboxy-2,2,5,5-tetramethyl-1-pyrrolidinyloxyl into lymphocytes.," *Org. Biomol. Chem.*, vol. 2, no. 1, pp. 99-102, 2004.

[124] S. R. Burks, J. Ni, S. Muralidharan, A. Coop, J. P. Kao and G. M. Rosen, "Optimization of labile esters for esterase-assisted accumulation of nitroxides into cells: a model for in vivo EPR imaging.," *Bioconjug. Chem.*, vol. 19, no. 10, pp. 2068-2071, 2008.

[125] Y. Liu, F. A. Villamena, J. Sun, T. Wang and J. L. Zweier, "Esterified trityl radicals as intracellular oxygen probes," *Free Rad. Biol. Med.*, vol. 46, no. 7, pp. 876-883, 2009.

[126] N. Khan, C. M. Wilmot, G. M. Rosen, E. Demidenko, J. Joseph, J. O'Hara, B. Kalyanaraman and M. Swartz, "Spin traps: in vitro toxicity and stability of radical adducts.," *Free Rad. Biol. Med.*, vol. 34, no. 11, pp. 1473-1481, 2003.

[127] L. Lumata, M. E. Merritt and Z. Kovacs, "Influence of deuteration in the glassing matrix on 13C dynamic nuclear polarization," *Phys. Chem. Chem. Phys.*, vol. 15, pp. 7032-7035, 2013.

[128] J. R. Biller, H. Elajaili, V. Meyer, G. M. Rosen, S. S. Eaton and G. R. Eaton, "Electron spin-lattice relaxation mechanisms of rapidly-tumbling nitroxide radicals," *J. Magn. Reson.*, vol. 236, pp. 47-56, 2013.

[129] D. A. Morozov, I. A. Kirilyuk, D. A. Komarov, A. Goti, I. Y. Bagryanskaya, N. V. Kuratieva and I. A. Grigor'ev, "Synthesis of a Chiral C2-Symmetric Sterically Hindered Pyrrolidine Nitroxide Radical via Combined Iterative Nucleophilic Additions and Intramolecular 1,3-Dipolar Cycoadditions to Cyclic Nitrones," *J. Org. Chem.*, vol. 77, pp. 10688-10698, 2012.

[130] V. V. Khramtsov, "In vivo Spectroscopy and Imaging of Nitroxide Probes," in Nitroxides- Theory, Experiment and Applications, I. A. Kokorin, Ed., 2012.

[131] J. R. Biller, V. M. Meyer, H. Elajaili, G. M. Rosen, S. S. Eaton and G. R. Eaton, "Frequency dependence of electron spin relaxation times in aqueous solution for a nitronyl nitroxide radical and perdeuterated-tempone between 250 MHz and 34 GHz," *J. Magn. Reson.*, vol. 225, pp. 52-57, 2012.

[132] Y. Liu, Y. Song, A. Rockenbauer, J. Sun, C. Hemann, F. A. Villamena and J. L. Zweier, "Synthesis of Trityl Radical-Conjugated Disulfide Biradicals for Measurement of Thiol Concentration," *J. Org. Chem.*, vol. 76, no. 10, pp. 3853-3860, 2011.

[133] M. Tseitlin, R. W. Quine, G. A. Rinard, S. S. Eaton and G. R. Eaton, "Digital EPR with an arbitrary waveform generator and direct detection at the carrier frequency," *J. Magn. Reson.*, vol. 213, no. 1, pp. 119-125, 2011.

[134] R. W. Quine, D. G. Mitchell and G. R. Eaton, "A General Purpose Q-Measuring Circuit Using Pulse Ring-Down," *Concepts Magn. Reson.*, vol. 39B, no. 1, pp. 43-46, 2011.

[135] R. W. Quine, D. G. Mitchell and G. R. Eaton, "A General Purpose Q-Measuring Circuit Using Pulse Ring Down," *Concepts Magn. Reson.*, vol. 39B, no. 1, pp. 43-46, 2011.

[136] S. R. Burks, M. Makowsky, Z. A. Yaffe, C. Hoggle, P. Tsai, S. Muralidharan, M. K. Bowman, J. P. Kao and G. M. Rosen, "The Effect of Structure on Nitroxide EPR Spectral Linewidth," *J. Org. Chem.*, vol. 75, no. 14, pp. 4737-4741, 2010.

[137] G. R. Eaton , S. S. Eaton , D. P. Barr and R. T. Weber, Quantitative EPR, New York: Springer-Verlag/Wien, 2010.

[138] V. V. Khramtsov and J. L. Zweier, "Functional in vivo EPR Spectroscopy and Imaging Using Nitroxide and Trityl Radicals," in Stable Radicals: Fundamentals and Applied Aspects of Odd-Electron Compounds, R. Hicks, Ed., John Wiley & Sons, Ltd, 2010.

[139] B. Epel, C. R. Haney, D. Hleihel, C. Wardrip, E. D. Barth and H. J. Halpern, "Electron paramagnetic resonance oxygen imaging of a rabbit tumor using localized spin probe delivery.," *Med. Phys.*, vol. 37, no. 6, pp. 2553-2559, 2010.

[140] S. S. Eaton and G. R. Eaton, "Frequency Dependence of Pulsed EPR Experiments," *Concepts Magn. Reson.* , vol. 34A, no. 6, pp. 315-321, 2009.

[141] H. J. Halpern, M. Elas, D. Bell, E. D. Hleihel, E. D. Barth, C. R. Chaney, K. Ahn, C. A. Pelizzari, M. Kocherginsky and R. R. Weichselbaum, "Electron Paramagnetic Resonance Oxygen Images Correlates Spatially and Quantitatively with Increased Vascular Endothelial Growth Factor Concentrations," *International Journal of Radiation Oncology * Biology * Physics* , vol. 75, no. 3, 2009.

[142] S. Subramanian, J. W. Koscielniak, N. Devasahayam, G. Salem, R. H. Pursley, T. J. Pohida and M. C. Krishna, "A novel fast imaging modality for free radicals in vivo: continuous wave (CW) EPR imaging with direct detection and rapid field

scan in the presence of rotating gradients," *SPIE Proceedings*, vol. 7170, 2009.

[143] C. R. Haney, X. Fan, A. D. Parasca, G. S. Karczmar, H. J. Halpern and C. A. Pelizzari, "Immobilization using dental material casts facilitates accurate serial and multimodality small animal imaging," *Concepts Magn. Reson.*, vol. 33B, pp. 138-144, 2008.

[144] H. Sato, S. E. Bottle, J. P. Blinco, A. S. Micallef, G. R. Eaton and S. S. Eaton, "Electron spin-lattice relaxation of nitroxyl radicals in temperature ranges that span glassy solutions to low-viscosity liquids," *J. Magn. Reson.*, vol. 191, no. 1, pp. 66-77, 2008.

[145] J. P. Kao, E. D. Barth, S. R. Burks, P. Smithback, C. Mailer, K. Ahn, H. J. Halpern and G. M. Rosen, "Very-Low-Frequency Electron Paramagnetic Resonance (EPR) Imaging of Nitroxide-Loaded Cells," *Magn. Reson. Med.*, vol. 58, no. 4, pp. 850-854, 2007.

[146] K. H. Ahn and H. J. Halpern, "Simulation of 4D spectral-spatial EPR images," *J. Magn. Reson.*, vol. 187, no. 1, pp. 1-9, 2007.

[147] S. Subramanian, N. Devasahayam and M. C. Krishna, "Radiofrequency time-domain EPR imaging: instrumentation development and recent results in functional physiological in vivo imaging," in Imaging, Manipulation, and Analysis of Biomolecules, Cells, and Tissues V, San Jose, 2007.

[148] H. Sato, V. Kathirvelu, A. Fielding, J. P. Blinco, A. Micallef, S. E. Bottle, S. S. Eaton and G. R. Eaton, "Impact of molecular size on electron spin relaxation rates of nitroxyl radicals in glassy solvents between 100 and 300 K," *Mol. Phys.*, vol. 105, pp. 2137-2151, 2007.

[149] A. J. Fielding, P. J. Carl, G. R. Eaton and S. S. Eaton, "Multifrequency EPR of Four Triarylmethyl Radicals," *Appl. Magn. Reson.* , vol. 28, pp. 231-238, 2005.

[150] K. Matsumoto, T. Yahiro, K. Yamada and H. Utsumi, "In vivo EPR spectroscopic imaging for a liposomal drug delivery system," *Magn. Reson. Med.*, vol. 53, no. 5, pp. 1158-1165, 2005.

[151] J. S. Hyde, J. J. Yin, W. K. Subczynski, T. G. Camenisch, J. J. Ratke and W. Froncisz, "Spin-labeled EPR T1 vaues using saturation recovery from 2 to 35 GHz," *J. Phys. Chem. B*, vol. 108, pp. 9524-9529, 2004.

[152] G. M. Rosen, A. Beselman, P. Tsai, S. Pou, C. Mailer, K. Ichikawa, B. H. Robinson, R. Nielsen, H. J. Halpern and A. D. MacKerell, "Influence of conformation on the EPR spectrum of 5,5-dimethyl-1-hydroperoxy-1-pyrrolidinyloxyl: a spin trapped adduct of superoxide.," *J. Org. Chem.*, vol. 69, no.

4, pp. 1321-1330, 2004.

[153] R. Owenius, G. R. Terry, M. J. Williams, S. S. Eaton and G. R. Eaton, "Frequency Dependence of Electron Spin Relaxation of Nitroxyl Radicals in Fluid Solution," *J. Phys. Chem. B.*, vol. 108, pp. 9475-9481, 2004.

[154] R. D. Nielsen, S. Canaan, J. A. Gladden, M. H. Gelb, C. Mailer and B. H. Robinson, "Comparing continuous wave progressive saturation EPR and time domain saturation recovery EPR over the entire motional range of nitroxide spin labels.," *J. Magn. Reson.*, vol. 169, no. 1, pp. 129-163, 2004.

[155] R. H. Pursley, J. Kakareka, G. Salem, N. Devasahayam, S. Subramanian, R. G. Tschudin, M. C. Krishna and T. J. Pohida, "Stochastic excitation and Hadamard correlation spectroscopy with bandwidth extension in RF FT-EPR," *J. Mag. Reson.*, vol. 162, no. 1, pp. 35-45, 2003.

[156] M. Elas, A. Parasca, D. J. Grdina and H. J. Halpern, "Oral administration is as effective as intraperitoneal administration of amifostine in decreasing nitroxide EPR signal decay in vivo," *Biochim. Biophys. Acta*, vol. 1637, no. 2, pp. 151-155, 2003.

[157] K. Matsumoto, B. Chandrika, J. B. Lohman, J. B. Mitchell, M. C. Krishna and S. Subramanian, "Application of continuous-wave EPR spectral-spatial image reconstruction techniques for in vivo oxymetry: Comparison of projection reconstruction and constant-time modalities," *Magn. Reson. Med.*, vol. 50, no. 4, pp. 865-874, 2003.

[158] P. Tsai, S. Porasuphatana, H. J. Halpern, E. D. Barth and G. M. Rosen, "In vivo in situ detection of nitric oxide using low-frequency EPR spectroscopy," *Methods Mol. Biol.*, vol. 196, pp. 227-237, 2002.

[159] B. B. Williams, H. al Hallaq, G. V. Chandramouli, E. D. Barth, J. N. Rivers, M. Lewis, V. E. Galtsev, G. S. Karczmar and H. J. Halpern, "Imaging spin probe distribution in the tumor of a living mouse with 250 MHz EPR: correlation with BOLD MRI," *Magn. Reson. Med.*, vol. 47, no. 4, pp. 634-638, 2002.

[160] G. A. Rinard, R. W. Quine, S. S. Eaton and G. R. Eaton, "Frequency dependence of EPR signal intensity, 248 MHz to 1.4 GHz.," *J. Magn. Reson.*, vol. 154, no. 1, pp. 80-84, 2002.

[161] G. A. Rinard, R. W. Quine, G. R. Eaton and S. S. Eaton , "Adapting a hall probe controller for current control of an air-core magnet," *Concepts Magn. Reson.*, vol. 15, pp. 47-50, 2002.

[162] S. S. Eaton, J. Harbridge, G. A. Rinard, G. R. Eaton and R. T. Weber, "Frequency Dependence of Electron Spin Relaxation for Three S=1/2 Species Doped into

Diamagnetic Solid Hosts," *Appl. Magn. Reson.*, vol. 20, pp. 151-157, 2001.

[163] B. B. Williams, M. Elas, C. Mailer, A. D. Parasca, E. D. Barth, V. E. Galtsev and H. J. Halpern, "Fast 4D Spectral-Spatial Electron Paramagnetic Resonance Imaging for In Vivo Oxymetry," in Nuclear Science Symposium Conference Record, 2001.

[164] S. J. Ellis, M. Velayutham, S. S. Velan , E. F. Petersen, J. L. Zweier, P. Kuppusmay and R. S. Spencer, "EPR oxygen mapping (EPROM) of engineered cartilage grown in a hollow-fiber bioreactor," *Magn. Reson. Med.*, vol. 46, no. 4, pp. 819-826, 2001.

[165] I. Panagiotelis, I. Nicholson and J. S. Hutchison, "Electron Spin Relaxation Time Measurements Using Radiofrequency Longitudinally Detected ESR and Application in Oximetry," *J. Magn. Reson.*, vol. 149, no. 1, pp. 74-84, 2001.

[166] L. Yong, J. Harbridge, R. W. Quine, G. A. Rinard, S. S. Eaton, G. R. Eaton, C. Mailer, E. Barth and H. J. Halpern, "Electron spin relaxation of triarylmethyl radicals in fluid solution.," *J. Magn. Reson.*, vol. 152, no. 1, pp. 156-161, 2001.

[167] G. A. Rinard, R. W. Quine, J. R. Harbridge, R. Song, G. R. Eaton and S. S. Eaton, "Frequency Dependence of EPR Signal-to-Noise," *J. Magn. Reson.*, vol. 140, pp. 218-227, 1999.

[168] B. H. Robinson, D. A. Haas and C. Mailer, "Molecular dynamics in liquids: spin-lattice relaxation of nitroxide spin labels," *Science*, vol. 263, pp. 490-493, 1994.

[169] S. S. Velan, R. S. Spencer, J. L. Zweier and P. Kuppusamy, "Electron paramagnetic resonance oxygen mapping (EPROM): Direct visualization of oxygen concentration in tissue," *Magn. Reson. Med.*, vol. 43, no. 6, pp. 804-809, 2000.

CHAPTER 2

ELECTRON PARAMAGNETIC RESONANCE THEORY

2.1 EPR In A Nutshell.

Unpaired electrons follow magnetic fields (B_x) via interaction of the field with spin angular momentum. The main static magnetic field is B_0, and establishes a thermal equilibrium (Sec. 2.1) with a slight excess of spins in the lower energy state (m_s=-1/2) aligned with B_0. Thermal equilibrium is upset by application of a weaker field called B_1 at the resonance frequency. Spins return to equilibrium (relaxation) by interactions with the combined magnetic field of their local environment B_{local}.

All magnetic resonance experiments are an investigation of B_{local}, which is determined by nearby nuclei in the radical structure, solvent or lattice. B_{local} is heavily influenced by vibrational modes in a lattice at low temperatures, and conformational and rotational motion at higher temperatures. For *in vivo* work scientists are interested in how B_{local} changes in the presence of other paramagnetic species, like oxygen. The way B_{local} affects the return of a spin system to equilibrium is reflected in the spin lattice (T_1) and spin-spin (T_2) relaxation time constants, discussed in more detail in sections 2.2.1 and 2.2.2, respectively.

The sensitivity of paramagnetic probe molecules to B_{local} is simultaneously the greatest advantage and disadvantage of EPR. The spin probes studied in this dissertation tumble rapidly (picosecond timescale) in aqueous solution at room temperature and are sensitive to a very complex B_{local}. Chapters 3, 4 and 5 of the dissertation describe measurements of T_1 and T_2 under controlled conditions to accurately define all the mechanisms which effect B_{local} under *in vivo*-like conditions. Some of the contributions to B_{local} are dependent on molecular structure, and can be modified so that their contribution to B_{local} is decreased or eliminated. By reducing some of the processes that modulate B_{local}, the interpretation of the remaining contributions, like collisions with paramagnetic oxygen, becomes much more clear and feasible in a clinical setting.

2.2 Spins In A Magnetic Field

In the presence of B_0 an ensemble of unpaired electrons (spins) will be separated based on their spin quantum number, m_s= +/- ½ into two spin states. Loss of energy degeneracy results from the interaction of B_0 with the magnetic moment (μ_e), a consequence of each unpaired electron's spin angular momentum. B_0 exerts a torque on μ_e which causes the spin to precess in the same way a top precesses in Earth's gravitational field (Fig. 2.1 A-D). Spin precession is a classical metaphor for a fundamentally quantum mechanical occurrence. (See sections 2.3 and 2.4).

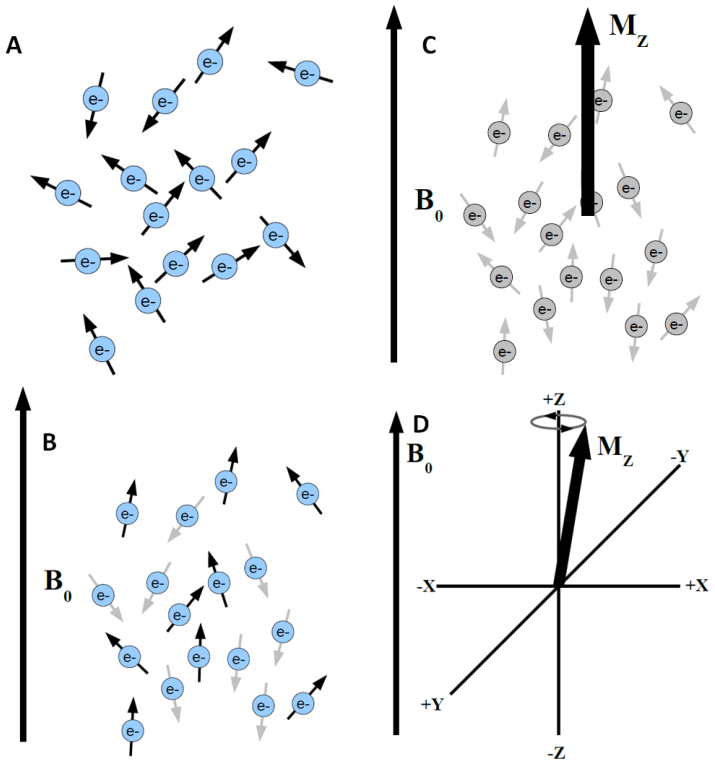

Figure 2.1. An ensemble of spins in a magnetic field can be represented with a single vector. An ensemble of spins in the absence of a magnetic field has degenerate energy states (A). Application of a magnetic field (B_0) causes a slight excess of spins to align in the direction of the field (B). The ensemble can be treated as a vector with a cumulative magnetic moment arising from the net effect of spins aligned with B_0 (C, D).

The gyromagnetic ratio, γ, is the proportionality constant relating B_0 to the frequency of precession (Larmor frequency, ω_L)

$$\omega_L = |\gamma|B_0 \qquad (2.1)$$

where $\gamma = g_e\mu_B/\hbar = 1.760859 \times 10$ rad T^{-1} s^{-1}. In continuous wave (CW) EPR, B_0 is swept while a constant microwave (or radio) frequency is applied. The resonance signal is observed (EPR spectrum) as the sweeping B_0 changes ω_L of the spins to match the frequency of constant radiation. The energy difference between the two levels (ΔE) is related to B_0 by:

$$\Delta E = g|\mu_B|B_0 \qquad (2.2)$$

where g is called the Lande factor or g-factor, which is equal to 2.002319 for a free electron. The atomic unit of magnetic moment, $\mu_B = -eh/4\pi m_e$ is called the Bohr magneton.

The interaction of B_0 with μ_e pushes spins towards the low energy m_s = -1/2 state aligned with B_0, while "violent thermal motions" [1] oppose such an ordering. The energy difference is very much smaller than kT so there is on average only a slight surplus of spins in the m_s= -1/2 state as compared to m_s= ½. The excess of spins in the more energetically favorable quantum state is governed by the Boltzmann distribution:

$$\frac{N_\alpha}{N_\beta} = e^{\frac{-g\mu_B B_0}{k_B T}} \qquad (2.3)$$

where k_B is the Boltzmann constant and T is the absolute temperature of the lattice [2], N_α and N_β represent the number of spins in the m_s = -1/2 and +1/2 states, respectively.

A net spin magnetization M_z (Fig 2.1 D) is used to describe the difference between populations of spins in the m_s= +/- ½ states. M_0 is related to B_0, temperature and the size of the sample (N_0).

$$M_0 = N_0 \frac{\gamma^2 \hbar^2 B_0 S(S+1)}{3k_B T} \qquad (2.4)$$

For the case of the S=1/2 radicals which are the focus of this dissertation, equation (2.4) simplifies to equation (2.5).

$$M_0 = N_0 \frac{\gamma^2 \hbar^2 B_0}{4 k_B T} \qquad (2.5)$$

The EPR signal is directly proportional to M_0, which increases as magnetic fields increase and temperature decreases. *In vivo* EPR is performed at low frequencies for deeper tissue penetration (low B_0) and "high" temperatures around 37° C. Since the non-resonant absorption of radiofrequency energy by water is much less than for microwave energy, sample size can be greatly increased for *in vivo* applications, recovering a substantial amount of the signal lost from lower B_0 and higher temperature [3, 4].

2.3 Conceptual Frame Work

Quantum mechanics explains the loss in degeneracy of the m_s= +/- ½ spin states in the presence of B_0 and the quantized absorption of energy (the "Why"). Since EPR is a measure of many thousands of spins (an ensemble), classical mechanics describes the changes in voltage or current, which are recorded during an experiment (the "How"). To reconcile these facets of EPR, our conceptual framework is composed of two pieces: the energy level diagram and the rotating frame.

2.3.1 The Energy Level Diagram Illustrates Longitudinal Relaxation, T_1

The spin-lattice relaxation time constant (T_1) describes the return of energy from the spin system to the environment (return to thermal equilibrium). T_1 is related to the enthalpy of the spin system. Absorption of energy which satisfies the resonance condition for the spin system also stimulates emission from the m_s=-1/2 to m_s=+1/2 states [2]. If the applied energy is great enough, the rate of absorption and emission are equal.

This case, called *saturation*, results when energy transfer to the lattice is inefficient in comparison to the power amplitude or time course of applied B_1, and is diagramed in the cartoon in Fig. 2.2. Though helpful for demonstrating saturation, Fig. 2.2 over-represents the population difference between the two spin states. At 250 MHz, the population difference at 295 K (22°C) is actually only 0.0013 %.

EPR probes with short T_1, such as nitroxides, have more efficient energy transfer to the lattice than trityl based probes with much longer T_1. If an ensemble of spins possessed "infinite" T_1 (zero coupling to B_{local}), there would be no EPR signal since application of any amount of power would cause immediate saturation.

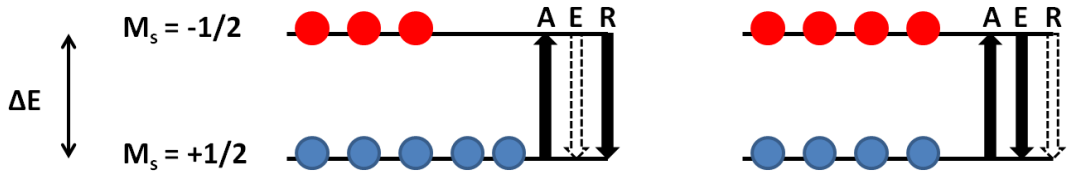

Figure 2.2. Resonance under power saturating conditions Power applied at the resonance condition causes a flip from m_s = +1/2 to m_s = -1/2 (stimulated absorption, **A**) and in the reverse direction (stimulated emission, **E**). Under non-saturating powers (left), thermal equilibrium is restored by release of the absorbed energy to the lattice (Relaxation, **R**). Under saturating conditions (right), the power is high enough that stimulated emission occurs at the same rate as absorption and no signal is observed since the populations are equalized. Adapted from [2].

The energy level diagram is also helpful for describing the hyperfine interaction of the unpaired electrons with the surrounding magnetically active nuclei (Fig. 2.3). The hyperfine splitting is a result of the interaction of the electron with nuclear spins within about 1 nm distance [2]. The hyperfine interaction is described by isotropic (A_I, Fermi contact) and anisotropic terms (A_D, dipole interaction), both of which are independent of B_0. The isotropic coupling arises from delocalization of the unpaired electron onto

different nuclei in the molecule. In the fluid solution EPR spectrum of the ^{14}N nitroxide shown in Fig. 2.3 the experimentally observed hyperfine (A_I) is the isotropic hyperfine. The anisotropic terms (A_D) are averaged to zero by fast molecular tumbling. Larger values of A_I indicate greater concentration of spin density on a nucleus, and smaller values of A_I indicate the spin is delocalized over the structure of the surrounding molecule. The largest values of A_I are ca. 16-23 G for ^{14}N and ^{15}N in the nitroxide radicals that are currently used. Values of A_I for ^{1}H and ^{2}H (D) on nitroxide radicals are smaller, of the order of a few gauss to hundreds of milligauss since these atoms are further removed from the $NO^{\bullet}$ fragment. Incomplete motional averaging of dipolar (anisotropic) interaction makes small contributions to the linewidth of the high field nitrogen hyperfine line. Some residual dipolar (anisotropic) interaction survives even at tumbling times from 4 to 50 ps which are considered to be in the fast-motion (isotropic) limit.

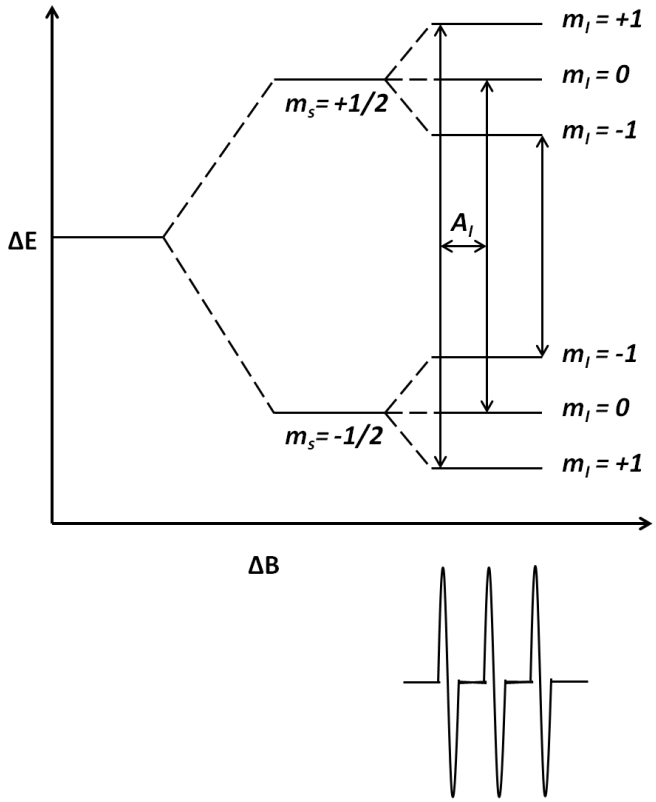

Figure 2.3. Electron-nuclear interaction gives rise to hyperfine splitting. The splitting drawn above is typical of a ^{14}N nitroxide where I = 1.

2.3.2 The Rotating Frame Illustrates Transverse Relaxation, T_2

The *spin-spin* relaxation time is the loss of spin phase coherence with time [5]. T_2 relates more to the order of the environment the spins experience, and is a descriptor of the entropy of the spin system. Conceptually T_2 is explained with a rotating coordinate system and phase diagram. In the rotating coordinate system T_2 describes the decay of the M_X and M_Y components in the plane transverse to B_0. The majority of EPR and NMR spectrometers are constructed to measure in this plane, so that most experiments measuring T_1 do so through the "lens" of T_2.

The effect of a linearly polarized oscillating field in the stationary laboratory frame (B_1) on the net magnetization vector is also easier to consider in the rotating frame (Fig. 2.4). The oscillating field may be represented as two components in a rotating frame. Each component rotates at the excitation frequency, but with a different directionality. If the observer is also "rotating" at the same frequency as one of the vectors, this vector seems to be static, and the description of the impact of B_1 on the spin ensemble is simplified.

Phase coherence of some of the spins in the ensemble is required to observe an EPR signal. Phase coherence is created by the excitation pulse. At thermal equilibrium, there is no magnetization in the XY plane, which also means there is no phase coherence. The timing of the B_1 applied to change this equilibrium state, defines the type of EPR experiment being performed.

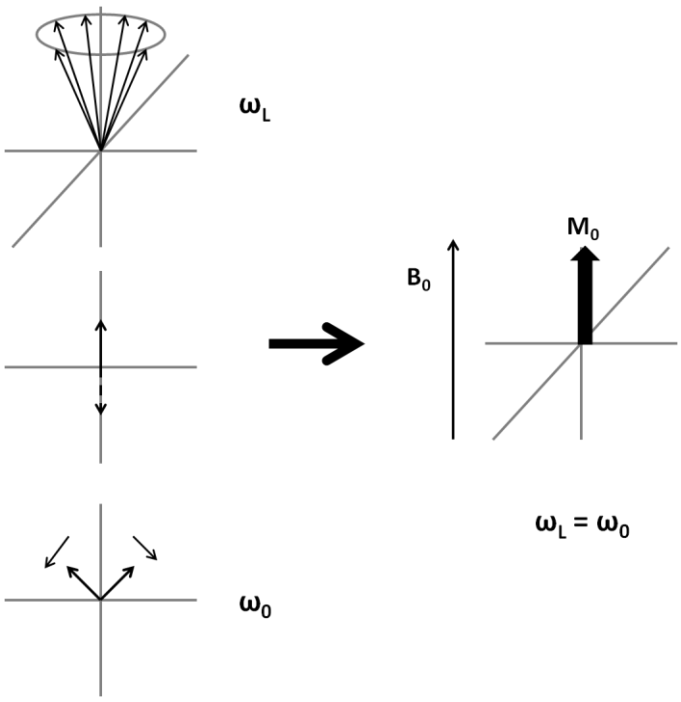

Figure 2.4. A rotating frame and phase diagram. The spins process with different phases at the Larmor frequency as determined by the strength of the magnetic field (B_0). The linearly polarized alternating micro- (or radio-) wave radiation can also be drawn as a circularly polarized with two components moving in opposite directions. The speed of the rotating frame is set by choosing one of the components and neglecting the other. At resonance, the frequency of Larmor precession matches the frequency of the radiation, causing the net magnetization vector to appear stationary. This is a simple example for the case of a group of homogeneous spin packets. Hyperfine structure results in groupings of spin packets with values that vary from the Larmor frequency.

The vector model is ubiquitous in explanations of ensemble magnetization manipulation for both electron and nuclear spins, but is appropriate only when considering just the electron or proton alone. Unfortunately the world is a complicated place. Borrowing a phrase (with slight modification) from English poet John Donne “no electron is an island”. The limits of the vector model are summarized by Dr. Michael Bowman in his chapter on Pulse EPR in the following way [2] ;

> "The vector model in 3D space is an exact description for the mathematical density system of a two-level system. However, a four level system, such as an unpaired electron interacting with the spin of a single proton, can be completely described only by a vector in 15-D space where intuition fails most of us."

Explaining the phenomena that are electron paramagnetic resonance is a bit like the story of the blind men and the elephant. Only by examining a spin system with a variety of experiments, and interpreting those results with multiple conceptual constructs can one really understand what is going on.

2.4 Pulse EPR

In pulse EPR, a single $\pi/2$ pulse applied at resonance completely focuses the spin phases resulting in a magnetization vector exclusively in the XY plane. The tip angle, θ, of M_0 away from $+Z$ after the application of B_1 is given in Equation 2.6 for S=1/2. The shorter the duration of the pulse, t_p, the more B_1 that must be applied to achieve a given tipping angle.

$$\theta = \gamma B_1 t_p \qquad (2.6)$$

For the case of B_1=1 G (at the sample), a single pulse with t_p = 90 ns would move the spin magnetization fully from +Z and focus the spin phases on the XY plane. If B_1 were half as much, then t_p = 180 ns would be needed to achieve the same effect.

2.4.1 One Pulse: Free Induction Decay (FID)

Immediately after the application of a $\pi/2$ pulse, the projection of the net magnetization vector will be aligned along the +Y axis with all spins sharing phase coherence (Fig. 2.5 A). As time progresses, the spins will begin to de-phase due to differences in ω_L and the magnetization vector will return to the +Z axis (Fig. 2.5 B, C) driven by T_1 relaxation. The result is free induction decay. This signal arises from two phenomena. First, the spin vector is rotating at the Larmor frequency and inducing an alternating current in the resonator. Secondly, the magnitude of the magnetization vector in the XY plane is disappearing with time, as a result of both T_1 and T_2 relaxation. The combination of these two phenomena yields the FID. The time constant for the decrease in FID amplitude is called T_2^*, which represents the true T_2 in addition to other processes which de-phase the spins. $T_2^* < T_2$.

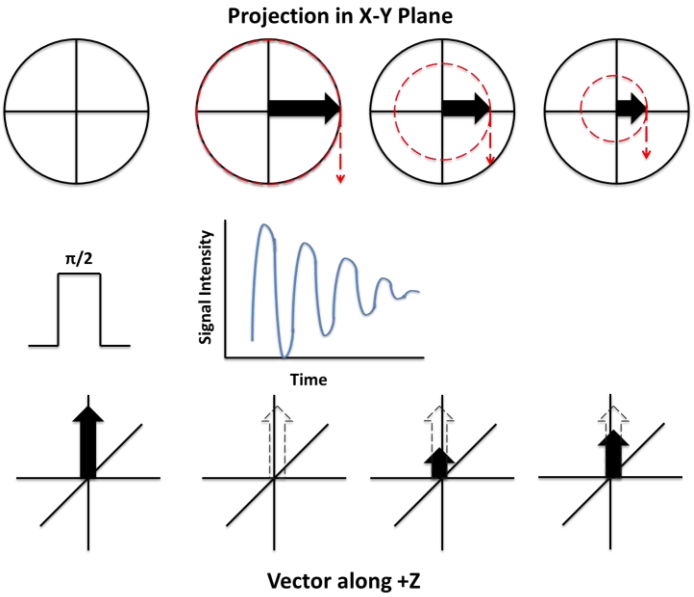

Figure 2.5. A π/2 pulse generates a free induction decay (FID) signal. At equilibrium the net magnetic moment is aligned in the direction of B_0, defined by convention as the +Z axis (bottom). In the rotating frame the vector along +Z appears stationary. There is no projection of the magnetic moment into the XY plane (top). After application of the π/2 pulse, the magnetization vector tips completely into the XY plane (A). In the laboratory frame the vector magnitude in the XY plane rotates at the Larmor frequency inducing an alternating current which is detected perpendicular to B_0. Simultaneously the vector in the XY plane decreases, while the vector magnitude in the +Z direction increases (B, C). The combination of decreasing signal intensity with the oscillating current gives rise to the FID pattern. The FID is observed when $\omega_S \neq \omega_0$. When $\omega_S = \omega_0$, a pure exponential decay without oscillation is observed.

2.4.2 Two Pulses: Echo Formation And Decay.

The phenomenon of the spin echo is based on the behavior of an ensemble of spins with differing Larmor frequencies [6]. The decrease in magnetization in the XY plane is not solely due to the return of the spins to the equilibrium position (T_1). At time 0 after application of the π/2 pulse, spins are in phase with one another (Fig. 2.6, A). As time progresses differences in ω_L due to interaction with neighboring nuclear spins causes the electron spins to fall out of phase (Fig. 2.6). The spins are refocused with application of a

π-pulse (Fig. 2.6 B). The π-pulse refocuses differences in ω_L, but not changes in ω_L that occur because of fluctuations of neighboring nuclear spins.

The time between pulses, τ, must be short relative to T_2. An echo is sometimes illustrated as "two back to back FID's". The height of the echo formed will decrease as τ is increased. Plotting the decrease in echo amplitude with increasing τ gives an exponential decay whose time constant is the phase memory time, T_m (Fig. 2.6, D). T_m reflects how fast magnetization is lost in the XY plane due to spin dephasing, which is due to the real T_2 plus other spin dephasing processes. For the fast tumbling radicals in room temperature studied in this dissertation , $T_m \approx T_2$, so two-pulse spin echo is used at all frequencies to measure the spin-spin relaxation time.

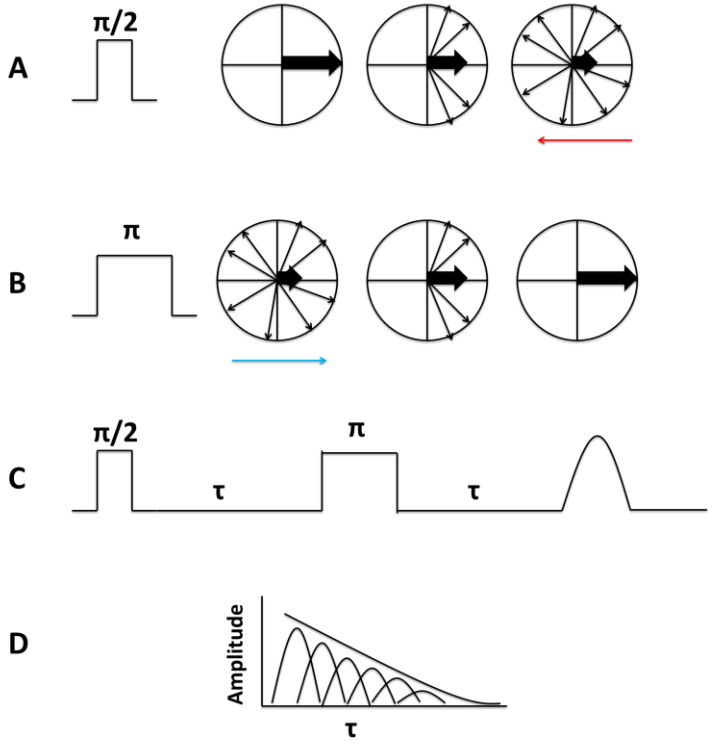

Figure 2.6. A spin echo is formed by re-focusing spins A π/2 pulse turns the magnetization vector into the XY plane (A). As time progresses, spin packets "de-phase", decreasing the intensity of the vector (blue arrow). Application of π pulse (B) "re-focuses" the spins and regenerates the magnetization vector in the XY plane (red arrow). For the formation of an echo, the π-pulse must be applied before spin phase is completely randomized. The time between the π/2 and π pulses is τ, and the echo appears 2τ after application of the π/2 pulse (C). The decay of the echo amplitude as a function of increasing τ is exponential, with a time constant called phase memory time, T_m (D). For fast tumbling organic radicals in fluid solution, $T_m \approx T_2$.

2.4.3 Three Pulses: Measuring T_1 By Inversion Recovery

If τ between the π/2 and π pulse is held constant, the echo amplitude may be used to monitor the effect on the spin system of a third pulse. In the case of an inversion recovery experiment, the third pulse is a π pulse, placed in front of the (π/2-τ-π) monitoring sequence to flip the magnetization to the –Z axis (Fig 2.7A). A time, *T*, is introduced between the inverting π-pulse and the monitor sequence. When *T* is very small, the

magnetization vector is still inverted to the –Z axis, and the reporter pulse sequence shows what looks like an upside down echo (Fig. 2.7 B). Each time *T* is increased, the magnetization vector relaxes further back to the +Z axis. The result is a signal that starts at a negative amplitude, increases through zero, and then continues to increase up to the amplitude of a normal echo (Fig. 2.7 A-C). Since this three pulse experiment is a probe of how long the magnetization vector takes to recover from the –Z to +Z axis, the inversion recovery experiment reports T_1.

Often spin diffusion processes obscure the true T_1 and the observed time for an inversion recovery signal is T_{1SD}. To investigate spin diffusion processes, it is common to increase the length of the first π-pulse, repeating the inversion recovery measurement. If spin diffusion is impacting T_1 values, the measured T_1 will continue to increase until a plateau is reached when the length of the inverting π-pulse is long relative to the spin diffusion time.

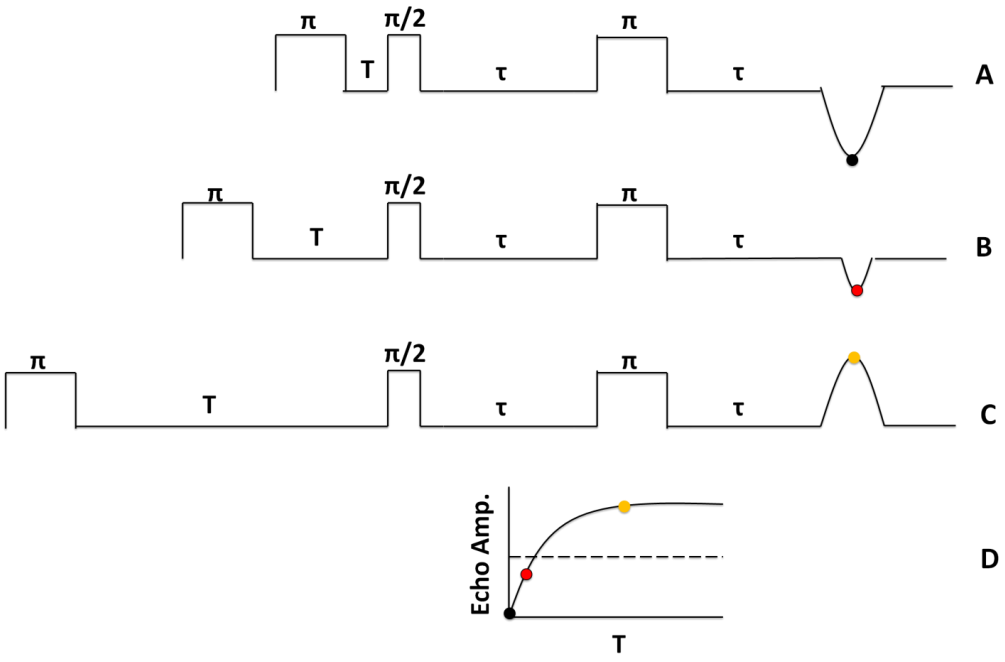

Figure 2.7. The three pulse inversion recovery sequence measures T_1. The first π-pulse inverts the spins and is separated by *T* from the "reporter" pulse sequence (π/2-π) which produces the echo. When *T* is very small in comparison to the relaxation time, the echo is fully inverted (A). As *T* increases more of the magnetization has returned to the +Z axis, resulting in fewer spins to be refocused and a smaller inverted echo (B). The echo amplitude goes through zero, and then increases when *T* is large enough between first π-pulse and the π/2 pulse (C). A plot of *T* vs. echo amplitude gives the inversion recovery trace (D).

2.5 Continuous Wave EPR

In continuous wave EPR the field (B_0) is swept slowly with respect to the relaxation time. The slow sweeping of B_0 changes the Larmor frequency of the spins until it matches the frequency of the constantly applied B_1 (at the carrier frequency, ω_C). The magnitude of B_1 applied in CW experiments is very small, resulting in a small tip angle of the magnetization from the +Z axis. A steady state of spin phase coherence is set up, so that a signal is recorded in the XY plane which is proportional to T_2 [5]. The phase coherence increases as the resonance condition is neared (Fig. 2.8 B), and decreases again

as the Larmor frequency moves past resonance (Fig. 2.8 C). In practice the signal recorded by CW EPR in the XY plane is that of T_2^* and reflects the effective linewidth. T_2^* is shortened relative to the true T_2 by Heisenberg exchange and unresolved hyperfine coupling, usually methyl or ring protons for the nitroxides studied in this dissertations.

The absorption spectra in a CW experiment is encoded in a modulation frequency and amplitude (phase sensitive detection), resulting in a derivative spectrum as the instrument output (Fig. 2.8, C). The disadvantage for this method of detection is that only a small part of the resonance signal is being observed for a given time. Increasing the modulation amplitude increases the observed signal at the expense of the line width, broadening it in a similar fashion to power saturation. Performing quantitative CW EPR is a difficult endeavor as it requires low modulation amplitudes and incident power so as not to distort the spectrum.

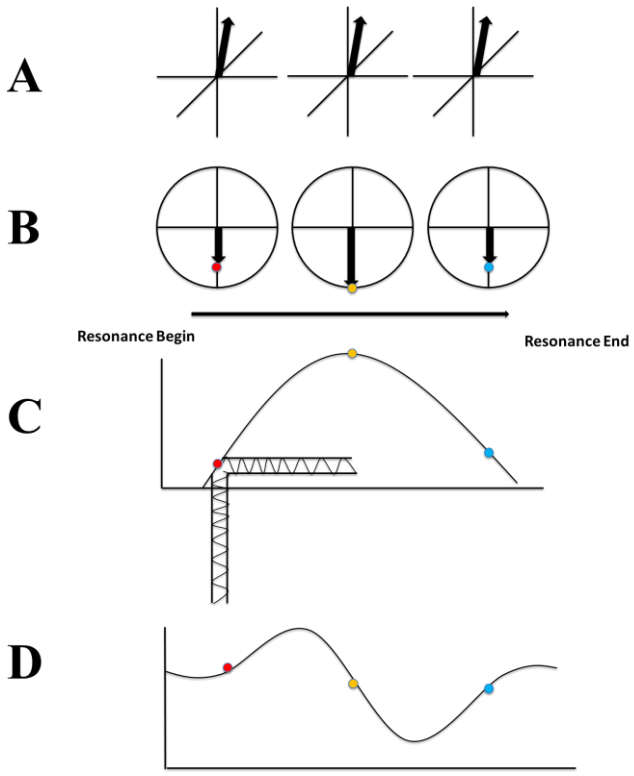

Figure 2.8. Continuous wave EPR At resonance, the continuously applied power tips M_Z very slightly away from alignment with B_0. The response in the XY plane as different spin packets come into resonance and exit resonance (B) is the absorption profile (C) (shown here is the case where individual spin packets are not resolved). Phase sensitive detection of the absorption signal gives the familiar derivative spectrum (D).

2.6 Rapid Scan EPR

In rapid scan EPR B_0 from the main magnet is held constant and specially designed magnetic field scan coils produce large uniform fields, B_{sweep}, across the sample. The absorption spectrum is detected directly by a quadrature mixer and digitized, as is done in pulse experiments. Many types of filters can be applied to post-processing to refine the spectrum. B_{sweep} is fast (MG/s or T/s) relative to relaxation time of the spins studied, and the characteristic oscillations of a rapid scan result from continuous variation of the effective B_1. The rapid scan spectrum can be viewed as two pieces, an absorption

component and a transient "FID" similar to those observed after application of a π-pulse. There are two differences between a pulse and rapid scan "FID". First, the tip-angle is much smaller than 90° due to the short dwell time of the spins on resonance. Second, the oscillation frequency does not remain constant, but rather increases. While the magnetization vector returns to equilibrium, ω_L is moving away from ω_C due to the quickly changing B_{sweep}.

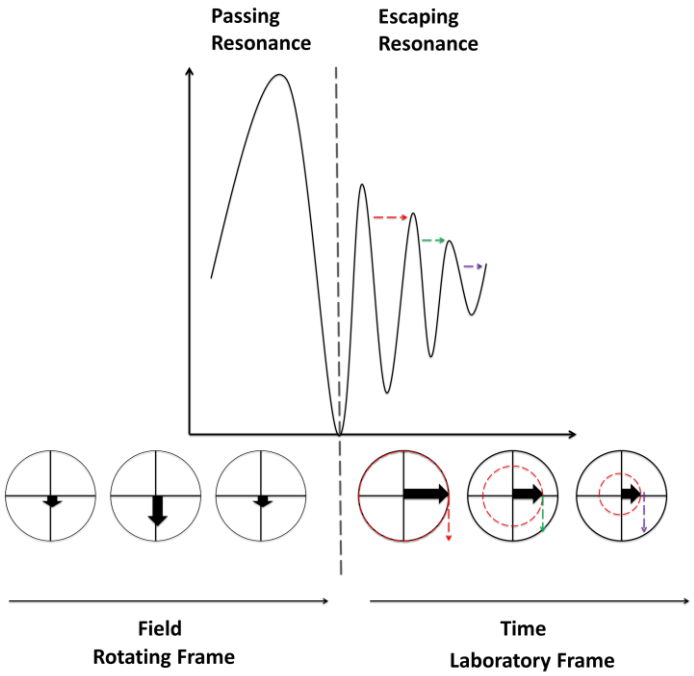

Figure 2.9. Rapid-scan EPR. The rapid scan signal can be thought of as arising from two periods with respect to the precessing spins. In the first period, the spins have a strong interaction with B_1 and pass through resonance in a similar fashion to the CW experiment. In the second period, the interaction of spins with B_1 decreases as they are being moved off resonance, yielding something that resembles a FID. Colored arrows represent, relative to the carrier frequency, increasing frequency of precession of the spins as they are moved off resonance.

2.7 Methods For Low-Frequency Pulsed EPR

The free-induction-decay (Fig. 2.5) is an idealized case where the entire signal can be captured from time zero. Resonators have a characteristic efficiency or "Q" value, and because of this experience "ringdown" after application of a $\pi/2$ pulse. The ringdown represents dissipation of the pulse energy from the resonator and has a signal that decays with a characteristic time constant, τ_{rd}. If τ_{rd} is the same length, or longer than the relaxation time to be studied then it will obscure the EPR signal.

Resonators with higher Q-values are more sensitive (increased SNR) but also have longer τ_{rd}. The ringdown time is dependent on the operating frequency, and for the same Q increases as operating frequency decreases. For instance, a resonator Q with 100 ns ringdown at X-band (9.5 GHz) may have a ringdown time of 4-5 μs at VHF (250 MHz). In addition, the higher Q-value can act as a bandwidth filter for very narrow $\pi/2$ pulses required to excite faster relaxing radicals (nitroxides). For this reason the resonators in pulse experiments are usually over-coupled to lower the Q-value. The penalty for lowering the Q is a decrease in SNR, and an increase in the power required for a given pulse length.

The only difference, especially for low-frequencies, in a pulse experiment for slow relaxing radicals (i.e. trityls) and fast relaxing radicals (i.e. nitroxides) is the margin for error in the balance between resonator Q, pulse length, input power and SNR. For short relaxing radicals, the margin is very narrow. Even with lowering resonator Q, the ringdown can seldom be reduced to the point where a nitroxide signal, with T_2 ca. 500 ns

-1 μs, is observed cleanly above the resonator ringdown and system noise. The key to achieving good (high SNR) relaxation data at low frequencies is understanding and optimizing the following aspects:

- Experiment Timings
- Power Requirements vs Pulse Length
- Phase Cycling Programs
- Resonator Overcoupling
- Q-spoiling [7]

The following sections address how each aspect was used to collect the low-frequency time domain data in this dissertation.

2.7.1 Experiment Timings

The basic spin echo sequence (Fig. 2.6) produces an echo at time τ after the π pulse, but capturing the echo signal relies on a complex set of digitizer timings, integration windows, detector blanking signals and Q-spoiling signals (for 250 and 600 MHz). A general timing diagram is presented in Fig. 2.10, with timings relative to the start of each experiment (Time Zero).

For the best signal-to-noise, all timings must be optimized. Resonator ringdown after the π-pulse can saturate the detector, so a detector blanking is employed (Fig. 2.10A). Correct positioning of detector blanking can improve the echo signal after averaging by reducing the input to the digitizer. If the blanking signal delay is too long, the echo amplitude can be diminished. Capture of the echo signal is done with a digitizer

positioned at the proper spot in time by the integrator window timing (Fig. 2.10 B). The digitizer collects data for the length of the integrator window time (Fig. 2.10 C). The two timings operate in tandem, and if either is not optimized signal to noise will be decreased. For the 250 MHz and 600 MHz pulse experiments Q-spoiling (Sec. 2.6.5) is employed and requires a signal for both the detector and power resonators (Fig. 2.10 D,E)

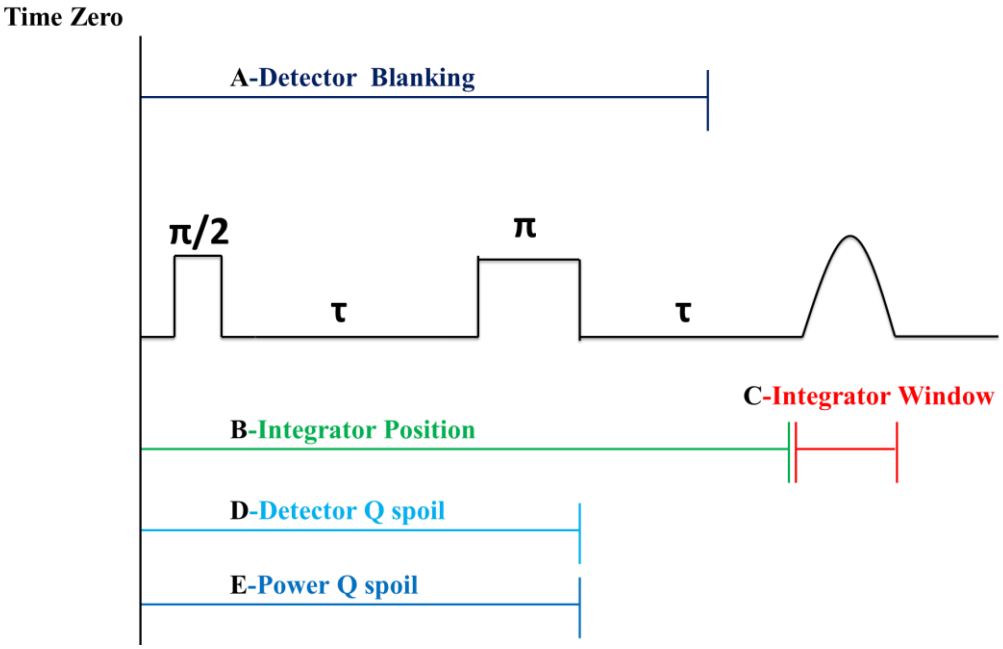

Figure 2.10 Understanding pulse experiment timings. Each system has a different nomenclature for the timings above. The Bruker systems (E580, E540) refer to **B** and **C** as $\mathbf{d_0}$ and **pg**, respectively. On the 250 MHz system power, detector Q-spoil and detector blanking are set by **U1, U2** and **U3**, respectively. The homebuilt systems (X-,S- and L-bands) have a digital boxcar designed by Richard W. Quine with knobs to adjust each timing.

2.7.2 Power Requirements vs. Pulse Length

In a pulse experiment power incident on the resonator is applied to the spins, tipping the magnetization away from the +Z axis. The conversion factor or resonator efficiency

($B_1/W^{-1/2}$) is reduced as the Q-value of the resonator is lowered. The B_1 required for a $\pi/2$ tip angle is given in Equation 2.7.

$$\frac{\pi}{2} = \gamma_e B_1 t_p \qquad (2.7)$$

Here t_p is the length of the $\pi/2$ pulse. To achieve a $\pi/2$ pulse in times which are short relative to nitroxide relaxation times, t_p must be < 40 ns. Shorter pulse times require either larger $B_1/\sqrt{W}$, or higher incident power.

The power amplifiers available at higher frequencies are 20 W (X-, L- and S-bands) or 1 kW (X-band), which are sufficient for small (4 mm-6 mm) samples to generate the required $\pi/2$ pulses for typical resonator efficiencies. At frequencies lower than 1 GHz sample size is increased (16-25 mm) and Q-values must be even lower to offset the increase in τ_{rd} with decreasing frequencies. Measurements made with the 600 MHz spectrometer have used a continuous wave 100 W amplifier or 300 W RF amplifier. Measurements made at 250 MHz used a 4 kW RF amplifier.

For optimizing the pulse power, a sample is inserted and the resonator(s) critically coupled. The dielectric loss of aqueous samples may lower the Q enough to decrease τ_{rd}, so further over-coupling only results in greater S/N loss. The Q can be estimated, by measuring the 1/e point on the decay curve from the reflected power of the incident pulse [8] and (Equation 2.8).

$$Q = 2\pi\nu\tau \qquad (2.8)$$

Here τ is the 1/e time and ν is the frequency of the resonator. Equation 2.8 is appropriate for crystal detection with max signal $\leq$ 15 mV [9] .

Samples of standard radicals with well characterized T_1 and T_2, prepared with similar solutions and concentrations as the radicals to be studied should be used first. Two trityl radicals were used as standard samples to calibrate the power vs. pulse length at a given resonator Q, the symmetric per-deuterated Nycomed trityl (Trityl-CD_3) [10] and Ox63 [11] provided to us by Dr. Halpern, University of Chicago. The relaxation characteristics for both radicals are well known from 9 GHz to 250 MHz [12], with T_2 varying from 6-12 μs. Such a long T_2 allows characterization of pulse length vs. incident power even at high resonator Q, since the τ value in the pulse sequence can be pushed out past τ_{rd} of the resonator.

A field swept echo detected spectrum is performed yielding the relevant resonance positions. For this dissertation such a sweep would reveal the 3, 2 or 1 resonance positions of the ^{14}N, ^{15}N, or trityl radicals, respectively. One line is selected, and an echo-decay experiment with $d\tau = 0$ is started. By holding τ constant, the echo never decays, and changes in its amplitude are due to power or phase changes, allowing optimization of both parameters. If signal to noise is insufficient to see the impact of parameter change on the echo, the signal can be averaged with a digitizer at each parameter setting and plotted point-by-point (Fig. 2.11).

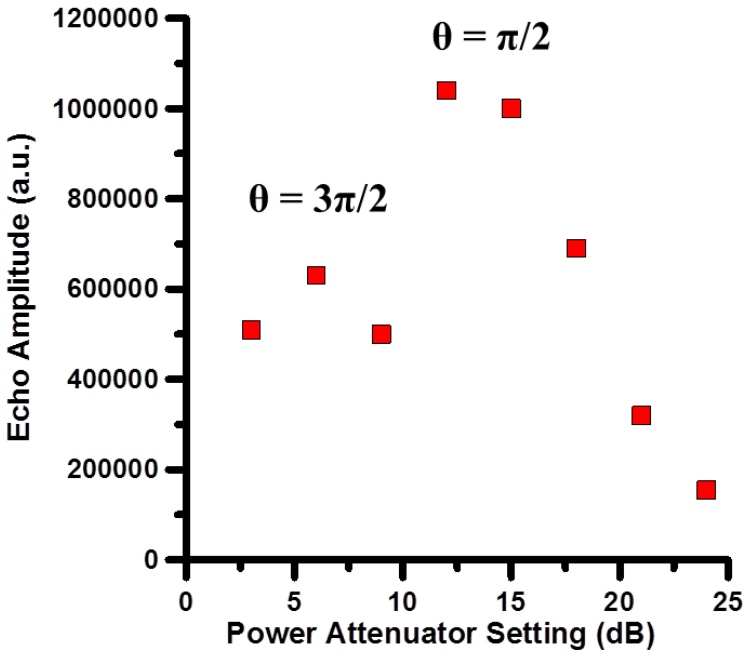

Figure 2.11. Optimizing pulse power at 250 MHz. Power attenuation is varied to find the optimum power for the $\theta = \pi/2$ pulse. Since 0 dB attenuation is maximum power, the graph is read from right to left. The second peak with smaller amplitude is the echo which results from a tipping of the magnetization vector by $\theta = 3\pi/2$. Data were collected with a pulse length of 80 ns.

The full range of attenuations (from 60 or 40 to 0 dB) must be explored for each resonator Q to determine how θ changes with power (for the same pulse length). For efficient (higher Q) resonators, or if enough power is available for a given τ_p, the magnetization vector can be tipped 270° from the +Z axis. This results in a 90° tip in the opposite direction and will also yield an echo, but of a smaller amplitude than the 90° echo. The 90° and 270° echoes are separated by ca. 12 dB attenuation change of the incident power. Measurement of the 270° echo yields artificially shortened relaxation times. In preliminary measurements of the nitroxide relaxation times, T_1 was shortened by 100 ns when measuring the θ=270° echo instead of the θ=90° echo. This was a difference of 12-17% for true T_1 values in the range of 600-800 ns.

2.7.3 Phase Cycling

Almost all pulse EPR experiments are performed with phase cycling. Any combination of two- or three-pulses will can yield unwanted echoes. Phase alternation (or phase cycling) is a method to remove the unwanted echoes and residual FID, and correct for imperfections in the pulse shapes. If resonator response is linear with input power, phase cycling can also be used to recover a wanted echo signal sitting just inside the ring-down. In the simplest design the microwave signal cycles twice, 0° and 180°. Resonator ring-down and FID are suppressed, while the echo is retained.

2.7.4 Resonator Overcoupling

The more overcoupled the resonator, the shorter the ringdown, but the more power that is required for a given tip angle. The power requirements for a short (ca. 40 ns) pulse are large, and grow even more as the efficiency of the resonator is lowered by over-coupling. Successful pulse experiments at frequencies lower than X-band in Chapters 3, 4 and 5 were achieved by carefully balancing the efficiency and ring down when adjusting the resonator coupling. Pulse experiments at 250 MHz were aided by Q-spoiling [7]. The use of bimodal (cross-loop) resonators allows up to 60 dB of isolation between the power and detection resonators. This is effectively a 60 dB reduction in the impact of ringing from the power resonator seen by the detection resonator, allowing higher Q values in the power resonator to increase efficiency and lower power demands.

The only way to be certain the correct balance has been struck is to complete a "calibration" using a standard sample with relaxation times longer than the ringdown of the resonator in the highest Q state (critically coupled). For all frequencies this was usually the Trityl-CD_3 or Ox63 radicals. For each value of Q an echo is formed with short $\pi/2$ pulses and decreasing values of τ. Tau is decreased until the ringdown is no longer linear with power and the signal is washed out in the ringdown. As the Q is lowered, the τ value is moved further and further back until the echo is overwhelmed. Completed pulse power optimization at each Q (Fig. 2.11) calibrates the instrument user for how much power (for a given $\pi/2$ pulse) is needed as Q is lowered. Over-coupling the resonator to the point where tau can be ca. 300 ns is sufficient for measuring most nitroxides in solution at room temperature.

2.7.5 Q-spoiling

The best example of the implementation of Q-spoiling with a cross loop resonator (CLR) in the Denver lab is given in [7]. During "active" Q-spoiling, voltage biased diodes cycle the power and detection resonators between "high Q" and "low Q" (shorted) states. The power resonator starts the experiment in the "high Q" state, so it has the highest sensitivity when receiving the pulses. The detection resonator is held in the "low Q" state, to make it insensitive to power coming from the power resonator, through the isolation. As the π pulse ends, the power resonator is cycled to the "low Q" state, making it insensitive to power and immediately spoiling the ringdown that was present due to high incident powers. Meanwhile the detection resonator has been cycled to its "high Q" state so it can be very sensitive to detect the electron spin magnetization.

"Passive" Q-spoiling may also be employed, and is favored by the collaborators in Chicago. Schottky diodes are placed across the gap of the receiving resonator. During the power pulses the diodes would sense enough voltage to conduct, "shorting out" the resonator. This would prevent the build up of energy to be dissipated, essentially making the detection resonator "blind" to the impact of the pulse power. After the power pulse is completed the voltage falls to a level where the diodes no longer conduct, and the detection resonator is sensitive again. The drawback to this design is that if isolation in between resonators is high, the voltage which reaches the diodes is insufficient to activate them, allowing the detection resonator to build up some energy which it must dissipate in the dead time.

2.8 Summary

The goal of this chapter was to give enough of an over view of EPR theory, methods and technique to provide the proper context for Chapters 3-7. Additional details on these topics are given in [2][5] [6][9] [13]. A comparison of pulse and CW techniques sets the stage for the experiments in Chapter 3, discussion of two and three pulse experiments is helpful for understanding Chapters 4 and 5, and an introduction to rapid-scan is necessary for Chapter 6, on rapid-scan imaging. Chapter 7 is more about the intricacies of different resonators, and gives some idea of how the proper hardware can "make or break" the experiment you are attempting.

Section 2.6 summarizes all of the helpful "bits" I have adopted over the last five years for pulsed EPR. A large effort went into method development just to measure relaxation times between 500 ns and 1 μs at frequencies in the L-band (1-2 GHz), at 600 MHz and especially at 250 MHz.

Dr. Gareth Eaton remarked to me in May of 2009 (after I had been in the lab one month) that finding an echo for the nitroxide samples at 250 MHz should be "relatively straight forward", and they were (two years later after a lot of effort). I'll end this chapter with my own quote, to any future graduate students who happen upon this dissertation in their quest to understand EPR.

"If the problem is only very challenging, we'll get it figured out right away. If the problem is impossible, it will just take us a couple of days"

G.R. Eaton

2.9 References

[1] J. D. Roberts, Nuclear Magnetic Resonance: Applications to Organic Chemistry, New York Toronto London: McGraw-Hill Book Company Inc., 1959.

[2] M. Brustalon and E. Giamello, Eds., Electron Paramagnetic Resonance: A Practicioner's Toolkit, Wiley, 2009.

[3] G. A. Rinard, R. W. Quine, R. Song, G. R. Eaton and S. S. Eaton, "Absolute EPR Spin Echo and Noise Intensities," *J. Magn. Reson.*, vol. 140, pp. 69-83, 1999.

[4] G. A. Rinard, R. W. Quine, J. R. Harbridge, R. Song, G. R. Eaton and S. S. Eaton, "Frequency Dependence of EPR Signal-to-Noise," *J. Magn. Reson.*, vol. 140, pp. 218-227, 1999.

[5] I. Bertini, G. Martini and C. Luchinat, "Relaxation,Background and Theory," in *Handbook of Electron Spin Resonance*, C. P. Poole and H. A. Farach, Eds., American Institute of Physics Press, 1994, pp. 51-77.

[6] A. Schweiger and G. Jeschke, Principles of pulse electron paramagnetic resonance, Oxford University Press, 2001.

[7] G. A. Rinard, R. W. Quine, G. R. Eaton and S. S. Eaton, "250 MHz Crossed-Loop Resonator for Pulsed Electron Paramagnetic Resonance," *Concepts Magn. Reson.*, vol. 15, no. 1, pp. 37-46, 2002.

[8] R. W. Quine, D. G. Mitchell and G. R. Eaton, "A General Purpose Q-Measuring Circuit Using Pulse Ring Down," *Concepts Magn. Reson.*, vol. 39B, no. 1, pp. 43-46, 2011.

[9] G. R. Eaton , S. S. Eaton , D. P. Barr and R. T. Weber, Quantitative EPR, New York: Springer-Verlag/Wien, 2010.

[10] J. H. Ardenkjaer-Larsen, I. Laursen, I. Leunback, G. Ehnhom, L. G. Wistrand, J. S. Petersson and K. Golman, "EPR and DNP properties of certain novel single electron contrast agents intended for oximetric imaging," *J. Magn. Reson.*, vol. 133, no. 1, pp. 1-12, 1998.

[11] B. Epel, C. R. Haney, D. Hleihel, C. Wardrip, E. D. Barth and H. J. Halpern, "Electron paramagnetic resonance oxygen imaging of a rabbit tumor using localized spin probe delivery.," *Med. Phys.*, vol. 37, no. 6, pp. 2553-2559, 2010.

[12] R. Owenius, G. R. Eaton and S. S. Eaton, "Frequency (250 MHz to 9.2 GHz) and viscosity dependence of electron spin relaxation of triarylmethyl radicals at room

temperature.," *J. Magn. Reson.,* vol. 172, no. 1, pp. 168-175, 2005.

[13] M. H. Levitt, Spin Dynamics: Basics of Nuclear Magnetic Resonance, Wiley, 2008.

CHAPTER 3

RELAXATION TIMES AND LINE WIDTHS OF ISOTOPICALLY SUBSTITUTED NITROXIDES IN AQUEOUS SOLUTION AT 9.5 GHZ.

3.1 Introduction

Optimization of nitroxides as probes for *in vivo* EPR imaging requires understanding of multiple factors that contribute to improved signal-to-noise (S/N). In this chapter the goal is to define for a set of nitroxides (Fig.3.1) (a) the features of the molecules that impact the inherent relaxation-determined spin packet line widths, (b) the relaxation mechanisms that dominate spin lattice relaxation, and (c) the structural features that determine the unresolved hyperfine splittings. These studies reveal patterns that guide the design and selection of nitroxides for imaging experiments.

For low molecular weight nitroxides in water, EPR spectra at X-band (9 GHz) and lower frequencies are near the rapid tumbling limit. Tumbling correlation times (τ) are of the order of 10 ps, $T_1 \approx T_2$, saturation recovery curves can be fit with a single exponential, and line widths and T_2 are weakly dependent on frequency because the dominant anisotropic interaction is the frequency independent nuclear hyperfine. Recent work on the frequency dependence of T_1 for nitroxides has focused on the slower tumbling regime with τ values in the range of 10^{-9}–10^{-10} s [1-3] where T_1 is dependent on frequency below X-band.

In the fast tumbling regime T_1 for nitroxides is predicted to be independent of frequency below X-band [4].The ultimate goal is imaging at frequencies in the 250 MHz to 1 GHz range, but advantage was taken of the higher signal-to-noise (S/N) achievable with smaller sample size at X-band to explore concentration and structure dependence of relaxation times and line widths.

The study included nitroxides with 6-member (**1**), unsaturated 5-member (**2**), or saturated 5-member (**3**) rings (Fig. 3.1). Each was studied with both ^{14}N and ^{15}N isotopes. Since substitution of ^{1}H by ^{2}H substantially narrows the EPR signal and improves S/N, the study focused on deuterium-substituted nitroxides. Nitroxide **2** was selected for study because the unique ring hydrogen has been shown to have a hyperfine splitting that is a convenient monitor of oxygen concentration [5]. The low concentration continuous wave (CW) line widths, spin-packet line widths required for simulations including all nuclear hyperfine splittings, and directly-measured relaxation T_1 and T_2 were compared. This work is published in [6].

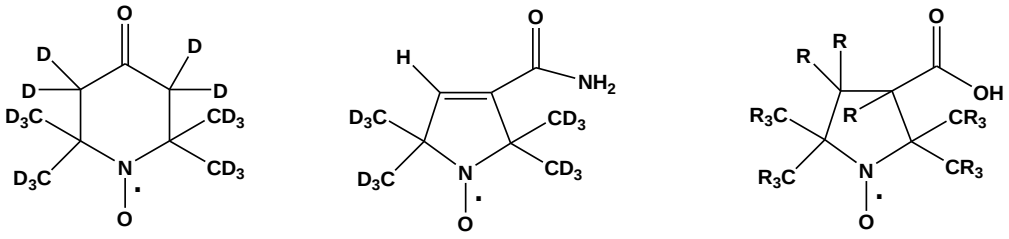

Figure 3.1. Structures of nitroxides studied. The designations **1**, **2** or **3** are used when referring to either nitrogen nuclear isotope. Tempone and mHCTPO are commonly used designations for **1** and **2**, respectively. PDT is also used for **1a**. Adapted from [6].

3.2 Experimental

1a and **1b** with >98% isotope purity were purchased from CDN Isotopes (Quebec, Canada). A second sample of **1a** was prepared as described in [6] and provided by Dr. Gerald Rosen (University of Maryland). **2a** and **2b** were prepared as previously reported [7] and provided by Prof. Halpern (University of Chicago). The syntheses of **3a** and **3b** were previously reported [8] and provided by Dr. Gerald Rosen (University of Maryland).

3.3 Preparation Of Solutions

Weighed samples of radicals were dissolved in water. Solutions in thin-wall 0.97 mm i.d. Teflon tubing were placed inside 4 mm o.d. quartz tubes. Gaseous N_2 was passed over the sample via a thin Teflon tube that extended to the bottom of the quartz sample tube. O_2 and N_2 exchange through the tubing. The purging was continued until no further change in line width or relaxation time was observed. Integrals of CW spectra were checked to ensure that water evaporation was small enough that it did not significantly change the solution concentrations.

3.4 Spectroscopy

Experiments were performed at room temperature, ca. 20–22 ˚C at the sample position in the resonator. X-band CW EPR spectra were obtained on a Bruker EMX-Plus spectrometer. Microwave power incident on the sample, magnetic field modulation amplitude, and modulation frequency were adjusted to ensure that the observed line widths were not broadened by experimental parameters. Reproducibility of oxygen

removal was checked. The effectiveness of the deoxygenation methodology was verified with an Oxylab pO_2 fluorescent probe (Oxford Optronix, UK). CW spectra of **1a**, **2a**, or **3b** in D_2O were essentially indistinguishable from those in H_2O. The slightly higher viscosity of D_2O than of H_2O causes proportional increases in tumbling correlation times that could be detected by changes in T_2 measured by spin echo. This change in T_2 is within the uncertainty in determination of T_2 by simulation of CW lineshapes.

T_2 relaxation times were measured by two-pulse electron spin echo on a Bruker E580 or on a locally-built pulsed spectrometer [9] with a Bruker ER4118-X5MS split ring resonator. Both spectrometers use nominal 1 kW TWT amplifiers. The time constant for spin echo dephasing is designated as T_m [10]. For a molecule tumbling rapidly in fluid solution $T_m = T_2$ so the spin echo dephasing time constant is designated as T_2.

T_1 relaxation times were measured by inversion recovery on these two spectrometers, or with saturation recovery by Virginia Meyer and Hanan Elajaili on the E580 with a Bruker ER4118-X5MS split ring resonator or a home-built spectrometer [11] using the 5-loop-4-gap resonator described in Ref. [12]. Values of T_1 obtained by inversion recovery and saturation recovery for selected samples were compared and found to be in good agreement, within experimental uncertainty. Inversion recovery inherently provides higher S/N, and is the method of choice for T_1 measurements of nitroxides in this fast motional regime. Values of T_1 obtained by inversion recovery are reported in the tables. Results obtained on different spectrometers with several operators were in good agreement.

3.5 Fitting Of Exponentials To Pulse Data And Simulations Of CW Spectra

Two-pulse echo decays, inversion recovery curves, and saturation recovery curves fit well with a single exponential, using a least-squares criterion. Reported relaxation times are averages of at least three replicates. CW EPR spectra were simulated using the shareware EasySpin 3.1.6 (http://www.easyspin.org/) and using locally-written Fortran programs, with guidance from published hyperfine values for **1a** [13], **2a** [13, 14], and saturated 5-member ring nitroxides (pyrrolidines) similar to **3a** [15]. ^{2}H couplings were calculated from literature values of ^{1}H couplings using the ratio $\gamma_D/\gamma_H = 0.153$. Hyperfine couplings are sensitive to solvent [14], so small differences from previously reported values were allowed in the simulations. Spin packet line widths calculated from T_2 were substituted into the Kivelson equation [16] for the dependence of line width on nuclear spin, $\Delta B=A+B\ m_I + C\ m_I^2$ [17]. Equations presented in Chasteen and Hanna were used to calculate the molecular tumbling correlation time τ from the value of B [18]. Since ^{14}N A = 16.1–16.4 G for **1a**, **2a**, and **3a** in water at 20 ˚C, it was assumed that the anisotropic g and A_N values also would be similar for the three nitroxides. Based on literature reports the following parameters were used in analyzing the tumbling correlation times: g_x = 2.0092, g_y = 2.0061, g_z = 2.0022. A_x = 5.5, A_y = 6.3, and A_z = 35.9 G for ^{14}N [19, 20]. Average values of τ based on CW spectra for ^{14}N and ^{15}N analogs at three concentrations are 9, 13, and 19 ps for **1**, **2**, and **3**, respectively. To fit these τ values to the Stokes–Einstein equation ($\tau = c_{slip}\ V\ g/kT$, V = molecular volume, k = Boltzmann's constant) required c_{slip} of 0.11, 0.15, and 0.21 for **1**, **2**, and **3**, respectively. The value of c_{slip} for **1** is similar to previously reported values of 0.12 in 1:1 water glycerol [21] and 0.13 in

glycerol [19]. Trends in the values of c_{slip} are consistent with the expectation of increasing solute-solvent interaction for ketone < amide < acid.

3.6 Calculation of Uncertainties

All of the uncertainties reported in this chapter, and chapters 4 and 5 were calculated as the standard deviation via Microsoft Excel (STDEV). The formula used by Excel is given in Eq. 3.1:

$$\mathrm{STDEV} = \sqrt{\frac{\sum(x - \bar{x})^2}{n - 1}} \qquad (3.1)$$

where $\bar{x}$ is the mean and n is the sample size. Most measurements were made in triplicate, with the exception of the experiments reported in Table 3.3

3.7 Results

3.7.1 Spin-spin and spin lattice relaxation times

Directly-measured relaxation times for the six radicals in 0.25 mM aqueous solutions are summarized in Table 3.1 for the center-field lines of the ^{14}N nitroxides and the low-field lines of the ^{15}N nitroxides. For the ^{14}N-nitroxides T_2 for the low-field line is 2–5% longer than for the center line and T_2 for the high-field line is 25–60% shorter than for the center line. For the ^{15}N-nitroxides T_2 for the high-field lines is 25–60% shorter than for the low-field lines. The modest dependence of T_2 on m_I and similarity in values of T_1 and T_2 (Table 3.1) are consistent with the fast tumbling regime.

Table 3.1 Relaxation times, spin packet linewidths and overall linewidths. For samples in H_2O at 0.25 mM[a]

Nitroxide	T_1 (μs)[b]	T_2 (μs)[c]	ΔB_{sp} (G)	ΔB_{pp} (G)
1a	0.59	0.56	0.12	0.16
2a	0.67	0.53	0.12	0.51[d]
3a	0.72	0.57	0.11	1.1
1b	0.81	0.64	0.10	0.16
2b	0.86	0.60	0.11	0.51[d]
3b	1.0	0.75	0.087	0.4

[a] Center-field line for ^{14}N and low-field line for ^{15}N in deoxygenated water at 20-22° C
[b] Uncertainties are about ± 0.03 μs
[c] Uncertainties are about ± 0.02 μs
[d] Partially-resolved doublet splitting is 0.51 G with ΔB_{pp} for each component of 0.26 G.

For comparison with simulations of CW spectra, T_2 was converted to peak-to-peak spin packet line widths, ΔB_{sp}, using the relationship for a Lorentzian line,

$$\Delta B_{sp}(G) = \frac{2}{\sqrt{3}\gamma T_2} = \frac{6.56 \times 10^{-8} Gs}{T_2(s)} \qquad (3.2)$$

The much larger overall line widths, ΔB_{pp}, than spin packet line widths ΔB_{sp} (Table 3.1) reflect the substantial contributions from hydrogen/deuterium hyperfine splittings.

3.7.2 Contributions to T_1

Values of T_1 in 0.25 mM aqueous solutions (Table 3.1) are in good agreement with a report at X-band for 0.5 mM solutions at 20˚C: T_1 = 0.49 μs for **1a** and T_1 = 0.68 μs for **2a** [2]. Although a dependence of T_1 on m_I was observed in the present study, recent models for nitroxide spin lattice relaxation do not include a m_I dependence [3] [4] [10] [17] [21-23]. The contributions to T_1 were analyzed first for the average values observed for the 3 (or 2) values of m_I as summarized in Table 3.2 for 0.030 mM solutions. The m_I

dependence is discussed separately in Section 3.5.4. At these low concentrations the Heisenberg exchange contributions to the measured T_1 are negligible.

Spin–lattice relaxation for nitroxides in fluid solution has been analyzed in terms of contributions from spin rotation Eq. (3.3), modulation of g and A anisotropy by molecular tumbling, and generalized spin diffusion [3,4][16][20–22].

$$\frac{1}{T_1^{SR}} = \frac{\sum_{i=1}^{3}(g_i - g_e)^2}{9\tau} \qquad (3.3)$$

where i=x,y,z and g_e is 2.0023.

For nitroxides tumbling rapidly in deoxygenated fluid solution, spin rotation Eq. (3.3) makes a larger contribution to T_1 than in slower tumbling regimes [4] [21], but as shown in Table 3.2 spin rotation alone is not sufficient to fully account for the relaxation times. Generalized spin diffusion (GSD) includes contributions from methyl rotation and modulation of intermolecular and intramolecular dipolar spin–spin interaction [4]. Other than the impact of slowing tumbling due to increased viscosity, substitution of H_2O by D_2O did not change the relaxation times, which indicates that the intermolecular contribution to GSD is not significant for these experiments. With the exception of **3a** and one hydrogen in **2**, the nitroxides selected for study are perdeuterated, so intramolecular contributions from GSD are much smaller than for natural isotope abundance. Therefore GSD was not included in the calculations of T_1. At X-band (and lower frequencies) the contribution from modulation of g anisotropy is more than an order of magnitude smaller than from modulation of A anisotropy [4] [21] [23] (Eq.

(3.4)) so inclusion of g anisotropy with an expression analogous to Eq. (3.4) had negligible impact on calculated T_1.

3.7.3 Modulation of anisotropic nuclear hyperfine by tumbling

In recent papers the modulation of anisotropic nuclear hyperfine by tumbling has been described by Eq. (3.4), and called the END (Electron-Nuclear-Dipole) mechanism [4] [23].

$$\frac{1}{T_1^A} = \frac{2}{9} I(I+1) \sum_i (A_i - \bar{A})^2 J(\omega) \qquad (3.4)$$

where A_i is a component of the nitrogen nuclear hyperfine in angular frequency units, $\bar{A}$ is the average nitrogen hyperfine, I is the nitrogen nuclear spin, and $J(\omega)$ is the spectral density function. Experimental values of T_1 (Tables 3.1 and 3.2) are systematically longer for nitroxides with ^{15}N than with ^{14}N, which is consistent with prior results [1] [21] [24]. The isotope effect arises from differences in both magnetic moment and nuclear spin I. ^{15}N has a larger magnetic moment than ^{14}N ($\mu_{14N}/\mu_{15N} = 0.71$) which increases A_i, but the I(I + 1) term offsets this difference, so the ratio of the $^{14}N/^{15}N$ coefficients in Eq. (3.4) is $(0.71)^2$ x I_{14N} $(I_{14N} + 1)/I_{15N}$ $(I_{15N} + 1) = 1.4$. Thus, if modulation of anisotropic nitrogen hyperfine were the only contribution to T_1, T_1 for a ^{15}N-containing nitroxide would be 1.4 times larger than for the analogous ^{14}N-nitroxide. The T_1 (^{15}N)/T_1 (^{14}N) ratios in Table 3.2 are about 1.2, which is consistent with modulation of nitrogen hyperfine anisotropy, in addition to spin rotation that is independent of nitrogen hyperfine.

When motion is isotropic, the Bloembergen Pound Purcell (BPP) spectral density function, Eq. (3.5) is frequently used [3] [23]

$$J_{BPP}(\omega) = \frac{\tau}{1 + (\omega\tau)^2} \qquad (3.5)$$

Calculations of T_1 using the experimentally determined values of the tumbling correlation time τ and Eqs. (3.3)–(3.5) gave values in reasonable agreement with the experimental data (Table 3.2).

Prior work on nitroxide relaxation has raised questions about the suitability of the BPP spectral density function. In studies of the temperature dependence of line widths of peroxylamine disulfonate (Fremy's salt) in glycerol:water mixtures [25], tumbling correlation times for **1a** in deuterated solvents [19], and T_1 for **1a** in toluene-d_8 [26] it was observed that the BPP spectral density function (Eq. (3.5)) did not adequately model the data and that better agreement could be obtained by adding a parameter $\varepsilon \sim 4$ as the coefficient of the $(\omega\tau)^2$ term. The Cole–Davidson spectral density function (Eq. (3.6)) was developed in studies of dielectric relaxation [27] and has been applied to NMR as well as dielectric relaxation [28-30].

$$J_{CD}(\omega) = \frac{1}{\omega}\frac{\sin(\beta * \arctan(\omega\tau))}{(1 + (\omega\tau)^2)^{\beta/2}} \qquad (3.6)$$

where β characterizes the distribution of correlation times. The smaller the value of β, the wider the distribution. For $\beta = 1$, $J_{CD}(\omega)$ reduces to $J_{BPP}(\omega)$. An EPR study of the temperature dependence of line widths for **1a** in toluene at L-band to X-band used a

Cole–Davidson spectral density function with β = 0.83 [31]. In a study of nitroxide T_1 over a wide range of tumbling correlation times it was found that the Cole–Davidson spectral density function (Eq.(3.6)) provided a better fit with experimental data than did the BPP model. The values of β ranged from 0.37 in o-terphenyl to 0.67 in 1:1 water:glycerol [21]. Calculation of T_1 including spin rotation (Eq. (3.3)) and modulation of hyperfine anisotropy using Eqs. (3.4) and (3.6) with β = 0.90 gave improved fit to the experimental data for **1**, **2**, and **3** (Table 3.2).

Table 3.2 Average T_1[a] at 0.03 mM for nitroxides in H_2O compared with calculations[b].

Nitroxide	Exp.[a]	Calc. with Eq. (3.2)	Calc. with Eq. (3.2)-(3.4)	Calc. with Eqs. (3.2), (3.3),(3.5)[c]
1a	0.75	1.3	0.72	0.75
2a	0.84	1.9	0.80	0.83
3a	0.87	2.7	0.91	0.94
1b	0.91	1.3	0.81	0.84
2b	1.0	1.9	0.94	0.97
3b	1.05	2.7	1.1	1.1

[a] Experimental T_1 , average of values obtained for low-field, center-field and high-field lines
[b] Calculations use τ = 9,13 and 19 ps for **1**,**2**, and **3**, respectively
[c] β=0.90

3.7.4 Dependence of T_1 on nitrogen m_I

A dependence of T_1 on nitrogen m_I was observed (Table 3.3) with T_1 decreasing in the order low field > center field > high field. Although the differences are small, they were reproducible and many replicate measurements gave values of the ratios that are significantly different from 1. In an early variable temperature study of nitroxides in sec-butyl-benzene a dependence of T_1 on m_I was observed, with magnitude comparable to experimental uncertainties [24]. A dependence of T_I on m_I was not observed in more recent studies of nitroxides in viscous solutions [21] [23], but differences of the order of

10% are comparable to estimated uncertainties. A combination of ELDOR and saturation data for **1a** in toluene between 188 and 233 K (τ = 11.8 x 10^{-11} to1.5x10^{-11} s) found ratios of T_1 for the low-field and high-field lines between about 1.1 and 1.25 (read from graph) [32], which indicates that the m_I dependence of T_1 (Table 3.3) persists at slower tumbling correlation times.

Table 3.3 Ratios of T_1 for nitrogen hyperfine lines.[a]

Nitroxide	T_1^{LF}/T_1^{CF}	T_1^{CF}/T_1^{HF}	T_1^{LF}/T_1^{HF}	Replicates
1a	1.11 $\pm$ 0.02	1.10 $\pm$ 0.04	1.22 $\pm$ 0.04	33
2a	1.12 $\pm$ 0.03	1.08 $\pm$ 0.07	1.22 $\pm$ 0.07	10
3a	1.16 $\pm$ 0.02	1.09 $\pm$ 0.04	1.26 $\pm$ 0.06	12
1b			1.18 $\pm$ 0.03	12
2b			1.19 $\pm$ 0.05	11
3b			1.23 $\pm$ 0.02	10

[a] LF,CF and HF designate the low-field, center-field and high-field lines. For ^{14}N m_I =+1,0 and -1 for the low-field, center-field and high-field lines. For ^{15}N m_I = 0.5 and -0.5 for the low-field and high-field lines.

Early models for nitroxide spin lattice relaxation [16] [25] [33] [34] included terms with m_I dependence as shown in the following equation.

$$\frac{1}{T_1^m} = \left[c_1 \Delta A \Delta g \frac{\mu B}{\hbar} m_I + c_2 (\Delta A)^2 m_I^2\right] J(\omega) \qquad (3.7)$$

where c_1=-0.4 or -0.65, c_2=0.033 or 0.05, $\Delta A = A_{zz} - 0.5(A_{xx} + A_{yy})$ with A in angular frequency units, and $\Delta g = g_{zz} - 0.5(g_{xx}+g_{yy})$.

Since Eq. (3.4) for the END mechanism expresses the anisotropy differently than in Eq. (3.7) a new empirical expression for the m_I dependence is proposed in the following equation.

$$\frac{1}{T_1^m} = \left[c_1' \sum_i |(A_i - \bar{A})(g_i - \bar{g})| \right] \frac{\mu B}{\hbar} m_I \qquad (3.8)$$

The value of c'_1 that gives the best fit to the combined experimental data for ^{14}N and ^{15}N nitroxides (Table 3.4) is -0.32 ± 0.03. The good agreement between the values of c'_1 required to model the m_I dependence of T_1 for the ^{14}N and ^{15}N nitroxides confirms the linear dependence of the m_I term on nitrogen hyperfine anisotropy. For typical nitroxide g and A values, ΔA Δg is 1.5 times $\Sigma(g_i-\bar{g})(A_i-\bar{A})$ so c'_1 = -0.32 makes the contribution from the m_I dependent term in Eq. (3.8) smaller by a factor of 2–3 than that proposed in Eq. (3.7). Consistent with the predictions of Eq. (3.7), the experimental dependence of T_1 on m_I^2 is about an order of magnitude smaller than on m_I, which is too small an effect, relative to experimental uncertainty, to accurately define.

Table 3.4 M_I dependence of relaxation rates[b] for nitrogen hyperfine lines.[a]

Nitroxide	$1/T_1^{LF}$-T_1^{HF} experimental[c]	$1/T_1^{LF}$-$1/T_1^{HF}$ Calc, Eq. (7)[d]
1a	-0.32 ± 0.06	-0.26
2a	-0.26 ± 0.08	-0.30
3a	-0.29 ± 0.06	-0.30
1b	-0.21 ± 0.03	-0.18
2b	-0.19 ± 0.04	-0.21
3b	-0.21 ± 0.01	-0.22

[a] Notation and number of replicates are the same as in Table 3
[b] Units are 10^6 s^{-1}
[c] Proportional to Δm_I=2 for ^{14}N, Δm_I=1 for ^{15}N
[d] c'_1 = -0.32

3.7.5 Concentration Dependence of T_1

The concentration dependence of T_1 is smaller than for T_2 (Table 3.5), which is discussed in the following paragraph. It has been shown previously that in the concentration range 0.57–53 mM T_2 for Fremy's salt was more dependent on

concentration than was T_1 (factor of 20 vs. factor of 3.4), and the concentration effect on T_1 was attributed to Heisenberg exchange [35]. A spin lattice Heisenberg exchange relaxation process, which shortens T_1, can occur when two colliding radicals have different m_s. Since the populations of the two m_s states are approximately equal, only half of the collisions involve radicals with different m_s. The probability of Heisenberg exchange is smaller than the probability of colliding with a radical with different hyperfine interaction, which shortens T_2.

Table 3.5 Concentration dependence of spin packet line widths and widths in H_2O at infinite dilution.

Nitroxide	Intercept of ΔB_{sp} [a,b]	Slope (mG/mM)[a]
1a	0.09	100
2a	0.09	160
3a	0.09	80
1b	0.07	120
2b	0.07	170
3b	0.07	80

3.7.6 Spin-spin Relaxation

The T_2 of 0.53 μs for **2a** (Table 3.1) is similar to values reported previously for aqueous solutions extrapolated to infinite dilution: 0.595 μs by electron spin echo at X-band and 0.47 μs by lineshape analysis at 250 MHz [36]. Near the rapid tumbling limit there are two contributions to T_2 – incomplete motional averaging of g and hyperfine anisotropy and spin–lattice relaxation, T_1. The similarity in T_1 and T_2 values in Table 3.1 indicates that T_1 makes a major contribution to T_2 and explains why T_2 is systematically longer for the ^{15}N- than for the ^{14}N-nitroxides. The concentration dependence of T_2 was examined at four points between 0.02 and 0.30 mM, and the results are summarized in Table 3.5. The spin packet line widths extrapolated to infinite dilution are smaller

(indicating longer T_2) for the ^{15}N-nitroxides than for the ^{14}N-nitroxides. There is substantial variation in the concentration dependence of ΔB_{sp} (Table 3.5). The concentration dependence for **2a**, 160 ± 10 mG/mM, agrees within experimental uncertainty with previous reports of 167 ± 3 mG [37] or 144 mG/mM [17]. The 170 ± 10 mG/mM concentration dependence for **2b** is similar to the previous report of 120 mG/mM [17]. The largest concentration dependence is observed for **2**. The large doublet hydrogen/deuterium hyperfine splitting (Table 3.6) for **2** results in a higher probability of collision with a radical in a different nuclear spin state. The concentration dependence is smallest for **3**, which is a carboxylic acid and is predominantly in its anionic form in neutral aqueous solution. The negative charge on **3** decreases the probability of collisions. The concentration dependence is slightly greater for ^{15}N than for ^{14}N. The smaller number of nitrogen nuclear spin states increases the effective concentration in each line, but also decreases the probability of colliding with a radical in a different spin state.

3.7.7 CW Lineshapes

As shown in Table 3.1 ΔB_{pp} is significantly larger than ΔB_{sp}, and within the set of nitroxides there are much larger variations in ΔB_{pp} than for ΔB_{sp}. Since decreasing ΔB_{pp} increases S/N, optimization of probes for in vivo imaging requires characterization of structural features that give rise to differences in hyperfine splittings. In addition, for EPR oxymetry the parameter of interest is the change in ΔB_{sp} due to collision with molecular O_2. Thus it is important to confirm that simulations that include all hydrogen/ deuterium hyperfine couplings give spin packet line widths that agree with values obtained directly by electron spin echo (Table 3.1). CW spectra of the $m_I = 0$ lines for **1a**, **2a**, **3a** and the

low-field line for **3b** are shown in Fig. 3.2. For each of the ring structures the low-field and center-field lines of ^{14}N- and low-field lines of ^{15}N species have very similar line widths. The low-field line of **3b** (Fig. 3.2 D and F) is much sharper than the center field line of **3a** (Fig. 3.2 C and E) because of the replacement of hydrogen by deuterium.

The spectra of **3** shown in Fig. 3.2 E and F were obtained in toluene, because the lower viscosity resulted in better resolution of the hydrogen hyperfine splitting (Fig. 3.2 E) than was obtained in water. For each of the simulations the ΔB_{sp} used in the simulation is in good agreement with the value obtained by electron spin echo. The hyperfine couplings used in the simulations are shown in Table 3.6. For **1** and **2** simulation of the CW spectra for natural isotope abundance samples (spectra not shown) using values of the ^{2}H hyperfine couplings appropriately scaled to ^{1}H also were in good agreement with experiment.

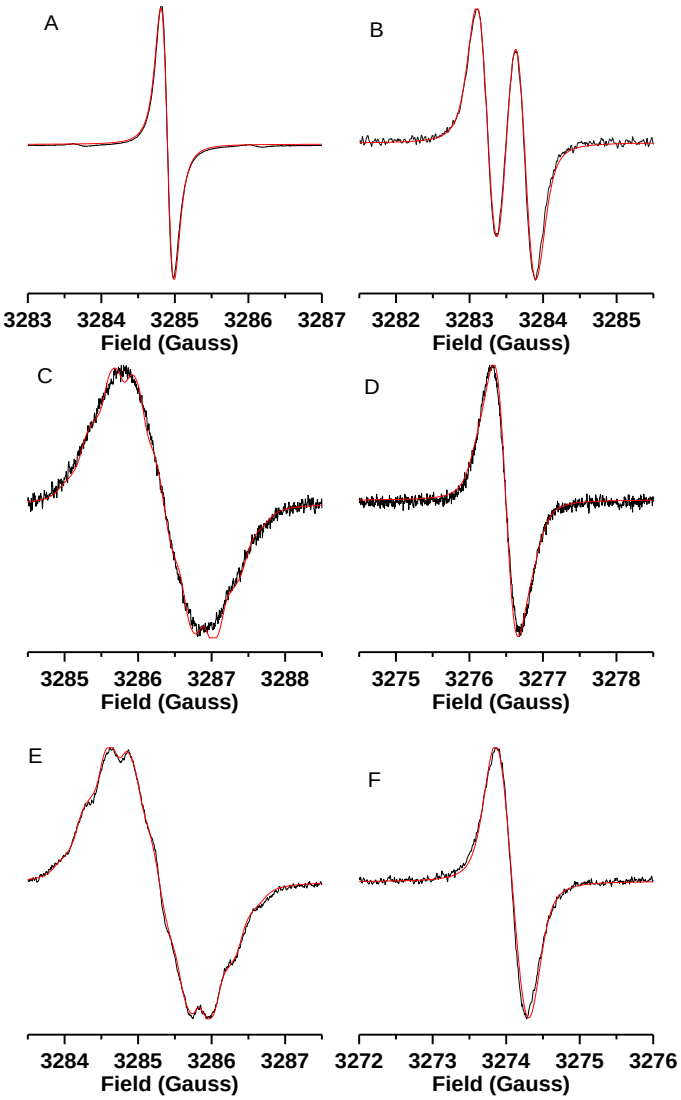

Figure 3.2 CW lineshapes of nitroxide radicals in the absence of oxygen Center-field lines of (A) **1a** in water, (B) **2a** in water, (C) **3a** in water, (D) low-field line of **3b** in water (E) center-field line of **3a** in toluene, and (F) low-field line of **3b** in toluene. For each of the plots the x axis spans 4 G and the y axis scale is arbitrary. Simulations (red lines) using the hydrogen/deuterium hyperfine couplings listed in Table 3.6 and the spin packet widths listed in Table 3.1 overlay the experimental spectra. Adapted from [6].

A striking feature of the simulations, and a key factor in the small ΔB_{pp} for **1**, is the small coupling to the ring methyls. Substituents such as $–NH_2$ or –OH (or derivatives of these) in the 4-position of a piperidine-1-oxyl, cause a conformation in which the bulky substituent is equatorial, and there is a large difference between the hyperfine

couplings to two inequivalent sets of six hydrogens: equatorial (a_H = 0.4–0.5 G) and axial (a_H ~0 G) methyl groups [15] [38], with resulting ΔB_{pp} > 1 G [8]. If conformational dynamics are fast enough, the couplings to the axial and equatorial methyls are averaged and the twelve methyl hydrogens are equivalent on the EPR timescale. This is the case in the hydrogen-containing analog of **1** (average a_H = 0.11 G) [40] and in 2,2,6,6-tetramethyl-1-piperidinyloxyl (average a_H = 0.22 G). A double bond or two hydrogens at the 4-position appears to be required for the conformational averaging to be fast enough on the EPR timescale to give small averaged couplings to the methyls [8].

Table 3.6 Nitrogen and hydrogen/deuterium coupling constants (G) in H_2O. [a,b]

	1a	**2a**	**3a**	**3b**
N	16.1	16.1	16.4	22.9
Methyl	0.018 (12D)	0.027 (12D)	0.32 (3H)	0.049 (3D)
			0.28 (3H)	0.043 (3D)
			0.05 (3H)	0.0008 (3D)
			0.04 (3H)	0.006 (3D)
Ring Hydrogen	0.0031 (4D)	0.51 (1H)	0.54 (1H)	0.54 (1H)/ 0.083 (1D) 1:3
			0.14 (1H)	0.021 (1D)
			0.12 (1H)	0.018 (1D)

[a] Coupling constants for **1b** and for **2b** are the same as for the corresponding ^{14}N analogs except for scaling of the nitrogen hyperfine coupling.
[b] Hyperfine coupling constants are in good agreement with literature values for **1a** [13], **2a** [13] [14], nitroxides similar to **3** [15].

In 3-carbamoyl-2,2,5,5-tetramethyl-3-pyrrolin-1-yloxyl, CTPO, **5**, there are four inequivalent sets of three hydrogens, with almost equal couplings of about 0.2 G [5]. For **5** with normal isotope abundance there is resolved hyperfine coupling to the methyl hydrogens and to the ring hydrogen [5]. The resolution of the hydrogen hyperfine splittings is sensitive to the O_2 concentration in solution. Complete deuteration of **5** results in hyperfine couplings that are too small to be resolved. The envelope of the

unresolved deuterium couplings is a line that is broader than the resolved hydrogen hyperfine lines of **5**, and is less responsive to O_2 collisions. Deuteration of only the methyl groups of **5** produces **2** in which there is resolved splitting by the single ring hydrogen.

Simulations were performed initially of the spectra of **3a** in toluene, where there is partial resolution of the larger splittings (Fig. 3.2 E), and then in water where the hyperfine splittings are not resolved (Fig. 3.2 C). The overall lineshape is consistent with previously reported hyperfine splittings for this class of nitroxides [14], but uncertainties are greater than for **1** or **2**. For **3** the asymmetric substitution of the ring and slow ring dynamics results in four inequivalent methyl groups with different hyperfine couplings, and a broad unresolved spectrum. When the hydrogen couplings were scaled to the values expected for deuterium the calculated lineshape was narrower than observed for **3b**. Simulations (Fig. 3.2 D) indicate the presence of about 25% H (instead of D) for the unique ring H/D with large hyperfine coupling. Mass spectrometry with a JEOL accuTOF-CS was interpreted by colleagues at the University of Maryland as indicating complete deuteration in **3b** [8]. However the EPR lineshapes are uniquely sensitive to incomplete deuteration at the site of the large hyperfine splitting. The author of the dissertation did not have access to the raw data from the University of Maryland for closer inspection.

3.7.8 Comparison with literature values for nitroxides

A summary of relaxation times for Fremy's salt reported T_1 = ca. 0.35 μs and T_2 = ca. 0.25 μs in air-saturated aqueous solutions at room temperature [38] and T_2 = 0.41 μs in degassed water [41]. Values of T_1 at X-band for low-molecular weight nitroxides in low viscosity solvents near 20 ˚C [10] include **1a** in sec-butyl-benzene, 0.47 μs [24]; tempol in sec-butyl-benzene, 0.41 μs [24]; **1a** in toluene-d_8, 0.45 μs [26]; **1a** in water, 0.30 μs [42] and perdeuterated ^{15}N-tempol in water, 1 μs (read from Fig. 3 in [23]). The Freed group has performed extensive studies of the impact of molecular motion on lineshapes and T_2 [43] [44]. These values are in the range of about 0.5–1 μs, consistent with the results reported here.

The spectrum of Fremy's salt does not have unresolved hyperfine coupling. The line width extrapolated to low concentration was 0.097 G [45], which is similar to the 0.09 G values reported for nitroxides in Table 3.5. The Fremy's salt line width increases with concentration with a slope of 46 mG/mM between ~1 and 40 mM in aqueous 0.05 M K_2CO_3 (read from Fig. 3 of Ref. [45]). The smaller concentration dependence of relaxation-determined line widths for Fremy's salt relative to neutral nitroxides such as **1** and **2** in water (Table 3.5) may be due to the negative charges on the anion, analogous to observations on collision broadening of nitroxides by paramagnetic transition metal complexes [46] [47].

The concentration dependence of T_2 and line width is expected to depend on charge surrounding the radical, spin distribution, overall size, solvent viscosity and pH. The trityl radicals used for in vivo imaging are larger than nitroxides and negatively charged [48], which makes relaxation less dependent on concentration than for neutral nitroxides such as **1** and **2**.

3.7.9 Predictions related to frequency dependence

In vivo EPR imaging experiments are performed at frequencies between about 250 MHz and 1.0 GHz [49]. The contributions to line widths from unresolved proton hyperfine are independent of frequency. At X-band and lower frequencies the anisotropy in nitrogen nuclear hyperfine dominates the terms that are averaged by tumbling and this contribution is independent of frequency, so the contributions to T_2 from incomplete motional averaging at 250 MHz to 1 GHz are predicted to be about the same as at X-band.

At 250 MHz the values of T_2 for the low-field and center-field lines of **1a** obtained by rapid scan are 0.41 and 0.53 μs for 0.50 and 0.10 mM solutions, respectively [50]. These are similar to T_2 at X-band for the center-field line of **1a** of 0.59 and 0.68 μs for 0.25 mM and 0.030 mM solutions, respectively. In this rapid tumbling regime $T_1 \sim T_2$ so the experimental values of T_2 provide a lower limit on T_1 and requires that for **1a** T_1 at 250 MHz is $\geq$ 0.53 μs in 0.10 mM aqueous solution.

Calculations of T_1 at 250 MHz including contributions from spin rotation Eq. (3.3) and modulation of nitrogen nuclear hyperfine interaction described by Eq. (3.4) + (3.5), (3.4)

+ (3.6), or (3.4) + (3.6) + (3.8) predict T_1 for **1a** at 250 MHz of 0.66–0.78 μs in dilute aqueous solution. For **2a** and **3a** the longer tumbling correlation times predict somewhat shorter values of T_1 at 250 MHz and 1.0 GHz than at X-band but all of the models predict values of $T_1 \leq 0.5$ μs at 250 MHz. For nitroxide parameters the dependence of T_1 on m_I (Eq. (3.8)) at 250 MHz is predicted to be smaller than that observed at X-band. The frequency dependence of nitroxides **1**,**2** and **3** are explored as part of a larger group of nitroxides in chapters 4 and 5.

3.8 Summary

The spin packet line widths in water (Table 3.1) are similar for the three ^{15}N-substituted radicals and somewhat narrower than for the ^{14}N-substituted analogs, due primarily to longer T_1 for ^{15}N than for ^{14}N. The negative charge on **3**, or a narrow line, such as for **1**, decreased the observed concentration dependence. The largest contribution to overall line width differences was from hydrogen (or deuterium) hyperfine splittings. As a result of the differences in hyperfine splittings, the CW peak-to-peak signal amplitude for **1a** is about nine times greater than that for **5** and four times greater than for **2a**.

Replacement of ^{14}N by ^{15}N improves signal amplitude by an additional factor of 1.5 due to the smaller number of hyperfine lines. The spectra and relaxation times show that in aqueous solution at ambient temperature the six nitroxides studied are near the rapid tumbling limit and have $T_1 \sim T_2$. The dominant contributions to spin lattice

relaxation are modulation of nitrogen hyperfine anisotropy and spin rotation. T_1 is less concentration dependent than T_2.

3.9 References

[1] W. Froncisz, T. G. Camenisch, J. J. Ratke, J. R. Anderson, W. K. Subczynski, R. A. Strangeway, J. W. Sidabra and J. S. Hyde, "Saturation recovery EPR and ELDOR at W band for spin labels," *J. Magn. Reson.,* vol. 193, pp. 297-304, 2008.

[2] J. S. Hyde, J. J. Yin, W. K. Subczynski, T. G. Camenisch, J. J. Ratke and W. Froncisz, "Spin-labeled EPR T_1 vaues using saturation recovery from 2 to 35 GHz," *J. Phys. Chem. B,* vol. 108, pp. 9524-9529, 2004.

[3] R. Owenius, G. R. Terry, M. J. Williams, S. S. Eaton and G. R. Eaton, "Frequency Dependence of Electron Spin Relaxation of Nitroxyl Radicals in Fluid Solution," *J. Phys. Chem. B,* vol. 108, pp. 9475-9481, 2004.

[4] C. Mailer, R. D. Nielsen and B. H. Robinson, "Explanation of spin-lattice relaxation rates of spin labels obtained with multifrequency saturation recovery EPR," *J. Phys. Chem. A,* vol. 109, pp. 4049-4061, 2005.

[5] H. J. Halpern, M. Peric, T. D. Nguyen, D. P. Spencer, B. A. Teicher, Y. J. Lin and M. K. Bowman, "Selective isotopic labeling of a nitroxide spin label to enhance sensitivity for T_2 oxymetry," *J. Magn. Reson.,* vol. 90, pp. 40-51, 1990.

[6] J. R. Biller, V. Meyer, H. Elajaili, G. M. Rosen, J. P. Kao, S. S. Eaton and G. R. Eaton, "Relaxation times and line widths of isotopically-substituted nitroxides in aqueous solution at X-band," *J. Magn. Reson.,* vol. 212, no. 2, pp. 370-377, 2011.

[7] Y. J. Lin, B. A. Teicher and H. J. Halpern, "Synthesis of 4-protio-3-carbamoyl-2,2,5,5-tetraperdeuteromethyl-3-pyrrolidin-1-yloxy (mHCTPO)," *J. Labelled Compd. Radiopharm.,* vol. 28, pp. 621-631, 1990.

[8] S. R. Burks, M. A. Bakhshai, M. A. Makowsky, S. Muralidharan, P. Tsai, G. M. Rosen and J. Y. Kao, "^{2}H, ^{15}N-Substituted nitroxides as sensitive probes for electron paramagnetic resonance imaging," *J. Org. Chem.,* vol. 75, pp. 6463-6467, 2010.

[9] R. W. Quine, G. R. Eaton and S. S. Eaton, "Pulsed EPR spectrometer," *Rev. Sci. Instrum.,* vol. 58, pp. 1709-1723, 1987.

[10] S. S. Eaton and G. R. Eaton, "Relaxation times of organic radicals and transition metal ions," in *Biological Magnetic Resonance 19,* 2000, pp. 29-154.

[11] R. W. Quine, S. S. Eaton and G. R. Eaton, "Saturation recovery electron paramagnetic resonance spectrometer," *Rev. Sci. Instrum.,* vol. 63, pp. 4251-4262, 1992.

[12] G. A. Rinard, R. W. Quine, S. S. Eaton, G. R. Eaton and W. Froncisz, "Relative benefits of overcoupled resonators vs. inherently low-Q resonators for pulsed magnetic resonance," *J. Magn. Reson.*, vol. 108, pp. 71-81, 1994.

[13] F. Gerson and W. Huber, Electron Spin Resonance Spectroscopy of Organic Radicals, Wiley-VCH,Weinheim, 2003.

[14] B. L. Bales, R. A. Blum, D. Mareno, M. Peric and H. J. Halpern, "Solvent and temperature dependence of the hyperfine coupling constants in CTPO," *J. Magn. Reson.*, vol. 98, pp. 299-307, 1992.

[15] A. Rockenbauer, M. Gyor, K. Hankovszky and K. Hideg, "ESR of the conformation of 5- and 6-membered cyclic nitroxide (aminoxyl) radicals," *Electron Spin Reson.*, vol. 11A, pp. 145-182, 1988.

[16] D. Kivelson, "Theory of EPR [electron paramagnetic resonance] line widths of free radicals," *J. Chem. Phys.*, vol. 33, pp. 1094-1106, 1960.

[17] B. H. Robinson, C. Mailer and A. W. Reese, "Linewidth analysis of spin labels in liquids II. Experimental," *J. Magn. Reson.*, vol. 138, pp. 210-2219, 1999.

[18] N. D. Chasteen and M. W. Hanna, "Electron paramagnetic resonance line widths of vanadyl (IV) α-hydroxycarboxylates," *J. Phys. Chem.*, vol. 76, pp. 3951-3958, 1972.

[19] J. S. Hwang, R. P. Mason, L. P. Hwang and J. H. Freed, "Electron spin resonance studies of anisotropic rotational reorientation and slow tumbling in liquid and frozen media. III. Perdeuterated 2,2,6,6-tetramethyl-4-piperidone-N-oxide and an analysis of fluctuating torques," *J. Phys. Chem.*, vol. 79, pp. 489-511, 1975.

[20] J. Labsky, J. Pilar and J. Lovy, "Magnetic resonance study of 4-amino -2,2,6,6-tetramethylpiperidine-N-oxyl and its deuterated derivatives," *J. Magn. Reson.*, vol. 37, pp. 515-522, 1980.

[21] H. Sato, S. E. Bottle, J. P. Blinco, A. S. Micallef, G. R. Eaton and S. S. Eaton, "Electron spin-lattice relaxation of nitroxyl radicals in temperature ranges that span glassy solutions to low-viscosity liquids," *J. Magn. Reson.*, vol. 191, no. 1, pp. 66-77, 2008.

[22] B. H. Robinson, C. Mailer and A. W. Reese, "Linewidth analysis of spin labels in liquids I. Theory and data analysis," *J. Magn. Reson.*, vol. 191, pp. 66-77, 1999.

[23] B. H. Robinson, D. A. Haas and C. Mailer, "Molecular dynamics in liquids: spin-lattice relaxation of nitroxide spin labels," *Science*, vol. 263, pp. 490-493, 1994.

[24] P. W. Percival and J. S. Hyde, "Saturation-recovery measurements of the spin-lattice relaxation times of some nitroxides in solution," *J. Magn. Reson.*, vol. 23, pp. 249-257, 1976.

[25] S. A. Goldman, G. V. Bruno and J. H. Freed, "ESR Studies of anisotropic rotational reorientation and slow tumbling in liquid and frozen media II. Saturation and nonsecular effects," *J. Chem. Phys.*, vol. 59, pp. 3071-3091, 1973.

[26] R. N. Schwartz, L. L. Jones and M. K. Bowman, "Electron spin echo studies of nitroxide free radicals in liquids," *J. Phys. Chem.*, vol. 83, pp. 3429-3439, 1979.

[27] N. Davidson and R. H. Cole, "Dielectric relaxation in glycerol, propylene glycol, and n-propanol," *J. Chem. Phys.*, vol. 19, pp. 1484-1490, 1951.

[28] T. Blochowicz, A. Kudik, S. Benkhof, J. Senker, E. Rossler and G. Hinze, "The spectral density in simple organic glass formers: comparison of dielectric and spin-lattice relaxation," *J. Chem. Phys.*, vol. 110, pp. 12011-12022, 1999.

[29] A. Friedrich, A. Doelle and M. D. Zeidler, "Reorientational dynamics of glycerol derived from temperature-dependent multi-nuclear magnetic relaxation data," *Magn. Reson. Chem.*, vol. 41, pp. 813-818, 2003.

[30] T. Ueda and N. Nakamura, "^{1}H MAS NMR study of local structure and dynamics of water molecule in (+/-) [Co(en)3]Cl3-nD2O," *J. Phys. Chem. B,* vol. 107, pp. 13681-13687, 2003.

[31] J. S. Hwang and Y. T. Al-Janavi, "Frequency dependent study of the correlation functions in EPR spectroscopy - the Cole Davidson Approach 1. Perdeuterated 2,2,6,6-tetramethyl-4-piperidone N-oxide in toluene," *Spect. Chim. Acta.A,* vol. 56, pp. 273-284, 2000.

[32] E. van der Drift, B. C. Rousseeuw and J. Smidt, "EPR and ELDOR studies on spin relaxation in perdeuterated 2,2,6,6-tetramethyl-4-piperidone-N-oxyl in liquid solutions: The slowly relaxing local structure mechanism," *J. Phys. Chem.*, vol. 88, pp. 2275-2284, 1984.

[33] J. H. Freed, "Theory of multiple resonance and ESR saturation liquids and related media," in *Multiple Electron Resonance Spectroscopy*, New York, Plenum, 1979, p. 100.

[34] L. Banci, I. Bertini and C. Luchinat, Electron relaxation in Dilute Systems, Nuclear and Electron Relaxation, VCH Wienheim, 1991, pp. 71-90.

[35] M. P. Eastman, G. V. Bruno and J. H. Freed, "ESR studies of Heisenberg spin

exchange III. An ELDOR study," *J. Chem. Phys.*, vol. 52, pp. 321-327, 1970.

[36] M. K. Bowman, T. J. Michalski, M. Peric and H. J. Halpern, "Fourier transform EPR and low frequency EPR studies of nitroxide radicals," *Pure Appl. Chem.*, vol. 62, pp. 271-274, 1990.

[37] H. J. Halpern, M. Peric, C. Yu and B. L. Bales, "Rapid quantitation of parameters from inhomogeneously broadened EPR spectra," *J. Magn. Reson.*, vol. 103, pp. 13-22, 1993.

[38] M. M. Kundalika, G. R. Eaton and S. S. Eaton, "Determination of T_1 and T_2 by Simulation of EPR Power Saturation Curves and Saturated Spectra. Application to Spin-Labeled Iron Porphyrins," *J. Magn. Reson.*, vol. 60, pp. 54-65, 1984.

[39] S. R. Burks, M. Makowsky, Z. A. Yaffe, C. Hoggle, P. Tsai, S. Muralidharan, M. K. Bowman, J. P. Kao and G. M. Rosen, "The Effect of Structure on Nitroxide EPR Spectral Linewidth," *J. Org. Chem.*, vol. 75, no. 14, pp. 4737-4741, 2010.

[40] L. L. Jones and R. N. Schwartz, "An electron paramagnetic resonance study of rotational and translational motion in solution," *Mol. Phys.*, vol. 43, pp. 527-555, 1981.

[41] R. G. Kooser, W. V. Volland and J. H. Freed, "E.S.R. relaxation studies on orbitally degenerate free radicals I. Benzene anion and tropenyl," *J. Chem. Phys.*, vol. 50, pp. 5243-5257, 1969.

[42] M. M. Mossoba, K. Makino, P. Riesz and R. C. Perkins, "Long-range proton hyperfine coupling in alicyclic nitroxide radicals by resolution-enhanced electron paramagnetic resonance," *J. Phys. Chem.*, vol. 88, pp. 4717-4723, 1984.

[43] V. S. Sastry, A. Polimeno, R. H. Crepeau and J. H. Freed, "Studies of spin relaxation and molecular dynamics in liquid crystals by two-dimensional Fourier transform electron spin resonance II. Perdeuterated-tempone in butoxy benzyidene octylaniline and dynamic cage effects," *J. Chem. Phys.*, vol. 105, pp. 5773-5791, 1996.

[44] J. H. Freed, "Theory of slow tumbling ESR spectra of nitroxides," in *Spin Labeling: Theory and Applications*, New York, Academic Press, 1976, pp. 53-132.

[45] M. P. Eastman, G. V. Bruno and J. H. Freed, "ESR studies of Heisenberg spin exchange II. Effects of radical charge and size," *J. Chem. Phys.*, vol. 52, pp. 2511-2522, 1970.

[46] T. D. Yager, G. R. Eaton and S. S. Eaton, "$[Cr(oxalate)_3]_3$- as a broadening agent in nitroxyl spin probe studies," *J. Chem. Soc. Chem. Comm.*, pp. 944-945, 1978.

[47] D. P. Dalal, R. Damoder, C. Benner, G. R. Eaton and S. S. Eaton, "Metal-nitroxyl interactions 44. Collision interactions between transition metal complexes and nitroxyl radicals in aqueous solution," *J. Magn. Reson.*, vol. 63, pp. 125-132, 1985.

[48] B. Epel, C. R. Haney, D. Hleihel, C. Wardrip, E. D. Barth and H. J. Halpern, "Electron paramagnetic resonance oxygen imaging of a rabbit tumor using localized spin probe delivery.," *Med. Phys.*, vol. 37, no. 6, pp. 2553-2559, 2010.

[49] B. B. Williams and H. H. Halpern, "In Vivo EPR imaging," in *Biological Magnetic Resonance 23*, pp. 283-319, 2005.

[50] M. Tseitlin, A. Dhami, R. W. Quine, G. A. Rinard, S. S. Eaton and G. R. Eaton, "Electron spin T_2 of a nitroxyl radical at 250 MHz measured by rapid scan EPR," *Appl. Magn. Reson.*, vol. 30, pp. 651-656, 2006.

CHAPTER 4

FREQUENCY DEPENDENCE OF ELECTRON SPIN RELAXATION TIMES IN AQUEOUS SOLUTION FOR A NITRONYL NITROXIDE RADICAL AND PERDEUTERATED TEMPONE BETWEEN 250 MHZ AND 34 GHZ

4.1 Introduction

The widespread application of electron paramagnetic resonance (EPR) of nitroxides, including spin labeling of proteins [1, 2], has led to extensive studies of nitroxide electron spin relaxation times over a wide range of motional regimes [3-6]. The focus of this chapter is on the rapid tumbling regime with rotational correlation times, τ_R, of tens of picoseconds, as expected for small spin probes *in vivo*. Hyde and co-workers reported spin lattice relaxation times (T_1) for 0.5 mM aqueous solutions of tempone (4-oxo-2,2,6,6-tetramethyl-4-piperidinyl-oxyl) and CTPO (3-carbamoyl-2,2,5,5-tetramethyl- 3-pyrrolinyl-1-oxyl) that decreased monotonically from 0.92 and 1.58 μs, respectively, at 34.6 GHz to 0.33 and 0.25 μs, respectively, at 2.54 GHz [7, 8]. Extrapolation of this trend to 250 MHz would predict $T_1 \approx 0.1$ μs, which would make pulsed EPR *in vivo* studies very difficult from 250 MHz to 1 GHz where they are commonly performed [9, 10]. To design molecules for pulsed EPR of nitroxides *in vivo* it is important to extend the measurements of relaxation times in Chapter 3 to lower frequencies and to model the relaxation processes to predict relaxation rates as structural and experimental conditions are varied.

There is interest in finding spin probes with longer T_1 to facilitate *in vivo* studies. For nitronyl nitroxides the nitrogen hyperfine couplings are smaller than in piperidin-yloxyls or pyrrolidinyloxyls due to the delocalization of the unpaired spin density over two nitrogens [11]. It was therefore of interest to determine the extent to which the smaller nitrogen hyperfine couplings would result in longer spin lattice relaxation times. Nitronyl nitroxides are used in identifying nitric oxide [12], dynamic nuclear polarization [13-15] and spintronics [16, 17]. After the completion of this work, we received a pre-publication copy of [18], which reports the temperature dependence of relaxation for another nitronyl nitroxide in toluene at X-band, which complements the work reported in this chapter, published in 2013 as ref. [27].

The goals of this work are to determine (i) to what extent the small nitrogen nuclear hyperfine splitting of a nitronyl nitroxide results in slower electron spin relaxation than for piperidinyl nitroxides, (ii) whether the trend to shorter T_1 at lower resonance frequency reported in Ref. [7] continues as frequency is decreased, (iii) whether the spin–rotation and modulation of A-anisotropy relaxation mechanisms, Eqns. (3.3)–(3.5), that were sufficient to model the relaxation of perdeuterated tempone (PDT, **1a**, at X-band in Chapter 3) solution are also sufficient to explain relaxation at lower frequencies, and (iv) whether a thermally activated process (Eq. (4.2)) makes a significant contribution in the fast tumbling regime.

The mechanisms for spin rotation (Eq. 3.3) and the modulation of A-anisotropy Eq. (3.4) and (3.5) were introduced in Chapter 3. Modulation of g anisotropy contributes to $1/T_1$ as described by Eq. (4.1). For nitroxide radicals this contribution is negligible at

9 GHz [26], but is significant at 34 GHz and higher frequencies and so is included in this chapter.

$$\frac{1}{T_1^g} = \frac{2}{(5\hbar)^2}(\mu_B B)^2 \left\{ \frac{(\Delta g)^2}{3} + (\delta g)^2 \right\} J(\omega) \qquad (4.1)$$

where B is the external magnetic field, μ_B is the Bohr magneton, $\Delta g = g_{zz} - \frac{1}{2}(g_{xx} + g_{yy})$, and $\delta g = \frac{1}{2}(g_{xx} - g_{yy})$. The same spectral density function (Eq. 3.5) is used for the modulation of g and A anisotropy.

The spin lattice relaxation rates in aqueous solution for three perdeuterated nitroxides, including **1a** (Chapter 3) are consistent with predictions based on Eqs. (3.3)–(3.5). In studies of tempol (4-hydroxy-2,2,6,6-tetramethylpiperidin-1-oxyl) in water:glycerol mixtures at 1.9, 3.1, and 9.2 GHz it was observed that for $\tau_R > \sim 1$ ns, $1/T_1$ was faster than predicted by contributions from mechanisms described by Eqs. (3.3), (3.4), and (3.5). Relaxation in the slower tumbling regime was dominated by a frequency- dependent process that was attributed to the same thermally- activated process that had been observed for tempol doped into a solid host [20]. This process is described by Eq. (4.2)

$$\frac{1}{T_1^{therm}} = C_{therm}\left(\frac{\omega}{\omega_{ref}}\right)\frac{\tau_{therm}}{(\omega\tau_{therm})^2} \qquad (4.2)$$

where $\tau_{therm} = \tau_C^0 \exp(E_a/RT)$, E_a is the activation energy, τ_C^0 is the pre-exponential factor, C_{therm} is the coefficient for the contribution of the thermally activated process, and $\omega_{ref} = 9.5$ GHz. The values of E_a (1100 K) and τ_C^0 (2.5×10^{-12} s) were assumed to be the

same in the water:glycerol solutions as in the doped solid. The assumption that E_a is independent of τ_R, seems reasonable for an intramolecular process. These values of E_a and τ_C^0 give τ_{therm} = 1.0 x 10^{-10}s at 295 K, which predicts a maximum effect of this process at $\omega = 1/\tau_{therm}$, or an operating frequency of 1.6 GHz.

Most prior studies of EPR relaxation processes in fluid solution have varied rotational correlation times by changing temperature [18][21-25] and/or by changing solvent [5] [22]. Relaxation rates as a function of frequency are particularly useful for characterizing relaxation processes that depend on ω [5-8] including modulation of g (Eq. 4.1) and A (Eq.3.4-3.5) anisotropy and thermally-activated processes (Eq.4.2). The frequency dependence of T_1 and T_2 at five frequencies that span more than three orders of magnitude, 250 MHz to 34 GHz, is reported in aqueous solution for two nitroxides that are of interest for *in vivo* EPR studies, PDT **1** and nitronyl nitroxide, **2** (Fig. 4.1). PDT was selected for comparison with the nitronyl because its narrow lines give improved signal-to-noise for *in vivo* studies and because its relaxation rates have been successfully modeled at X-band (Chapter 3, referred to there as **1a**).

Motion is a major factor in electron spin relaxation in fluid solution. As discussed below, the values of τ_R are 9 and 25 ps for **1** and **2**, respectively. For both radicals, $\omega\tau_R < 1$ at low frequencies and $\omega\tau_R > 1$ at 34 GHz. Thus the range of frequencies studied includes two limiting regimes for the spectral density function, Eq. (3.5), which provides a rigorous test of the model for the contribution of modulation of g and A to spin relaxation and a check on the values of τ_R.

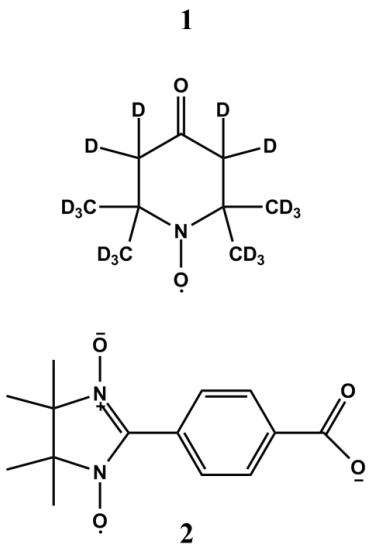

Figure 4.1 Structures of nitroxide **1** (PDT) and nitronyl nitroxide **2.** Adapted from [27].

4.2 Methods

4.2.1 Sample Preparation

PDT (**1**) was prepared as described previously [26] and provided by Dr. Gerald Rosen (University of Maryland). Solutions were 0.5 mM in water. This concentration was selected to give adequate signal-to-noise for a range of frequencies and resonators. Although Heisenberg exchange makes a detectable contribution to T_2, and to a lesser extent to T_1, at this concentration [26], these contributions are independent of frequency and will not alter conclusions concerning frequency-dependent contributions to relaxation. The nitronyl radical (**2**) was prepared as described in [27] and provided by Dr. Gerald Rosen (University of Maryland). The ester of 2-(4-acetoxymethoxycarbonylphenyl)-4,4,5,5- tetramethylimidazoline 3-oxide 1-oxyl was hydrolyzed to anion **2** (Fig. 4.1) by dissolving the acetoxy ester in 2 mM NaOH.

Sonication was used to speed dissolution. Samples for EPR spectroscopy were 0.5 mM in 2 mM NaOH.

4.2.2 Oxygen Removal

The procedure for solution deoxygenation depended on sample geometry. The effectiveness of oxygen removal was monitored by measuring T_2. Deoxygenation was continued, or repeated, until a maximum value of T_2 was observed.

Method 1 – nitrogen purge of resonator or tube:

The Q-band samples were contained in 0.3 mm i.d. thin-wall Teflon tubing supported in a 1.6 mm o.d. quartz tube open at both ends. The resonator and cryostat were purged with nitrogen for a minimum of 1 h. At X-band the sample was in 0.97 mm i.d. Teflon tubing that was doubled over to give 2 lengths of tubing supported in a 4 mm quartz tube. At S-band the 0.97 mm i.d. tubing could be folded three times for six lengths of sample in a 6 mm quartz tube. Nitrogen was purged through the 4 (or 6) mm tube via an additional thin-wall Teflon tube.

Method 2 – Freeze–Pump–Thaw (FPT):

L-band samples were contained in heavy or medium wall 4 mm quartz tubes. A length of empty 0.97 mm i.d. Teflon tubing was placed in the sample to relieve the strain caused by water expansion during freezing and thawing. Seven FPT cycles were applied and the vacuum gauge reading on the last cycle was 5–10 mTorr, before the sample was flame sealed.

Method 3 – nitrogen bubbling:

For 250 MHz, nitrogen was bubbled through samples in 25 mm tubes to displace oxygen. The head space above the sample was purged with N_2 for 20 min, followed by 15 min N_2 bubbling in the sample, and an additional 20 min purge of the head space before flame sealing. The bubbling was slow enough that evaporation was not detectable.

4.2.3 Spectroscopy

Measurement of spin–spin relaxation times (T_2) by two pulse spin echo and of spin lattice relaxation times (T_1) by inversion recovery were performed at ca. 22 °C at 34.5 GHz (Q-band) on a Bruker E580 , and at 9.5 GHz (X-band) [28], 3.0 GHz (S-band), 1.5 GHz (L-band) [29], and 250 MHz (VHF) [30] on locally designed and built spectrometers. Inversion recovery and spin echo decay measurements of **1** and **2** at Q-band were performed by Virginia Meyer. The resonators were Q-band, Bruker ER5107 dielectric pulse resonator; X-band, Bruker ER4119-X5MS; S-band, copper cross-loop resonator [29] [31]; L-band, loop-gap resonator [32]; 250 MHz, copper cross-loop resonator [33]. The 250 MHz resonator uses Q-spoiling to decrease the dead-time and facilitate measurement of short relaxation times. Saturation recovery measurements at X-band were performed on a locally designed and built spectrometer [34] by Hanan Elajaili with pump times that were long relative to T_1 (T_{1e}) or T_{1N}. Values of T_1 and T_2 were measured in triplicate for each hyperfine line of **1** and for M_I = -1, 0, and 1 of **2**. Due to the lower intensities of the $M_I = \pm 2$ lines of 2, these were not studied.

CW spectra with fully resolved proton hyperfine splitting were collected on a Bruker EMX spectrometer with an ER4122SHQE-W1/0913 resonator. The sample was drawn up into a Teflon tube, and oxygen was removed via method 1 described above.

4.2.4 Data fitting to obtain relaxation times

The spin echo decay curves and saturation recovery curves fit well with a single exponential, using a least squares criterion. At X-band and lower frequencies, the inversion recovery curves fit well with a single exponential, as expected in the regime where $\omega\tau_R \leq \sim 1$ [22]. For these radicals at 34 GHz, $T_{1N} < T_1$ and two components were observed, as expected [35] [36], for the inversion recovery curves; the longer relaxation time is assigned as T_1. The uniform penalty (UPEN) fitting procedure [37] [38] was used to confirm the presence of two contributions to the exponential decays at 34 GHz. Values of T_1 measured by saturation recovery at 9.5 GHz were in good agreement with the values obtained by inversion recovery, which confirmed the validity of the inversion recovery measurements.

4.3 Results

The values of T_1 and T_2 for the nitrogen m_I = -1, 0, and +1 lines for **1** and M_I = -1, 0, and +1 for **2** in deoxygenated aqueous solution at 22 °C at the five frequencies studied are summarized in Tables 4.1 and 4.2. The data show that the trend to shorter relaxation times between 34 and 3 GHz does not continue as frequency is decreased further. At frequencies up to 9 GHz for **1** and up to 3 GHz for **2** $1/T_1 \sim 1/T_2$ as expected in the rapid tumbling regime where motional averaging of g and A anisotropy is

essentially complete, and T_1 is the dominant contribution to T_2. At 34 GHz the higher resonant field enhances the contribution to T_2 from incomplete motional averaging of g anisotropy, and $1/T_2$ is larger than at lower fields/frequencies. The increase in $1/T_2$ at 34 GHz is greater for **2** than for **1**, because of the slower tumbling of **2**, which is discussed in the following section. Since T_1 dominates T_2 in water over most of the frequency range studied, the focus of this paper is on the frequency dependence of T_1.

For **1**, the systematically longer values of T_1 and T_2 for m_I = +1 and 0 than for m_I = -1 are similar to observations at X-band for **1** and other nitroxides in aqueous solution [26]. For **2**, the longest values of T_1, and T_2 at all frequencies except 34 GHz, are for M_I = 0. Since current models for nitroxide T_1 do not include a dependence on nitrogen nuclear spin, the data for $m_I(M_I)$ = 0 are shown in Fig. 4.2 and analyzed in the following sections.

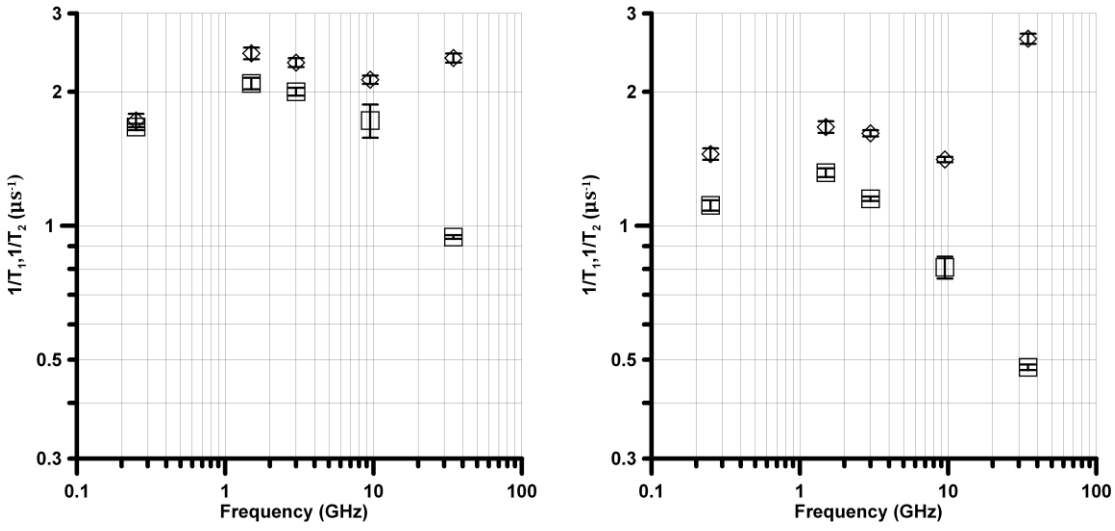

Figure 4.2 Frequency dependence of relaxation times $1/T_1$ (squares) and $1/T_2$ (diamonds) for 0.5 mM **1**, m_I = 0 (left) and 0.5 mM **2** M_I=0 (right) in aqueous solution at 22°C from 250 MHz to 34 GHz. Error bars show the standard deviation of replicate measurements. Adapted from [27].

Table 4.1 Frequency dependence of T_1 (μs) in deoxygenated H_2O at 22°C[a]

Frequency (GHz)	PDT (**1**)			Nitronyl (**2**)		
m_I	+1	0	-1	+1	0	-1
0.25	0.58	0.60	0.56	0.60	0.90	0.60
1.5	0.48	0.48	0.46	0.54	0.76	0.50
3.0	0.51	0.50	0.46	0.64	0.87	0.60
9.5	0.61	0.58	0.52	1.0	1.2	0.84
34.5	1.0	1.1	1.0	2.1	2.1	2.1

[a] Standard deviations for replicate measurements were about 3%

Table 4.2 Frequency dependence of T_2 (μs) in deoxygenated H_2O at 22°C[a]

Frequency (GHz)	PDT (**1**)			Nitronyl (**2**)		
m_I	+1	0	-1	+1	0	-1
0.25	0.55	0.58	0.55	0.56	0.69	0.44
1.5	0.39	0.41	0.37	0.45	0.60	0.39
3.0	0.42	0.43	0.38	0.46	0.62	0.40
9.5	0.49	0.47	0.38	0.61	0.71	0.44
34.5	0.52	0.42	0.31	0.46	0.38	0.25

[a] Standard deviations for replicate measurements were about 3%

*4.3.1 Analysis of the frequency dependence of $1/T_1$ for PDT **1***

The literature values for T_1 of 0.5 mM tempone in water: 0.25 μs at 2.54 GHz, 0.32 μs at 3.45 GHz, 0.49 μs at 9.2 GHz, and 0.92 μs at 34.6 GHz [7] agree within better than 10% with the values in Table 4.1 at 9.1 and 34 GHz and are shorter by about 40% at lower frequencies. Since the literature values are for natural isotope abundance tempone and these studies were for the perdeuterated analog, this agreement is consistent with prior studies that reported relatively small H/D isotope effects on nitroxide T_1 in solution [5][39].

The literature g values for **1** and **2** are shown in Table 4.3. The tumbling correlation time for **1**, determined from the m_I dependence of T_2 [40, 41] in H_2O at X-band, is 9 ps [26]. The value of $1/T_1^{SR}$, calculated using Eq. (3.3) and the g values in

Table 4.3 is shown as a solid line in Fig. 4.3. The calculation agrees well with the experimental data at 34 GHz and indicates that spin rotation is the dominant contribution to $1/T_1$ at this frequency. The increase in relaxation rates for **1** with decreasing frequency is due to frequency dependent processes. In the limit where $(\omega\tau_R)^2<<1$ the denominator of the equation for $J(\omega)$ (Eq. (3.5)) is approximately 1, and the spectral density becomes equal to τ with no frequency dependence. For τ_R = 9 ps, $\omega\tau_R$ is 1.9 at 34 GHz and 0.5 at 9.5 GHz, but decreases to less than 1 at frequencies below 9.5 GHz. This explains why $1/T_1^A$ and $1/T_1^g$ (Eqs. (3.4) and (4.1)) increase as frequency is decreased from 34 to 9 GHz and then plateau at lower frequencies (Fig. 4.3). The combined contributions to $1/T_1$ for **1** from spin rotation and modulation of g and A anisotropy explain the frequency dependence between 34 and 1.5 GHz, but cannot account for the slower relaxation (longer T_1) at 250 MHz than at 1.5 GHz (Fig. 4.3). In the calculations of spin rotation and modulation of g and A anisotropy there were no adjustable parameters and the good agreement with the experimental data confirms both the model and the value of τ_R. Variation of τ_R by more than about 10% resulted in significantly poorer agreement with the experimental data.

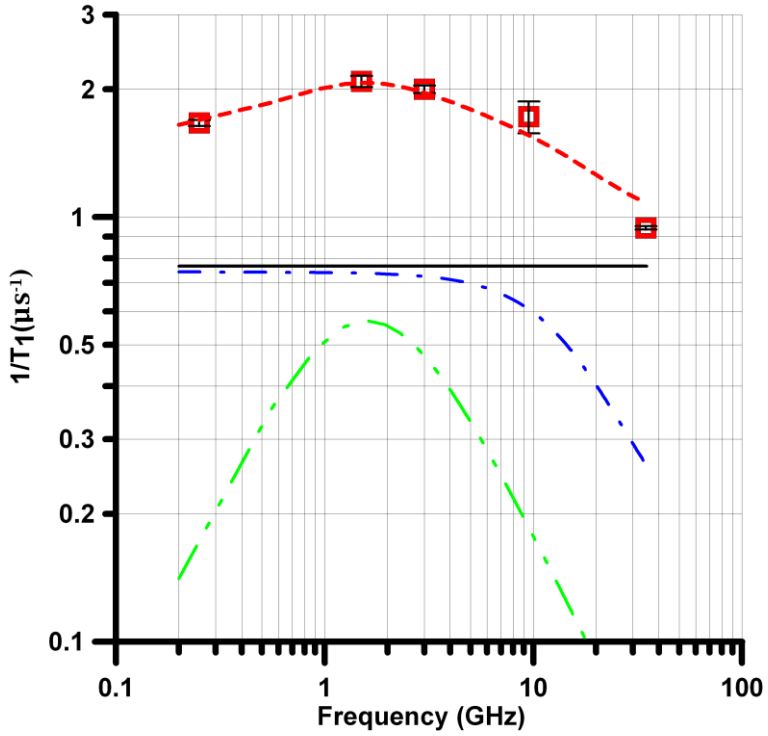

Figure 4.3 Modeling the frequency dependence of $1/T_1$ for 1 The frequency dependence of $1/T_1$ for **1** (□) was modeled (- - -) as the sum of contributions from spin rotation (▬) (Eq. 3.3), modulation of **g** and **A** anisotropies (- ▪ -) (Eqs. (3.4), (3.5), (4.1)), and a thermally-activated process (- ▪▪ -) (Eq. 4.2). Error bars show the standard deviation of replicate measurements. Adapted from [27].

The fit line in Fig. 4.3 includes a small contribution from a thermally- activated process described by Eq. (4.2) and proposed by analogy with studies of tempol in water:glycerol mixtures[5]. The fit shown in Fig. 4.3 was obtained by adjusting only C_{therm} to match the experimental data (Fig. 4.3). The resulting value of $C_{therm} = 7 \times 10^{16}$ s^{-2} is within a factor of 3 of the value of $C_{therm} = 2.8 \times 10^{16}$ s^{-2} found for slowly tumbling tempol in water:glycerol mixtures[5]. The combined contributions from spin rotation, modulation of g and A anisotropy, and the thermally activated process are in excellent agreement with the experimental frequency dependence of $1/T_1$ (Fig. 4.3). Further

experiments with a wider range of nitroxides are needed to assign the thermally activated process to a physical motion, but the maximum contribution at about 1.5 GHz supports the plausibility of the proposal that the same process dominates at long τ_R at a range of frequencies [5] and for short τ_R at lower frequencies. As τ_R approaches 10^{-9} s (slow motion), the contributions from spin rotation and modulation of g and A anisotropy are predicted to become negligible and all that remains is the contribution from the thermally-activated process.

Table 4.3 g and A-values

	g_{xx}	g_{yy}	g_{zz}	A_{xx} (G)	A_{yy} (G)	A_{zz} (G)
1[a]	2.0092	2.0061	2.0022	5.5	6.3	35.6
2[b]	2.0110	2.0065	2.0021	3.6	3.6	18.6

[a] From [24]
[b] From [11]

*4.3.2 Analysis of the frequency dependence of $1/T_1$ for nitronyl **2***

Because of the equivalent couplings to two nitrogen nuclei, τ_R for nitronyl **2** cannot be determined by the Kivelson formulae [40] that were used for **1**. Analysis of the frequency dependence of $1/T_1$ for **1** demonstrated that spin rotation is the dominant contribution at 34 GHz, so the assumption was made that this is also the case for **2**. Using the literature g values [11] and Eq. (3.3), τ for **2** was varied to give $1/T_1$ less than the experimental value at 34 GHz. The shortest value of τ_R that is consistent with the experimental data is 25 ps. Values of τ longer than 25 ps would require a contribution from an additional process at 34 GHz, beyond those required to interpret the data for **1**. To fit τ = 25 ps to the Stokes–Einstein equation ($\tau = c_{slip}V\eta/kT$, V = molecular volume calculated from the molar mass assuming a density of 0.9 g/mL which is typical of

organic molecules, η = viscosity, k = Boltzmann's constant) requires c_{slip} = 0.20. This c_{slip} is comparable to the value of 0.21 for 3-carboxy-2,2,5,5-tetramethyl-1-pyrrolidinyloxyl [26], which also has a carboxy group that can hydrogen-bond to water, so τ = 25 ps is a plausible value for **2**. The contribution from spin rotation to $1/T_1$ for **2** is shown as a solid line in Fig. 4.4. The slower relaxation for **2** than for **1** at 34 GHz (Table 4.1) is due primarily to longer τ_R for **2** than for **1**. If τ_R for **2** were similar to that for **1**, the contribution to $1/T_1$ for **2** due to spin rotation would be about 1.5 times larger than for **1** because of the larger g anisotropy (Table 4.3) and $1/T_{1e}$ would be about 0.7 μs with little frequency dependence. In water at 22 °C, the slower tumbling of **2** than of **1** offsets the difference in g values and results in slower relaxation for **2** than for **1** at 34 GHz (Tables 4.1 and 4.2). Based on this analysis a value of τ_R = 25 ps was used in analyzing other contributions to $1/T_1$ for **2**.

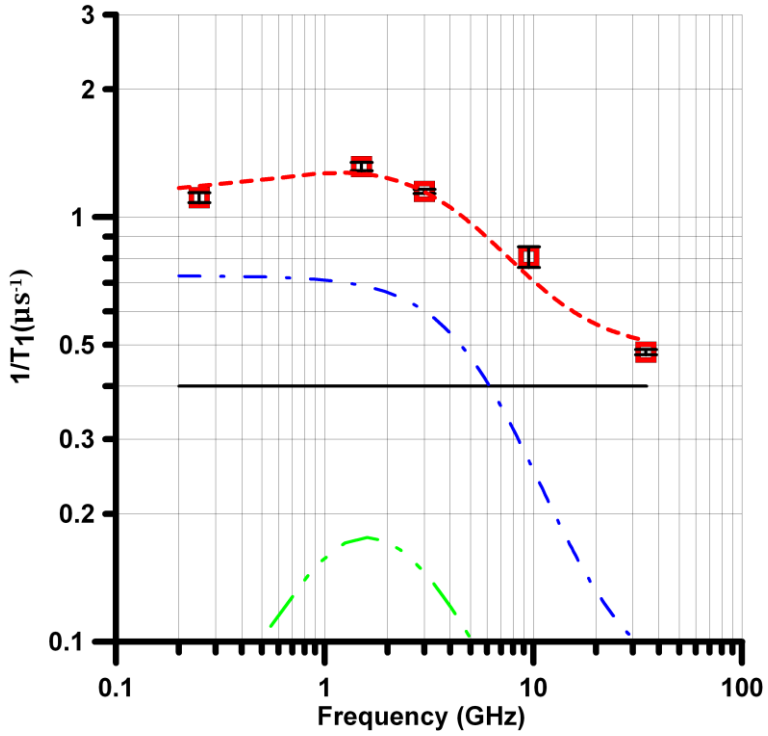

Figure 4.4 Modeling the frequency dependence of $1/T_1$ for 2. The frequency dependence of $1/T_1$ for **1** (□) was modeled (- - -) as the sum of contributions from spin rotation (—) (Eq. 3.3), modulation of **g** and **A** anisotropies (- ▪ -) (Eqs. (4.1), (3.4), (3.5)), and a thermally-activated process (- ▪▪ -) (Eq. 4.2). Error bars show the standard deviation of replicate measurements. Adapted from [27].

Eq. (4.1), the contribution to relaxation from modulation of g anisotropy, is valid for **2** as well as for **1**. The model for the contribution to $1/T_1$ from modulation of A anisotropy (Eq.(3.4)) was derived for a nitroxide with anisotropic hyperfine coupling to a single nitrogen nucleus, so it is not directly transferable to the nitronyl which has hyperfine couplings to two equivalent nitrogens. Molecular orbital calculations and modeling of the motional dynamics for p-(methylthio) phenyl nitronyl nitroxide in toluene [42] found that the principal axes of the two nitrogen hyperfine interactions were not collinear and that tumbling was anisotropic, which complicates the interpretation of

the contribution to $1/T_1$ for **2** from modulation of A anisotropy. However, it is reasonable to assume that modulation of couplings to the two nitrogens can be approximated by an expression of the form shown in Eq. (4.3).

$$\frac{1}{T_1^{A'}} = C_A J(\omega) \qquad (4.3)$$

where C_A is determined by the nitrogen hyperfine couplings of **2**. For τ_R = 25 ps $\omega\tau_R$ is 1.5 at 9.5 GHz and 0.24 at 1.5 GHz so the contribution to $1/T_1$ for **2** becomes frequency independent at lower frequency than for **1** (Fig. 4.4), which explains why the increase in $1/T_1$ for **2** between 34 and 2 GHz is substantially greater than for **1**. Since the frequency dependence of $1/T_1$ is strongly dependent on τ_R, the fit to the experimental data confirms the value of τ_R. The contribution to $1/T_1$ for **2** from modulation of g and A-anisotropy was modeled as the sum of contributions from Eq. (4.1) using literature values of g [11], τ = 25 ps, and Eq. (4.3) with C_A treated as an adjustable parameter. The contribution from Eq. (4.3) that is shown in Fig. 4.4 was obtained with $C_A = 3 \times 10^{16}$ s^{-2}. If the parameters for **1** had been used to calculate C_A, the value would be 8.2×10^{16} s^{-2}. The substantially smaller value of C_A for **2** than for **1** seems plausible because of the dependence on the square of the anisotropy of the hyperfine interaction and the much smaller hyperfine splitting for **2** than for **1** (Table 4.3).

For **2**, as for **1**, $1/T_1$ at 250 MHz is smaller than at 1.5 GHz, which requires an additional frequency-dependent contribution to relaxation. Because of the similarities in structures, it is proposed that the thermally-activated process that contributes to the relaxation of **1**, also contributes to the relaxation of **2**. The contribution shown in Fig. 4.4

for the thermally-activated process was calculated assuming the same parameters E_a and τ^0_c as for 1. To fit the data, decreasing C_{therm} requires a compensating change in C_A, within a range of about 7%. The combination of contributions from spin rotation, modulation of g and A anisotropy and the thermally-activated process is in excellent agreement with the experimental data (Fig. 4.4).

As shown in Eqs. (3.3)-(3.5),(4.1) spin lattice relaxation rates depend on both τ_R and resonance frequency. In Ref. [18] the relaxation rates for a nitronyl nitroxide **3**, analogous to **2** but without the carboxyl group, were studied in toluene as a function of temperature. Based on analysis of the temperature dependence of $1/T_2$-$1/T_1$, the hydrodynamic radius (α) of **3** was found to be 1.5 times larger than for tempone [18]. Since τ_R is proportional to α^3, the difference in radii predicts a ratio of τ_R values for **3** to that for tempone of ~3, which is in good agreement with the ratio of τ_R values for **2** and **1** = 2.8. Based on these differences in τ_R our modeling indicates that the longer values of T_1 and T_2 for **3** than for tempone in toluene at 300 K [18] are due predominantly to the slower tumbling of **3** than of tempone, analogous to what was observed in our studies in water. We predict that if both a nitroxyl and a nitronyl had τ_R of 5–10 ps, the relaxation rates at X-band would be faster for the nitronyl than for tempone by up to 20%, due to the dominant effect of spin rotation. For longer τ_R in the range of 25–50 ps for both radicals, the X-band spin lattice relaxation rates for the nitronyl would be slower than for the nitroxyl by up to 30%. At Q-band, the nitronyl relaxation rates at the same τ_R, between 5 and 50 ps, are predicted to be faster than for tempone provided that only the mechanisms described by Eqs. (3.3)-(3.5),(4.1) apply.

*4.3.3 Modeling of proton-hyperfine in aqueous solution for **2**.*

Fig. 4.5 shows the CW spectrum of **2** at room temperature recorded under low power and modulation amplitude. The super-hyperfine splitting due to methyl and phenyl protons is visible. A close-up of the $m_I = 0$ line is shown in Fig. 4.5, and the parameters for the fit (red-dashed line) are given in Table 4.4. A spin-packet linewidth of ca. 50 mG was used for fitting, based off spin-echo decay measurements on a 50 μM sample. The concentration is low enough that the effects of Heisenberg exchange are negligible and the measured T_2 is nearly inversely proportional to the spin-packet linewidth.

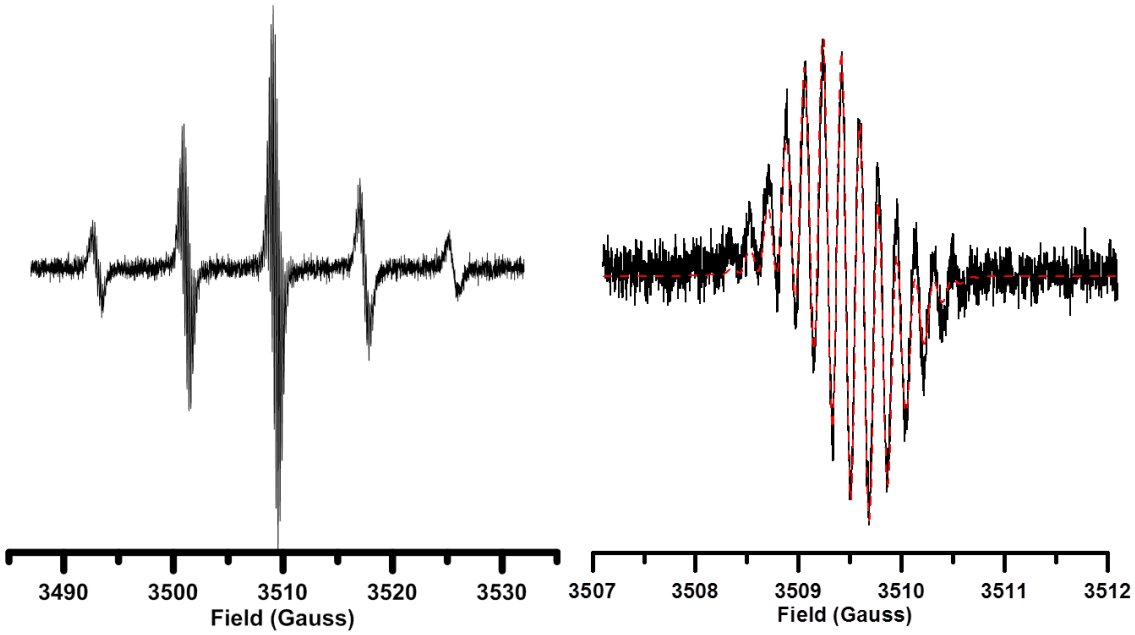

Figure 4.5 Resolution of hyperfine structure for 2. When the CW spectrum of **2** was recorded with 40 mG modulation amplitude and 26 dB attenuation, proton super-hyperfine splittings were visible in the full spectrum (left). The $m_I = 0$ line (right) was used to model the proton hyperfine (- - -).

Table 4.4 Proton hyperfine for nitronyl **2**

Nuclei	Splitting (G)[a]
6 H (gem-di-methyl)	0.165
6 H (gem-di-methyl)	0.200
2 H (phenyl ring)	0.135
2 H (phenyl ring)	0.190

[a] Modeled with a spin-packet linewidth of ca. 50 mG.

The spectrum for a nitronyl similar to **2** was recently published for the radical in toluene [43]. Analysis of the $m_I = 0$ line at 270 K gave coupling constants of 0.47 G for two-equivalent *ortho*-protons, 0.28 G for two equivalent *meta*-protons and 0.21 G for 12 equivalent methyl-protons. Assignment was confirmed by CW-ENDOR of the radical recorded at 270 K. The 0.21 G assignment for *meta* protons, and ca. 0.2 G assignment for the CH_3 protons are similar to values for **2**, but there was no coupling as large as 0.47 G found for the spectrum in Fig. 4.5. Nitronyl radicals with protons in all positions on the benzene ring have been studied. In [44] isotropic hyperfine were 0.21 G for the methyl protons, and 0.49 or 0.17 G for the *ortho* or *meta* protons. The *para* proton had a value of 0.47 G. Another nitroxide was studied in DMSO in [45]. No designations are given, but two protons have a coupling of 0.42 G, two have 0.17 G, a third has 0.37 G and the 12 equivalent CH_3 protons are at 0.19 G.

Attempting to use the hyperfine parameters from [43-45] results in a poor fit for the spectrum of **2** (Fig. 4.5). The "best" fit includes a broader spin packet linewidths than were measured. Radical **2** has a carboxy group in the *para* position of the benzene ring. The larger electron withdrawing capability of the carobxy group may result in less radical density near the ring protons, leading to smaller hyperfine couplings.

4.4 Summary

Spin lattice relaxation rates ($1/T_1$) for both PDT and nitronyl **2** between 250 MHz and 34 GHz are due predominantly to spin rotation and modulation of g and A anisotropy. The frequency dependence is dominated by the modulation of g and A anisotropy, and rates are approximately constant between about 250 MHz and 3 GHz. For both radicals, the smaller values of $1/T_1$ at 250 MHz than at 1.5 GHz are attributed to a contribution from a thermally-activated process that has its maximum contribution at about 1.5 GHz. The decreasing ratio of $1/T_1$ for **2** to that for **1** with decreasing frequency is due to different ratios of contributions to relaxation at different frequencies. The slower spin lattice relaxation rate for **2** than for **1** at 34 GHz (Table 4.1) is due primarily to spin rotation and longer τ_R for **2** than for **1**. At the same τ_R, relaxation rates at 9 GHz and higher would be faster for **2** than for **1** because of larger g anisotropy. The relaxation rates for **1** and **2** from 250 MHz to 3 GHz are more similar than at higher frequencies because modulation of A anisotropy is increasingly important at these frequencies, and $(\omega\tau_R)^2 < 1$, so the spectral density function is proportional to τ_R at lower frequencies. The longer τ_R for **2** than for **1** partially compensates for the smaller value of C_A for **2** than for **1** and the resulting values of $1/T_1$ differ by only a factor of 1.5 between 250 MHz and 3 GHz.

4.5 References

[1] L. Berliner, Ed., Spin Labeling II, New York: Academic Press, 1979.

[2] L. Columbus and W. L. Hubbell, "A new spin on protein dynamics," *Trends Biochem. Sci.,* vol. 27, pp. 288-295, 2002.

[3] S. S. Eaton and G. R. Eaton, "Relaxation times of organic radicals and transition metal ions," in *Biological Magnetic Resonance 19*, 2000, pp. 29-154.

[4] B. H. Robinson, C. Mailer and A. W. Reese, "Linewidth analysis of spin labels in liquids I. Theory and data analysis," *J. Magn. Reson.,* vol. 191, pp. 66-77, 1999.

[5] R. Owenius, G. R. Terry, M. J. Williams, S. S. Eaton and G. R. Eaton, "Frequency Dependence of Electron Spin Relaxation of Nitroxyl Radicals in Fluid Solution," *J. Phys. Chem. B,* vol. 108, pp. 9475-9481, 2004.

[6] C. Mailer, R. D. Nielsen and B. H. Robinson, "Explanation of spin-lattice relaxation rates of spin labels obtained with multifrequency saturation recovery EPR," *J. Phys. Chem. A,* vol. 109, pp. 4049-4061, 2005.

[7] J. S. Hyde, J. J. Yin, W. K. Subczynski, T. G. Camenisch, J. J. Ratke and W. Froncisz, "Spin-labeled EPR T1 vaues using saturation recovery from 2 to 35 GHz," *J. Phys. Chem. B,* vol. 108, pp. 9524-9529, 2004.

[8] W. Froncisz, T. G. Camenisch, J. J. Ratke, J. R. Anderson, W. K. Subczynski, R. A. Strangeway, J. W. Sidabra and J. S. Hyde, "Saturation recovery EPR and ELDOR at W band for spin labels," *J. Magn. Reson.,* vol. 193, pp. 297-304, 2008.

[9] J. P. Kao, E. D. Barth, S. R. Burks, P. Smithback, C. Mailer, K. Ahn, H. J. Halpern and G. M. Rosen, "Very-Low-Frequency Electron Paramagnetic Resonance (EPR) Imaging of Nitroxide-Loaded Cells," *Magn. Reson. Med.,* vol. 58, no. 4, pp. 850-854, 2007.

[10] S. Subramanian and M. C. Krishna, "Time-Domain Radio Frequency EPR Imaging," in *Biological Magnetic Resonance: Biomedical EPR- Part A: Free Radicals, Metals, Medicine and Physiology*, vol. 23, 2005, pp. 321-382.

[11] L. B. Volodarsky, Imidazoline Nitroxides, Synthesis and Properties, vol I., Boca Raton: CRC Press, 1988.

[12] G. M. Rosen, B. E. Britigan, H. J. Halpern and S. Pou, Free Radicals: Biology and Detection by Spin Trapping, Oxford: Oxford University Press, 1999, pp. 225-226.

[13] B. D. Armstrong and S. Han, "A new model for Overhauser enhanced nuclear magnetic resonance using nitroxide radicals," *J. Chem. Phys.,* vol. 127, pp. 104508/1-104507/10, 2007.

[14] D. Sezer, M. Gafurov, M. J. Prondolini, V. P. Denysenkov and T. F. Prisner, "Dynamic nuclear polarization of water by a nitroxide radical: rigorous treatment of the electron spin saturation and comparison with experiments at 9.3 Tesla," *Phys. Chem. Chem. Phys.,* vol. 11, pp. 6638-6653, 2009.

[15] M. T. Turke and M. Bennati, "Saturation factor of nitroxide radicals in liquid DNP by pulsed ELDOR experiments," *Phys. Chem. Chem. Phys. ,* vol. 13, pp. 3630-3633, 2011.

[16] S. Sanvito, "Molecular spintronics," *Chem. Soc. Rev.,* vol. 40, pp. 3336-3355, 2011.

[17] I. Ratera and J. Veciana, "Playing with organic radicals as building blocks for functional materials," *Chem. Soc. Rev.,* vol. 41, pp. 303-349, 2012.

[18] A. Collauto, A. Barbon and M. Brustolon, "First determination of the spin relaxation properties of a nitronyl nitroxide in solution by electron spin echo at X-band: a comparison with tempone," *J. Magn. Reson.,* vol. 223, pp. 180-186, 2012.

[19] P. W. Atkins, "Spin-rotation interaction," in *Electron Spin Relaxation in Liquids,* L. T. Muus and P. W. Atkins, Eds., New York, Plenum Press, 1972, pp. 279-312.

[20] S. S. Eaton, J. Harbridge, G. A. Rinard, G. R. Eaton and R. T. Weber, "Frequency Dependence of Electron Spin Relaxation for Three S=1/2 Species Doped into Diamagnetic Solid Hosts," *Appl. Magn. Reson.,* vol. 20, pp. 151-157, 2001.

[21] B. H. Robinson, A. W. Reese, E. Gibbons and C. Mailer, "A unified descriptionof the spin-spin and spin-lattice relaxation rates applied to nitroxide labels in viscous liquids," *J. Phys. Chem. B,* vol. 103, pp. 5881-5894, 1999.

[22] B. H. Robinson, D. A. Haas and C. Mailer, "Molecular dynamics in liquids: spin-lattice relaxation of nitroxide spin labels," *Science,* vol. 263, pp. 490-493, 1994.

[23] J. H. Freed, "Theory of slow tumbling ESR spectra of nitroxides," in *Spin Labeling: Theory and Applications,* L. Berliner, Ed., New York, Academic Press, 1976, pp. 53-132.

[24] J. S. Hwang, R. P. Mason, L. P. Hwang and J. H. Freed, "Electron spin resonance studies of anisotropic rotational reorientation and slow tumbling in liquid and frozen media. III. Perdeuterated 2,2,6,6-tetramethyl-4-piperidone-N-oxide and an analysis of fluctuating torques," *J. Phys. Chem.,* vol. 79, pp. 489-511, 1975.

[25] P. W. Percival and J. S. Hyde, "Saturation-recovery measurements of the spin-lattice relaxation times of some nitroxides in solution," *J. Magn. Reson.*, vol. 23, pp. 249-257, 1976.

[26] J. R. Biller, V. Meyer, H. Elajaili, G. M. Rosen, J. P. Kao, S. S. Eaton and G. R. Eaton, "Relaxation times and line widths of isotopically-substituted nitroxides in aqueous solution at X-band," *J. Magn. Reson.*, vol. 212, no. 2, pp. 370-377, 2011.

[27] J. R. Biller, V. M. Meyer, H. Elajaili, G. M. Rosen, S. S. Eaton and G. R. Eaton, "Frequency dependence of electron spin relaxation times in aqueous solution for a nitronyl nitroxide radical and perdeuterated-tempone between 250 MHz and 34 GHz," *J. Magn. Reson.*, vol. 225, pp. 52-57, 2012.

[28] R. W. Quine, G. R. Eaton and S. S. Eaton, "Pulsed EPR spectrometer," *Rev. Sci. Instrum.*, vol. 58, pp. 1709-1723, 1987.

[29] R. W. Quine, G. A. Rinard, B. T. Ghim, S. S. Eaton and G. R. Eaton, "A 1-2 GHz pulsed and continuous wave electron paramagnetic resonance spectrometer," *Rev. Sci. Instrum.*, vol. 67, pp. 2514-2527, 1996.

[30] R. W. Quine, G. A. Rinard, S. S. Eaton and G. R. Eaton, "A pulsed and continuous wave 250 MHz electron paramagnetic resonance spectrometer," *Concepts Magn. Reson.*, vol. 15, no. 1, pp. 59-91, 2002.

[31] G. A. Rinard, R. W. Quine, S. S. Eaton and G. R. Eaton, "Dispersion and superheterodyne EPR using a bomodal resonator," *J. Magn. Reson.*, vol. 122, pp. 58-63, 1996.

[32] G. A. Rinard, R. W. Quine and G. R. Eaton, "An L-band Crossed Loop (Bimodal) EPR Resonator," *J. Magn. Reson.*, vol. 144, pp. 85-88, 2000.

[33] G. A. Rinard, R. W. Quine, G. R. Eaton and S. S. Eaton, "250 MHz Crossed-Loop Resonator for Pulsed Electron Paramagnetic Resonance," *Concepts Magn. Reson.*, vol. 15, no. 1, pp. 37-46, 2002.

[34] R. W. Quine, S. S. Eaton and G. R. Eaton, "Saturation recovery electron paramagnetic resonance spectrometer," *Rev. Sci. Instrum.*, vol. 63, pp. 4251-4262, 1992.

[35] C. A. Popp and J. S. Hyde, "Electron-electron double resonance and saturation recovery studies of nitroxide electron andn nuclear spin-lattice relaxation times and Heisenberg exchange rates: lateral diffusion in dimyristoyl phosphatidylcholine," *Proc. Natl. Acad. Sci. USA*, vol. 79, pp. 2559-2563, 1982.

[36] Y. J. Yin and J. S. Hyde, "Use of high observing power in electron spin resonance saturation-recovery experiments in spin-labeled membranes," *J. Chem. Phys.*, vol. 91, pp. 6029-6035, 1989.

[37] G. C. Borgia, R. S. Brown and P. Fantazzini, "Uniform-penalty inversion of multiexponential decay data II. Data spacing, T2 data, systematic errors, and diagnostics," *J. Magn. Reson.*, vol. 147, pp. 273-285, 2000.

[38] G. C. Borgia, R. S. Brown and P. Fantazzini, "Uniform-penalty inversion of multiexponential decay data," *J. Magn. Reson.*, vol. 132, pp. 65-77, 1998.

[39] H. Sato, S. E. Bottle, J. P. Blinco, A. S. Micallef, G. R. Eaton and S. S. Eaton, "Electron spin-lattice relaxation of nitroxyl radicals in temperature ranges that span glassy solutions to low-viscosity liquids," *J. Magn. Reson.*, vol. 191, no. 1, pp. 66-77, 2008.

[40] D. Kivelson, "Theory of EPR [electron paramagnetic resonance] line widths of free radicals," *J. Chem. Phys.*, vol. 33, pp. 1094-1106, 1960.

[41] N. D. Chasteen and M. W. Hanna, "Electron paramagnetic resonance line widths of vanadyl (IV) a-hydroxycarboxylates," *J. Phys. Chem.*, vol. 76, pp. 3951-3958, 1972.

[42] V. Barone, M. Brustolon, P. Cimino, A. Polimeno, M. Zerbetto and A. Zoleo, "Development and validation of an integrated computational approach for the modeling of CW-ESR spectra of free radicals in solution: p-(methylthio) phenyl nitronylnitroxide in toluene as a case study," *J. Am. Chem. Soc.*, vol. 128, pp. 15685-15873, 2006.

[43] A. Collauto, M. Mannini, L. Sorace, A. Barbon, M. Brustolon and D. Gatteschi, "A slow relaxaing species for molecular spin devices: EPR characterization of static and dynamic magnetic propertis of a nitronyl nitroxide radical," *J. Mat. Chem.*, vol. 22, pp. 22272-22281, 2012.

[44] J. Goldman, T. E. Petersen, K. Torssell and J. Becher, "19F and 1H NMR and ESR investigations of aryl-t-butyl nitroxides and nitronyl nitroxides," *Tetrahedron*, vol. 29, pp. 3833-3843, 1973.

[45] J. Cirujeda, J. Vidal-Gancedo, O. Jurgens, F. Monta, J. J. Novoa, C. Rovira and J. Veciana, "Spin Density Distribution of alpha-Nitronyl Aminoxyl Radicals from Experimental and ab Initio Calculated ESR Isotropic Hyperfine Coupling Constants," *J. Am. Chem. Soc.*, vol. 122, pp. 11393-11405, 2000.

[46] N. Bloembergen, E. M. Purcell and R. V. Pound, "Relaxation effects in nuclear resonance absorption," *Phys. Rev.*, vol. 73, pp. 679-712, 1948.

[47] E. F. Ullman, J. H. Osiecki, D. B. Boocock and R. Darcy, "Studies of stable free radicals. X. Nitronyl nitroxide monoradicals and biradicals as possible small molecule spin labels," *J. Am. Chem. Soc.,* vol. 94, pp. 7049-7059, 19972.

[48] T. Akaike, M. Yoshida, Y. Miyamoto, K. Sato, M. Kohno, K. Sasamoto, K. Miyazaki, S. Ueda and H. Maeda, "Antagonistic action of imidazolineoxyl N-oxides against endothelium-derived relaxation factor/NO through a radical reaction," *Biochem.* , vol. 32, pp. 827-832, 1993.

CHAPTER 5

ELECTRON SPIN-LATTICE RELAXATION MECHANISMS OF RAPIDLY-TUMBLING NITROXIDE RADICALS

5.1 Introduction

Nitroxide T_2 has been studied extensively, both experimentally and theoretically, to understand motional dynamics in fluid solutions [1-4]. Early studies of T_1 focused primarily on ~ 9.5 GHz [5-7]. The utility of T_1 to measure oxygen concentrations in membranes [8-10] and tissues [11] and the use of nitroxides for *in vivo* imaging [12, 13] motivated characterization of the frequency dependence of T_1 below 2 GHz, for reasons discussed in Chapter 4.

In chapter 4 the T_1 and T_2 were reported for aqueous solutions of a nitronyl nitroxide and of PDT at five frequencies between 250 MHz and 34 GHz in the fast motional regime where the tumbling correlation time, τ_R, is less than about 25 ps. Other empirical studies at frequencies $\leq$ 250 MHz support the observation that T_1 is longer than what current theory predicts [5, 6] [14]. For instance, the lines in the spectrum of Fremy's salt ($(SO_3)_2NO_2^-$) in aqueous solution at 60 MHz are Lorentzian with $T_1 = T_2 = 0.5$ μs [15]. Rapid-scan EPR of perdeuterated 2,2,6,6-tetramethyl-4-piperidone-1-oxyl (PDT, **1a**) in aqueous solution at 250 MHz [16] found $T_2 = 0.5$ μs. Since $T_2 \leq T_1$, T_2 puts a

lower limit on T_1. These results motivate examination of nitroxide T_1 at frequencies lower than 2.5 GHz for a wider range of nitroxides and solvents.

The goal of this chapter is to investigate (i) the relative importance of spin rotation (Eq. 3.3) and modulation of nitrogen hyperfine anisotropy (Eq.3.4) for τ_R = 4–50 ps at ambient temperature, (ii) whether additional mechanisms contribute to relaxation at frequencies lower than ~9.5 GHz, and (iii) the thermally-activated process (Eq. 4.2) that is proposed to have maximum impact on T_1 at 1–2 GHz, and has been observed previously in both the fast [37] and slow tumbling regimes [19]. T_1 and T_2 were measured by pulsed methods for the nitroxides shown in Fig. 5.1, at frequencies between 250 MHz and 34 GHz. This work has been published in [17].

5.1.1 A review of spin-lattice relaxation mechanisms

Mechanisms of spin-lattice relaxation are discussed in the introductions to Chapters 3 and 4. A brief review is given here. $1/T_1^{SR}$ (Eq. 3.3) is independent of resonance frequency and decreases as τ_R increases. Modulation of the large anisotropic (dipolar) nitrogen nuclear hyperfine coupling by molecular tumbling (the END process, (Eq. 3.4) is a major contributor to nitroxide relaxation in certain motional regimes [5] [6] [14]. The spectral density function (Eq. 3.5) gives the END mechanism as well as the modulation of g-anisotropy (Eq. 4.1) a dependence on τ_R and ω. In the rapid-tumbling regime the BPP spectral density function is indistinguishable from the Cole-Davidson spectral density function that has been found to give better agreement than BPP with the temperature dependence of nitroxide $1/T_1$ under slower tumbling conditions [18, 19].

For τ_R in the range of 4-50 ps, $\omega\tau_R$ (see Eq. 3.5) changes from <1 at 250 MHz to >1 at 34 GHz. For $\omega\tau_R > 1$, $1/T_1^A$ increases as ω decreases. For $\omega\tau_R << 1$, $1/T_1^A$ is independent of ω and increases as τ_R increases. Because $1/T_1^A$ is proportional to $\gamma^2 I(I+1)$, where γ is the gyromagnetic ratio, the ratio $[1/T_1^{A\ 14}N]/[1/T_1^{A\ 15}N] = 1.36$. The $^{15}N/^{14}N$ isotope effect on $1/T_1$ provides a test of the contribution from the END mechanisms [5, 6]. Modulation of *g* anisotropy (Eq. 4.1) by molecular tumbling [5, 6] enhances relaxation of radicals with larger g anisotropy, particularly at higher microwave frequency.

The enhancement of electron spin $1/T_1$ by thermally-activated methyl rotation has been demonstrated in a variety of solid samples [20-23]. Nuclear spin–lattice relaxation enhancement by thermally-activated processes has been studied extensively in NMR [24-26]. For nitroxides in viscous water/glycerol solutions at 1.9, 3.1, and 9.2 GHz at room temperature $1/T_1$ was larger than predicted by Eqs.(3.3)–(3.5),(4.1),(4.2) [27], as described in chapter 4.

5.1.2 Nitroxides Studied

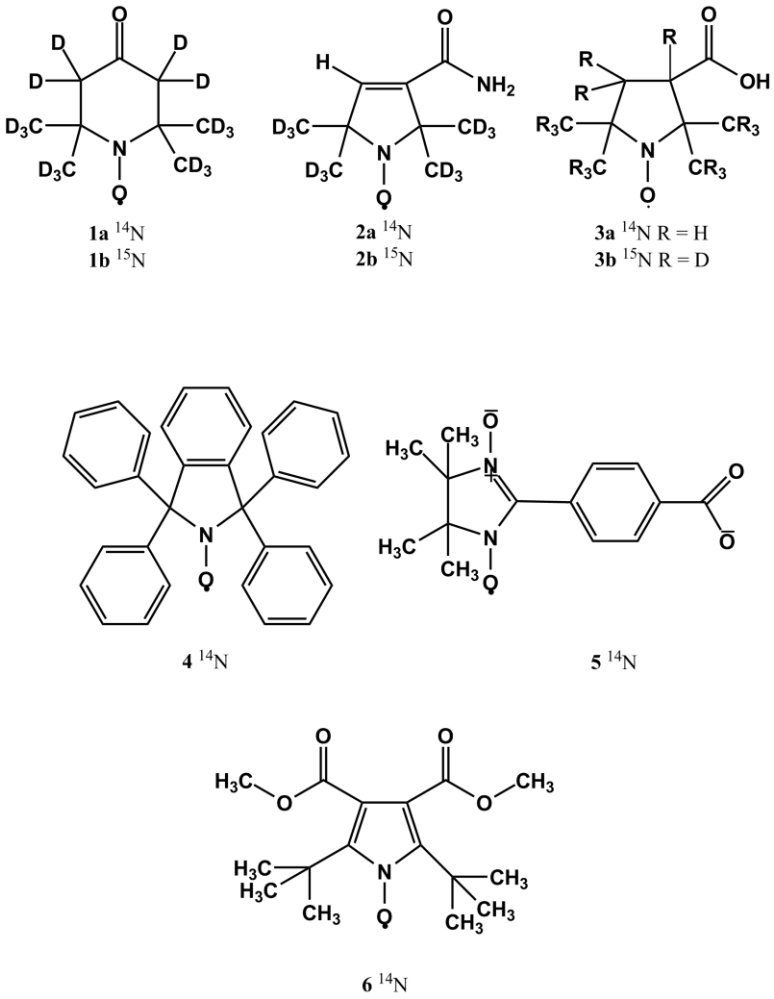

Figure 5.1 Nitroxide structures studied from 250 MHz to 34 GHz. Adapted from [17]

Several of the radicals selected for this study (Fig. 5.1) have been used for *in vivo* imaging: PDT (**1a**) to monitor redox activity [28], mono-hydrogenated deuterated CTPO (mHCTPO, **2a**) [29] for in vivo imaging of local oxygen concentration [30,31], and 3-carboxy- 2,2,5,5 tetra-methyl-1-pyrrolidinyloxyl radical (carboxyproxyl, **3a**) for *in vivo* O_2 quantitation in mouse brain [32-34]. T_1 and T_2 for **1a–3a**, along with their ^{15}N derivatives (denoted as **1b–3b**) were reported at ~9.5 GHz in Chapter 3. Other nitroxides

with different ring structures, and g- and A-anisotropies were selected for comparison. The phenyl isoindoline nitroxide (**4**) [18] contains no methyl groups and the central ring is expected to be more rigid than in **1a–3a**. Nitroxides that are similar to **4**, including some that are isotopically labeled, have recently been investigated for *in vivo* O_2 quantitation [35, 36]. The nitronyl nitroxide **5** was included because the nitrogen hyperfine splittings are smaller than for **1a–3a** and the g anisotropy is larger [37]. **6** has smaller nitrogen hyperfine splittings than **1a–3a** due to extensive delocalization of the unpaired electron into the aromatic ring, the ring is expected to be more rigid, and the four ring methyls of **1a–3a** are replaced by two t-butyl groups. Relaxation times T_1 and T_2 for **1–6** were measured at frequencies between 250 MHz and 34 GHz. For **1a** τ_R was varied by changing solvent, including both nonpolar organics and water:glycerol mixtures.

5.2 Experimental

5.2.1 Samples

1b with >98% isotope purity were purchased from CDN Isotopes (Quebec, Canada). **1a**[38], **3a** [39], **3b** [39], **4** [18], and **5** [37] were prepared as reported. **3a** and **3b** were provided by Dr. Gerald Rosen (University of Maryland). **2a** and **2b** were prepared as previously reported [40] and provided by Prof. Howard Halpern (University of Chicago). **6** was prepared as reported [41], and was a gift from Prof. Andre Rassat.

For slower tumbling radicals, **4**, **1a** in 44% glycerol, and **1a** in 69% glycerol, solutions were 0.2 mM. Most solutions were 0.4–0.5 mM (Table 5.1). Between 0.2 mM

and 0.5 mM in aqueous solution of **1a–3a** in water there is only a 5–15% increase in $1/T_1$ due to Heisenberg exchange [38], so the higher concentrations were used to improve signal-to-noise (S/N), particularly at the lower frequencies. The contribution from Heisenberg exchange is expected to be independent of resonance frequency so it will not alter the frequency dependence of $1/T_1$ that is the focus of this study.

O_2 was removed by one of three methods as described in Chapter 4 (Sec. 4.4.2).

Table 5.1 Nitroxide Parameters Concentrations are 0.5 mM except for **1a** in toluene (0.4 mM), **1a** in glycerol (0.2 mM) and **4** in toluene (0.2 mM).

	FW	Solv.	τ_R (ps)	A_{iso} (G)	A_{xx} (G)	A_{yy} (G)	A_{zz} (G)	g_{xx}	g_{yy}	g_{zz}	Lit.
1a	186	Tol.	4	14.5	4.1	5.1	33.6	2.0094	2.0063	2.0023	[67]
1a	186	H_2O	9	16.3	5.5	6.3	35.9	2.0092	2.0061	2.0022	[56]
1a	186	Min. oil	9	14.5	4.1	5.1	33.6	2.0094	2.0063	2.0023	[67]
1a	186	44% Gly.	19	16.3	5.5	6.3	35.9	2.0092	2.0061	2.0022	[56]
1a	186	69% Gly.	50	16.3	5.5	6.3	35.9	2.0092	2.0061	2.0022	[56]
1b	187	H_2O	9	22.6	7.7	8.8	50.3	2.0092	2.0061	2.0022	[56]
2a	195	H_2O	13	16.3	5.5	6.3	35.9	2.0092	2.0061	2.0022	[68]
2b	196	H_2O	13	22.6	7.7	8.8	50.3	2.0092	2.0061	2.0022	[68]
3a	186	H_2O	19	16.3	5.5	6.3	35.9	2.0092	2.0061	2.0022	[68]
3b	202	H_2O	19	22.9	7.7	8.8	50.3	2.0092	2.0061	2.0022	[68]
4	410	Tol.	26	13.4	3.2	3.2	31.8	2.0090	2.0058	2.0020	[26,27]
5	276	2 mM NaOH	25	8.7	3.6	3.6	18.6	2.0110	2.0065	2.0021	[69]
6	310	Tol.	10	4.7	0.4	0.4	13.2	2.0094	2.0060	2.0024	[26]

5.2.2 Spectroscopy

Relaxation times were measured with the same instruments and resonators as described in Chapter 4 (Sec. 4.2.3) at 21° ± 2 °C. The relaxation times at ~640 MHz for **1a** in 69% glycerol and for **4** were obtained on a prototype multi-frequency spectrometer

(600-900 MHz). Each measurement was performed at least three times. The S/N for T_1 was 80–100, except for **1a** in 69% glycerol at 630 MHz and for **4** at 640 MHz and 250 MHz where S/N was lower because relaxation times were of the same order as the resonator ringdown time. T_2 was measured as the time constant of 2-pulse echo decays. Most T_1 measurements were by 3-pulse inversion recovery, and some were also measured by long-pulse saturation recovery. Q-band measurements of radicals **1a**/**1b**, **2a**/**2b**, **3a**/**3b**, **4**, **5**, and **1a** in 44% glycerol were acquired by Virginia Meyer. The spin echo decay and saturation recovery curves (recorded by Hanan Elajaili) fit well with a single exponential, using a least squares criterion. A potential complication in the measurement of T_1 by inversion recovery is the need to distinguish T_1 from nitrogen T_{1N}, which also can contribute to the return of magnetization to equilibrium [42]. At long τ_R, T_{1N} is shorter than T_{1e}, but becomes equal to T_1 for short τ_R [6]. If the S/N is low, it may be difficult to distinguish between one- and two-component decays. At lower resonance frequencies, the inversion recovery curves fit well with a single exponential, as expected when $\omega\tau_R \leq 1$ [6]. For slower tumbling radicals at ~9.5 GHz and most radicals at 34 GHz, two components were observed in the fits to the inversion recovery curves, as expected for $\omega\tau_R > 1$ [43, 44]. The longer relaxation time is assigned as T_{1e}. The uniform penalty (UPEN) fitting procedure [45] [46] was used to confirm the presence of two contributions to the exponential decays at 34 GHz (Fig. 5.2). Values of T_1 at ~9.5 GHz for **1a** in 69% glycerol, **3a**, and **4** obtained by saturation recovery with pump times that are long relative to T_1 were in good agreement with values obtained by inversion

recovery, which confirmed that the inversion recovery experiments were accurately reporting T_1.

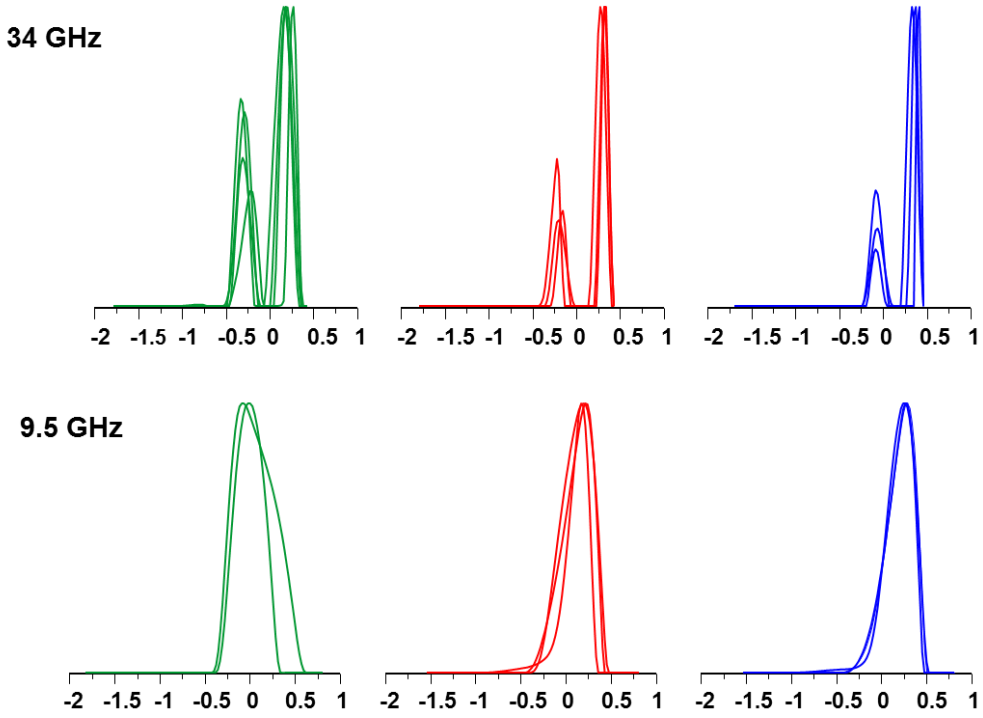

Figure 5.2 Exponent fitting as a function of frequency. Fits with the UPEN program are shown for the m_I = -½ line for **3b** (—), **2b** (—) and **1b** (—). The x-axis is log ($1/T_1$) with T_1 in μs. In the data acquired at Q-band (34 GHz, top) two populations of relaxation times are observed (T_{1e} and T_{1N}), as expected in the regime where $\omega\tau_R > 1$. For data acquired at X-band (9.5 GHz, bottom) only a single broad population is observed, reflecting the case $T_{1e} \sim T_{1N}$ when $\omega\tau_R \leq 1$. Multiple traces display the variation between replicate data sets. Q-band data courtesy of Virginia Meyer.

Values of T_1 and T_2 for each of the nitrogen hyperfine lines at each of the frequencies studied are listed in Appendix A (Tables A1 and A2). As observed previously (Chapter 4), there is a systematic m_I dependence of both T_1 and T_2 (Chapters 3 and 4).Values of T_1 decrease in the order m_I = +1 (low-field) ≥ m_I = 0 (center field) > m_I = - 1 (high-field) for ^{14}N and m_I = 0.5 > m_I = - 0.5 for ^{15}N (Table A1). In tumbling regimes

where the END process Eq. (3.4) is the dominant contribution to $1/T_1$ the ratio of T_1 for ^{14}N $m_I = 1$ to $m_I = -1$ is about 1.2, which is in good agreement with prior results (Chapter 3). The m_I dependence is smaller at concentrations above 0.5 mM (Table 5.2) where Heisenberg exchange may be significant, and in tumbling regimes where the END mechanism Eq. (3.4) is a smaller fraction of the combined contributions to $1/T_1$. Since the available models for the END mechanism do not include an m_I dependent contribution, the values of $1/T_1$ plotted in Figs. 5.2, 5.4 and 5.5, and included in the modeling, are $m_I = 0$ (^{14}N) or the average for $m_I = \pm 0.5$ (^{15}N).

Table 5.2 Dependence of T_1 on m_I and concentration for **3a** at X-band

	2.7 mM	1.35 mM	0.68 mM	0.5 mM	0.25 mM	0.125 mM	0.06 mM	0.03 mM
M_I = +1	0.34	0.48	0.68	0.73	0.83	0.92	0.96	0.98
M_I = 0	0.32	0.49	0.62	0.63	0.73	0.81	0.82	0.83
M_I = -1	0.32	0.49	0.58	0.59	0.66	0.74	0.73	0.76
LF/CF	1.06	0.98	1.10	1.16	1.14	1.14	1.17	1.18
LF/HF	1.06	0.98	1.17	1.24	1.26	1.24	1.32	1.29

5.2.3 Modeling the frequency dependence of $1/T_1$

The g- and nitrogen A-values are summarized in Table 5.1. A-values for **1b–3b** were calculated from the values for the ^{14}N analogs multiplied by the ratio of the gyromagnetic ratios for $^{15}N/^{14}N = 1.40$. For **6** immobilized in sucrose octaacetate, simulation of the ~9.5 GHz spectrum (unpublished data from Hideo Sato) gave a well-defined $A_{zz} = 13.2$ G. Values of $A_{xx} = A_{yy} = 0.4$ G were estimated by assuming that $A_{xx} = A_{yy}$ and using $A_{iso} = 4.7$ G in toluene. Values of τ_R for all radicals, except **5**, were calculated from the m_I dependence of T_2 at X-band (Chapter 3). The uncertainties in τ_R are about ±20%. The value of $\tau_R = 4$ ps for PDT (**1a**) in toluene is in good agreement with the literature value

of 5 ps [47]. The value of τ_R for **5** is taken from Chapter 4. The $1/T_1$ data in Figs. 5.2, 5.4 and 5.5 are modeled as the sum of contributions from spin rotation (Eq. (3.3), solid black line), modulation of A- and g-anisotropy by molecular tumbling Eqs. (3.4)–(3.5),(4.1), blue dashed line) and a thermally-activated process Eq. (4.2), green dashed line). The sum of the contributions is the red fit line. The contribution from modulation of g-anisotropy is negligible except at 34 GHz. For **1–4** and **6**, there are no adjustable parameters in the calculations of the contributions to relaxation from Eqs. (3.4)–(3.5),(4.1). The only adjustable contribution to $1/T_1$ was from the thermally-activated process, Eq. (4.2). Independent variation of C_{therm} and τ_{therm} did not give significantly improved fit to the data, so τ_{therm} was fixed at 1.0×10^{-10} s as in chapter 4. The contribution of the END process for nitronyl nitroxide **5** was also discussed in chapter 4.

5.3 Results And Discussion

Much of the prior work on electron spin lattice relaxation of nitroxides has focused on lower temperatures and/or relatively long tumbling correlation times as described in Sec. 4.1. Understanding relaxation in the faster tumbling regime provides exciting new insights for designing small molecule spin probes for applications to in vivo imaging and dynamic nuclear polarization (DNP).

Relaxation times were measured at 0.25, 1.5, 2.5–3.0, 9.4–9.5 and 34 GHz, with the exception of **1a** in 69% glycerol for which the lowest frequency data were measured at ca. 0.63 GHz (Fig. 5.4). For **1b–3b** relaxation times also were measured at 1.0 and 1.9 GHz. Relaxation times for **1a** in water and for **5** are reproduced from Chapter 4. At ~9.5

and 34 GHz the T_1 for **1a** in water is in good agreement with values for 0.5 mM natural abundance tempone reported in [48] as discussed in Chapter 4.

5.3.1 Interpretation of frequency dependence of relaxation

The frequency dependence of $1/T_1$ and $1/T_2$ for PDT (**1a**) in five solvents (toluene, water, light mineral oil, 44% glycerol in water, and 69% glycerol in water) is shown in Fig. 5.4. For τ_R < ~20 ps and resonance frequencies ≤ 9 GHz, $1/T_1 \sim 1/T_2$ as expected in the fast tumbling regime. At 34 GHz, $1/T_2 - 1/T_1$ is substantial (Fig. 5.3) due to increased contributions from incomplete motional averaging of g-anisotropy. The slope of the plot of $1/T_2 - 1/T_1$ vs τ_R is 2.3×10^{17} s^{-2} (Fig. 5.3). Calculation of the predicted slope of the plot based on the A, B, and C terms in the Kivelson model of linewidths [49, 50] and typical g and A hyperfine anisotropy predicts a slope of 1.6×10^{17} s^{-2}. Given the approximations in the model and the range of solvents and nitroxides included in the plot, the agreement is good, which lends credence to the values of τ_R.

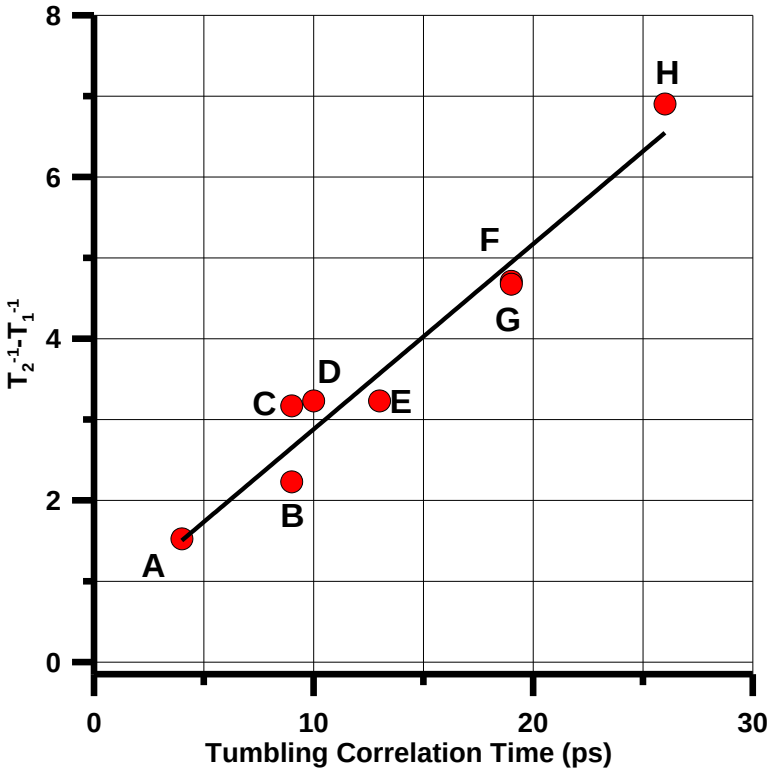

Figure 5.3 Dependence of $1/T_2 - 1/T_1$ on τ_R for the high-field ^{14}N hyperfine line at Q-band for: **A**, **1a** in toluene; **B**, **1a** in water; **C**, **1a** in light mineral oil; **D**, **6** in toluene; **E**, **2a** in water; **F**, **3a** in water; **G**, **1a** in 44% glycerol; **H**, **4** in toluene. Slope of the least-squares fit line is 2.3×10^{17} s^{-2}. Adapted from [17].

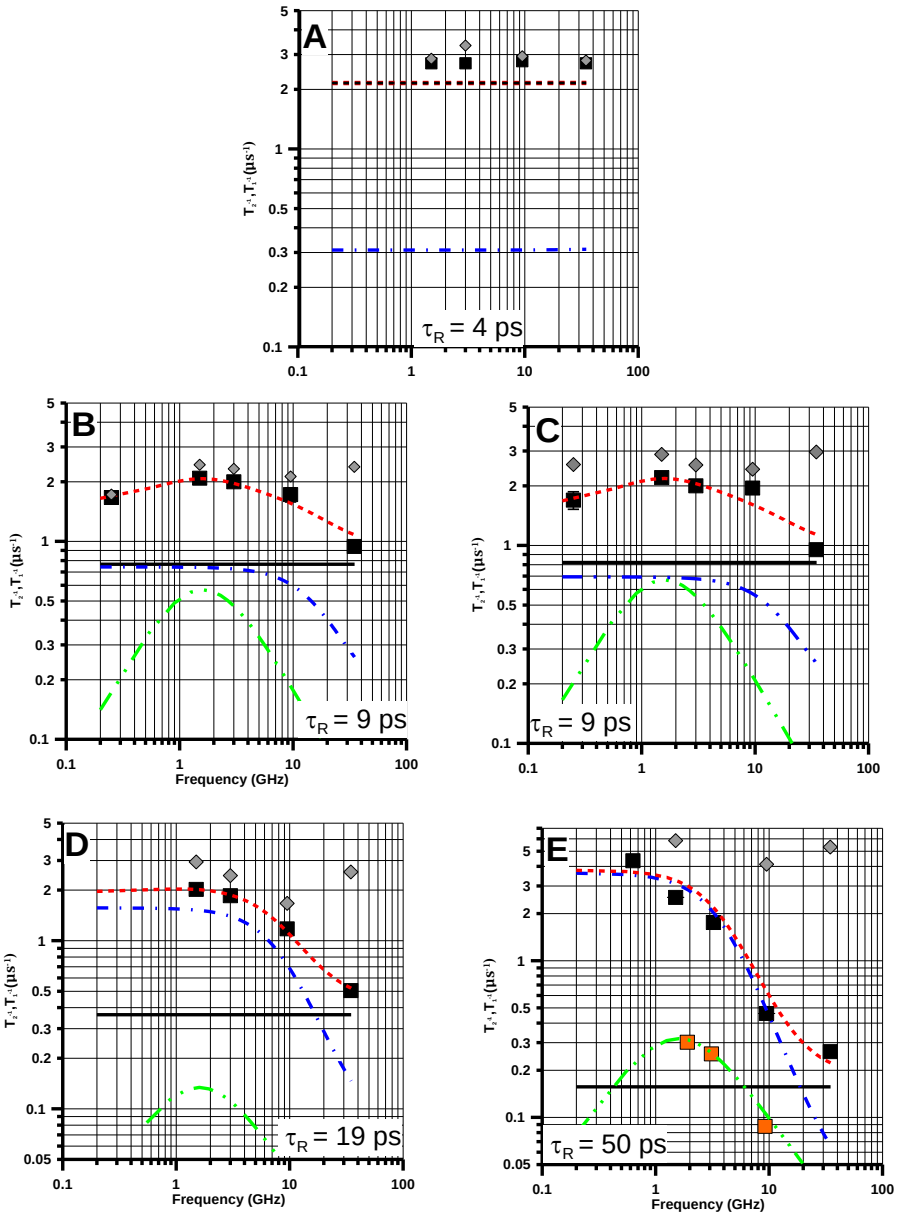

Figure 5.4 Frequency dependence of $1/T_1$ (■) and $1/T_2$ (♦) for 1a with τ_R from 4 to 50 ps Radical **1a** in (A) toluene, (B) water, (C) light mineral oil, (D) 44% glycerol in water, and (E) 69% glycerol in water. Spin lattice relaxation is modeled as the sum (— — —) of contributions from spin rotation (Eq. 3.3, ———), the modulation of g- and A-anisotropy (Eq. 3.4 – 3.5, 4.1 — · —), and a thermally-activated process (Eq. 4.2, — · · —). In (E) the gold squares and fit line — · · · — are the contribution from the thermally-activated process observed previously for $\tau > \sim 3x10^{-9}$ s [27]. Adapted from [17].

As τ_R *increases* the frequency-independent contribution from spin rotation (Eq. 3.3) *decreases* (Fig. 5.4). At τ_R = 4 ps spin rotation dominates $1/T_1$ and relaxation is independent of frequency (Fig. 5.4A). The agreement between experiment and calculation at τ_R = 4 ps is not as good as at longer τ_R. For the small PDT molecule (**1a**) in low-viscosity toluene, Heisenberg exchange due to nitroxide-nitroxide collision, which is not included in the simulation, may contribute more to relaxation than for other samples studied. In contrast to the dependence for spin rotation, as τ_R *increases* the contribution from modulation of A and g-anisotropy *increases*. As τ_R increases from 4 ps to 50 ps, the relaxation at frequencies less than 34 GHz changes from domination by spin rotation to domination by modulation of A anisotropy. The frequency at which the contribution from modulation of A changes from frequency independent to frequency dependent is a strong function of τ_R (Eq. 3.4-3.5,4.1). The longer the value of τ_R, the lower the frequency at which the change in slope occurs. Thus the agreement between the observed and calculated frequency dependence of $1/T_1$ is a validation of the model and of the values of τ_R. For τ_R = 9 ps, in either water (Fig. 5.4 B) or light mineral oil (Fig. 5.4 C), $1/T_1$ is smaller at 250 MHz than at 1-2 GHz. This frequency dependence is not predicted by the spin rotation (Eq. 3.3) or modulation of A or g-anisotropy (Eq. 3.4-3.5,4.1). Modeling of the relaxation rates therefore included a contribution from a thermally-activated process, Eq. (4.2). The effect of the thermally-activated process is maximum when $\omega = 1/\tau_{therm}$, which was observed to occur at about 1.6 GHz (Fig. 5.3 and 5.4), and corresponds to $\tau_{therm} = 1.0 \times 10^{-10}$ s. This is the same value of τ_{therm} that was used to model the frequency dependence of $1/T_1$ for tempol with $\tau_R > \sim 3 \times 10^{-9}$ s (300 ps) in

viscous water:glycerol mixtures [27]. The value of τ_{therm} was fixed at $1.0x10^{-10}$ s and the coefficient C_{therm} (Table 5.4) was adjusted to match the experimental data for $1/T_1$. The value of C_{therm} was similar in water (Fig. 5.4 B) or light mineral oil (Fig. 5.4 C), which indicates that the process does not require a protic solvent. C_{therm} is smaller in 44% glycerol (Fig. 5.4 D), which demonstrates a dependence on viscosity. For comparison, the contributions to $1/T_1$ from the thermally-activated process for tempol with τ_R > $\sim 3x10^{-9}$ s in viscous water:glycerol mixtures [22] is shown as orange squares in Fig. 5.4 E, and is negligibly small relative to the contributions from modulation of A and g anisotropy at τ_R = 50 ps.

The frequency dependence of relaxation in water for $^{14}N/^{15}N$ pairs of radicals is shown in Fig. 5.5. These radicals have τ_R in the range of 9 to 19 ps. At 34 GHz spin rotation (Eq. 3.3) dominates $1/T_1$ which is about the same for ^{14}N and ^{15}N (Fig. 5.4). As seen in Fig. 5.2 the contribution from $1/T_1^A$ (Eq. 3.4) increases as frequency decreases from 34 to about 3 GHz. If the END process were the only relaxation mechanism, the dependence on nuclear spin I and the hyperfine coupling constants, A, would cause the ratio of $[T_1^{-1}(^{14}N)]/[T_1^{-1}(^{15}N)]$ to be 1.36 [19]. For the pairs **1a**/**1b**, **2a**/**2b**, and **3a**/**3b** the ratios of relaxation rates increase, as expected, as the contribution from the END process increases (Table 5.3) and is in the range of 1.3 to 1.4 where the END process dominates. The limiting value of $1/T_1^A$ at low frequency increases as τ_R increases (Eq. 3.4). Because of the increasing role of the END process at lower frequencies, $1/T_1$ becomes more frequency dependent as τ_R *increases*.

Table 5.3 Frequency dependence of $1/T_1$ and relative contributions from relaxation mechanisms.[b,c] $(1/T_1$ for ^{14}N $m_I = 0)/ (1/T_1$ for ^{15}N $m_I = \pm 0.5)$[a]

Freq. (GHz)	1a/1b		2a/2b		3a/3b	
33.9	1.05	SR > END > THM	1.00	SR > END > THM	1.12	SR > END > THM
9.4-9.5	1.16	SR > END > THM	1.28	END > SR > THM	1.38	END > SR > THM
2.5-3.0	1.16	SR ~ END > THM	1.35	END > SR ~ THM	1.32	END > SR ~ THM
1.5	1.18	SR~ END ~ THM	1.27	END > SR ~ THM	1.34	END > SR ~ THM
0.25	1.13	SR ~ END > THM	1.12	END > SR > THM	1.25	END > SR > THM

[a] Uncertainties in ratios of T_1 are 5 to 7%.
[b] Abbreviations for relaxation mechanisms are spin rotation (SR), modulation of A anisotropy (END), and thermally-activated process (THM).
[c] The contributions from relaxation mechanisms are displayed quantitatively in Fig. 5.5.

For the two nitroxides with smaller nitrogen hyperfine couplings, **6** and nitronyl nitroxide **5**, the contribution to $1/T_1$ from $(1/T_1^A)$ is substantially reduced (Fig. 5.6 A,B). Even though τ_R for **5** in water (25 ps) is about the same as for **4** in toluene (26 ps), $1/T_1$ for **5** at low frequencies is about a factor of two smaller than for **4**, due to the decreased contribution from $(1/T_1^A)$. Nitroxide **6** has nitrogen hyperfine couplings that are less than 1/3 of those for **1** – **4**. The τ_R for **6** in toluene (10 ps) (Fig. 5.5 A) is intermediate between those for **1a** (τ_R = 9 ps) (Fig. 5.4 A) and **2a** (τ_R = 13 ps) (Fig. 5.5 B) in water, so the contributions from spin rotation are similar. However, the contribution from $(1/T_1^A)$ for **6** in toluene is so much smaller than for **1** or **2** in water that $1/T_1$ for **6** is approximately equal to the value predicted for spin rotation alone (Fig. 5.6 A).

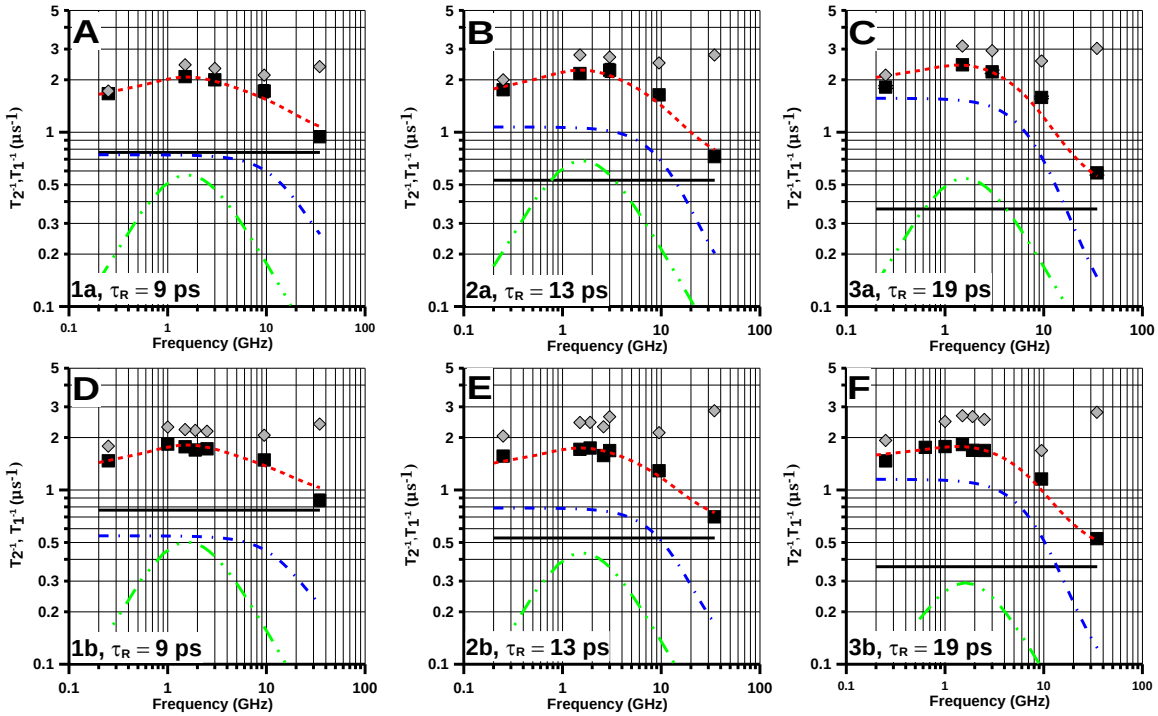

Figure 5.5 Frequency dependence of $1/T_1$ (■) and $1/T_2$ (♦) for radicals 1-3 in water. Plots for $m_I = 0$ lines of (A) **1a**, (B) **2a**, (C) **3a** or the $m_I = \pm 0.5$ lines of (D) **1b**, (E) **2b**, and (F) **3b**. Spin lattice relaxation is modeled as the sum (– – –) of contributions from spin rotation (Eq. 3.3, ———), the modulation of g- and A- anisotropy (Eq. 3.4 – 3.5,4.1 —·—) and a thermally-activated process (Eq. 4.2 —··—). Adapted from [17].

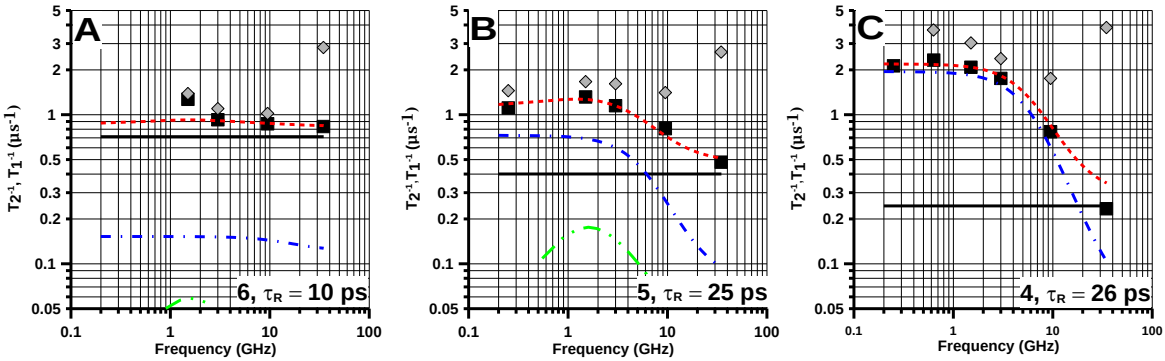

Figure 5.6 Frequency dependence of $1/T_1$ (■) and $1/T_2$ (♦) for radicals 4-6. Plots for the m_I=0 lines of (A) **6** in toluene, (B) **5** in 2 mM aqueous NaOH and (C) **4** in toluene. Spin lattice relaxation is modeled as the sum (— — —) of contributions from spin rotation (——), the modulation of g- and A- anisotropy (— · —) and a thermally activated process (— · · —). Adapted from [17].

Analogous to what was observed for **1a** in water and mineral oil (Fig. 5.4 B,C) $1/T_1$ for **1b**, **2a**, **2b**, **3a**, **3b**, and **5** at 250 MHz is smaller than at 1-2 GHz (Figs. 5.5 and 5.6), which cannot be accounted for by Eq. (3.3-3.5)(4.1). The enhanced relaxation at 1-2 GHz is attributed to a thermally-activated process. C_{therm} is larger for **1a - 3a** (containing ^{14}N) than for **1b - 3b** (containing ^{15}N) (Table 5.4), which indicates a nitrogen isotope effect on C_{therm}. The nitrogen isotope is observed independent of whether the $1/T_1$ for ^{14}N is analyzed for $m_I = 0$ or for the average of all three nitrogen hyperfine lines. For the pairs **1a**/**1b** and **2a**/**2b** the only substitution is ^{14}N to ^{15}N. For the pair **3a**/**3b** H is substituted by D as well as ^{14}N by ^{15}N so the larger ratio of values of C_{therm} for **3a**/**3b** (2.6) than for **1a**/**1b** or **2a**/**2b** (1.4 or 1.7) suggests that there is an additional H/D isotope effect.

Table 5.4 Values of C_{therm} used to model $1/T_1$ from 33.9 GHz to 250 MHz.

		C_{therm} ($x10^{16}$)			
ID	**Solvent**	**$M_I = 0$**	**Average M_I[a]**	**Average M_I[b]**	**$^{14}N/^{15}N$**
1a	Water	7	7.7		1.4
	LMO	8.6	8.5		
	44% Gly	3.8	4.5		
1b	Water			5.7	
2a	Water	8.2	9.0		1.7
2b	Water			5.2	
3a	Water	6.5	9.0		
3b	Water			3.5	2.6
4	Toluene	<0.7			
5	NaOH	2.8			
6	Toluene	0.7			

[a] An average of $m_I = +1,0,-1$

[b] An average of $m_I = \pm 1/2$

5.3.2 Potential assignments of the thermally-activated process

The characteristic time for the thermally-activated process is about $1x10^{-10}$ s, which is longer than the τ_R of 10 to $50x10^{-12}$ s. Thus the thermally-activated process is modulating an interaction that is not averaged by τ_R, which therefore excludes modulation of anisotropic dipolar couplings. The values of C_{therm} decrease with increasing solvent viscosity, in the order **1a** in water > **1a** in 44% glycerol > tempol in highly viscous solvents [27]. Values of C_{therm} for **1a** – **3a** are substantially larger than for **4**, **5**, or **6**. The nitroxide rings for **4 - 6** are expected to be less flexible than for **1** – **3** because of bulkier substituents for **4** and **5** and the additional double bond in **6**. Because of the higher molecular weight of **4**, τ_R = 26 ps even in low-viscosity toluene. The contribution from $(1/T_1^A)$ is so large for **4** that it is difficult to determine whether the contribution from the thermally-activated process is small or absent, but it cannot be as

large as for **1a** – **3a**. These observations suggest that the thermally-activated process is modulation of the nitrogen isotropic g or A.

One possible mechanism for modulation of g or A is conformational changes of the geometry at the nitroxide nitrogen. Substantial temperature dependence of nitroxide g and A-values in fluid solution has been observed and attributed to fast exchange between conformations [51]. For **1a**, **1b** the interconversion of twist-crossover conformations averages axial and equatorial methyl group on the ENDOR timescale above about 230 K in a doped crystal [52] and results in equal hyperfine couplings to all twelve methyl protons in fluid solution (Chapter 3). The lifetime of about $1x10^{-7}$ s at 230 K predicts a lifetime at 298 K that is substantially longer than $1x10^{-10}$ s. For 5-member ring nitroxides interconversion of ring conformations is slow on the EPR time scale at 298 K and inequivalent couplings are observed for axial and equatorial methyls [53]. The large differences in rates of interconversion for 5- and 6- member ring nitroxides and estimates of lifetimes substantially longer than 10^{-10} s at 298 K indicate that interconversion of ring conformations is too slow to be assigned as the thermally-activated process for nitroxide relaxation. Recent molecular dynamics calculations have shown that the intramolecular out-of-plane motion of the N-O moiety is a 'soft' mode [54] [55]. For both 5- and 6-member ring nitroxides the angle between the N-O group and the plane of the molecule can vary by $\pm 10^{o}$ within a low-energy range of about 0.5 kcal/mole [55]. This angular variation is sufficient to cause substantial changes in the isotropic g and A values. Modulation of either or both of these parameters is an effective spin-lattice relaxation process. Modulation of isotropic A and g would be consistent with

a nitrogen isotope effect on C_{therm}. The dependence of C_{therm} on viscosity could indicate that a smaller range of orientations is encompassed by these motions when solvent viscosity is higher. The value of τ_{therm} is approximately what is predicted for methyl rotation at room temperature based on ENDOR studies of tempone [52]. In these sterically hindered molecules methyl rotation may couple to the motion of the NO bond and be involved in the bond angle variation that dominates the thermally-activated process.

5.3.3 Other potential contributions to relaxation

The discussion of the role of the thermally-activated process (Eq 4.2) in the relaxation for these rapidly tumbling nitroxides assumes that this process is the same as the one that contributes to the frequency-dependent relaxation of tempol for $\tau_R > \sim 3x10^{-9}$ s in viscous water:glycerol mixtures [27]. At those long values of τ_R the contributions to $1/T_1$ from spin rotation and modulation of g and A anisotropy become very small. Robinson and co-workers proposed generalized spin diffusion (GSD) as the process that dominated spin-lattice relaxation for slowly tumbling nitroxides [14], which raises the question whether GSD might also contribute for rapidly tumbling samples The GSD mechanism contributes to relaxation by modulation of electron-nuclear interspin distances via diffusion of solvent nuclei or intramolecular motions, which would have a large H/D isotope effect. In Ref. [15] it was shown that for Fremy's salt in water at 60 MHz the relaxation rate was the same in H_2O and D_2O. It was also shown previously that at ~9.5 GHz for $\tau_R < 5x10^{-9}$ s there was no difference in relaxation rate for a nitroxide in water:glycerol or in D_2O:glycerol-d_8 mixtures [27]. Thus, solvent diffusion does not

appear to be an effective relaxation mechanism for the nitroxides studied here. Furthermore, the proposed frequency dependence of GSD does not predict smaller relaxation rates at 250 MHz than at higher frequencies, so it is not an alternative to the thermally-activated process.

In an early discussion of potential relaxation processes for Fremy's salt, Lloyd and Pake [15] proposed that modulation of spin-orbit coupling by solid-state-like processes would be significant. The temperature dependence at ~9.5 GHz of $1/T_1$ for tempone in glycerol, 1:1 water:glycerol, decalin, and 3-methylpentane did not exhibit a discontinuity in the region of the glass transition temperature, which was interpreted as indicating that solid-state mechanisms persisted at higher temperatures [19]. In the slow tumbling regime the temperature dependence was modeled with contributions from Raman and local-mode processes. In glycerol, the most viscous of the solvents studied, these processes dominated relaxation at room temperature. However, in the fast tumbling regime these contributions are much smaller than the contributions from spin rotation and modulation of g- and A-anisotropy.

5.4 Summary

Understanding electron spin relaxation has been a goal of magnetic resonance spectroscopists from the earliest days of the field. Most prior studies of electron spin lattice relaxation in fluid solution were performed at ~9.5 GHz and τ_R was varied by changing temperature. The frequency dependence of relaxation is a powerful way to distinguish contributions from proposed mechanisms. The contribution from spin

rotation is independent of ω, and decreases as τ_R increases. The contribution from modulation of g- and A-anisotropy (END process) depends on both ω and τ_R. The contribution from the thermally-activated process depends on ω, but not τ_R. For rapidly tumbling nitroxides, T_1 decreases with decreasing ω between about 34 and 3 GHz [48] as previously reported, because of the frequency dependence of the END process. However, this trend does not continue at lower frequencies because the END process becomes frequency independent. The frequency dependence of $1/T_1$ between 34 and 3 GHz is smaller when τ_R = 10 ps than when τ_R = 50 ps. The thermally-activated process has maximal impact on T_1 in the range of 1 to 2 GHz. These three processes are sufficient to model $1/T_1$ over the full frequency range studied. The net effect of the contributions from spin rotation, modulation of anisotropy by tumbling, and the thermally-activated process is that for small rapidly tumbling nitroxides there is a maximum in relaxation rate at about 1 to 2 GHz and relaxation rates become smaller again at lower frequency. Consequently, relaxation rates at very low frequency (e.g., 60 MHz, 250 MHz) are similar to those at ~9.5 GHz, which is fully consistent with the earliest estimates of nitroxide relaxation rates.

In addition to understanding relaxation mechanisms, a goal of this work is to guide synthesis of application-specific nitroxide radicals. To maximize nitroxide relaxation times at low microwave frequencies, such as for *in vivo* studies, the nitroxide should be designed to minimize nitrogen hyperfine, thus reducing the effect of the END process (Eq. 3.3). If the contributions from the END process are decreased, increasing

molecular size to increase τ_R is advantageous. The radical should be as rigid as possible to minimize the impact of the thermally-activated process.

5.5 References

[1] D. J. Schneider and J. H. Freed, "Calculating slow motional magnetic resonance spectra: a user's guide," in *Biol. Magn. Reson. Vol. 8*, L. J. Berliner and J. Reuben, Eds., 1989, pp. 1-76.

[2] J. H. Freed, "ESR and molecular dynamics," in *Biol. Magn. Reson. Vol. 24*, 2005, pp. 239-268.

[3] J. H. Freed, "Theory of slow tumbling ESR spectra of nitroxides," in *Spin Labeling: Theory and Applications*, L. Berliner, Ed., New York, Academic Press, 1976, pp. 53-132.

[4] D. E. Budil, S. Lee, S. Saxena and J. H. Freed, "Nonlinear least-squares analysis of slow-motion EPR spectra in one and two dimensions using a modified Levenberg-Marquardt algorithm," *J. Magn. Reson. A*, vol. 120, pp. 155-189, 1996.

[5] B. H. Robinson, D. A. Haas and C. Mailer, "Molecular dynamics in liquids: spin-lattice relaxation of nitroxide spin labels," *Science*, vol. 263, pp. 490-493, 1994.

[6] B. H. Robinson, A. W. Reese, E. Gibbons and C. Mailer, "A unified descriptionof the spin-spin and spin-lattice relaxation rates applied to nitroxide labels in viscous liquids," *J. Phys. Chem. B*, vol. 103, pp. 5881-5894, 1999.

[7] J. Huisjen and J. S. Hyde, "A pulsed EPR spectrometer," *Rev. Sci. Instrum.*, vol. 45, pp. 669-675, 1974.

[8] W. K. Subczynski, L. Mainali, T. G. Camenisch, W. Froncisz and J. S. Hyde, "Spin-label oximetry at Q- and W-band," *J. Magn. Reson.*, vol. 209, pp. 142-148, 2011.

[9] J. J. Yin and J. S. Hyde, "Spin-label saturation-recovery electron spin resonance measurements of oxygen transport in membranes," *Zeitschrift fuer Physikalische Chemie*, vol. 153, pp. 57-65, 1987.

[10] J. J. Yin, M. Pasenkiewicz-Gierula and J. S. Hyde, "Lateral diffusion of lipids in membranes by pulse saturation recovery electron spin resonance," *Proc. Natl. Acad. Sci.* , vol. 84, pp. 964-968, 1987.

[11] B. Epel, S. V. Sundramoorthy, E. D. Barth, C. Mailer and H. J. Halpern, "Comparison of 250 MHz electron spin echo and continuous wave oxygen EPR imaging methods for in vivo applications," *Med. Phys.*, vol. 38, pp. 2045-2052, 2011.

[12] R. M. Davis, S. Matsumoto, M. Bernardo, A. Sowers, K. I. Matsumoto, M. Krishna and J. B. Mitchell, "Magnetic resonance imaging of organic contrast agents in mice:

capturing the whole-body redox landscape," *Free Rad. Biol. Med.,* vol. 50, pp. 459-468, 2011.

[13] K. I. Matsumoto, F. Hyodo, A. Matsumoto, A. P. Koretsky, A. L. Sowers, J. B. Mitchell and M. Krishna, "High-resolution Mapping of Tumor Redox Status by Magnetic Resonance Imaging Using Nitroxides as Redox-Sensitive Contrast Agents," *Clin. Cancer Res.,* vol. 12, pp. 2455-2462, 2006.

[14] C. Mailer, R. D. Nielsen and B. H. Robinson, "Explanation of spin-lattice relaxation rates of spin labels obtained with multifrequency saturation recovery EPR," *J. Phys. Chem. A,* vol. 109, pp. 4049-4061, 2005.

[15] J. P. Lloyd and G. E. Pake, "Spin relaxation in free radical solutions exhibiting hyperfine structure," *Phys. Rev.,* vol. 94, pp. 579-591, 1954.

[16] M. Tseitlin, A. Dhami, R. W. Quine, G. A. Rinard, S. S. Eaton and G. R. Eaton, "Electron spin T2 of a nitroxyl radical at 250 MHz measured by rapid scan EPR," *Appl. Magn. Reson.,* vol. 30, pp. 651-656, 2006.

[17] J. R. Biller, H. Elajaili, V. Meyer, G. M. Rosen, S. S. Eaton and G. R. Eaton, "Electron spin-lattice relaxation mechanisms of rapidly-tumbling nitroxide radicals," *J. Magn. Reson.,* vol. 236, pp. 47-56, 2013.

[18] H. Sato, V. Kathirvelu, A. Fielding, J. P. Blinco, A. Micallef, S. E. Bottle, S. S. Eaton and G. R. Eaton, "Impact of molecular size on electron spin relaxation rates of nitroxyl radicals in glassy solvents between 100 and 300 K," *Mol. Phys.,* vol. 105, pp. 2137-2151, 2007.

[19] H. Sato, S. E. Bottle, J. P. Blinco, A. S. Micallef, G. R. Eaton and S. S. Eaton, "Electron spin-lattice relaxation of nitroxyl radicals in temperature ranges that span glassy solutions to low-viscosity liquids," *J. Magn. Reson.,* vol. 191, no. 1, pp. 66-77, 2008.

[20] S. K. Hoffmann, W. Hilczer, J. Goslar, S. Kiczka and I. Polus, "Resonance-type effects in free radical electron spin-lattice relaxation and electron spin echo dephasing due to dynamics of a homogeneous-chain oligomeric system," *Phys. Chem. Chem. Phys.,* vol. 4, pp. 4944-4951, 2002.

[21] J. R. Harbridge, S. S. Eaton and G. R. Eaton, "Electron spin-lattice relaxation in radicals containing two methyl groups, generated by g-irradiation of polycrystalline solids," *J. Magn. Reson.,* vol. 159, pp. 195-206, 2002.

[22] J. R. Harbridge, S. S. Eaton and G. R. Eaton, "Electron Spin-Lattice Relaxation Processes of Radicals in Irradiated Crystalline Organic Compounds," *J. Phys. Chem.*

A, vol. 107, pp. 598-610, 2003.

[23] J. R. Harbridge, S. S. Eaton and G. R. Eaton, "Spin Relaxation of Radicals in g-irradiated Malonic Acid and Methyl Malonic Acid," *Appl. Magn. Reson.*, vol. 24, pp. 261-276, 2003.

[24] J. Yamauchi and C. A. McDowell, "NMR Study of molecular motion in some molecules containing t-butyl groups," *J. Chem. Phys.*, vol. 75, pp. 1051-1058, 1981.

[25] P. A. Beckmann, H. A. Al-Hallaq, A. M. Fry, A. L. Plofker, B. A. Roe and J. A. Weiss, "Solid state proton spin relaxation and methyl and t-butyl reorientation," *J. Chem. Phys.* , vol. 100, pp. 752-753, 1994.

[26] P. A. Beckmann and E. Schneider, "Methyl group rotation, 1H spin-lattice relaxation in an organic solid and the analysis of nonexponential relaxation," *J. Chem. Phys.*, p. 054508, 2012.

[27] R. Owenius, G. R. Terry, M. J. Williams, S. S. Eaton and G. R. Eaton, "Frequency Dependence of Electron Spin Relaxation of Nitroxyl Radicals in Fluid Solution," *J. Phys. Chem. B*, vol. 108, pp. 9475-9481, 2004.

[28] F. Hyodo, S. Matsumoto, N. Devasahayam, C. Dharmaraj, S. Subramanian, J. B. Mitchell and M. C. Krishna, "Pulsed EPR imaging of nitroxides in mice," *J. Magn. Reson.*, vol. 197, pp. 181-185, 2009.

[29] Y. J. Lin, B. A. Teicher and H. J. Halpern, "Synthesis of 4-protio-3-carbamoyl-2,2,5,5-tetraperdeuteromethyl-3-pyrrolidin-1-yloxy (mHCTPO)," *J. Labelled Compd. Radiopharm.*, vol. 28, pp. 621-631, 1990.

[30] M. Elas, R. Bell, D. Hleihel, E. D. Barth, C. McFaul, C. R. Haney , J. Bielanska, K. Pustelny, K. Ahn, C. A. Pelizzari, M. Kocherginsky and H. J. Halpern, "Electron Paramagnetic Resonance Oxygen Image Hypoxic Fraction Plus Radiation Dose Strongly Correlates With Tumor Cure in FSa Fibrosarcomas," *International Journal of Radiation Oncology Biology Physics*, vol. 71, no. 2, pp. 542-549, 2008.

[31] M. Elas, K. Ichikawa and H. J. Halpern, "Oxidative Stress Imaging in Live Animals with Techniques Based on Electron Paramagnetic Resonance," *Radiation Research,* vol. 177, no. 4, pp. 514-523, 2012.

[32] J. Shen, S. Liu, M. Miyake, W. Liu, A. Pritchard, J. P. Kao, G. M. Rosen, Y. Tong and K. J. Liu, "Use of 3-acetoxymethoxycarbonyl-2,2,5,5-tetramethyl-1-pyrrolidinyloxyl as an EPR oximetry probe: potential for in vivo measurement of tissue oxygenation in mouse brain," *Magn. Reson. Med.,* vol. 55, no. 6, pp. 1433-1440, 2006.

[33] J. Shen, R. Sood, J. Weaver, G. S. Timmins, A. Schnell, M. Miyake, J. P. Kao, G. M. Rosen and K. J. Liu, "Direct visualization of mouse brain oxygen distribution by electron paramagnetic resonance imaging: application to focal cerebral ischemia.," *J. Cereb. Blood Flow Metab.,* vol. 29, no. 10, pp. 1695-1703, 2009.

[34] J. P. Kao, E. D. Barth, S. R. Burks, P. Smithback, C. Mailer, K. Ahn, H. J. Halpern and G. M. Rosen, "Very-Low-Frequency Electron Paramagnetic Resonance (EPR) Imaging of Nitroxide-Loaded Cells," *Magn. Reson. Med.,* vol. 58, no. 4, pp. 850-854, 2007.

[35] J. Shen, S. Bottle, N. Khan, O. Grinsberg, D. Reid, A. Micallef and H. M. Swartz, "Development of Isoindoline Nitroxides for EPR Oximietry in Viable Systems," *Appl. Magn. Reson.,* vol. 22, pp. 357-368, 2002.

[36] N. Khan, J. P. Blinco, S. E. Bottle, K. Hosokawa, H. M. Swartz and A. S. Micallef, "The evaluation of new and isotopically labeled isoindoline nitroxides and azaphenalene nitroxides for EPR oximetry," *J. Magn. Reson.,* vol. 211, pp. 170-177, 2011.

[37] J. R. Biller, V. M. Meyer, H. Elajaili, G. M. Rosen, S. S. Eaton and G. R. Eaton, "Frequency dependence of electron spin relaxation times in aqueous solution for a nitronyl nitroxide radical and perdeuterated-tempone between 250 MHz and 34 GHz," *J. Magn. Reson.,* vol. 225, pp. 52-57, 2012.

[38] J. R. Biller, V. Meyer, H. Elajaili, G. M. Rosen, J. P. Kao, S. S. Eaton and G. R. Eaton, "Relaxation times and line widths of isotopically-substituted nitroxides in aqueous solution at X-band," *J. Magn. Reson.,* vol. 212, no. 2, pp. 370-377, 2011.

[39] S. R. Burks, M. A. Bakhshai, M. A. Makowsky, S. Muralidharan, P. Tsai, G. M. Rosen and J. Y. Kao, "2H, 15N-Substituted nitroxides as sensitive probes for electron paramagnetic resonance imaging," *J. Org. Chem.,* vol. 75, pp. 6463-6467, 2010.

[40] H. J. Halpern, M. Peric, T. D. Nguyen, D. P. Spencer, B. A. Teicher, Y. J. Lin and M. K. Bowman, "Selective isotopic labeling of a nitroxide spin label to enhance sensitivity for T2 oxymetry," *J. Magn. Reson.,* vol. 90, pp. 40-51, 1990.

[41] R. Ramasseul and A. Rassat, "Nitroxydes XXXIII: radicaux nitroxydes pyrroliques encombres. Un pyrryloxyle stable.," *Bulletin de la Societe Chimique de France,* pp. 4330-4341, 1970.

[42] W. Froncisz, T. G. Camenisch, J. J. Ratke, J. R. Anderson, W. K. Subczynski, R. A. Strangeway, J. W. Sidabra and J. S. Hyde, "Saturation recovery EPR and ELDOR at W band for spin labels," *J. Magn. Reson.,* vol. 193, pp. 297-304, 2008.

[43] C. A. Popp and J. S. Hyde, "Electron-electron double resonance and saturation recovery studies of nitroxide electron andn nuclear spin-lattice relaxation times and Heisenberg exchange rates: lateral diffusion in dimyristoyl phosphatidylcholine," *Proc. Natl. Acad. Sci. USA,* vol. 79, pp. 2559-2563, 1982.

[44] Y. J. Yin and J. S. Hyde, "Use of high observing power in electron spin resonance saturation-recovery experiments in spin-labeled membranes," *J. Chem. Phys.,* vol. 91, pp. 6029-6035, 1989.

[45] G. C. Borgia, R. S. Brown and P. Fantazzini, "Uniform-penalty inversion of multiexponential decay data II. Data spacing, T2 data, systematic errors, and diagnostics," *J. Magn. Reson.,* vol. 147, pp. 273-285, 2000.

[46] G. C. Borgia, R. S. Brown and P. Fantazzini, "Uniform-penalty inversion of multiexponential decay data," *J. Magn. Reson.,* vol. 132, pp. 65-77, 1998.

[47] J. S. Hwang, R. P. Mason, L. P. Hwang and J. H. Freed, "Electron spin resonance studies of anisotropic rotational reorientation and slow tumbling in liquid and frozen media. III. Perdeuterated 2,2,6,6-tetramethyl-4-piperidone-N-oxide and an analysis of fluctuating torques," *J. Phys. Chem.,* vol. 79, pp. 489-511, 1975.

[48] J. S. Hyde, J. J. Yin, W. K. Subczynski, T. G. Camenisch, J. J. Ratke and W. Froncisz, "Spin-labeled EPR T1 vaues using saturation recovery from 2 to 35 GHz," *J. Phys. Chem. B,* vol. 108, pp. 9524-9529, 2004.

[49] D. Kivelson, "Theory of EPR [electron paramagnetic resonance] line widths of free radicals," *J. Chem. Phys.,* vol. 33, pp. 1094-1106, 1960.

[50] N. D. Chasteen and M. W. Hanna, "Electron paramagnetic resonance line widths of vanadyl (IV) a-hydroxycarboxylates," *J. Phys. Chem.,* vol. 76, pp. 3951-3958, 1972.

[51] D. Siri, A. Guadel-Siri and P. Tordo, "Conformational Analysis of five-membered rings by molecular mechanics: applications to nitroxides," *J. Mol. Struct. (Theochem.),* vol. 582, pp. 171-185, 2002.

[52] A. Barbon, M. Brustolon, A. L. Maniero, M. Romanelli and L. C. Brunel, "Dynamics and spin relaxation of tempone in a host crystal. An ENDOR, high field EPR and electron spin echo study," *Phys. Chem. Chem. Phys.,* vol. 1, pp. 4015-4023, 1999.

[53] A. Rockenbauer, L. Korecz and K. Hideg, "Ring pseudorotation of pyrroline N-oxyl radicals: an analysis of carbon-13 hyperfine structure of EPR spectra," *J.C.S. Perkin Trans,* vol. 22, pp. 2149-2156, 1993.

[54] M. Pavone, M. Biczysko, N. Rega and V. Barone, "Magnetic Properties of Nitroxide Spin Probes: Reliable Account of Molecular Motions and Nonspecific Solvent Effects by Time-Dependent and Time-Independent Approaches," *J. Phys. Chem. B,* vol. 114, pp. 11509-11514, 2010.

[55] A. Savitsky, M. Plato and K. Mobius, "Temperature Dependence of Nitroxide Spin-Label Interaction Parameters: a High-Field EPR Study of Intramolecular Motional Contributions," *Appl. Magn. Reson.,* vol. 37, pp. 415-434, 2010.

[56] J. S. Hyde , J. J. Yin, J. B. Feix and W. L. Hubbell, "Advances in spin label oximetry," *Pure Appl. Chem.,* vol. 62, pp. 255-260, 1990.

[57] R. Owenius, G. R. Eaton and S. S. Eaton, "Frequency (250 MHz to 9.2 GHz) and viscosity dependence of electron spin relaxation of triarylmethyl radicals at room temperature.," *J. Magn. Reson.,* vol. 172, no. 1, pp. 168-175, 2005.

[58] P. W. Atkins, "Spin-rotation interaction," in *Electron Spin Relaxation in Liquids,* L. T. Muus and P. W. Atkins, Eds., New York, Plenum Press, 1972, pp. 279-312.

[59] P. W. Atkins and D. Kivelson, "Linewidths in Solution II. Analysis of Spin-Rotational Relaxation Data," *J. Chem. Phys.,* vol. 44, pp. 169-174, 1966.

[60] S. K. Rengan, M. P. Khakhar, B. S. Prabhananda and B. Venkataraman, "Electron Spin-Lattice Relaxation in Organic Free Radicals in Solutions," *Pure. Appl. Chem.,* vol. 32, pp. 287-305, 1972.

[61] J. D. Beckmann, M. C. McKean and F. E. Frerman, "Inhibition of general acyl-CoA dehydrogenase by electron transfer flavoprotein semiquinone," *Biochem. Biophys. Res. Comm.,* vol. 102, pp. 1290-1294, 1981.

[62] R. W. Quine, G. A. Rinard, S. S. Eaton and G. R. Eaton, "A pulsed and continuous wave 250 MHz electron paramagnetic resonance spectrometer," *Concepts Magn. Reson.,* vol. 15, no. 1, pp. 59-91, 2002.

[63] R. W. Quine, G. A. Rinard, B. T. Ghim, S. S. Eaton and G. R. Eaton, "A 1-2 GHz pulsed and continuous wave electron paramagnetic resonance spectrometer," *Rev. Sci. Instrum.,* vol. 67, pp. 2514-2527, 1996.

[64] R. W. Quine, G. R. Eaton and S. S. Eaton, "Pulsed EPR spectrometer," *Rev. Sci. Instrum.,* vol. 58, pp. 1709-1723, 1987.

[65] S. S. Eaton, J. Harbridge, G. A. Rinard, G. R. Eaton and R. T. Weber, "Frequency Dependence of Electron Spin Relaxation for Three S=1/2 Species Doped into Diamagnetic Solid Hosts," *Appl. Magn. Reson.,* vol. 20, pp. 151-157, 2001.

[66] S. A. Goldman, G. V. Bruno and J. H. Freed, "ESR Studies of anisotropic rotational reorientation and slow tumbling in liquid and frozen media II. Saturation and nonsecular effects," *J. Chem. Phys.*, vol. 59, pp. 3071-3091, 1973.

[67] E. van der Drift, B. C. Rousseeuw and J. Smidt, "EPR and ELDOR studies on spin relaxation in perdeuterated 2,2,6,6-tetramethyl-4-piperidone-N-oxyl in liquid solutions: The slowly relaxing local structure mechanism," *J. Phys. Chem.*, vol. 88, pp. 2275-2284, 1984.

[68] K. A. Earle, D. E. Budil and J. H. Freed, "250 GHz EPR of Nitroxides in the Slow-Motional Regime: Models of Rotational Diffusion," *J. Phys. Chem.*, vol. 97, pp. 13289-13297, 1993.

[69] J. Labsky, J. Pilar and J. Lovy, "Magnetic resonance study of 4-amino -2,2,6,6-tetramethylpiperidine-N-oxyl and its deuterated derivatives," *J. Magn. Reson.*, vol. 37, pp. 515-522, 1980.

[70] L. B. Volodarsky, Imidazoline Nitroxides, Synthesis and Properties, vol I., Boca Raton: CRC Press, 1988.

CHAPTER 6

IMAGING OF NITROXIDES AT 250 MHZ USING RAPID-SCAN ELECTRON PARAMAGNETIC RESONANCE

6.1 Introduction

Relative to other medical imaging modalities, electron paramagnetic resonance (EPR) is uniquely able to quantitatively image physiological properties including pO_2 [1-4], perfusion and viability of tissues [5], pH [6-9], temperature [10], microviscosity and ease of diffusion of small molecules [11, 12], oxidative stress [13], thiol reduction [14], and thiol redox status of cells, as estimated by the ease of disulfide reduction by glutathione (GSH) in the tissue [15]. The synthetic versatility of nitroxides makes them attractive as imaging probes. For *in vivo* imaging, EPR in the frequency range between 250 MHz and 1 GHz is chosen because these frequencies provide sufficient depth of tissue penetration (several cm) to generate images that are not distorted by dielectric loss effects. Consequently, this chapter focuses on imaging nitroxide phantoms (aqueous nitroxide standard samples with a well-defined geometry) at 250 MHz to demonstrate rapid-scan EPR methodology.

Although 300 MHz pulsed EPR imaging of nitroxides has been accomplished by the NCI group [16], the ~0.5 μs relaxation times [17] are short relative to resonator ring-down even for resonator *Q* of 10 to 20 at 250 to 300 MHz, which makes pulse detection

challenging. We have proven the advantages of rapid scan relative to continuous wave (CW) and pulse EPR for many classes of samples, with improvements in signal-to-noise per unit time as high as 250 [18, 19]. The electron spin relaxation times and linewidths of nitroxides [17, 20] are in the range for which rapid-scan EPR is expected to be a better imaging method than pulse or CW EPR. In this chapter we show that rapid-scan imaging of a phantom composed of three different nitroxides provides better signal-to-noise per unit time than does CW imaging. We conclude that for nitroxide spin probes rapid scan is the EPR method of choice for low frequency imaging. This work is published in [39].

6.2 Experimental

6.2.1 Nitroxides and construction of phantom

^{15}N-PDT (4-oxo-2,2,6,6-tetra($^{2}H_3$)methyl-1-(3,3,5,5-$^{2}H_4$,1-^{15}N)piperidinyloxyl) with >98% isotope purity was purchased from CDN Isotopes (Quebec, Canada). ^{15}N-Proxyl (3-^{2}H, 4-$^{2}H_2$-3-carboxy-2,2,5,5-tetra($^{2}H_3$)methyl-1-(1-^{15}N)pyrrolidinyloxyl) and ^{15}N-mHCTPO (4-^{1}H-3-carbamoyl-2,2,5,5-tetra($^{2}H_3$)methyl-3-pyrrolinyloxyl) were synthesized as described in the literature [21, 22] and provided by Dr. Gerald Rosen (University of Maryland). Quartz tubes were purchased from Wilmad Glass (Buena, NJ).

The phantom consisted of three 4.05 mm OD (2.4±0.2 mm ID) quartz tubes containing 0.5 mM aqueous solutions of ^{15}N,^{2}H-substituted-nitroxides. In addition to the aqueous solution each tube contained a one-inch long piece of 1.57 mm OD (0.97 mm ID) Teflon tubing to relieve stress on the quartz tube during the seven cycles of freeze-pump-thaw degassing that were used to deoxygenate the solutions. The Teflon tubing

was distorted by the freeze-pump-thawing and was not vertical in the quartz tubes. The heights of the solutions in the 3 tubes were 1.8 cm, 2.0 cm, and 2.4 cm for ^{15}N-PDT, ^{15}N-mHCTPO, and ^{15}N-Proxyl, respectively. CW and rapid scans were recorded of the tubes individually using low incident powers and conservative modulation amplitudes for CW. Linewidths were 0.4, 0.39 and 0.25 G (1 G = 10^{-4} T) for ^{15}N-Proxyl, ^{15}N-mHCTPO and ^{15}N-PDT, respectively, and the resolved proton hyperfine splitting for mHCTPO was 0.48 ± 0.01 G, which is in good agreement with the literature [22]. In the phantom the distance between the centers of the tubes containing ^{15}N-PDT and ^{15}N-Proxyl was 8.1 mm. The total volume of solution in each tube was about 100 μL.

6.2.2 Spectrometer

Projections for CW and rapid-scan 2D spectral-spatial images were acquired at 251 MHz with a modified Bruker E540 console and the magnet and gradient coils described previously [23-25]. The maximum z-gradient was 8 G/cm ($8x10^{-2}$ T/m). The original rapid-scan bridge [25] provided a maximum RF output of 50 mW. A 7 W amplifier (MiniCircuits model ZHL-03-5WF) was added to provide increased power to the resonator. The sinusoidal rapid scans were generated with a driver similar to the one described in [26], but with an additional option to trigger the digitizer once per N cycles, with N selectable between 1 and 255. This modification permits acquiring multiple scans after a single trigger. Combining the data in the multiple scans functions like a comb filter and decreases noise [19, 27-29].

6.2.3 Resonator design and characterization

A cross-loop resonator (CLR), modified from prior designs [30-32], was used for both CW and rapid-scan imaging. The resonator was designed and constructed by Dr. George Rinard (University of Denver). It consists of a 16 mm diameter by 15 mm long resonator for the sample and a larger, 25 mm diameter by 19 mm long, double saddle coil, excitation resonator (Fig. 6.1). The isolation between the excitation (transmit) and detection (receive) resonators was at least 60 dB. The RF shield is a rectangular solenoid of AWG 20 copper magnet wire that is coated inside with silver paint. This design allowed good penetration of the scan field without distortion, provided a good shield for the RF, and allowed the scan coils to be external to the RF shield. It reduces the rapid-scan background signal relative to resonator assemblies in which the scan coils are inside the RF shield [32]. The saddle coil arrangement (Fig. 6.1, bottom) allows the excitation resonator to be smaller than in parallel-coil designs [32], which increases efficiency. The saddle coils were wound using a single turn of 220/46 Litz wire. The fine wire was essentially transparent to the scanning field, thus reducing undesirable eddy current effects. The saddle coils were resonated with a common parallel capacitor, which was a 0.254 mm thick alumina substrate gold-plated on both sides, with overall dimensions of ~2 × 20 mm. A small variable capacitor was mounted in parallel with the main capacitor to allow tuning the resonant frequency to match that of the sample resonator. The Q was about 75. The B_1 field produced by the Litz wire saddle coils was perpendicular to the axis of the sample resonator. Based on comparison of power saturation curves for mHCTPO at 250 MHz and X-band [33] this resonator had an efficiency of $0.20\,G/$

$\sqrt{Watt}$. It can be operated with input power as high as 1.0 Watt producing a B_1 of 0.20 G.

The sample resonator (Fig. 6.1) was constructed of 6 parallel, 16 mm diameter coils of 0.1 mm bare copper wire. There is a 0.8 mm gap at the top of each coil to provide for the resonator capacitor. The capacitor consists of six, 1.4 mm square, non-magnetic ceramic chip capacitors (Voltronics Inc., Salisbury, MD) with a total capacitance of 24 pF. A 0.08 mm thick substrate of Cuflon (Polyflon Corp., Norwalk, CT) with 2 parallel etches, 15 mm long and 1.2 mm wide spaced 0.8 mm apart supports the ends of the coils and the capacitors. There was a layer of 1.2 mm thick Teflon between the coils and the sample. The resonator was mounted inside a Rexolite support using Q-dope (polystyrene dissolved in acetone).

Both the excitation and sample resonators were coupled to bazooka-balun coax lines using two identical series capacitors to attain nearly critical coupling. The total capacitance was about 3 pF for the sample resonator and somewhat less for the excitation resonator. There was no coupling adjustment. In a crossed-loop resonator it is not important to have precise critical coupling, since reflected power from the excitation resonator does not reach the detector circuit. The excitation resonator coils were mounted on a Rexolite support that could be rotated to adjust the angle between the two resonator coils and thereby fine tune the isolation of the CLR.

The Q of the sample resonator containing the phantom was about 90, which is similar to that used previously for a comparison of spin echo and CW imaging of trityl radicals [34]. The active volume of the sample resonator is about 3.0 mL, so the filling

factor for the solutions in the phantom is about 3%. This low filling factor is similar to what is expected when imaging a mouse tumor using the same resonator.

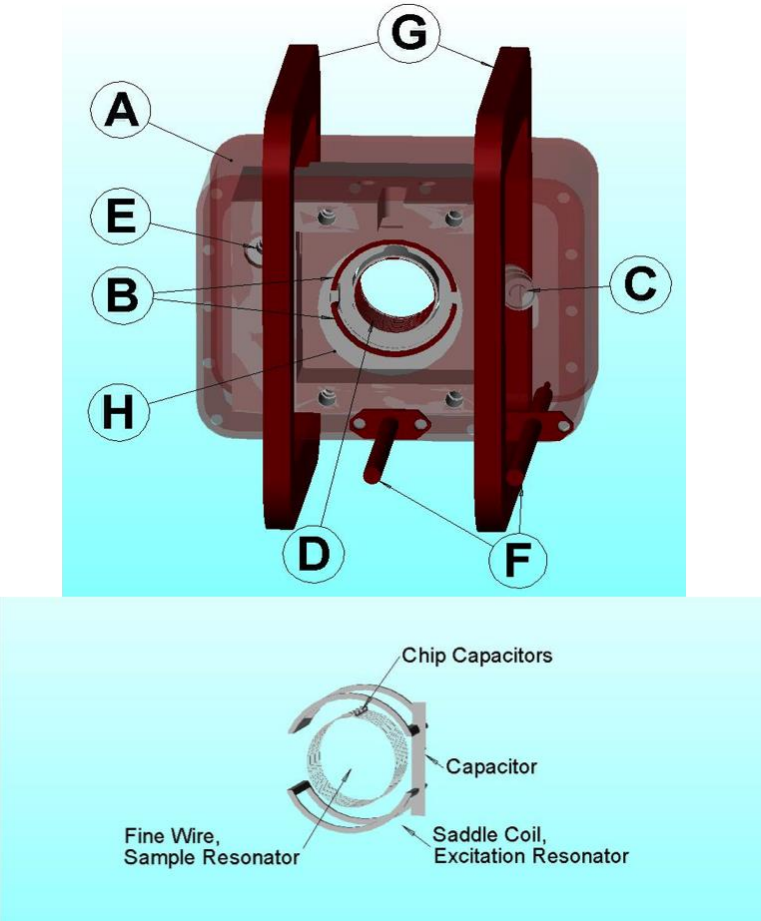

Figure 6.1 Diagram of cross loop resonator with wire-wound shield Top – Cross-loop resonator assembly with scan coils: A - Wire wound RF shield; B - 25 mm saddle coil excitation resonator; C - frequency adjustment for excitation resonator; D - 16 mm fine-wire sample resonator; E - isolation adjustment; F - input and output coaxial cables; G - 89 mm square Helmholtz scan coils; H – 30 mm sample access hole in RF shield. Bottom - sketch of the resonator coils, without the shield and support structure. Graphic courtesy of Dr. George Rinard. Adapted from [39].

Rapid-scan background signals were decreased by avoiding scan frequencies that are mechanical resonances of the CLR. The mechanical resonances were characterized by two methods, which gave results that are in good agreement. Method 1 used a "chirp"

pulse from 1 – 15 kHz in 35 ms. The time response to the chirped pulse was digitized and averaged about 55 times before Fourier transformation into the frequency domain (Fig. 6.2 A). In method 2 the amplitude of the background signal was measured point-by-point at 100 Hz increments between 1 and 11 kHz (Fig. 6.2 B). Both methods found mechanical resonances below about 2 kHz and near 5 kHz. The amplitude of the background signal was smaller at scan frequencies >~ 8 kHz, so scan frequencies > 8 kHz were used for imaging.

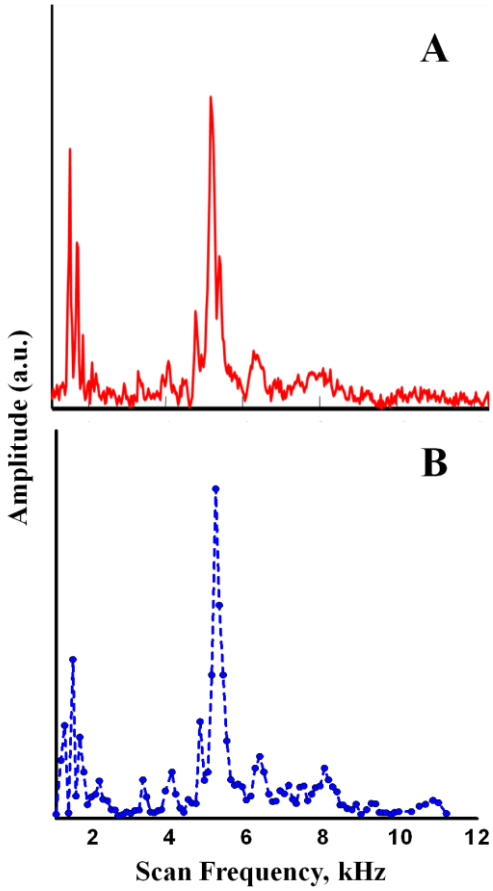

Figure 6.2 Mechanical resonances of cross-loop resonator characterized by A) by applying a chirp pulse from 1 – 15 kHz or (B) stepping the scan frequency and recording the rapid scan background signal. Amplitudes are in arbitrary units and are different for the two plots. Adapted from [39].

6.2.4 Rapid-scan imaging

Eighteen equally-spaced projections were recorded at $\theta = \pm 5^{o}$ to $\pm 85^{o}$ in the spectral-spatial pseudo-plane [35]. The magnetic field gradient was 8 G/cm for the projections at $\pm 85^{o}$ and decreased proportional to tan θ. The maximum gradient was selected to permit imaging one line of the ^{15}N hyperfine-split nitroxide spectrum without overlap of the second line at high gradient. In traditional spectral-spatial imaging the sweep widths are increased proportional to 1/(cos θ). Depending on the dimensions of the object, this may result in substantial regions of baseline for projections at high gradients. For the experiments reported here the sweep widths were selected to encompass the full gradient-broadened spectrum plus a modest baseline region at each end of the scan. To permit image reconstruction by filtered backprojection the high-gradient spectra were 'padded' with zeros at the low- and high-field ends to generate projections with the widths required for the spectral-spatial imaging algorithm. The magnetic field was centered on the low-field nitrogen hyperfine line. The sweep widths for the 9 projections in each quadrant were 7.2, 7.5, 7.8, 8.2, 8.8, 9.5, 10.8, 13.5, and 27.0 G. A scan frequency of 9.369 kHz was selected to avoid mechanical resonances of the CLR. The scan rate at the center of a sinusoidal scan is $a_s = \pi\, fs\, B_m$ G s^{-1} where f_s is the scan frequency and B_m is the scan width. At the scan rates used for the imaging, the signal bandwidth is consistent with the resonator *Q*. As discussed below, the rapid-scan signal saturates less readily as the scan rate is increased. Projections for $\theta = \pm 5^{o}$ to $\pm 55^{o}$ had a_s = 0.21 to 0.28 MG/s (21 to 28 T/s) so B_1 = 44 mG was used (Fig. 6.4). Projections for $\theta = \pm 65^{o}$, $\pm 75^{o}$, and $\pm 85^{o}$ had a_s = 0.32 to 0.79 MG/s (32 to 79 T/s) and were acquired with B_1 = 64 mG. Signals

were digitized with a Bruker Specjet II using 64k points per gradient and a 10 ns sampling interval which therefore encompassed 6.14 sinusoidal scan cycles within the digitizer time window (Figure 6.3).

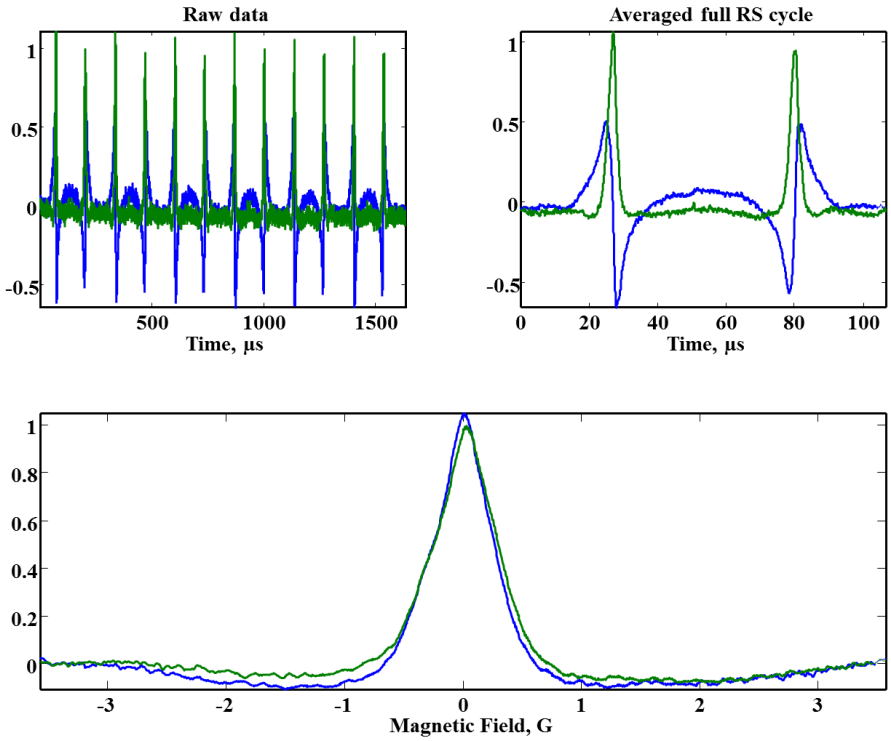

Figure 6.3 Rapid-scan experimental data and post-processing for the projection with $\theta = -5^{o}$ from the data set with a total acquisition time of 5 minutes. The 64 k points of raw data encompassing 6.14 sinusoidal cycles were obtained by signal averaging 22k scans, which required 17 s. Data from the six sinusoidal cycles were summed (upper right). Background correction, sinusoidal deconvolution, and combination of the spectra from the up- and down- scans produced the projection shown in the lower panel. The absorption (green) and dispersion (blue) signals are shown. Adapted from [39].

Images were acquired with total data acquisition times of 29 s (2k averages, 1.6 s/gradient) or 5 min (22k averages, 17 s/gradient). For the '29s' image the 1 MHz filter bandwidth on the bridge output was used. For the '5 min' image a Krohn-Hite model 3955

low-pass Butterworth filter with a bandwidth set to 1.5 MHz was used on the bridge output. The absorption signals were obtained by background correction [36], sinusoidal deconvolution [37], and combination of up-field and down-field scans.

6.2.5 CW Imaging

CW projections were obtained at the same 18 angles and magnetic field gradients as for the rapid-scan projections. The magnetic field modulation frequency was 30 kHz. The modulation amplitude was 0.5 G for $\theta = \pm 75^{o}$ and $\pm 85^{o}$ and 0.2 G for other projections. To ensure that the signal was in the linear response regime B_1 = 22 mG was used (Fig. 6.4).

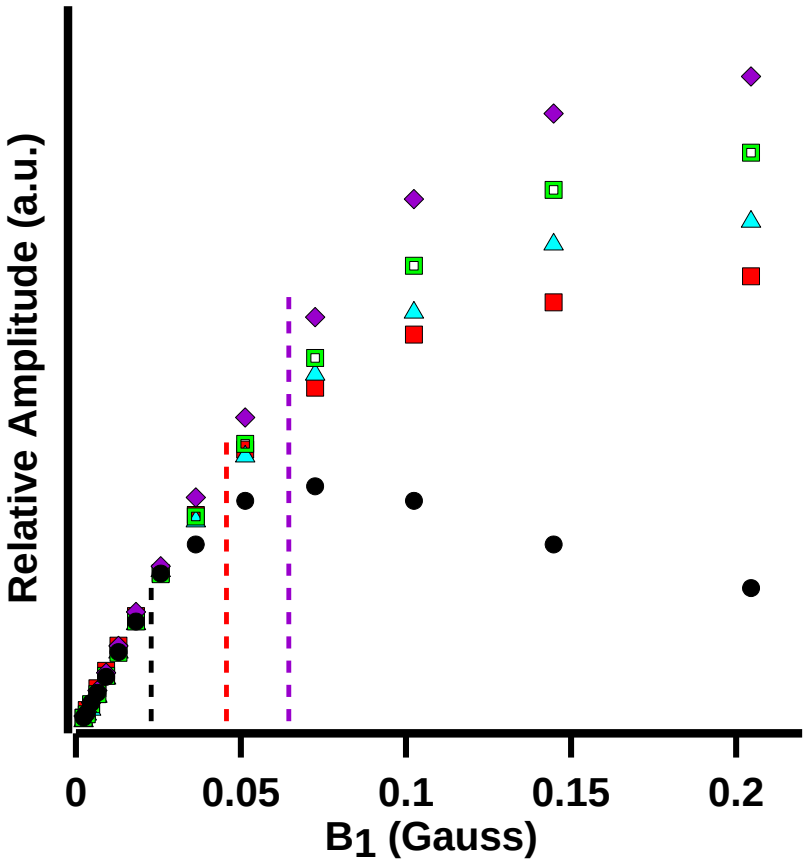

Figure 6.4 Comparison of power saturation curves for CW and rapid-scan methods for 0.25 mM ^{15}N-mHCTPO in deoxygenated water in a 16 mm OD quartz tube obtained by CW (●) and sinusoidal rapid scan at 0.15 MG/s (15 T/s) (■), 0.3 MG/s (30 T/s) (▲), 0.59 MG/s (59 T/s) (□) and 0.74 MG/s (74 T/s) (♦). Amplitudes for CW spectra were peak-to-peak. Rapid-scan amplitudes were calculated from spectra that had been deconvolved and background corrected. Signal amplitudes are in arbitrary units, which were scaled such that the rapid-scan signals overlay the CW data points at low power. Adapted from [39].

The magnetic field was centered on the low-field nitrogen hyperfine line. Spectra were acquired with Bruker Xepr software and a BMC20 power supply with current control, which permits only certain values of the sweep widths. The sweep widths were 6.7 G for $\theta = \pm 5^{o}$ to $\pm 55^{o}$, 8.9 G for $\theta = \pm 65^{o}$, 11.1 G for $\theta = \pm 75^{o}$, and 24.4 G for $\theta = \pm 85^{o}$. The actual sweep widths required for filtered backprojection were obtained by interpolation and/or padding with zero's as needed. A single scan with 512 points was

recorded for each projection, using a Bruker SPU digitizer. Two sets of projections were acquired with total data acquisition times of 5 or 15 min. Since the Bruker system uses an integrating digitizer, increasing scan time improves signal-to-noise. Within each data set, projections at $\theta = \pm 5^{o}$ to $\pm 65^{o}$ were recorded with the same sweep time, which was increased by a factor of ~3.3 for $\theta = \pm 75^{o}$, and a factor of ~6.7 for $\theta = \pm 85^{o}$. A 3-point binomial smoothing (n=1) in Xepr was applied to the raw data as it was collected. This corresponds to about 40 mG to 140 mG smoothing for the lowest to highest gradient projections, respectively. Projections were integrated to obtain the absorption spectra that were used to generate the images.

6.2.6 Image reconstruction

2D spectral-spatial images (2.0 G by 2.5 cm) were reconstructed from the 18 equally-spaced projections using filtered backprojection on a 512 x 512 grid. A Gaussian filter was applied to slices through the rapid-scan and CW images after reconstruction, with full width at half amplitude corresponding to 0.6 mm in the spatial dimension and 20 mG in the spectral dimension. The linewidths of the signals were determined by least-squares fitting to spectral slices using published values of resolved and unresolved nuclear hyperfine splittings [20]. The percent RMS error was calculated for the fits to individual slices through the image. The criteria for determining the linewidth was minimization of the error for all points in the slice, including the baseline. There are systematic deviations in the linewidths toward the edges of the tubes. The scatter in the linewidth values could be decreased by manually selecting the best fit at half height but this approach would be difficult to automate, particularly in the presence of noise. This

observation reinforces the importance of minimizing low frequency noise that impacts the image baseline.

6.3 Results and Discussion

2D spectral-spatial images of a phantom consisting of three tubes containing 0.5 mM solutions of ^{15}N,^{2}H-substituted nitroxides were obtained by CW and rapid-scan EPR for several acquisition times. The microwave powers used for the data acquisition were based on the power saturation curves in Fig. 6.4 for 0.25 mM ^{15}N-mHCTPO. The relaxation times for the three radicals at 250 MHz are similar and about 0.50 μs [17] for deoxygenated aqueous solutions. The linear region of the plot for the CW signals extend only to about B_1 ~ 22 mG, but for rapid scans the linear response region extends to B_1 about 40, 50, or 64 mG for scan rates of 0.25, 0.3 and 0.59 MG/s (25, 30, and 59 T/s), respectively. The decreased power saturation at higher scan rates is similar to what was observed previously for nitroxides at X-band [33] and is characteristic of rapid-scan EPR [18, 38].

6.3.1 Comparison of rapid-scan and CW images

The spatial information in EPR images is encoded with magnetic field gradients. For a distributed sample the signal broadens approximately proportional to the gradient. For the first-derivative signal that is recorded in CW EPR the amplitude decreases approximately quadratically with the increase in gradient, which makes the signal-to-noise (*S/N*) substantially poorer in the higher gradient projections. These projections provide the most information about the spatial distribution of spin density. Poor *S/N* in

any projection also impacts the complete image. To partially mitigate the poorer *S/N* at higher gradients the modulation amplitude was increased and more signal averaging was performed than for projections at lower gradient. The amplitude of the absorption spectrum that is recorded by rapid-scan EPR decreases approximately linearly with the increases in gradient, so the impact of high gradient on *S/N* is less severe than for CW [38]. The projections at higher gradients have wider sweep width, which makes the scan rate higher. Because of the decrease in power saturation at higher scan rate (Fig. 6.4), higher B_1 was used for the higher gradient rapid-scan projections. The same acquisition time was used for each of the rapid-scan projections. Rapid-scan images were obtained with 29 s and 5 min total acquisition times and CW images were obtained with 5 and 15 min total data acquisition times.

Six examples of projections obtained by rapid-scan and CW for the 5 min images are compared in Fig. 6.5. The CW images were reconstructed from integrals of the first-derivative CW spectra as shown in the figure. Although high-frequency noise is reduced by integration, low-frequency noise that negatively impacts baselines and lineshapes in an image is enhanced by integration [27]. At small θ (low gradient) (Fig. 6.5 E,F) the *S/N* is comparable between projections obtained by CW and rapid-scan, although low-frequency noise is greater for the CW projections than for the rapid-scan projections. At intermediate θ (Fig. 6.5 C,D) noise in the CW projections is conspicuously greater than in the rapid-scan projections. At the highest θ, baseline wander and high-frequency noise is substantially greater for CW than for rapid scan. The corresponding rapid-scan projections obtained with a total of 29 sec acquisition time are shown in Figure 6.6.

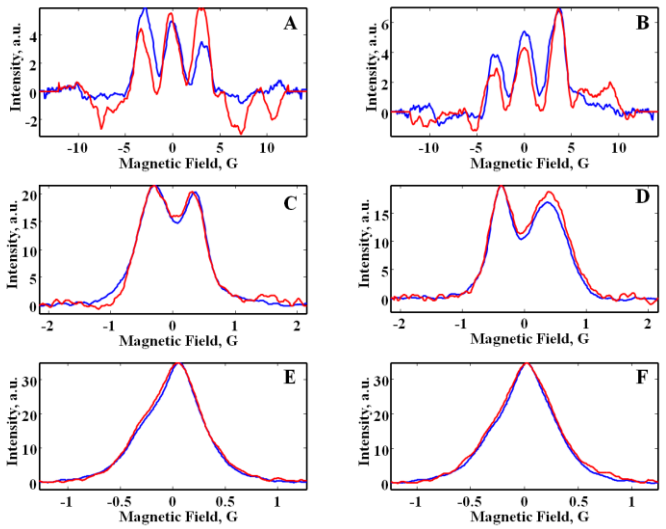

Figure 6.5 Comparison of projections for images acquired in 5 minutes Projections obtained by rapid scan (blue) and CW EPR (red) for the phantom shown in Fig. 6.7 at (A) θ = -85°, (B) θ = 85°, (C) θ = -55°, (D) θ = 55°, (E) θ = -5°, and (F) θ = 5° from data sets obtained with a total of 5 min acquisition time. Adapted from [39].

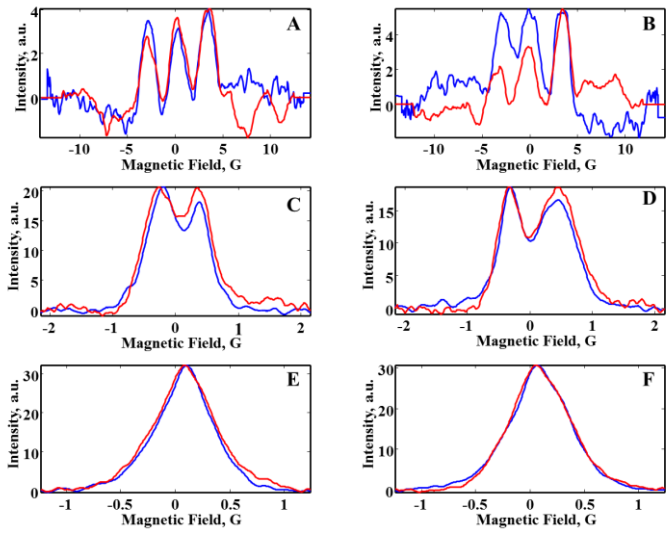

Figure 6.6 Comparison of projections for images acquired in 29 s (RS) or 5 min (CW) Projections obtained by rapid scan with a 29 s total acquisition time (blue) and CW with a total of 5 min acquisition time (red) for the phantom shown in Fig. 6.7 at (A) θ = -85°, (B) θ = 85°, (C) θ = -55°, (D) θ = 55°, (E) θ = -5°, and (F) θ = 5°. Adapted from [39].

Figure 6.7 displays 2D images of the 3-tube nitroxide phantom (Fig. 6.7 D) reconstructed from 18 projections with a total data acquisition time of 5 min for rapid scan (Fig. 6.7 A) or continuous wave (Fig. 6.6 B). Also shown is the rapid-scan image with total data acquisition time of 29 s (Fig. 6.7 C).

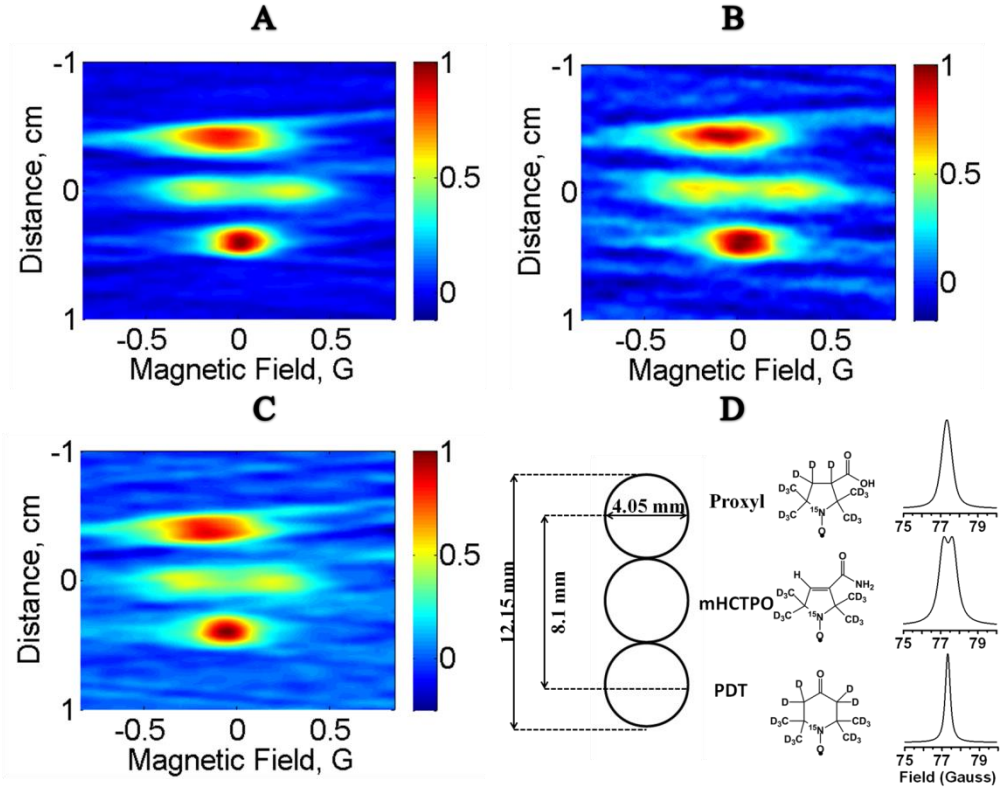

Figure 6.7 Comparison of 2D spectral–spatial images obtained with rapid scan or CW methods Images reconstructed from 18 projections with a total data acquisition time of (A) 5 min for rapid scan, (B) 5 min for CW or (C) 29 s for rapid scan. (D) The phantom consisted of 3 tubes containing ^{15}N-nitroxides, aligned along the direction of the z gradient. The structures of the nitroxides and the corresponding absorption lineshapes are shown. Adapted from [39].

The contours for the sample-containing regions are substantially better defined and the baselines are smoother in the 5 min rapid-scan image (Fig. 6.7 A) than in the 5 min CW image (Fig. 6.7 B) because of the differences in the projections as shown in Fig.

6.5. The contours and baseline for the 29 s rapid-scan image (Fig. 6.7 C) are comparable to the 5 min CW image (see absorption lineshapes in Fig. 6.7 D). The extent of the PDT signal in the spectral dimension is smaller than for Proxyl, because the PDT linewidth is narrower than the Proxyl linewidth. The spatial distribution of signal amplitude is not that of a perfect cylinder due to the presence of the deformed Teflon tube inserts. The amplitudes of the signals from mHCTPO are smaller than for PDT or Proxyl because the linewidth is relatively large and because the signal is split into a doublet with a_H = 0.48 G due to coupling to the ring proton. The dimensions of the tubes and spacing between the tubes in the images are in good agreement with the known dimensions (Fig. 6.7 D). Center to center distances between tubes containing ^{15}N-Proxyl and ^{15}N-PDT in the three images are similar. For the rapid-scan images acquired in 29 s and 5 min, the distances are 7.8 and 8.2 mm, respectively. From the CW image acquired in 5 min, the distance measures 8.2 mm. The distances between tubes containing ^{15}N-Proxyl and ^{15}N-mHCTPO, and between ^{15}N-mHCTPO and ^{15}N-PDT should be ca. 4 mm which is reproduced well by rapid scan imaging in 29 s (3.9 mm/3.9 mm) or 5 min (4.4 mm/3.8 mm) and by CW imaging in 5 min (3.9 mm/3.9 mm). Based on the maximum gradient applied (8 G/cm) the theoretical spatial resolution for the narrowest-line PDT sample is ca. 0.2 mm. The inability to resolve the 0.3 mm wall thickness of the Teflon tube in each sample is attributed to the limited resolution of the image and the fact that the Teflon tubing was not vertical, which blurs its location in images with a single spatial dimension.

6.3.2 Lineshape parameters obtained from slices through the image

Since the goal of the imaging is to obtain spectral information as a function of position in the sample, spectral models were fit to slices through the image. The linewidths, along with the RMS errors in the fitting, are shown for the rapid-scan (Fig. 6.8, left) and CW (Fig. 6.8, right) images acquired in 5 min.

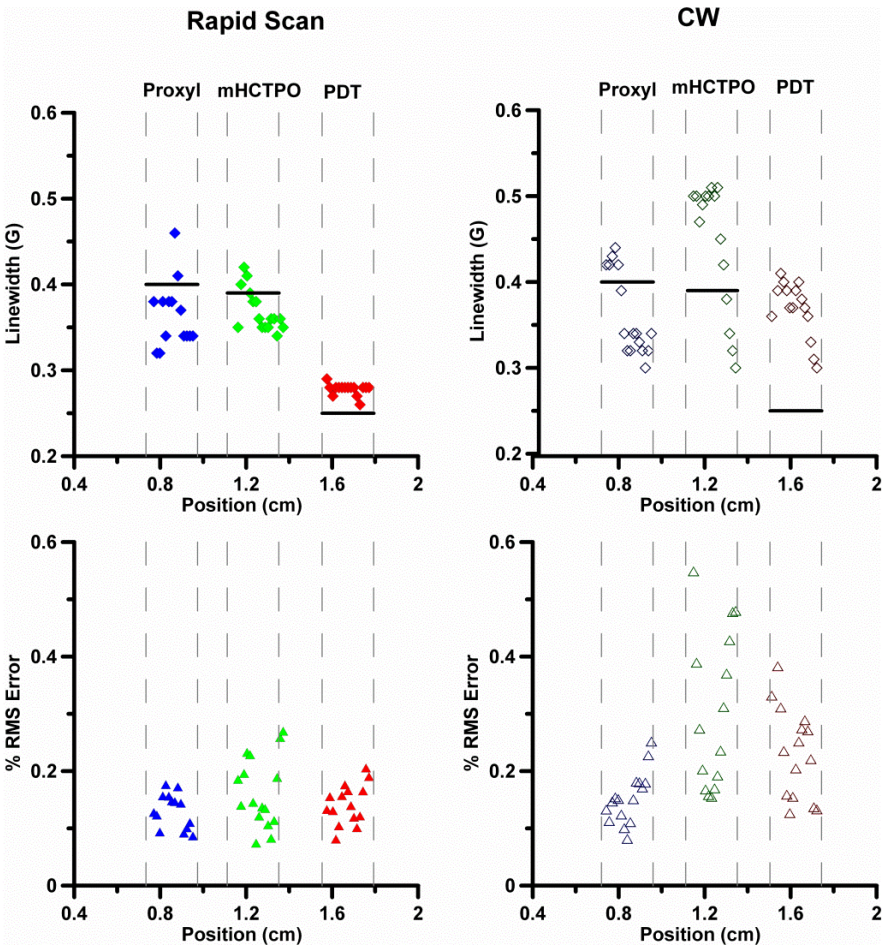

Figure 6.8 Slice fitting of linewidths for 5 min. images Linewidths for ^{15}N-Proxyl (♦, ◊), ^{15}N-mHCTPO (♦,◊) and ^{15}N-PDT (♦,◊) calculated by fitting spectral slices through the images obtained with a total of 5 min acquisition time and the corresponding RMS fitting errors for ^{15}N-Proxyl (▲,Δ), ^{15}N-mHCTPO (▲ ,Δ) and ^{15}N-PDT (▲,Δ). The RMS error is calculated for individual slices. Closed symbols designate rapid scan and open symbols designate CW. Adapted from [39].

The locations of the walls of the tube are indicated with gray dashed lines, and the black horizontal lines indicate the linewidths calculated from spectra of the tubes of the phantom measured individually. In principle the linewidths should be constant across a tube. However the small number of projections results in a 'star effect' that impacts the baselines for the images. Uncertainties in the baseline and noise in projections contribute to uncertainties in the fitted lineshapes.

For the rapid-scan image, the linewidths for ^{15}N-PDT are 0.27-0.28 G across (nearly) the entire tube, which is in reasonable agreement with the expected value of 0.25 G. The percent RMS error for the fits to each slice is ≤0.2. The linewidths for slices across the ^{15}N-mHCTPO sample vary from ca. 0.4 G on one side to 0.35 G on the other, with percent RMS error ≤0.23 for a slice in the middle of the sample, increasing to 0.27 for a slice at the edge of the sample. The linewidth fits for ^{15}N-Proxyl also have RMS errors ≤0.2, but the scatter in linewidths is larger, ca. 0.32 to 0.45 G across the sample. Of the three nitroxides in the image, ^{15}N-Proxyl has the broadest line, and its linewidths are most sensitive to baseline variations.

For the CW image the scatter in linewidths and percent RMS errors for each slice are larger than for the rapid-scan image. Both observations are attributed to the poorer baselines in the CW images. The least scatter and variation in linewidths is for ^{15}N-PDT, but the fitted linewidths for the CW image are 60% larger than the linewidth for the single tube recorded under non-line-broadening conditions. The modulation amplitude used for imaging was 0.2 G, in an effort to increase the signal to noise (*S/N*) of the CW image when acquired in the short time of 5 min. This use of modulation amplitude

comparable to linewidth contributes a small amount to the broadening of the ^{15}N-PDT and ^{15}N-mHCTPO lineshapes in the CW image, but is not sufficient to explain all of the broadening. Percent RMS errors are substantially larger for the CW image slices, so there is greater uncertainty in the fit parameters. The linewidth scatter, and percent RMS error for ^{15}N-Proxyl are similar for rapid-scan and CW slices.

A major benefit of the rapid-scan technique is the ability to obtain higher *S/N* per unit time compared with CW. For comparison with the CW image acquired in 5 min, a rapid-scan image was acquired in 29 s (Fig. 6.7 C). Linewidth and error plots are shown in Fig. 6.9. Decreasing the rapid-scan acquisition time by a factor of ten results in increased scatter in the fitted linewidths for all three nitroxides, although the linewidth fidelity for ^{15}N-PDT is still quite good and superior to that for the CW image collected in 5 min. The percent RMS errors for slices in the 29 s rapid-scan image are comparable to those in the 5 min CW image. The scatter in the linewidths for ^{15}N-Proxyl increased substantially to 0.15-0.5 G, reflecting the noisier background resulting from only 2k averages per projection. In the 29 s rapid-scan image the fitted linewidths in the middle of the tube for ^{15}N-mHCTPO are more uniform across the sample, but are smaller than the expected value (0.35 vs 0.39 G).

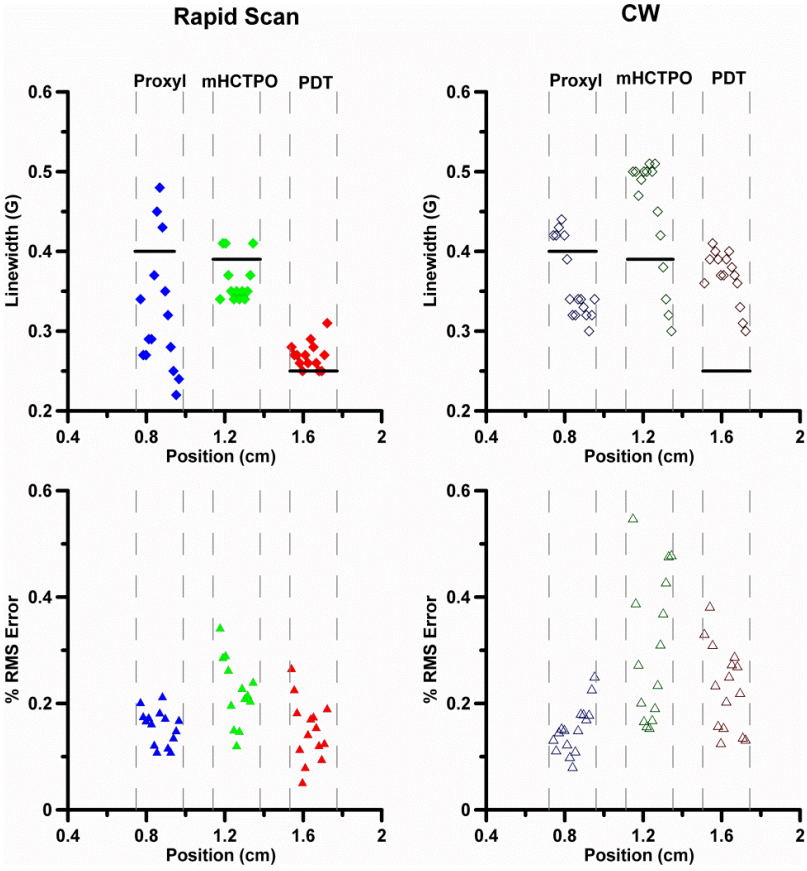

Figure 6.9 Slice fitting of linewidths for 29 s (RS) or 5 min (CW) images Comparison of linewidths obtained from an image obtained by rapid scan with 29 s total acquisition time and CW with 5 min total acquisition time. Linewidths for ^{15}N-Proxyl (♦, ◊), ^{15}N-mHCTPO (♦,◊) and ^{15}N-PDT (♦,◊) calculated by fitting spectral slices through the images and the corresponding percent RMS fitting errors for ^{15}N-Proxyl (▲, Δ), ^{15}N-mHCTPO (▲,Δ) and ^{15}N-PDT (▲,Δ). Closed symbols designate rapid scan and open symbols designate CW. The dashed lines mark the locations of tube walls. The black horizontal lines indicate the linewidths calculated from spectra of the tubes measured individually. Adapted from [39].

A CW image with 15 min acquisition time also was acquired, and the calculated linewidths are compared with those from the 5 min rapid-scan image in Fig. 6.10.

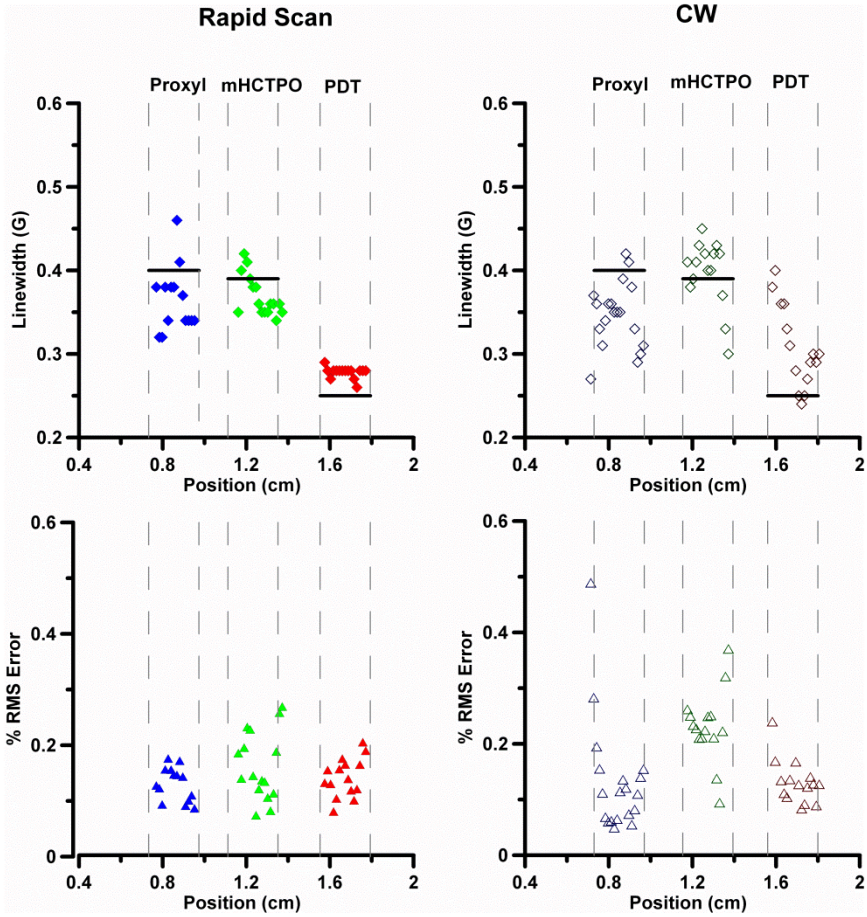

Figure 6.10 Slice fitting of linewidths for 5 min (RS) or 15 min (CW) images Comparison of linewidths obtained from an image obtained by rapid scan with 5 minutes total acquisition time and CW with 15 min total acquisition time. Linewidths for ^{15}N-Proxyl (♦, ◊), ^{15}N-mHCTPO (♦,◊) and ^{15}N-PDT (♦,◊) calculated by fitting spectral slices through the images and the corresponding percent RMS fitting errors for ^{15}N-Proxyl (▲, Δ), ^{15}N-mHCTPO (▲,Δ) and ^{15}N-PDT (▲,Δ). Closed symbols designate rapid scan and open symbols designate CW. The dashed lines mark the locations of tube walls. The black horizontal lines indicate the linewidths calculated from spectra of the tubes measured individually. Adapted from [39].

The percent RMS errors for linewidth fits to individual slices from the image are substantially lower than for the CW 5 min image, but are higher than for the 5 min rapid-scan image, particularly toward the edges of the tubes. Linewidths for the ^{15}N-PDT sample are closer to the expected value of 0.25 G, ranging from 0.25 to 0.35, but the scatter still is larger than for the 5 min rapid-scan image. The improved linewidth accuracy suggests that the major source of broadening of the ^{15}N-PDT linewidth in the 5 min CW image was due to baseline variations. Fitted linewidths for ^{15}N-mHCTPO are stable across much of the sample, and just above the expected value of 0.39 G. There is still substantial scatter (0.3-0.4 G) in the linewidths of ^{15}N-Proxyl, but the range is smaller than for the 5 min CW and rapid-scan images.

6.4 Summary

For the same data acquisition time, rapid-scan EPR provides projections with significantly improved *S/N* than CW EPR, particularly at higher magnetic field gradients. The improved *S/N* in the projections results in improved accuracy in linewidths calculated from slices through spectral-spatial images. The ability to acquire data more quickly and with improved *S/N* will facilitate *in vivo* applications of nitroxide imaging.

6.5 References

[1] M. Elas, R. Bell, D. Hleihel, E.D. Barth, C. McFaul, C.R. Haney, J. Bielanska, K.Pustelny, K.-H. Ahn, C.A. Pelizzari, M. Kocherginsky, and H.J. Halpern, Electron Paramagnetic Resonance Oxygen Image Hypoxic Fraction Plus Radiation Dose Strongly Correlates With Tumor Cure in FSa Fibrosarcomas, Int. J. Radiation Oncology Biol. Phys., vol. 71, pp. 542-549, 2008.

[2] H.J. Halpern, C. Yu, M. Peric, E. Barth, D.J. Grdina, and B.A. Teicher, Oxymetry deep in tissues with low-frequency electron paramagnetic resonance, Proc. Natl. Acad. Sci. U. S. vol. 91, pp. 13047-13051, 1994.

[3] S. Matsumoto, F. Hyodo, S. Subramanian, N. Devasahayam, J. Munasinghe, E. Hyodo, C. Gadisetti, J.A. Cook, J.B. Mitchell, and M.C. Krishna, Low-field paramagnetic resonance imaging of tumor oxygenation and glycolytic activity in mice, J. Clin. Invest. vol. 118, pp. 1965-1973. 2008.

[4] S.S. Velan, R.G. Spencer, J.L. Zweier, and P. Kuppusamy, Electron paramagnetic resonance oxygen mapping (EPROM): direct visualization of oxygen concentration in tissue, Magn. Reson. Med., vol. 43, pp. 804 - 809, 2000.

[5] B. Gallez, K. Mader, and H.M. Swartz, Noninvasive measurements of the pH inside the gut by using pH-sensitive nitroxides. An in vivo ESR study, Magn. Reson. Med., vol. 36, pp. 694-697, 1996.

[6] A.A. Bobko, T.D. Eubank, J.L. Voorhees, O.V. Efimova, J.L. Zweier, I.A. Grigor'ev, A. Samouilov, and V.V. Khramtsov, In vivo monitoring of pH, redox status, and glutathione using L-band EPR of assessment for therapeutic effectiveness in solid tumors, Magn. Reson. Med., vol. 67, pp. 1827-1836, 2012.

[7] H. Utsumi, K.-I. Yamada, K. Ichikawa, K. Sakai, Y. Kinoshita, and S. Matsumoto, Simultaneous molecular imaging of redox reactions monitored by Overhauser-enhanced MRI with 14N- and 15N-labeled nitroxyl radicals, Proc. Nat. Acad. Sci. U.S.A., vol. 103, pp. 1463-1468, 2006.

[8] V.V. Khramtsov, L.M. Weiner, I.A. Grigoriev, and L.B. Volodarsky, Proton exchange in stable nitroxyl radicals. EPR study of the pH of aqueous solutions, Chem. Phys. Lett., vol. 91, pp. 69 - 72, 1982.

[9] V.V. Khramtsov, I.A. Grigor'ev, M.A. Foster, D.J. Lurie, and I. Nicholson, Biological applications of spin pH probes, Cell. Mol. Biol., vol. 46, pp.1361 - 1374, 2000.

[10] M.R. Dreher, M. Elas, K. Ichickawa, E.D. Barth, A. Chilkoti, G.M. Rosen, H.J. Halpern, and M. Dewhirst, Nitroxide conjugate of a thermally responsive elastin-like polypeptide for noninvasive thermometry, Med. Phys., vol. 31, pp. 2755 - 2762, 2004.

[11] H.J. Halpern, C. Yu, M. Peric, E. Barth, and B.A. Teicher, Using very low frequency EPR to define bulk characteristics of pharmacologic compartments of specific tissues in vivo, Current Topics in Biophysics, vol. 18, pp. 26-28. 1994.

[12] H.J. Halpern, G.V.R. Chandramouli, E.D. Barth, C. Yu, M. Peric, D.J. Grdina, and B.A. Teicher, Diminished aqueous microviscosity of tumors in murine models measured with in vivo radiofrequency electron paramagnetic resonance, Cancer Research, vol. 59, pp. 5836-5841, 1999.

[13] M. Elas, K. Ichikawa, and H.J. Halpern, Oxidative stress in live animals with techniques based on electron paramagnetic resonance, Radiat. Res., vol. 177, pp. 514 - 523, 2012.

[14] V.V. Khramtsov, V.I. Yelinova, Y.I. Glazachev, V.A. Reznikov, and G. Zimmer, Quantitative determination and reversible modification of thiols using imidazolidine biradical disulfide label, J. Biochem. Biophys. Methods, vol. 35, pp. 115-128, 1997.

[15] P. Kuppusamy, H. Li, G. Ilangovan, A.J. Cardounel, J.L. Zweier, K. Yamanda, M.C. Krishna, and J.B. Mitchell, Noninvasive imaging of tumor redox status and its modification by tissue glutathione levels, Cancer Res., vol. 62, pp.307 - 312, 2002.

[16] F. Hyodo, S. Matsumoto, N. Devasahayam, C. Dharmaraj, S. Subramanian, J.B. Mitchell, and M.C. Krishna, Pulsed EPR imaging of nitroxides in mice, J. Magn. Reson., vol. 197, pp.181-185, 2009.

[17] J.R. Biller, H. Elajaili, V. Meyer, G.M. Rosen, S.S. Eaton, and G.R. Eaton, Electron Spin Lattice Relaxation Mechanisms of Rapidly-Tumbling Nitroxide Radicals, J. Magn. Reson., vol. 236, pp. 47 - 56, 2013.

[18] D.G. Mitchell, M. Tseitlin, R.W. Quine, V. Meyer, M.E. Newton, A. Schnegg, B. George, S.S. Eaton, and G.R. Eaton, X-Band Rapid-scan EPR of Samples with Long Electron Relaxation Times: A Comparison of Continuous Wave, Pulse, and Rapid-scan EPR, Mol. Phys., vol. 111, pp.2664 - 2673, 2013.

[19] D.G. Mitchell, G.M. Rosen, M. Tseitlin, B. Symmes, S.S. Eaton, and G.R. Eaton, Use of Rapid-Scan EPR to Improve Detection Sensitivity for Spin-Trapped Radicals, Biophys. J., vol. 105, pp. 338 - 342, 2013.

[20] J.R. Biller, V. Meyer, H. Elajaili, G.M. Rosen, J.P.Y. Kao, S.S. Eaton, and G.R. Eaton, Relaxation Times and Line Widths of Isotopically-Substituted Nitroxides in Aqueous Solution at X-band, J. Magn. Reson., vol. 212, pp. 370-377, 2011.

[21] S.R. Burks, J. Bakhshai, M.A. Makowsky, S. Muralidharan, P. Tsai, G.M. Rosen, and J.P.Y. Kao, 2H,15N-Substituted Nitroxides as Sensitive Probes for Electron Paramagnetic Resonance Imaging J. Org. Chem., vol. 75, pp.6463 - 6467, 2010.

[22] Y.J. Lin, B.A. Teicher, and H.J. Halpern, Synthesis of 4-protio-3-carbamoyl-2,2,5,5-tetraperdeuteromethyl-3-pyrrolin-1-yloxy (mHCTPO): a selectively isotopically

labeled compound for use in T2 spin label oxymetry, J. Labelled Compds. Radiopharm., vol 28, pp.621-631, 1990.

[23] R.W. Quine, G.A. Rinard, S.S. Eaton, and G.R. Eaton, A pulsed and continuous wave 250 MHz electron paramagnetic resonance spectrometer, Magn. Reson. Engineer., vol. 15, pp. 59-91, 2002.

[24] G.A. Rinard, R.W. Quine, S.S. Eaton, G.R. Eaton, E.D. Barth, C.A. Pelizzari, and H.J. Halpern, Magnet and Gradient Coil System for Low-Field EPR Imaging, Magn. Reson. Engineer., vol. 15, pp.51-58, 2002.

[25] R.W. Quine, G.A. Rinard, S.S. Eaton, and G.R. Eaton, Quantitative Rapid Scan EPR Spectroscopy at 258 MHz, J. Magn. Reson., vol. 205, pp.23-27, 2010.

[26] R.W. Quine, D.G. Mitchell, S.S. Eaton, and G.R. Eaton, A Resonated Coil Driver for Rapid Scan EPR, Concept. Magn. Reson., vol. 41B, pp.95 - 110, 2012.

[27] M. Tseitlin, S.S. Eaton, and G.R. Eaton, Uncertainty analysis for absorption and first-derivative EPR spectra, Conc. Magn. Reson., vol. 40A, pp. 295 - 305, 2012.

[28] M.P. Klein and B.W. Barton, Enhancement of signal-to-noise ratio by continuous averaging: application to magnetic resonance, Rev. Sci. Instrum., vol. 34, pp. 754 - 759, 1963.

[29] S.S. Eaton, R.W. Quine, M. Tseitlin, D.G. Mitchell, G.A. Rinard, and G.R. Eaton, Rapid Scan Electron Paramagnetic Resonance in Handbook of High Frequency EPR S. K. Misra, Ed., Wiley 2014,

[30] G.A. Rinard, R.W. Quine, and G.R. Eaton, An L-Band crossed-loop (bimodal) EPR resonator, J. Magn. Reson., vol. 144, pp.85-88, 2000.

[31] G.A. Rinard, R.W. Quine, G.R. Eaton, and S.S. Eaton, 250 MHz crossed loop resonator for pulsed electron paramagnetic resonance, Magn. Reson. Engineer., vol. 15, pp. 37- 46, 2002.

[32] G.A. Rinard, R.A. Quine, J.R. Biller, and G.R. Eaton, A Wire Crossed-Loop-Resonator for Rapid Scan EPR, Concepts Magn. Reson., vol. 37B, pp. 86-91, 2010.

[33] D.G. Mitchell, R.W. Quine, M. Tseitlin, S.S. Eaton, and G.R. Eaton, X-band Rapid-Scan EPR of Nitroxyl Radicals, J. Magn. Reson., vol. 214, pp.221-226, 2012

[34] B. Epel, S.V. Sundramoorthy, E.D. Barth, C. Mailer, and H.J. Halpern, Comparison of 250 MHz electron spin echo and continuous wave oxygen EPR imaging methods for in vivo applications, Med. Phys., vol. 38, pp. 2045-2052, 2011.

[35] G.R. Eaton and S.S. Eaton, Introduction to EPR imaging using magnetic-field gradients, Concepts Magn. Reson., vol 7, pp. 49-67, 1997.

[36] M. Tseitlin, D.G. Mitchell, S.S. Eaton, and G.R. Eaton, Corrections for sinusoidal background and non-orthogonality of signal channels in sinusoidal rapid magnetic field scans, J. Magn. Res., vol. 223, pp.80 - 84, 2012.

[37] M. Tseitlin, G.A. Rinard, R.W. Quine, S.S. Eaton, and G.R. Eaton, Deconvolution of Sinusoidal Rapid EPR Scans, J. Magn. Reson., vol. 208, pp. 279-283, 2011.

[38] J.P. Joshi, J.R. Ballard, G.A. Rinard, R.W. Quine, S.S. Eaton, and G.R. Eaton, Rapid-Scan EPR with Triangular Scans and Fourier Deconvolution to Recover the Slow-Scan Spectrum, J. Magn. Reson., vol. 175, pp. 44-51, 2005.

[39] J.R. Biller, M.Tseitlin, R.Q. Quine, G.A. Rinard, H.A. Weismiller, H.Elajaili, G.M. Rosen, J.P.Y. Kao, S.S. Eaton, G.R. Eaton, Imaging of nitroxides at 250 MHz using rapid-scan electron paramagnetic resonance, J. Magn. Reson., vol. 242, pp. 162-168, 2012

CHAPTER 7

RESONATOR AND POWER AMPLIFIER CHARACTERIZATION

7.1 Introduction

A resonator focuses energy onto a sample to excite electron spins, and then detects the resulting magnetization. Old resonators were modified, or new resonators constructed to improve the experiments described in Chapters 3-6. Most of the resonators used for rapid scan and pulse experiments were cross-loop-resonators (CLR) [1, 2].The term CLR refers to a two-resonator assembly, where one piece is designated as the power resonator and the other the detection resonator. In the CLR design, the microwave (or RF) B_1 delivered to the power resonator is perpendicular to the detection resonator (the two resonators are *orthogonal* to one another).

The sample lies in a region common to the two circuits of the CLR. If perfect orthogonality were achievable the detection resonator would not observe any power incident on the sample. Only the spin magnetization would be observed in the detector resonator leading to higher sensitivity. In practice perfect electromagnetic orthogonality cannot be achieved. The two resonators of the CLR can be physically adjusted relative to one another to try and achieve perfect orthogonality with the *isolation* screw. During each experiment the isolation is adjusted to bring the power and detection resonators as close

to orthogonal as possible.

7.2 Resonator design for Pulse and Rapid Scan EPR

7.2.1 Resonators for Pulse EPR

Bi-modal resonators used for pulse EPR in the Eaton lab are often constructed of a tellurium copper alloy [1]. The goal for pulse resonators is excellent isolation and high Q. For the studies reported in Chapters 4 and 5 of this dissertation, the long ringdown times characteristic of pulse resonators at 250 MHz require the addition of Q-spoiling circuits. Q-spoiling allows high sensitivity to incident power during the pulse, but "short" the Q (lower the Q) after the pulse is over to decrease ringdown. Two types of Q-spoiling were introduced in section 2.6.5. Questions surrounding pulse CLR development include which style gives the best resonator efficiency, and whether or resonator design is scalable from 25 mm to 51 mm.

7.2.2 Resonators for Rapid-Scan EPR

For a rapid-scan CLR at 250 MHz, resonator design is dictated by accessibility for animal use and good isolation between the two resonators [3]. The solid copper designs used in pulse resonators do not offer enough penetration of sweep field for rapid scan, even with the normal slots that suffice for modulation of the field during a CW experiment. In addition, rapid-scan resonators are designed to minimize the amount of metal present, to decrease the impact of eddy currents. Rapid scan resonators usually have lower Q values than pulse resonators, as the signals created by large amplitude

magnetic field scans require a larger resonator bandwidth. Any high frequency noise or baseline changes which are not coherent with the rapid scan experiment are reduced by time averaging of the signal. Any noise that is coherent with the field scan will be recorded along with the EPR signal. A major source of coherent background signal in the rapid-scan experiment is derived from the scan frequency and its harmonics.

The rapid-scan background is currently divided into two main effects: direct electrical effects and electrical effects derived from mechanical vibrations. Direct electrical effects concern modulation of the background radiofrequency (RF) signal by the scan frequency. From a design perspective, this type of background seems to be tied to where the scan coils are in position to the detector resonator in the CLR. The scan coils also play a role in the mechanical vibration derived background. Any current flowing through a conductor (i.e. scan coils or metal in resonator) at the scan frequency will interact with applied steady magnetic field. This produces a "motor" effect, which vibrates the conductor. If amplitude or phase modulation of the RF is produced from these vibrations, a background signal will be observed in the rapid-scan spectrum.

Attempting to "shield" the resonator or block RF noise from the resonator has undergone a variety of iterations. The term "shielding" has had three definitions from 2009 to 2014, referring to a copper box shield around the entire assembly, copper tape shield around only the scan coils, or a wound-wire shield between the resonators and the scan coil. Shielding the scan coils made of Litz wire with copper tape decreased RF noise, but eddy currents in the copper tape raised the AC resistance of the coils. Litz wire was used to decrease the AC resistance relative to solid copper wire, and the addition of

copper tape on Litz wire scan coils negated most of that advantage.

The scan coils evolved with advancements in the coil drivers. Initial coil driver designs used a linear (triangular) scan current, which provided a linear field scan over ca. 85% of the sweep width. Development of sinusoidally driven currents simplified background subtraction and was first implemented at X-band [4]. A new observation from the middle of 2013 to early 2014 was frequency dependence of contributions to the background signal. For instance, differences in the background signal caused by the power amplifiers installed in various coil driver versions observed at 250 MHz were non-existent at X-band.

7.3 Methods For Characterization Of Resonators

Resonators were characterized by their range of operating frequencies and changes in the Q-value between empty (Q_E) and sample containing (Q_S) states. Further characterization can include measurement of the resonator efficiency. For pulse resonators, the required power vs. pulse length was mapped out at several Q values. In some cases the ringdown of both power and detection resonators was studied from the highest to lowest Q-values. For samples with relaxation times <500 ns (i.e. many nitroxides), a combination of resonator over-coupling and Q-spoiling are required. For rapid-scan resonators the “mechanical resonance” background was quantitatively probed with a manual scan, in 100 Hz increments, or with a chirp pulse. See section 6.2.3 for an example.

7.3.1 Measurement of Resonator Q

Figure 7.1 demonstrates the most straightforward measurement of resonator Q. The frequencies at the -3dB point on either side of resonance are recorded (ν_1 and ν_2). The center of the resonator dip is recorded (ν_0). Using equation 7.1, the Q of the resonator can be calculated from the relationship of these three frequencies.

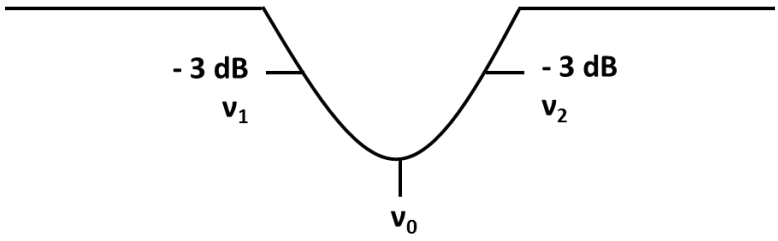

Figure 7.1 Measuring resonator Q at the – 3 dB point.

$$Q^{-1} = \frac{\nu_2 - \upsilon_1}{\upsilon_0} \qquad (7.1)$$

The reflected power ringdown from a pulse incident on the resonator can also be used to measure the Q of the resonator. There must be less than 15 mV separation for standard crystal detectors between the baseline and peak of the trailing edge of the response. An illustration of how the measured ringdown of the pulse response relates to Q is given in Figure 4 of [5]. For very low Q values the transient decay may be so fast that the measurement is limited by the oscilloscope. To ensure it is not the response of the system being measured, a second frequency away from the tuned frequency of the resonator can be selected for comparison.

7.3.2 Measurement of Resonator Efficiency

Resonator efficiencies have been measured for a number of the resonators and are listed in Tables 7.1 and 7.2 at the end of this section. The methods by which resonator efficiencies were measured are described below.

7.3.2.1 Maximum echo amplitude by field sweep with echo detection

A field-swept echo detected spectrum was acquired at several attenuation settings for the incident powers and the echo amplitude was recorded. The maximum echo amplitude is obtained when the B_1 corresponds to a 90° pulse. The $\pi/2$ pulse was 600 ns for all resonators, so calculation of the $W^{1/2}$ corresponding to the maximum echo response is simplified. Echo parameters used for each resonator were $\pi/2$ = 600 ns, x-axis = 128 points, tau 2.4-3 microseconds, integrator position (d_0) = 1.52 microseconds, integrator window (pg) = 4 microseconds, shot repetition time (SRT) = 500 microseconds and a sweep width of 4 G. A single scan was completed for each case. Since resonators were used at critical coupling, without the aid of Q-spoiling, tau values less than 2.4 microseconds could not be used due to resonator ringdown. The same sample (Trityl CD_3 0.2 mM aqueous, ID# B13) was used for the four 25 mm resonators. A 16 mm 0.2 mM trityl CD_3 sample (ID E162) was used for AGLGR-CH-5.

For CLR-DU-6, the Q_S of the power resonator was 400 which gave a ringdown time of 500 ns. Using a $\pi/2$ pulse of 600 ns doesn't allow enough time for delivery of 100% of the power to the resonator, so the measurement was repeated for CLR-DU-6 with a $\pi/2$=1200 ns pulse. All of the other resonators tested had Q_S<100, so use of the longer

pulse was not required. Additional methods were pursued for CLR-DU-6 after initial $B_1/\sqrt{W}$ = 0.32-0.40 was measured using the echo amplitude optimization. The $B_1/\sqrt{W}$ was reported to be 1 G/$\sqrt{W}$ in a prior publication [1].

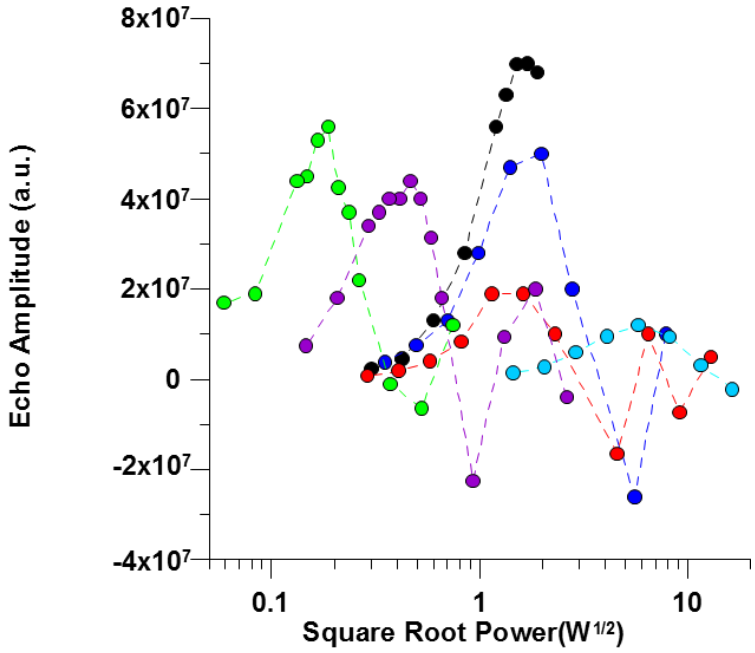

Figure 7.2 Echo Amplitude vs. the square root of power. Data points are connected only as an aid to guide the eye. The echo amplitude plots are given for CLR-DU-4 (●), CLR-CH-4 (●), LGR-DU-5 (●) and AGLGR-CH-5 (●) for different attenuations of the power incident on each resonator. The echo amplitude test was completed for CLR-DU-6 with $\pi/2$ = 600 ns (●) and $\pi/2$=1200 ns (●).

7.3.2.2 Maximum real time amplitude of single pulse FID or two pulse echo.

A two-pulse experiment was digitized with the Bruker Specjet so the echo could be observed. The field was stepped 0.1 G off resonance so a strong "FID" signal could be seen, and the attenuator setting was varied until a maximum in the signal was seen. The signal maximum was gauged by careful inspection with a ruler on the computer monitor

by one person while a second person varied the attenuation. From this peak in signal amplitude a $B_1/\sqrt{W} = 0.63$ was calculated for CLR-DU-6 (Table 7.2).

A single pulse FID experiment operating real time with digitization into the Bruker SpecJet window was also used. With the $\pi/2$ pulse = 1200 ns, the attenuation at maximum signal was recorded and a $B_1/\sqrt{W} = 0.25$ was calculated. Tip angle (θ) is related to B_1 and pulse duration (τ_p) by equation 2.6:

$$\theta = \gamma B_1 \tau_p \qquad (2.6)$$

Where θ= turning angle in radians, $\gamma = 1.7608 \times 10^7$ rad s^{-1} G^{-1} τ_p = pulse length in seconds = 600×10^{-9} s (600 ns pi/2 pulse). Solving for B_1 gives 0.1487 G for $\pi/2$=600 ns, or 0.0743 for $\pi/2$ = 1200 ns. From the attenuation where the echo maximum is achieved (Fig. 7.2) the $\sqrt{W}$ can be calculated, and then $B_1/\sqrt{W}$.

7.3.2.3 Nutation Experiment with Torrey Oscillations

Torrey oscillations are related to the magnitude of B_1 during an applied pulse, and the damping of the oscillations depends on T_1 and T_2. A good example of how these oscillations have been used to measure B_1 is given in [6]. A nutation program from the E580 instrument was modified to work on the VHF E540 system. The period of the oscillations (Fig. 7.3) provides a means of calculating B_1, and dividing the $B_1/\sqrt{W}$ at attenuations of 50, 40 and 30 dB gave values of 0.44, 0.46 and 0.49, respectively. From these values an average $B_1/\sqrt{W}$ of 0.46 was calculated. A sample calculation is given below using values from the VHF nutation experiment.

For the spectrum at 40 dB attenuation (Figure 7.3), one cycle of the oscillation is 2.2 μs.

2.2 μs/cycle = 2.2 x 10^{-6} s/cycle = 4.545 x 10^{5} cycle/s

4.545 x 10^{5} cycles/s x 2π = 2.86 x 10^{6} rad/s

(2.86 x 10^{6} rad/s) / (1.7608 x 10^{7} rad/s/G) = ***0.167 G***

40 dB attenuation from 1310 W (TOMCO 2 kW RF Amplifier) = 0.131 W

√0.131 W = ***0.362*** *$W^{-1/2}$*

$B_1/\sqrt{W}$ = 0.167/0.362 = 0.46 $GW^{-1/2}$

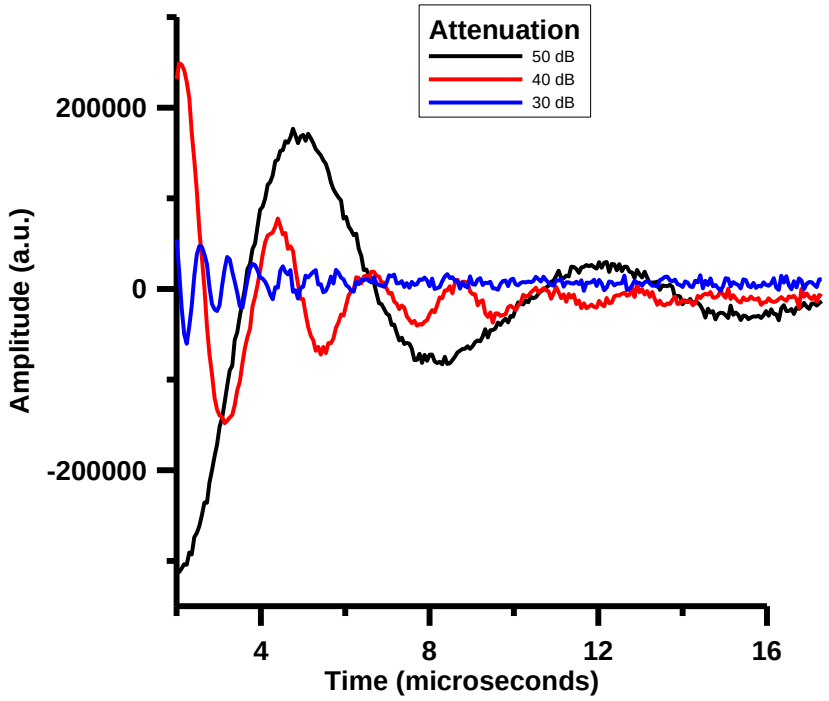

Figure 7.3 Example of the nutation experiment at 250 MHz. The time for a full cycle (peak to peak) is 50 dB (7.4 μs), 40 dB (2.2 μs) and 30 dB (0.65 μs).

Table 7.1 Measured $B_1/\sqrt{W}$ by method in 7.2.2.1 for five resonators ca. 250 MHz. Unless otherwise noted, the resonators were critically coupled for these measurements.

Resonator	$B_1/W^{1/2}$	Q_S (Power Resonator)
CLR-DU-6	0.32-0.40	400
LGR-DU-5	0.09-0.13	20
CLR-DU-4[1]	0.09-0.10	85
CLR-CH-4	0.08-0.11	25
AGLGR-CH-5[2]	0.025	16

1 No coupling adjust; coupling determined by sample.

2 $B_1/\sqrt{W}$ measured in Chicago was 0.0512, resonator critically coupled

Table 7.2 Measured $B_1/\sqrt{W}$ by four methods for CLR-DU-6 at ca. 250 MHz

Measurement Method (Section)	$B_1/W^{1/2}$
7.2.2.1 ($\pi/2$=600 ns)	0.32-0.4
7.2.2.1 ($\pi/2$=1200 ns)	0.44
7.2.2.2 (Two Pulse)	0.63
7.2.2.2 (Single Pulse)	0.25
7.2.2.3	0.46

7.3.3 Measurement of Mechanical Resonances for Rapid Scan Experiments

A detailed account of this technique is given in Chapter 6, Section 6.2.3. A range of scan frequencies are swept, either manually or by using a "chirped" frequency pulse. At frequencies where the scan field/frequency matches some mechanical feature of the resonator, large (orders of magnitude) increase in the amplitude of background signal was observed. The exact identity of the "mechanical features" are unknown. As more quantitative empirical evidence is gathered, the relationship between resonator design and mechanical resonances will be become clearer. After reviewing the mechanical resonance work on the resonators in this chapter, and comparing with mechanical resonance measurements made by Zhelin Yu, the shape of the scan coils may play a role. The main mechanical resonance frequency for scan coils of a square geometry was around 5 kHz,

while those with a circular geometry had the largest mechanical resonance between 11 and 15 kHz. The reason for this difference is not currently known.

7.4 Resonators at the University of Denver

7.4.1 CLR-DU-1 and CLR-DU-2

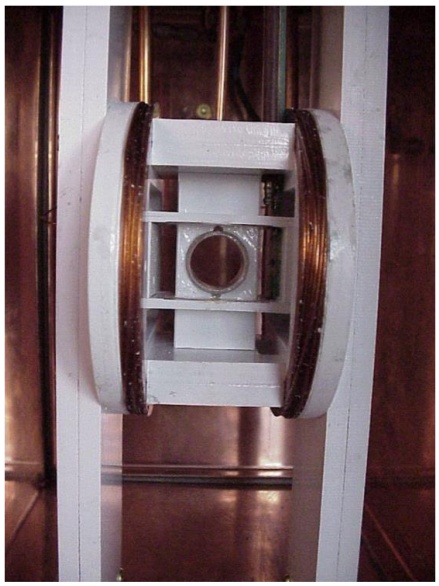

Figure 7.4 Example of design for CLR-DU-1 and CLR-DU-2. Shown in the figure is the PVC support. Power resonator is 32 mm (o.d.) with efficiency of 0.085 $G/W^{-1/2}$. Detection resonator is 16 mm o.d. and 15 mm in length, with 0.45 $G/W^{-1/2}$. Scan coils are a Helmholtz pair, 89 mm (o.d.) made of AWG 20 enameled copper wire.

Design for both these resonators was published in [3] and focused on rigid support for the wire detection resonator and the scan coils. The support structure was composed of either PVC (CLR-DU-1) (Fig. 7.4) or Rexolite (CLR-DU-2). Both resonators gave good isolation (-47 and -44 dB, respectively) and had the characteristic low Q thought to be desirable for animal imaging. Mechanical resonances are noted in the area of 1.04 to 2.25 kHz, but no amplitudes are reported, or any information given on the amplitudes of

frequencies above 2.25 kHz. These resonators were the first published examples of a resonator designed for rapid-scan. Of the two, one would stay in Denver (becoming CLR-DU-3) and the other would be sent to Chicago (becoming CLR-CH-1)

7.4.2 CLR-DU-3

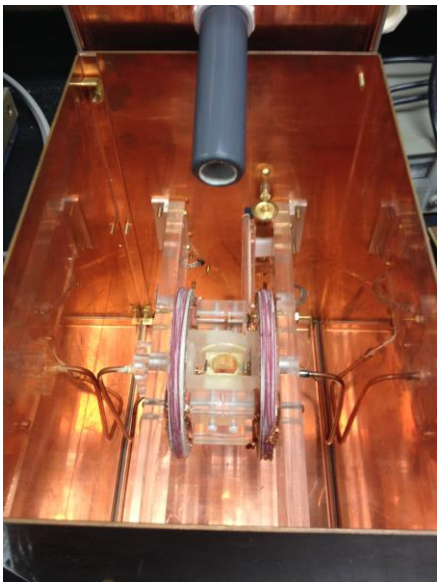

Figure 7.5 CLR-DU-3 as of March 2014. Power resonator is two coils of 0.1 mm diameter wire, 32 mm in diameter, spaced 21 mm. The detection resonator is 16 mm in diameter and consists of a single turn resonator consisting of parallel coils of 0.1 mm diameter wire. Scan coils are 90 mm circular Helmholtz pair made of AWG 20 magnet wire with an estimated coil constant of 12.9 G/A.

Formerly (CLR-DU-1) this 16 mm resonator is now outfitted with Litz wire scan coils (instead of solid copper) inside a solid copper box. In the early part of 2013, these coils were wrapped in copper tape as a form of shielding, but this was later removed. The overall design of shielding both the scan coils and the resonator together was abandoned in 2013 during optimization of the rapid scan imaging experiments.

7.3.3 CLR-DU-4

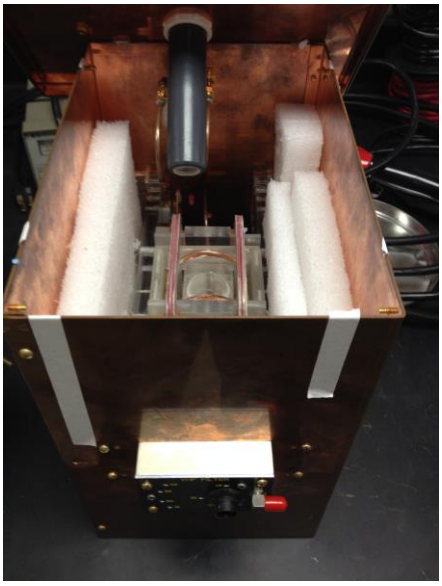

Figure 7.6 CLR-DU-4 as of March 2014**.** Power resonator is two 60 mm diameter coils made of copper foil and spaced 38 mm. Detection resonator is 26 mm diameter single turn coil 25 mm long consisting of 25 coils of 0.1 mm diameter wire spaced ~1 mm. Scan coils are 102 mm square Helmholtz type pair made of Litz wire 240/46 wire with 1.8 mH inductance and coil constant between 12.5 and 13 G/A.

The power resonator in CLUR-DU-4 is made of copper foil, which allows for greater incident powers and was requested for animal work by the Chicago group. Coupling cannot be adjusted and for efficiency measurements was determined by the aqueous Trityl-CD_3 sample used. The maximum power input to this resonator did not exceed 3.56 W out of concern for damaging the resonator. During investigations into background suppression, foam was added to increase rigidity and decrease any mechanical or acoustic vibrations. Some decrease in background amplitude was observed by very fine tuning of the RF trap (black box on front of resonator).

In June of 2013 the measured coil constant was found to vary with sweep width in the rapid scan experiment. The same coils were used as CW modulation coils, and results

from CW modulation amplitude calibration experiments are shown in Tables 7.3 and 7.4. The discrepancy came to light when trying to fit image slices from preliminary rapid-scan 2D images. The problem had not been observed with initial CW projections obtained with very small modulation amplitudes. As modulation amplitude was increased, the trends in coil constant began to match what was observed with de-convolved rapid-scan spectra. The larger modulation values more nearly approximate the true modulation, resulting in a more consistent calculation of the coil constant.

Another confounding variable was the use of SpecJet I as a digitizer, which had a 3% clock jitter which was previously unknown. This caused rapid scan frequencies to be inaccurate, which effected the deconvolution, which is very sensitive to the exact scan frequency, and therefore calculation of the coil constant. The SpecJet II digitizer was installed, and had only a 0.3% jitter. Rapid-scan collected with SpecJet II indicated a coil constant of 16.4 G/A.

The current output from RCD3 was discovered to be 40% higher than the readout on the coil driver. A faulty resistor was found and was replaced. After implementation of SpecJet II, and repair of RCD3 current output, measured coil constants were usually between 12.5 and 13 G/A. Some non-uniformity in the observed coil constant existed, and frustrated attempts to image the low-field lines of the ^{15}N-nitroxides described in Chapter 6.

Table 7.3 Calibration of coil constant with a trityl radical. The splitting of a trityl CD_3 signal by increasing modulation amplitude was monitored. The trityl-CD_3 signal is almost Lorentzian with a linewidth ca. 0.03 G.

XEPR MA Input (G)	Signal Split, ΔB_{pp} (G)	Measured Current (A)[1]	Calculated Coil Constant, G/A
1	0.47	0.044	10.6
4	2.13	0.162	13.1
9	5	0.364	13.7
15	8.3	0.608	13.7

[1] V_{pp} measured on scope with 50 Ω load

Table 7.4 Calibration of coil constant with a nitroxide radical. The splitting of the low-field line of a ^{15}N nitroxide signal was monitored while increasing modulation amplitude. Nitroxide linewidth is ca. 0.5 G with a Lorentzian component of the linewidth would ca. 0.07 G.

Input MA (G)	Signal Split, ΔB_{pp} (G)	Current (A)	Coil Constant, G/A
4	2	0.164	12.2
9	4	0.344	11.6
15	8	0.608	13.2
20	10.7	0.808	13.2

7.4.4 LGR-DU-5

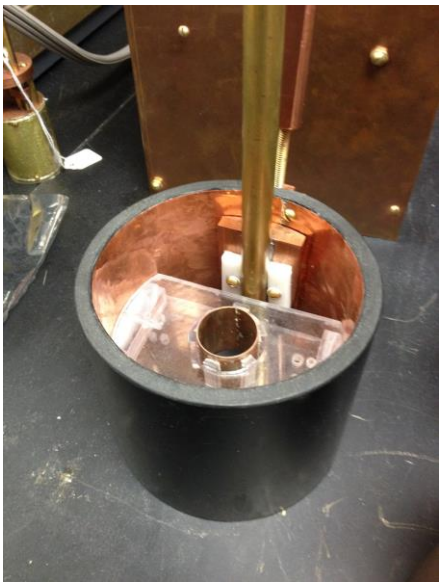

Figure 7.7 LGR as of March 2014. Single solid copper resonator 25 mm (o.d.).

The 25 mm LGR was made for comparison with CLR during efficiency measurements and the resonator was critically coupled. This resonator was not routinely used for the experiments described in Chapters 3-6. If LGR-DU-5 could be outfitted with rapid scan coils, comparing the rapid-scan background from this single resonator with the CLR design may give insight as to what the dominant causes of the background signal are.

7.4.5 CLR-DU-6

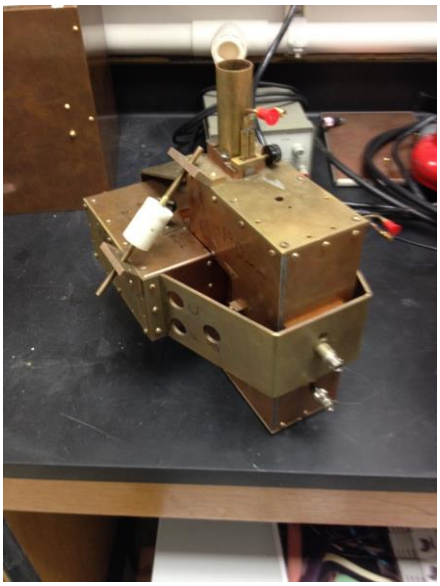

Figure 7.8 CLR-DU-6 as of March 2014. Dimensions are given in [1]. This resonator is equipped with Q-spoiling, with a fixed voltage bias on the detection side of 9 V. The voltage bias on the power side varies with the type of RF amplifier being used, but is within the range of 400-550 V.

CLR-DU-6 was the main resonator used to make relaxation measurements at 250 MHz and has been described in [1]. It is a solid copper design with Q-spoil diodes on both power and detection resonator. For efficiency measurements both resonators were critically coupled.

7.4.6 CLR-DU-7

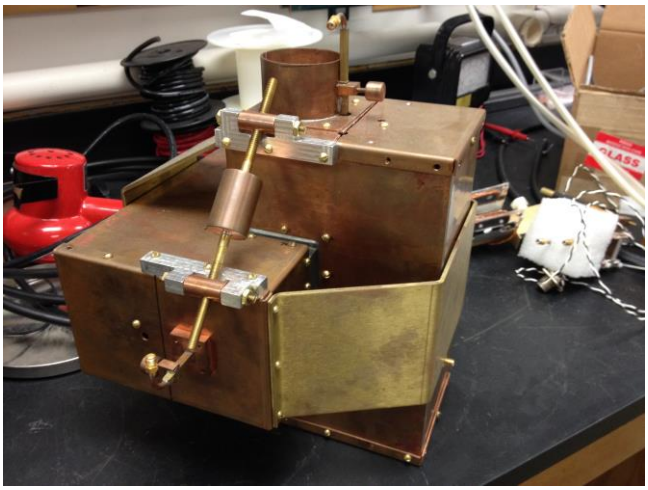

Figure 7.9 CLR-DU-7 as of March 2014. The power resonator is 51.6 mm (i.d.) and 152 mm in length. Detection resonator is nearly oval, 38 mm wide and 65.8 mm long. The sides are parallel for 27.8 mm and the ends are 19 mm circular radius. The "traditional" Q-spoiling can be used, along with a "dial-a-Q" feature by changing out resistors across the gap of the power or detection resonators.

Each half of the resonator structure for CLR-DU-7 is made of aluminum and contained in a copper casing. Measurements with this resonator were made using four trityl samples (trityl CD_3 and Ox 63) to fill the resonator space:, two 25 mm and two 16 mm were taped together and inserted into the 51 mm resonator to give sufficient filling factor for a good signal. The voltage bias required for Q-spoiling on the power resonator was 400 V. An isolation of -54 dB was measured and Q_S of the power resonator was ca. 250. An echo decay of the composite sample was measured with $T_m = 9$ µs.

CLR-DU-7 is equipped with what has been named the "dial-a-Q" feature. The Q-value of the critically coupled resonator can be lowered or raised depending on the size of resistor placed across the gap of either power or detection resonators.

The effect on the Q of a range of resistances (0.866 to 10 kΩ) was explored. In the absence of any resistors, the resonant frequency of the power and detection sides were measured and found to be 268.5 and 250 MHz, respectively. A quartz tube with distilled water (55 mm o.d. x 105 mm high) added to the resonator shifted resonances down by 30 MHz (239 and 220 MHz, respectively). Eventually the coupling and frequency of both resonators were adjusted to 251 MHz, with an isolation of – 44 dB and Q_S = 170 for the power resonator and Q_S= 130 for the detection resonator.

Measurements of Q (Table 7.5) were taken first with the aqueous sample in the resonator, and then with the actual sample to be used with the nutation experiments. The sample consisted of two smaller samples (trityl CD_3, 0.2 mM. o.d. = 25 mm and 10 mm) placed into a large quartz tube (o.d.45 mm). Since these two samples were insufficient to lower the Q of the 51 mm resonator, water was added to a height of 120 mm to increase dielectric loss and further lower the Q.

Table 7.5 Effect of resistors from 10 to 0.866 kΩ on the Q of CLR-DU-7. Q-values for detection resonator, with two different samples are shown.

	Resistor Value (kΩ)					
	None	**10**	**6**	**3**	**1.78**	**0.866**
Resonator Q Aqueous Sample	134	105	84	64	45	28
Resonator Q EPR Sample	271	149	115	84	53	29

The Q in the detection resonator was higher for the EPR sample than the aqueous sample with no resistor over the gap, from 10 kΩ to 1.78 kΩ. Since the EPR sample was

smaller in diameter than the aqueous sample, the loss was not as great and the Q was higher. The 0.866 kΩ resistor resulted in similar Q (ca. 30) in both cases.

Further analysis (Table 7.6) was done for the resonator with no resistor across the gap of resonator #1, or with the 0.866 kΩ. The efficiency of the resonator with no resistor present was compared to the case where the smallest value resistor (0.866 kOhm) was present. Both the power and detection resonators were critically coupled for these measurements and neither resonator had a resistor across the gap. For a power resonator Q = 380, the measured $B_1/\sqrt{W} = 0.15$ (Sec. 7.2.2.3). A field sweep with echo detection experiment was used to judge the shortest $\pi/2$ pulse which could be used. The amplitude peaked for $\pi/2$ = 80 ns at 4 dB, and a decrease in signal could be observed at 1 dB. The frequency of the experiment was 260 MHz. At this frequency the output of the TOMCO amplifiers at 0 dB is 1310 W.

For the case where the 0.866 kΩ was used, the power and detection resonators were critically coupled. The nutation experiment was repeated, and the Q of the power resonator was measured under experimental conditions. For a power resonator Q = 37, the measured $B_1/\sqrt{W} = 0.05$. $\pi/2$ = 160 ns was the shortest pulse length where an echo amplitude could be optimized and occurred at 8 dB attenuation of the incident power. $\pi/2$ = 80 ns yielded an echo at 2 dB, but did not decrease in amplitude at 1 or 0 dB. Analysis frequency was 265 MHz, for which the TOMCO output at 0 dB was only 995 W (Fig. 7.15).

Table 7.6 Comparison of $B_1/\sqrt{W}$ under low Q or high Q conditions. In the high Q condition there is no resistor across the gap. In the low Q condition the 0.866 kΩ resistor is in place.

	$B_1/\sqrt{W}$	Smallest π/2	Q #1
No Resistor	0.15	80 ns	380
0.866 kΩ	0.05	160 ns	37

7.3.6.1 Comparing Changes in Efficiency with Changes in Measured Q.

Equation 7.3 relates B_1 and Q [8] for a TE_{102} rectangular cavity when α = 0.02.

$$B_1 = \alpha \sqrt{PQ} \qquad (7.3)$$

In this case P is the incident power in Watts for a particular B_1 (π/2 pulse) and α is an experimentally determined proportionality constant. To answer the question of whether or not the changes in efficiency correlated with changes in measured Q (Table 7.6), Eq. 7.3 was rearranged to equation Eq. 7.4 to solve for α.

$$\alpha = \frac{B_1}{\sqrt{PQ}} \qquad (7.4)$$

B_1 for the resonator in the high Q (no resistor) or low Q (0.866 kΩ resistor) was the same (=0.134 for π/2 = 660 ns), but the Q-values were different. If the changes in efficiency between the high and low Q states make sense in comparison to one another, the factor J should be the same or similar in each case.

For the high Q state:

$$\alpha_{High\ Q} = \frac{0.134}{\sqrt{1.309\ W * 380}} = 0.006 \qquad (7.5)$$

For the low Q state:

$$\alpha_{Low\ Q} = \frac{0.134}{\sqrt{9.94\ W * 37}} = 0.007 \qquad (7.6)$$

The two factors are the same within the experimental uncertainty, so the change in required power with the addition of the 0.866 kΩ was consistent with the dependencies predicted by Eq. 7.4.

7.3.6.2 Scaling Comparison between CLR-DU-7 and CLR-DU-6

The most recent measurement of CLR-DU-06 gave a $B_1/\sqrt{W} = 0.45$ with a Q = 400 for the critically coupled power resonator. This is 3x more efficient than the 51 mm resonator with a similar Q (0.15 and Q=380). Calculations by George Rinard based on the dimensions of CLR-DU-6 and CLR-DU-7 estimated efficiencies of 0.67 and 0.22 G/√W, respectively. The ratio of efficiencies between the two resonators matches well with experimental measurements. Calculated efficiencies are about √2 larger than efficiencies measured experimentally. The experimentally determined efficiencies for CLR-DU-6 were verified using two different methods (Table 7.2). The addition of the resistors across the gap (CLR-DU-7) and Q-spoiling diodes (CLR-DU-6) complicate the estimation of the inductance and resistance in these resonators, which could result in an over-estimation of calculated efficiency.

7.4.7 CLR-DU-8

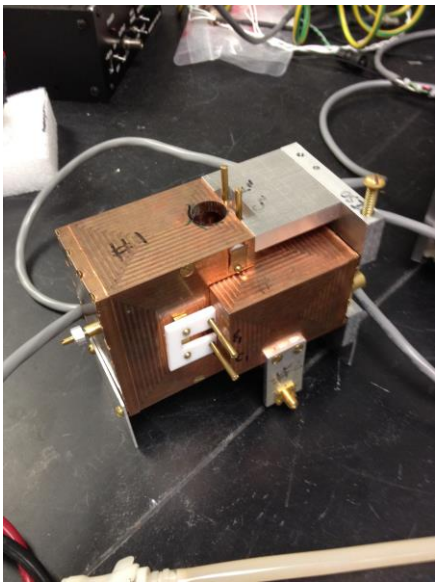

Figure 7.10 CLR-DU-8 as of March 2014. The power resonator is 16.5 mm in diameter and 30.5 mm in length. Detection resonator is nearly oval, 12 mm wide and 20.4 mm long. The sides are parallel for 28.4 mm and the ends are 6 mm circular radius. Detection resonator is 25.4 mm long. The frequency of each resonator is tunable by means of a 32 mm diameter copper disk in the reentrant cavity whose distance from the respective resonator gap can be adjusted. Active Q-spoiling with voltage biased diodes is used on both power and detection resonators.

CLR-DU-8 is a 16 mm variable frequency (585 to 900 MHz) solid copper resonator with Q-spoiling. No efficiency has been measured as of March 2014. The first Q-measurements around June 2012 gave Q = ca. 370 for the power resonator and Q= ca. 420 for detection resonator in the absence of a sample, and with both resonators critically coupled. After addition of 16 mm sample the Q of the power resonator was ca. 270 while the Q of the detection resonator remained unchanged. To reduce ringdown the power resonator could be overcoupled to Q=90. In July of 2012 Q-spoiling was added to the resonator. CLR-DU-8 was used to collect some data confirming the trend for nitroxide relaxation times reported in Chapters 5 and 6 from 1.5 GHz to 250 MHz (unpublished),

and also used to add another data point to the frequency dependence of $1/T_1$ and $1/T_2$ for the trityl radical Ox63(Fig7.9) which was previously measured in [9].

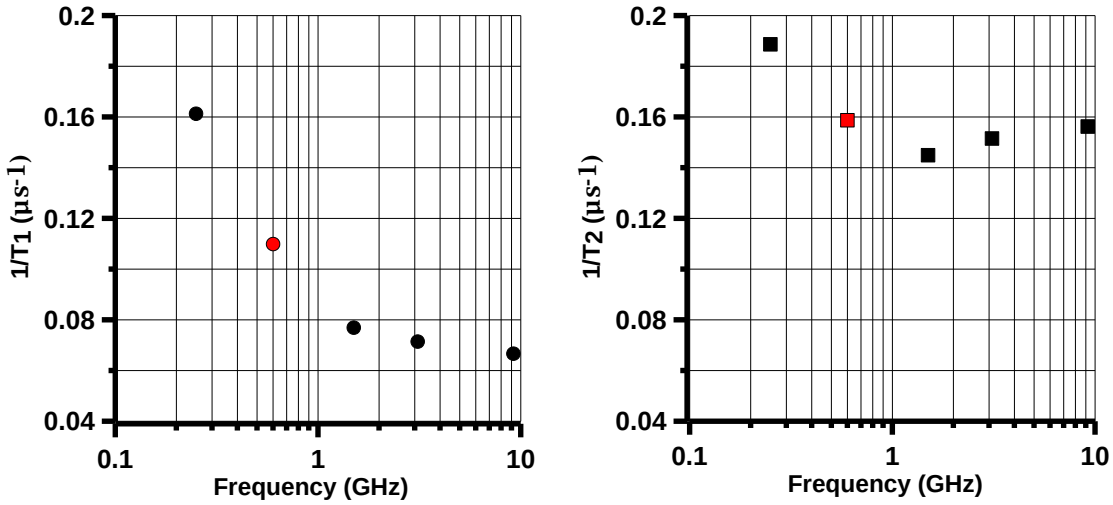

Figure 7.11 Measurement of T_1 and T_2 for Ox63 at 600 MHz with CLR-DU-8 T_1 (●) and T_2 (■) Ox63 fit very well with the data collected by Rikard Owenius at X-, S- and L-band and VHF [9].

7.5 Resonators Constructed At DU In Use At The University of Chicago.

7.5.1 CLR-CH-1

Modifications to this resonator in 2012 to increase the $B_1/\sqrt{W}$ included replacing the power resonator with foil which gave a higher Q, replacing the scan coils with "shielded" coils and removing the R.F. Filter box (replaced with empty box). Prior to the modification, the power resonator had been composed of the same 4 mm copper wire used for the sample resonator in an effort to keep the amount of copper in the resonator to a minimum. Characterizations centered on measuring background mechanical resonances and the efficiency of the power resonator.

The Q-value of the power resonator was measured with the network analyzer empty (Q=114), with a saline (0.5g/5g water) solution (Q=65) and with the trityl-CD_3 standard sample used for the measurement (Q = 124). Measured isolation with the trityl sample in the resonator was -39 dB. A qualitative examination of mechanical resonances was made with the linear driver and HP function generator. For the span of frequencies from 0.5 to 20 kHz, the mechanical resonance at 12.3 kHz was 3-4 times larger in amplitude than any other frequency. "Quiet" regions were found between 1-6 kHz and between16 and 20 kHz. There were also frequency regions where the background was hardly detectable at 4.4, 6.6 and 10.9 kHz. The background at a resonant frequency disappears when B_0 was set to zero and seemed to be approximately linear in amplitude proportional to B_0.

A measurement of efficiency was made for the newly modified power resonator. A single pulse experiment was run with three pulse lengths that varied from 256 ns to 1000 ns. For each pulse length the power required for the largest amplitude FID was recorded for a 0.2 mM sample of Trityl-CD_3. The B_1 was calculated for each pulse length using equation 7.2. The derived value of B_1 decreased with increasing pulse length (Table 7.7).

The power was measured and extrapolated to be 1.3 kW at 0 dB. This matched a previous measurement of 1.34 kW. Attenuation of the amplifier output was 10 dB in the bridge with an additional 20 dB attenuator between the power resonator and the VHF compensation box. Pulse duration was 2 μs with a pulse repetition period of 200 x 1.02 μs for a duty cycle of 1%. This gave peak powers that are safe for the power meter probe (15 W max for 2 μs) and average power values in the measureable range. B_1 values from

were divided by the square root of power at each attenuation, and are recorded in Table 7.7

Table 7.7 Calculation of efficiency for CLR-CH-1. The measured efficiency of the power resonator was about 0.3 G / √ W.

Pulse (ns)	Calc. B_1 (G)	Attenuation (dB)	Power (W)	$(Watt)^{-1/2}$	$(B_1 /\sqrt{W})$
256	0.349	30	1.3	1.14	0.31
500	0.178	35	0.41	0.640	0.28
1000	0.089	40	0.13	0.361	0.25

A report from the engineer Subramanian V. Sundramoorthy in Chicago on 03/03/14 confirmed they still have this resonator, and that it suffers from large background. This seems to fit our observations of the other “copper box” resonators in comparison to the wound-wire shield between resonator and scan coil.

7.5.2 CLR-CH-2

Figure 7.12 CLR-CH-2 as of March 2014. The power resonator is two coils of 0.1 mm diameter wire, 52 mm in diameter and spaced 38 mm in. Detection resonator is a single turn resonator, 26 mm in diameter and consists of 25 parallel coils of 0.1 mm diameter wire spaced about 1.3 mm.

This resonator has been used in Chicago during 2013 and 2014, and gives improved background over CLR-CH-1. The cyclindrical sample support (copper pipe) on the outside of the resonator is 50 mm long and 25 mm (i.d.). The power resonator can be adjusted for coupling and frequency, while the sample resonator is fixed in frequency and coupling.

7.5.3 CLR-CH-3

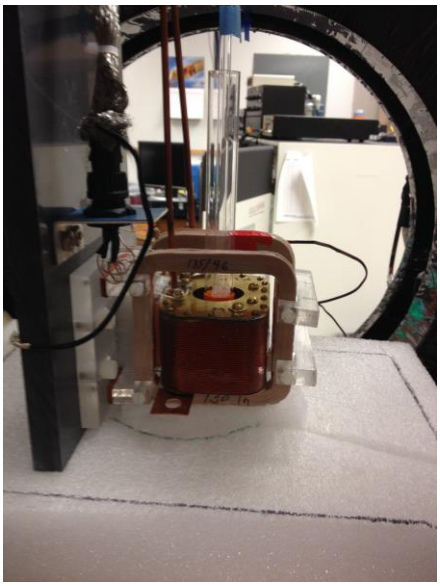

Figure 7.13. **CLR-CH-3** as of March 2014. This resonator is fully described in Sec.6.2.3

CLR-CH-3 is a 16 mm resonator with square scan coils (Litz wire) outside a wire wound shield. The inside of the shield is coated with a fine layer of silver paint. The current scan coils have an inductance of 4.9 mH and a coil constant of 23.75 G/A. These coils are able to sweep fields up to 95 G. A description of this resonator with smaller inductance scan coils (1.2 mH) is given in Chapter 6 (Sec. 6.2.3). The coil constant in that case was ca. 12.5 G/A.

7.5.4 CLR-CH-4

CLR-CH-4 is a 25 mm smaller version of CLR-DU-6, designed for use in animal imaging at Chicago. For efficiency measurements both resonators were critically coupled (Table 7.1). The resonator can be arranged in a horizontal position to facilitate mouse imaging with pulse EPR in Chicago.

7.5.5 AGLGR-CH-5

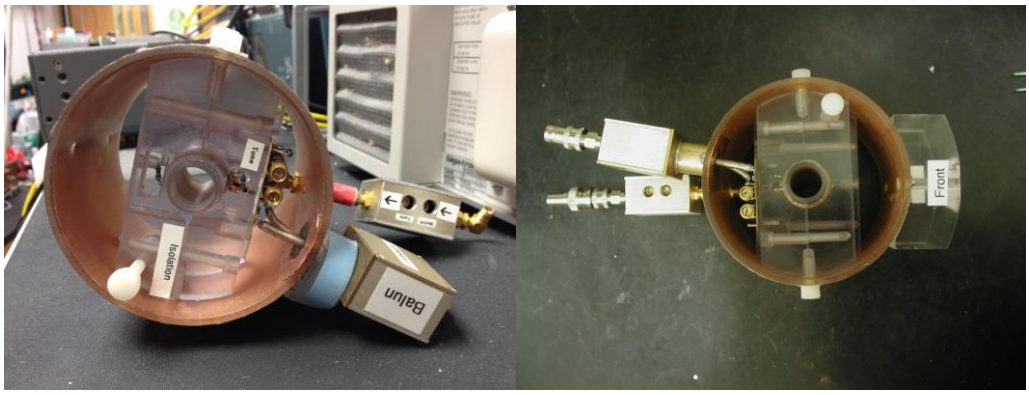

Figure 7.14 AGLGR-CH-5 as of March 2014. The detection resonator is 16 mm (i.d.) The photo on the left is from the Chicago group. This resonator was constructed in Chicago.

The Alderman-Grant (AG) resonator combined with a loop gap resonator (LGR) is a bi-modal design favored by the Chicago group. The Alderman Grant section is the power resonator, and the detection resonator is a slotted loop-gap-resonator (LGR). The "passive" Q-spoiling with Schotke diodes employed for this resonator was discussed in Sec.2.6.5. Measurements at DU in December of 2012 of the efficiency were done with the resonator in an over-coupled state. Recently the Chicago group published a paper on an updated version of AGLGR-CH-5 for pulse *in vivo* imaging [10].

7.6 Testing Of Pulse RF Amplifiers

7.6.1 TOMCO 4 kW RF Amplifier for 250 MHz

The maximum output of this amplifier is 4 kW when 1 mW of input power is supplied by the pulse bridge. The pulse control unit (PCU) on top of the bridge controls the output of the TOMCO by attenuation of the input power from the bridge. For the measurements

reported at 250 MHz in chapters 4 and 5, the pulse control unit was set so that the maximum power produced by the TOMCO at the resonator was 1.3 kW. The power output (under the same PCU conditions) varies with frequency (Fig. 7.15). A similar 2 kW amplifier from TOMCO was described in [11].

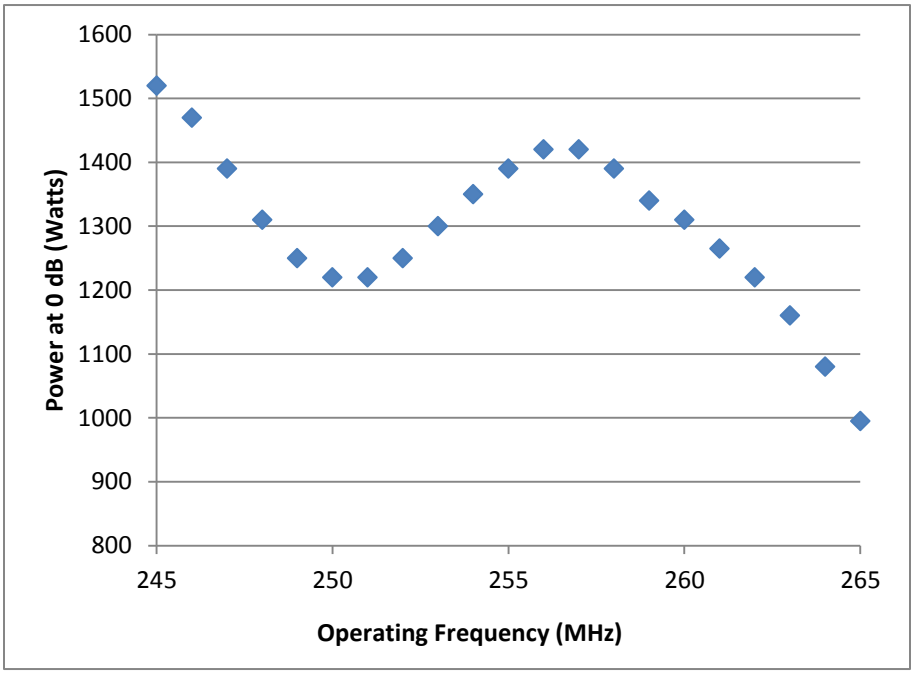

Figure 7.15 Output of TOMCO 4 kW amplifier between 245 MHz and 265 MHz. Output at 0 dB attenuation was measured with a calibrated power meter as a function of frequency. The variation in power output is common for RF amplifiers constructed for a range of operating frequencies.

7.6.2 Bruker BLAH-300 RF Amplifier

The BLAH300 is a NMR amplifier available from Bruker with a range of 180 to 600 MHz. It was tested by Bruker and shown to have output at 630 MHz, with rise and fall times of about 25 ns. The amplifier was tested in the Denver lab to determine potential utility for pulsed EPR at frequencies between 600 and 700 MHz.

Pulse timings created by a Bruker PatternJet were used to look directly at the output of the BLAH300 through attenuators to a 1 GHz bandwidth scope (Tek MDO4104-6), thereby avoiding the effect of the resonator. The Tek scope also has a spectrum analyzer (6 GHZ bandwidth) built in, so that one can measure the voltage signal and measure its spectral components simultaneously. The RF frequency was generated by mixing the standard 250 MHz (generated by a Fluke 6080A synthesizer) of the VHF spectrometer with a frequency of, e.g. 880 MHz from a Fluke 6082A synthesizer and taking the lower sideband.

The rise and fall times of the pulses and the maximum voltage of the attenuated output of the BLAH300 (as measured by the Tek Scope) were acquired. Estimating rise and fall times was complicated by the oscillations in the amplitude of the pulse. Different judgments about where to pick the 10 and 90 yielded different values. Output powers were measured with an HP436A power meter and 8481H power sensor, using a low pulse duty cycle. For "long" pulses (100-500 ns) the rise time was between 16 and 20 ns. For "short" pulses (40 ns) the rise time was measured as 9-10 ns. This shortened rise time is misleading. For such a short pulse duration, the amplifier did not reach full response, and only the approach to the first oscillation is observed in the pulse response.

At both 587 and 630 MHz, the length of the output pulse recorded on the scope did not match the pulse length input to the Bruker software. Output pulses were 20% shorter than requested at all attenuations except 0 dB. The lag could have originated from the XEPR software or the pulse forming unit, so the VHF pulse unit was connected directly into the scope to ensure sure the pulse signals generated was the same as being

requested in the software. Pulse lengths at all powers were <5% shorter than input into the software.

Fig. 7.16 shows the shape of a 40 ns pulse, and a "close up" at the beginning of a 500 ns pulse. The settling time on the 500 ns pulse was long and "bumpy". Oscillations on the pulse were also present at 587 MHz. At 630 MHz the Vpp for the 500 ns pulse was 4.6 V, and changed to 2.2 V when the pulse length was shortened to 40 ns, corresponding to a peak power of only 48 W. This power was not sufficient for a $\pi/2$ turning angle at 40 ns. Both the 500 ns and 40 ns pulse lengths were recorded at 0 dB attenuation setting on the pulse bridge. The output signal from the amplifier was attenuated by 50 dB before the signal was acquired with the Tek scope.

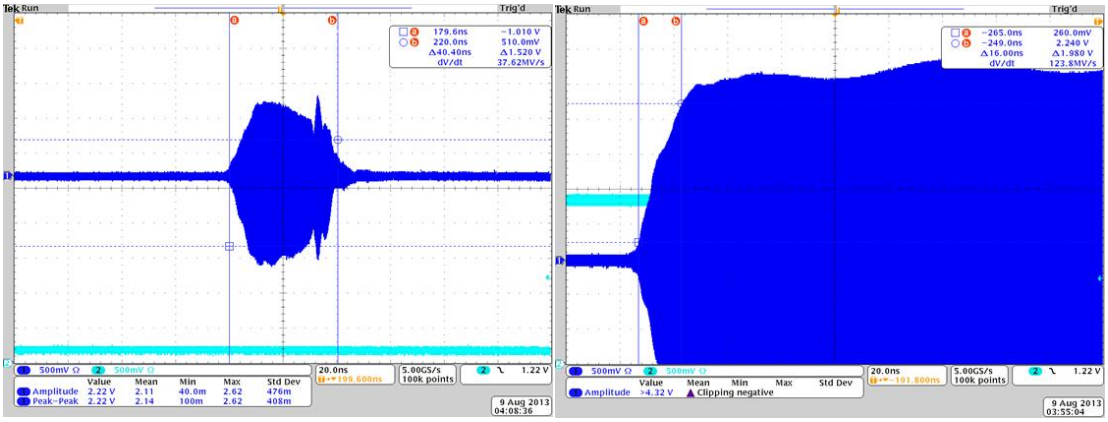

Figure 7.16 Short rectangular pulses on BLAH-300 amplifier. The whole of a 40 ns pulse is shown (top), and a fraction of a 500 ns pulse (bottom).

The output power as a function of input attenutation was roughly linear until 7 dB attenuation at 587 and 630 MHz (Fig.7.17). From here the power level saturates resulting in a max power of 300 W at 587 MHz and only 150 W at 630 MHz. The loss of

maximum output power is approximately 5 W/MHz past an operating frequency of 600 MHz (Fig. 7.18)

Massive shifts in baseline of both field swept echo detected spectrum and echo decay traces were present for 2-3 hours if the instrument had been cold for two or more days, requiring a "warm up" time before signal acquisition could begin. If the amplifier was operated on consecutive days, the warm up time was ca. 30 minutes. The baseline shifts add uncertainty to the measurement of short relaxation times (i.e. nitroxides) or to samples with limited stability (i.e. semiquinones).

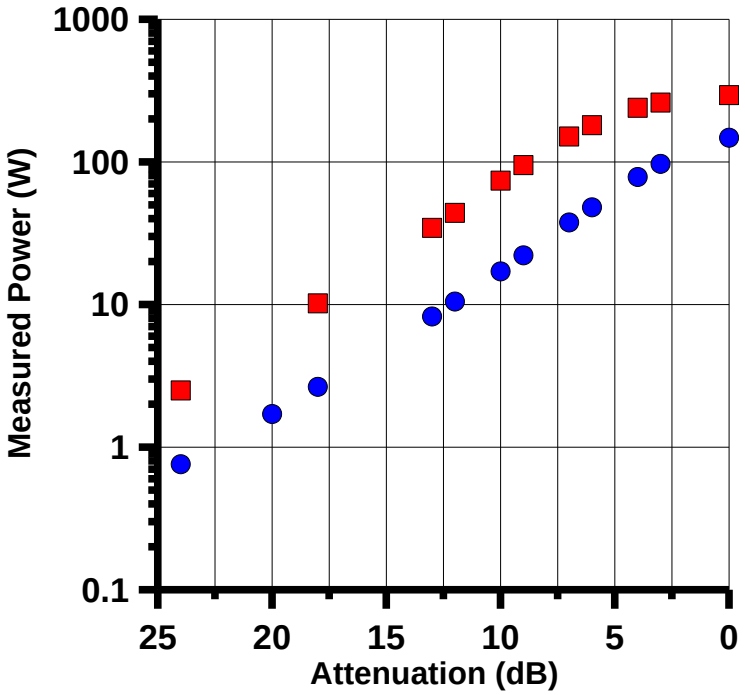

Figure 7.17 BLAH-300 amplifier linear power regions at 587 and 630 MHz. Power output was measured with a calibrated power meter at each frequency. The output power is linear until 7-8 dB in both cases. The maximum power output at 587 MHz (■) is 300 W, while at 630 MHz (●) the output is only 150 W. The attenuation is of the input to the amplifier.

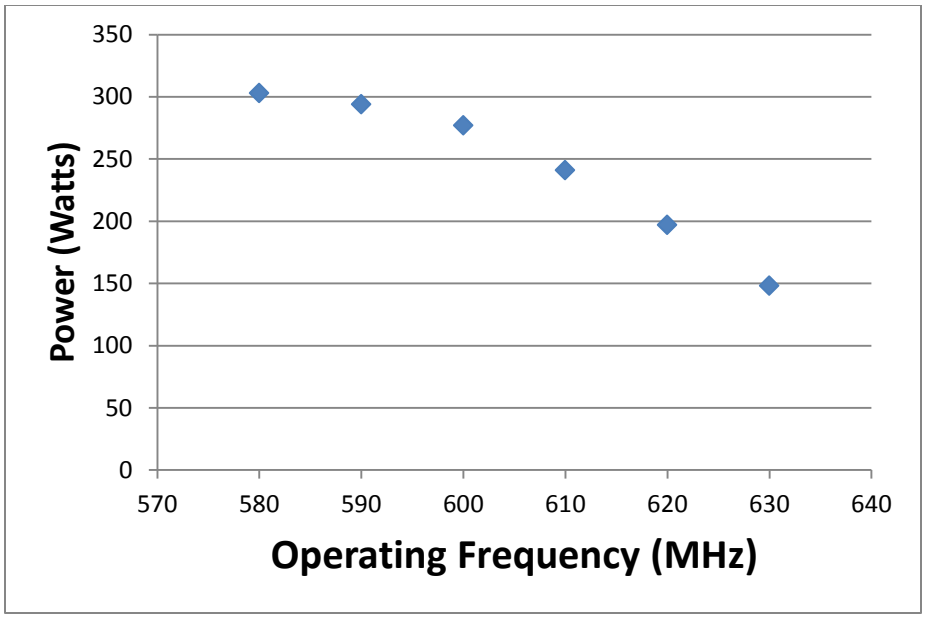

Figure 7.18 Output of BLAH-300 amplifier from 580 to 630 MHz. Power output was constant and measured with a calibrated power meter at each frequency with 0 dB on the bridge attenuator setting.

The Tektronix 1 GHz bandwidth oscilloscope with spectrum analyzer capabilities (Model MDO4104-6) allowed acquisition of RF vs time displays (Figure 7.19). At 630 MHz there is distortion of pulse shape for $\pi/2$ = 100,200 and 500 ns (Fig. 7.19 B,C,D). For $\pi/2$=40 ns (Fig. 7.19 A), the distortion is less conspicuous since the Bruker amplifier cannot reach full response in the short pulse time.

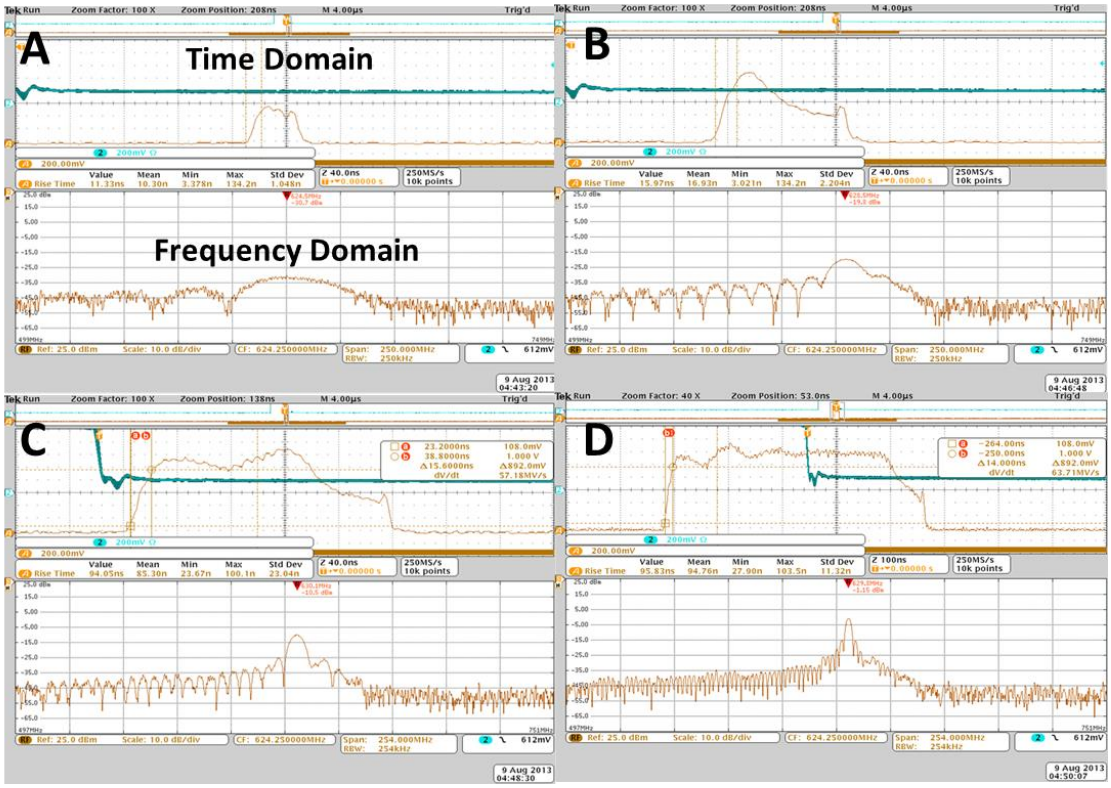

Figure 7.19 BLAH-300: Time and frequency domain displays of pulses at 630 MHz. A Tektronix scope equipped with a spectrum analyzer was used to observe the output of the Bruker amplifier at pulse widths of 40 ns (A), 100 ns (B), 200 ns (C) and 500 ns (D). In the time response of the RF amplitude and the bandwidth of the pulse are simultaneously plotted as identified in (A)The span of the spectrum analyzer is 250 MHz centered on 630 MHz.

Measurements of the amplifier output were made without the use of a resonator, representing a best case scenario. Given the sharp loss in power above 600 MHz, the Bruker 300 W amplifier was not an appropriate choice for pulse measurements in the range of 600-800 MHz, which was technically outside the specified range of the amplifier. The shape of the output pulses would make it difficult to properly define input pulse shapes that would compensate for resonator Q and increase spectral excitation bandwidth.

7.6.3 TOMCO 400 MHz – 1 GHz RF Amplifier

The TOMCO 400 MHz-1 GHz amplifier was evaluated at frequencies of 586 MHz and 698 MHz. According to the final test results from TOMCO, the peak power output at 0 dB is 480 W at 600 MHz, and 435 W at 700 MHz.

Testing in the Denver lab used pulse timing created by a PatternJet and measured the output of the amplifier through attenuators (total of 50 dB) to a 1 GHz bandwidth scope (Tek MDO4104-6). The RF frequency was generated as described in Sec. 7.4.2 Pulses of 12 ns to several hundred ns were created by the PatternJet. The rise and fall times and the maximum voltage of the attenuated output of the amplifier were measured.

At a pulse length of 200 ns, the magnitude of the amplifier output (in mV, after attenution) was measured as a function of power. The signal measured in mV_{pp} was converted to V_{pp} converted and then to V_{rms}. The power into a 50 Ohm load can be calculated by equation (7.7).

$$Power\ (Watts) = \frac{V_{rms}^2}{50\ \Omega} \qquad (7.7)$$

The power output from the TOMCO is calculated by correcting for the 50 dB of attenuation between the amplifier and the scope. The first system was first set to operate near 600 MHz. The pulses shown in Fig. 7.20 were collected at 586 MHz with 1 dB of attenuation in the bridge, and both have rise times ca. 5-10 ns

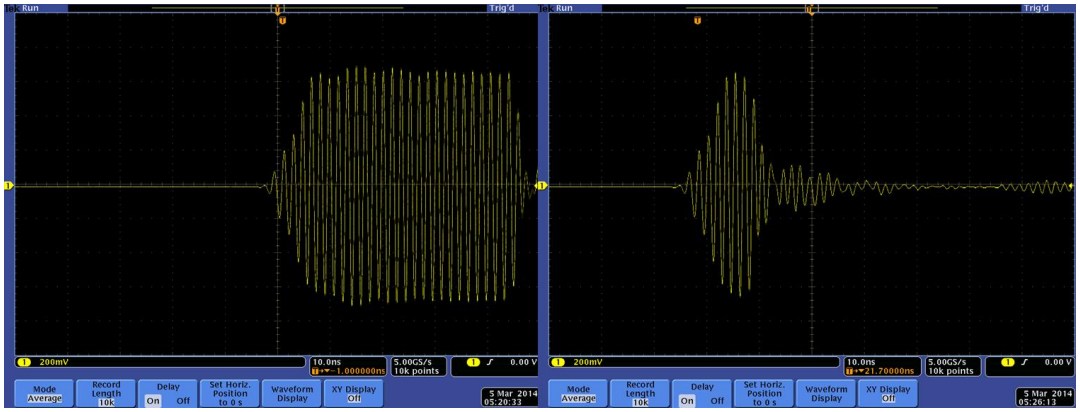

Figure 7.20 TOMCO 400 MHz-1 GHz amplifier: RF pulse at 586 MHz. Pulse lengths are 52 ns (left) and 16 ns (right).

The shape of the 40 ns pulse from the BLAH300 amplifier (Fig. 7.16) was distorted in comparison to the 52 ns pulse (Fig 7.20) from the TOMCO amplifier. The comparison was at essentially the same frequency (586 vs. 587 MHz). The 16 ns pulse from the TOMCO (Fig 7.20, right) rose and fell symmetrically in contrast with the 40 ns pulse for the BLAH-300 amplifier (Fig.7.16). At an attenuation of 9 dB (ca. 60 W) there was sufficient power to optimize echo amplitude with this short pulse length.

An interest from the Chicago group in pulse trityl imaging at 700 MHz led to further characterization at that frequency. The increase in T_1 from 250 MHz to 600 MHz (see Fig. 7.11) would offer better signal to noise (though penetration depth would be sacrificed). The pulse shapes in Figures 7.21 were recorded under 12 dB attenuation at 698 MHz (ca. 27 W). Rise times were about 10 ns.

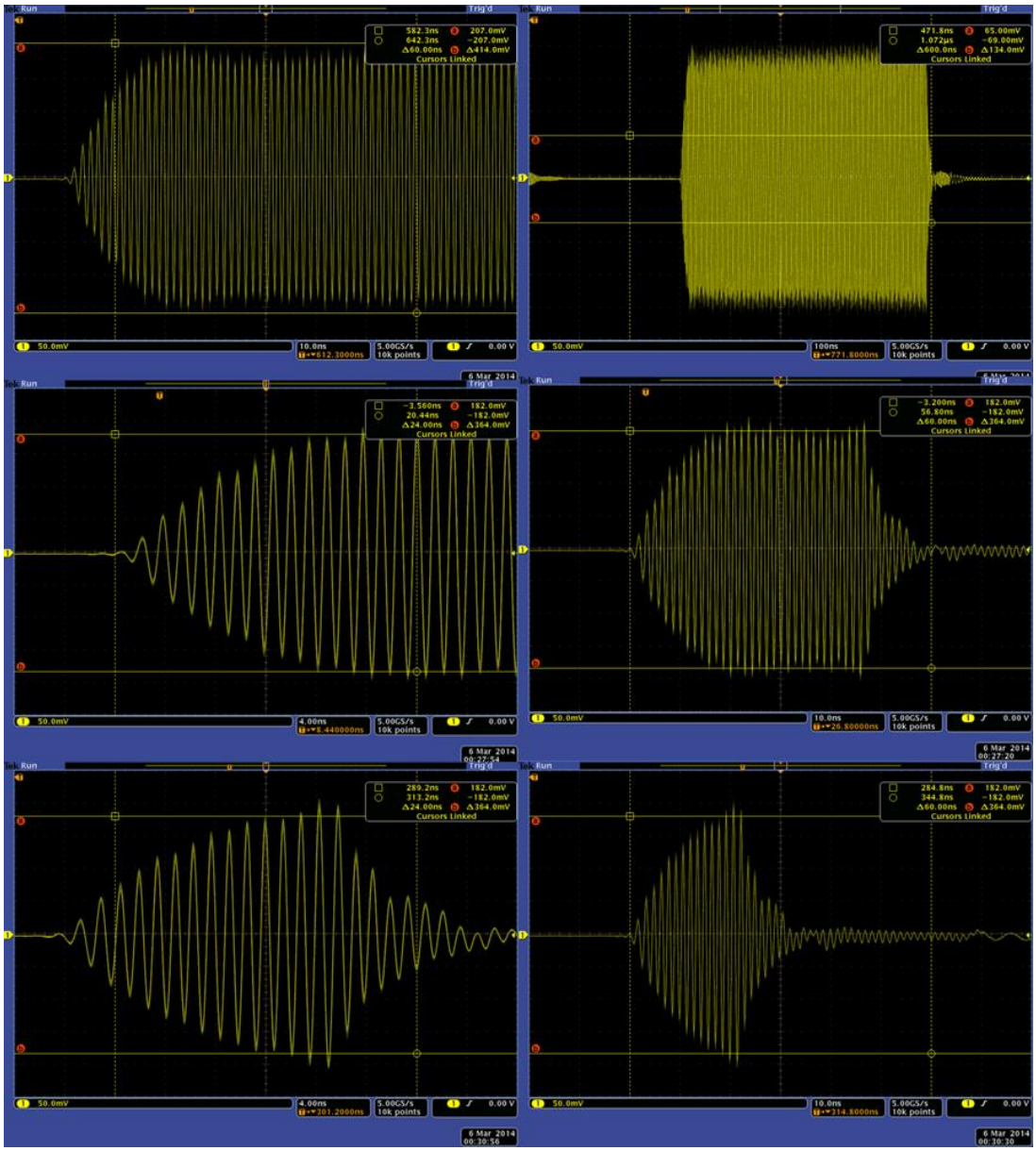

Figure 7.21 TOMCO 400 MHz-1 GHz amplifier: RF pulse at 698 MHz. The full pulse is shown on the right hand side, and an expanded view is shown on the left for estimation of rise time. Pulse lengths are 512 ns (top), 52 ns (middle) and 24 ns (bottom).

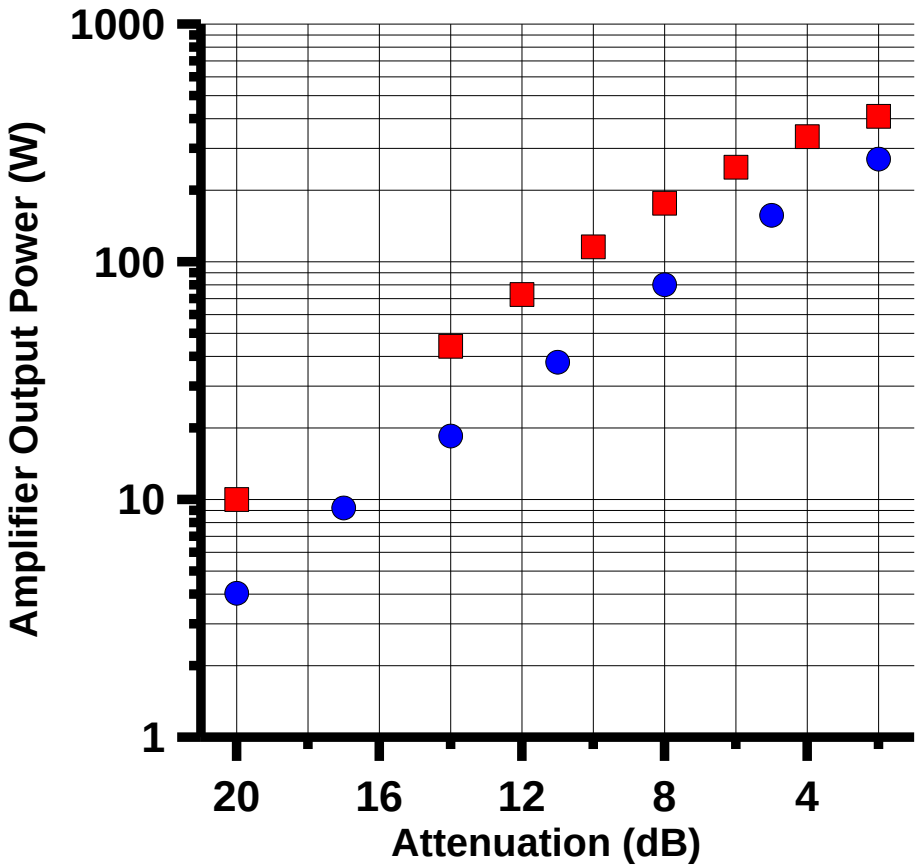

Figure 7.22 TOMCO 400MHz/1GHz: Linear power regions at 586 amd 698 MHz. Power delivered at 586 MHz (■) and 698 MHz (●).

For the amplifier power output vs. input attenuation (Fig. 7.22), the response was measured on the Tek scope. For every 6 dB change in attenuation, an increase of 2x was expected in the height (measured in mV) of the signal on the scope. In contrast with the BLAH300 amplifier at 587 and 630 MHz (Fig. 7.17), the TOMCO amplifier only began to saturate slightly around 6 dB attenuation at 586 MHz. At 698 MHz, the power output appeared to be linear up to the last measured point of 2 dB attenuation.

For both the BLAH300 and TOMCO 400MHz-1GHz amplifiers, two-pulse echoes from a standard trityl sample were recorded to compare echo amplitude vs. pulse length and delivered power. Information regarding these tests are in single page “spec-sheets” in

Appendix C, along with a blank template spec-sheet for use with characterization of future RF amplifiers.

7.7 Testing Of High Power Amplifiers For Rapid Scan

7.7.1 High power RF amplifier for rapid scan experiments

In the rapid scan experiment, spins spend less time on resonance in comparison with a continuous wave experiment. This allows for higher incident power (with an increase in signal-to-noise) at increasing scan rate of the experiment. To provide high operating powers to capitalize on the "rapid-scan" effect, a high power amplifier was developed for the VHF rapid-scan system. Since the RF is applied continuously during the experiment, lower noise characteristics are required than for high power pulse amplifiers. The first amplifier tested was manufactured by RF Bay, and had a maximum output of 5 W, but the amplified scan current was noisy and an enormous rapid-scan background was observed. A second amplifier, nominally 7 W, was purchased from Mini-Circuits and delivered a clean signal with a much smaller observed background signal. The actual measured output of the amplifier at 0 dB is 10 W.

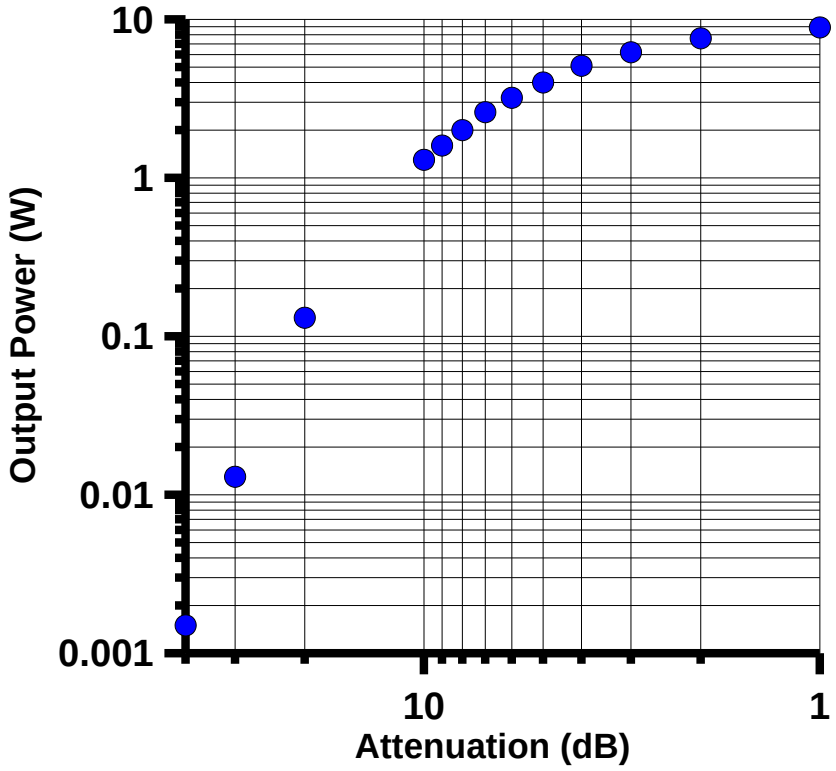

Figure 7.23 Rapid Scan 7 W Amplifier: power output at 250 MHz is linear until about 10 dB attenuation (1.3 W), as the power measured at 20 dB was 130 mW.

Figure 7.23 shows the power output for the amplifier at attenuator settings from 40 to 0 dB. The output power at each attenuation was recorded directly into a power-meter with a 3W probe. A 10 dB attenuator was placed between the amplifier output and powermeter to stay within the linear region of the probe. The amplifier was also tested with resonator CLR-DU-4, to see how much power could be input to the resonator before leakage to the detection resonator overwhelmed the detection system. The reflected power at the rapid scan bridge was used as a readout of the isolation between the power and detection resonators. The detection system can become overwhelmed when isolation results in > 0 dBm on this readout. Up to 2.6 W incident on the resonator the reflected power remained stable. From 3.2-5.1 W the reflected power reading was not stable and

quickly rose to 0 dBm reflected power. The loss of isolation is likely due to heating of the resonator by the high incident powers. The rapid scan amplifier has also been used routinely with resonator CLR-CH-3, which is a higher efficiency resonator and was not designed for the same levels of incident power as CLR-DU-4. For short amounts of time, CLR-CH-3 can be used with up to 1 W of incident power without changing the isolation. CLR-CH-3 was routinely used with powers of 850 mW or less where the isolation was very stable.

7.7.2 Rapid Scan Resonated Coil Driver(s)

Of the five coil-driver types available in the DU lab, RCD 2B and RCD 3 were used most extensively for development of the rapid scan imaging in Chapter 6. During the rapid-scan experiment, a trigger is used by the RCD to synchronize data collection by the digitizer (SpecJet II) in the Bruker system. RCD3 triggers once every cycle, whereas RCD2B has an option to trigger one time every "n" cycles. At the high powers available from the amplifier described in 7.5.1, and at the largest imaging gradients where the EPR signal is smallest, the trigger signal is sufficient in amplitude to become a "glitch" which distorts the image. To overcome this problem one trigger from RCD2B could be used for the number of cycles to be collected up to 256. The number of rapid scan cycles is calculated by equation (7.8).

$$Cycles = Scan\ Freq.\,(Hz)\ x\ Timebase\ (ns)\ x\ Number\ of\ Points \qquad (7.8)$$

If the calculated number of cycles was an integer number, the trigger could be set to that number of cycles exactly. Usually the number of cycles was not an integer number, so the trigger was set to the next highest cycle count.

A major contribution to the rapid scan background signal was discovered accidentally when comparing coil drivers RCD2B, RCD2A and RCD3 under high RF power conditions with the wide sweep coils (28 G/A). Figure 7.24 shows the difference between the background amplitude, which seemed to stem from the power amplifiers in each unit. RCD 2B was built with power amplifier PAD 111, while 2A was built with PAD 135.

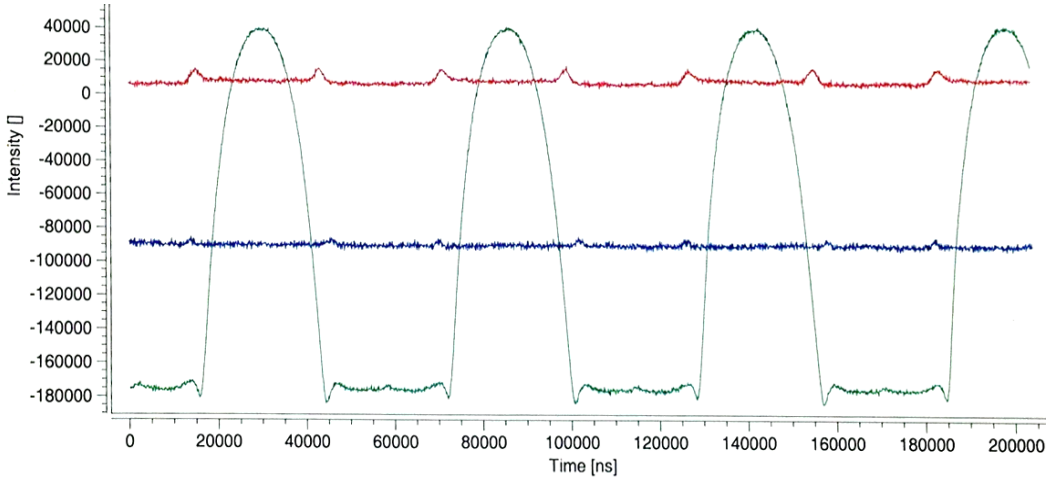

Figure 7.24 Rapid scan background signal as a function of power amplifier chip. Initial tests between RCD 2B (red) and RCD 2A (green) showed large differences in background signal (raw rapid scan data). Upgrading the amplifier in RCD 2A to the PAD 111chip (blue) eliminated the large background signal.

For the spectra in Figure 7.24, experimental parameters were the same, but the difference in background signal for RCD2A with PAD135 amplifier (Fig. 7.24, green trace) compared with RCD2B with the PAD 111 amplifier (Fig. 7.24, red trace) was striking. RCD2A was retro-fitted with a PAD111 amplifier, and the observed background

signal improved dramatically (Fig.7.24, blue trace). RCD3, which was also originally constructed with a PAD135 amplifier was retrofitted with the PAD11 as well, and showed a similar decrease in the background signal amplitude.

7.8 Summary

Development of pulse amplifiers and resonators is robust, and future characterization of amplifier specifications and resonator efficiencies serves to inform the operator of the correct set of conditions for a particular pulse experiment. The ability to measure relaxation times between 250 MHz and 1 GHz with CLR-DU-6 and CLR-DU-8 is exciting. The work in chapters 4 and 5 shows relaxation contributions can be varied and change quickly in this span of only 750 MHz. It will be important to continue comparison of scaling pulse resonators by looking at CLR-DU-6 and CLR-DU-7, since the *in vivo* collaborators in Chicago continue to put an emphasis on pulse EPR imaging.

A major contribution to the commercial development of rapid scan will be quantitative characterization of resonators, coil drivers and power amplifiers. Design of rapid scan resonators has focused on different themes from 2009 to 2014. From 2009-2011 the focus was different structural support for fine wire detection resonators (CLR-DU-1, CLR-DU-2). From 2011 into 2013 the focus was making the power resonator more robust, to increase the incident power which could be applied (CLR-DU-3, CLR-DU-4). Most recently we have turned towards mitigating the background signal so it does not overwhelm the EPR signal (CLR-CH-2 and CLR-CH-3). The sensitivity of rapid scan for *in vivo* imaging will be directly tied to the ability to suppress background signal in the

rapid-scan resonators. Fortunately the background which is coherent with the rapid scan experiment is derived from some feature of the resonator which can be changed, so that continued study of resonator design vs. background signal will most assuredly result in a more powerful rapid-scan technique.

7.9 References

[1] G. A. Rinard, R. W. Quine, G. R. Eaton and S. S. Eaton, "250 MHz Crossed-Loop Resonator for Pulsed Electron Paramagnetic Resonance," *Concepts Magn. Reson.,* vol. 15, no. 1, pp. 37-46, 2002.

[2] G. A. Rinard, R. W. Quine, B. T. Ghim, S. S. Eaton and G. R. Eaton, "Easily tuneable crossed-loop (bimodal) EPR resonator," *J Magn. Reson. A,* vol. 122, pp. 50-57, 1996.

[3] G. A. Rinard, R. W. Quine, J. R. Biller and G. R. Eaton, "A Wire Crossed-Loop-Resonator for Rapid Scan EPR," *Concepts Magn. Reson.,* vol. 37B, pp. 86-91, 2010.

[4] M. Tseitlin, G. A. Rinard, R. W. Quine, S. S. Eaton and G. R. Eaton, "Deconvolution of Sinusoidal Rapid EPR Scans," *J. Magn. Reson.,* vol. 208, no. 2, pp. 279-283, 2011.

[5] R. W. Quine, D. G. Mitchell and G. R. Eaton, "A General Purpose Q-Measuring Circuit Using Pulse Ring-Down," *Concepts Magn. Reson.,* vol. 39B, no. 1, pp. 43-46, 2011.

[6] M. Huisjen and J. S. Hyde, "A pulse EPR spectrometer," *Rev. Sci. Instrum.,* vol. 45, pp. 669-675, 1974.

[7] G. A. Rinard, R. W. Quine, G. R. Eaton and S. S. Eaton, "250 MHz crossed-loop resonator for pulsed electron paramagnetic resonance," *Concepts Magn. Reson.,* vol. 15, no. 1, pp. 37-46, 2002.

[8] M. M. Kundalika, G. R. Eaton and S. S. Eaton, "Determination of T_1 and T_2 by Simulation of EPR Power Saturation Curves and Saturated Spectra. Application to Spin-Labeled Iron Porphyrins," *J. Magn. Reson.,* vol. 60, pp. 54-65, 1984.

[9] R. Owenius, G. R. Eaton and S. S. Eaton, "Frequency (250 MHz to 9.2 GHz) and viscosity dependence of electron spin relaxation of triarylmethyl radicals at room temperature," *J. Magn. Reson.,* vol. 172, no. 1, pp. 168-175, 2005.

[10] V. S. Subramanian, B. Epel and H. J. Halpern, "Orthogonal resonators for pulse in vivo electron paramagnetic imaging at 250 MHz," *J. Magn. Reson.,* vol. 240, pp. 45-51, 2014.

[11] R. W. Quine, G. R. Eaton and S. Dillon, "Fast-response VHF pulsed 2 kW power amplifiers," *Concepts Magn. Reson.,* vol. 29B, no. 4, pp. 185-190, 2006.

CHAPTER 8

SUMMARY AND COMMENTS ON FUTURE WORK

8.1 Review

The development of EPRI over the past twenty years has been amazing. The topics covered in Chapters 3-7 are small pieces in the context of the overall effort, and summarize the stories we are fairly confident about. In this final chapter, one example of the "next step" for each chapter topic from 3-7 is given. The hope is for a presentation of continuity, from where we have been, to the exciting places we have yet to explore.

8.2 Spin-Packet Linewidth, Experimental-Linewidth And Signal Intensity

Chapter 3 shows how complicated the relationship between observed linewidth, and true spin-spin relaxation time (T_2) can be. An interesting comparison is made between nitroxides ^{14}N and ^{15}N PDT (**1a, 1b** in Chapter 3) and the trityl radical Ox63 (**6,** base structure given in Fig. 1.2), all of which have $\Delta B_{pp} \sim 0.16$ G. For **1a** and **1b** the ΔB_{sp} = 0.09 G and 0.07 G, respectively. The isotropic couplings to the deuterons of the four gem-dimethyl groups are relatively small, so ΔB_{sp} and ΔB_{pp} differ only by about a factor of two. For **6** the ΔB_{sp} is ~ 0.005 G at X-band [1] , but the isotropic hyperfine is non-zero for many spins, so the line is broadened substantially and $\Delta B_{pp} >> \Delta B_{sp}$. Figure 8.1 shows power saturation curves at X-band for **1a, 1b** and **6**. Spectra for all three were

recorded with the same gain settings and parameters on a Bruker EMX spectrometer. At low powers, the signal from **6** is clearly larger than from **1a.** About 70% of the spectral intensity is present for the "single" line of **6**, compared to only 33% in the center-field line of **1a** and 50% in the low-field line of **1b**. At high powers the signal from **1a** and **1b** are more intense than for **6**. Since T_1 of **6** is an order of magnitude longer than for **1a** and **1b,** saturation begins to impact signal amplitude at much lower powers. The shorter T_1 of **1a/1b** results in signal linearity with higher power compared to **6**. The result at high power is higher signal intensity for **1a**/**1b** than for **6**, because the T_1 of **6** is much longer than **1a/1b**. A central question for EPRI is "which radical gives the largest signal?" In order to answer, one must have knowledge of the conditions of the experiment, the observed ΔB_{pp} and the inherent ΔB_{sp} of the radical. Blanket statements of one radical type being the "best" under all conditions should be avoided. Instead, careful study of radical types will allow scientist to match the most appropriate radical to the EPRI technique required.

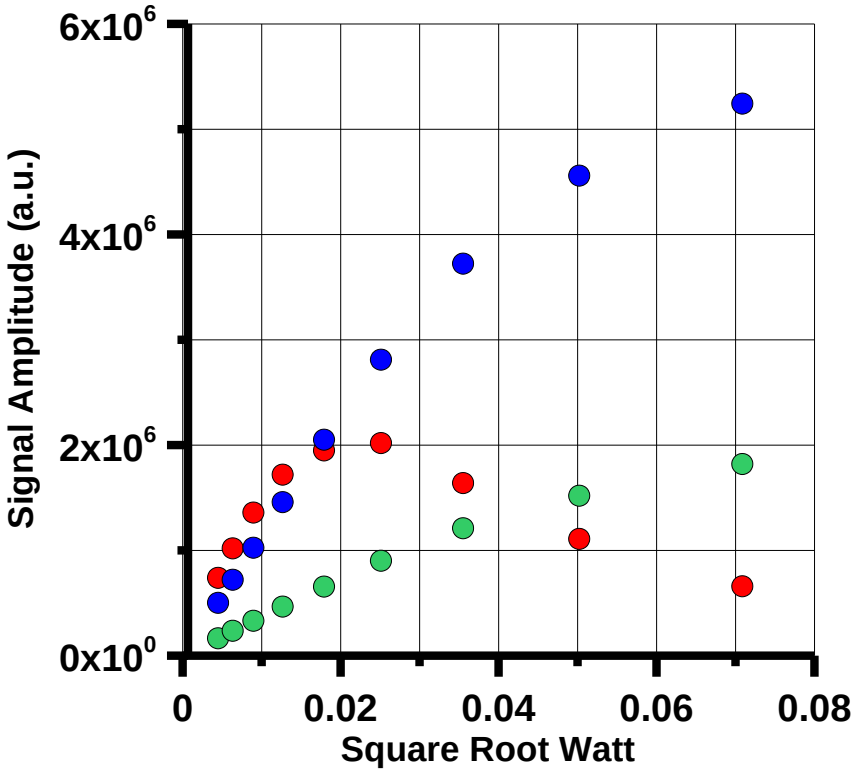

Figure 8.1 Power saturation curves at X-band. Data was collected on an EMX spectrometer with gain, modulation amplitude, time constant, conversion time, sweep time and sweep width kept the same for each radical. Plots of the signal amplitude as a function of the square root of power are given for **1a** (Ch. 3) (●), **1b** (Ch. 3) (●) and **6** (Ch.1) (●). Concentrations of **1a** and **1b** were 0.25 and 0.24 mM, respectively, while the concentration of **6** was 0.19 mM. Signal intensity for **1a** and **1b** was scaled to take into account the difference in concentration.

8.3 Tumbling Correlation Times For Nitroxides With Two Nitrogen Nuclei

The nitroxide tumbling correlation time modulates contributions to relaxation from spin rotation (Eq.3.3) and the modulation of A-anisotropy (Eq.3.3-3.5). In order to double check the tumbling time for the nitronyl radical (**2)** found in Sec. 4.3.2, the Denver lab collaborated with Dr. Stefan Stoll at the University of Washington to develop a simulation method for nitroxides with two nitrogen nuclei, similar to the theory for nitroxides with one nitrogen nucleus developed by Daniel Kivelson [2]. Dr. Stoll has

created and maintains the EasySpin© simulation software used by many in the EPR community.

Modeling uses parameters measured in the rigid-limit where the anisotropic parameters can be observed and also in the fast-motion regime where isotropic couplings are observed. By matching experimental data from 100 K to 300 K for the radical with simulations, an empirical model can be developed for how changes in τ_R average anisotropies in the spectrum of **2**. Components of the spectrum due to g-anisotropy have larger field separation as the frequency is increased, so CW spectra were recorded at both X-band and Q-band. From the empirical model a new simulation can be developed to calculate τ_R for radicals like **2**.

As described in Sec. 4.2.1 the acetoxy ester of the nitronyl radical is dissolved in NaOH to produce the EPR active **2**. During preliminary experiments, a basic solution of **2** was simply combined 1:1 with 100% glycerol (added as a super-cooled glass-forming agent), yielding a solution that was ca. 0.25 mM in **2** and 50% glycerol. Under these conditions, values of T_1 for **2** were ca. 250 μs. The CW spectrum suffered badly from passage effects, and resembled a field-swept-echo-detected spectrum (Fig. 8.2). Passage effects are observed when the modulation frequency (1/100 kHz = 10 μs) is fast relative to the spin lattice relaxation rate, $1/T_1$ (1/250 μs = 4 kHz). Distortions are greater when the signal is also power saturated.

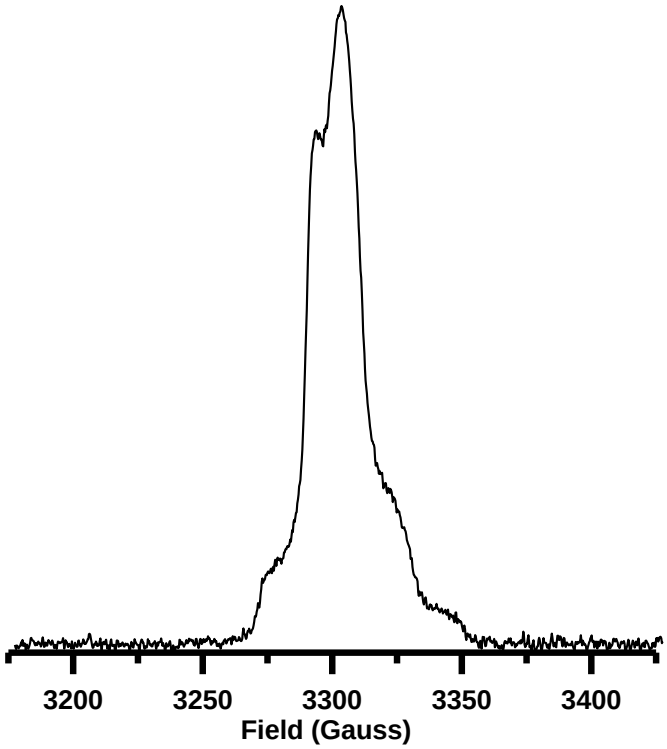

Figure 8.2 CW spectrum of nitronyl radical (2) in 1:1 H_2O:glycerol at 100 K at X-band. Modulation frequency is 100 kHz with 0.5 G modulation amplitude. 250 G sweep width in 41.9 seconds and 1024 points. Time constant = conversion time = 41 ms. Power incident on the resonator was 0.22 mW in this spectrum. The distortion was still present at incident powers of 0.022 mW.

In order to get well resolved CW spectrum free of passage effects, the T_1 would have to be shortened. At the same time, the T_2 must remain relatively unchanged so the amplitude of the CW signal is not reduced. This was accomplished by addition of ca. 30 mM $Er(NO_3)_3$ salt. (The details of why this lanthanide was selected over others will be found in the dissertation of fellow graduate student P. Aggarwal). Lanthanide salts precipitate out of solution at pH $\geq$ 6, and nitroxides decompose in strongly acidic solutions, which complicated the preparation. Unlike many nitroxides, **2** has a deep violet color which served as a good indicator of how low the pH could be adjusted while retaining some of the radical. Eventually a solution $\leq$ 0.3 mM in **2**, 50% glycerol, 30 mM

in $Er(NO_3)_3$ at pH = 4 was made up and analyzed at Q-band (Fig. 8.3) and X-band (Fig. 8.4). In the presence of the lanthanide, T_1 was between 20 and 40 μs (dependent on m_I), while T_2 remained ca. 2μs, as it was in the absence of the lanthanide.

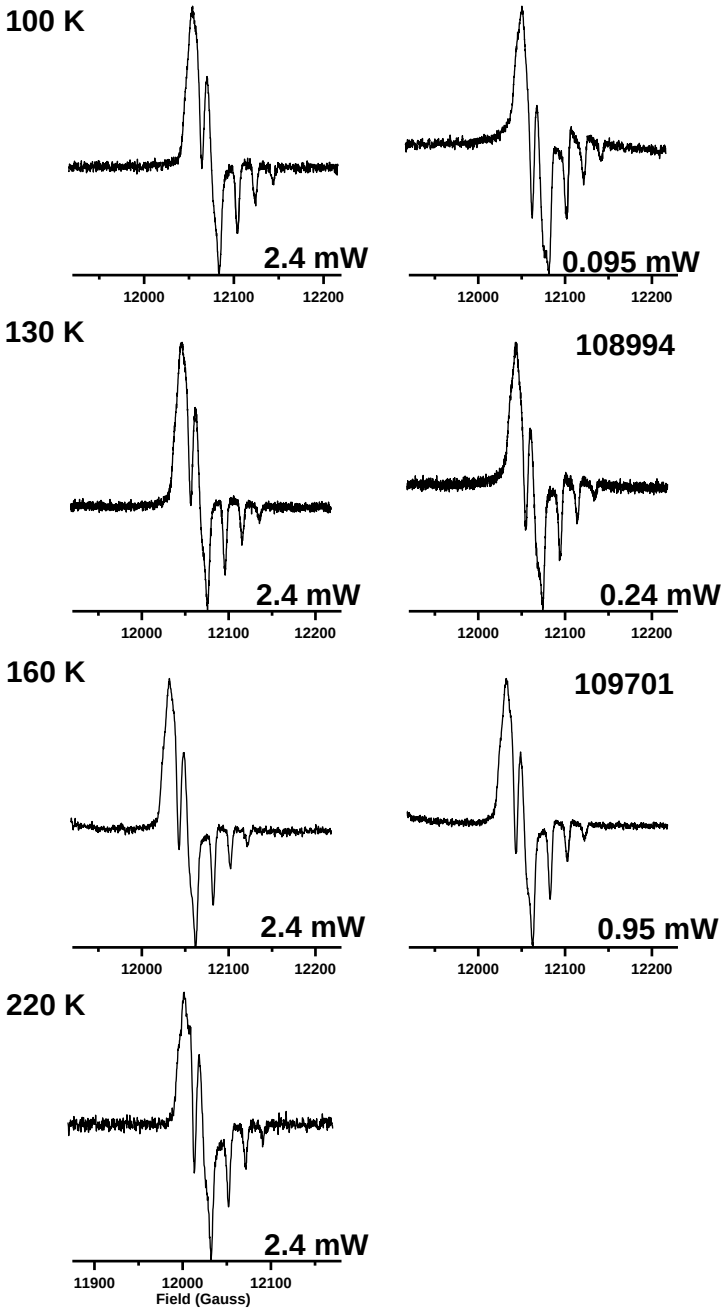

Figure 8.3 CW Spectra for 2 in the presence of lanthanide at Q-band. Small amounts of lineshape distortion can still be observed between high power (left) and lower power, (right).

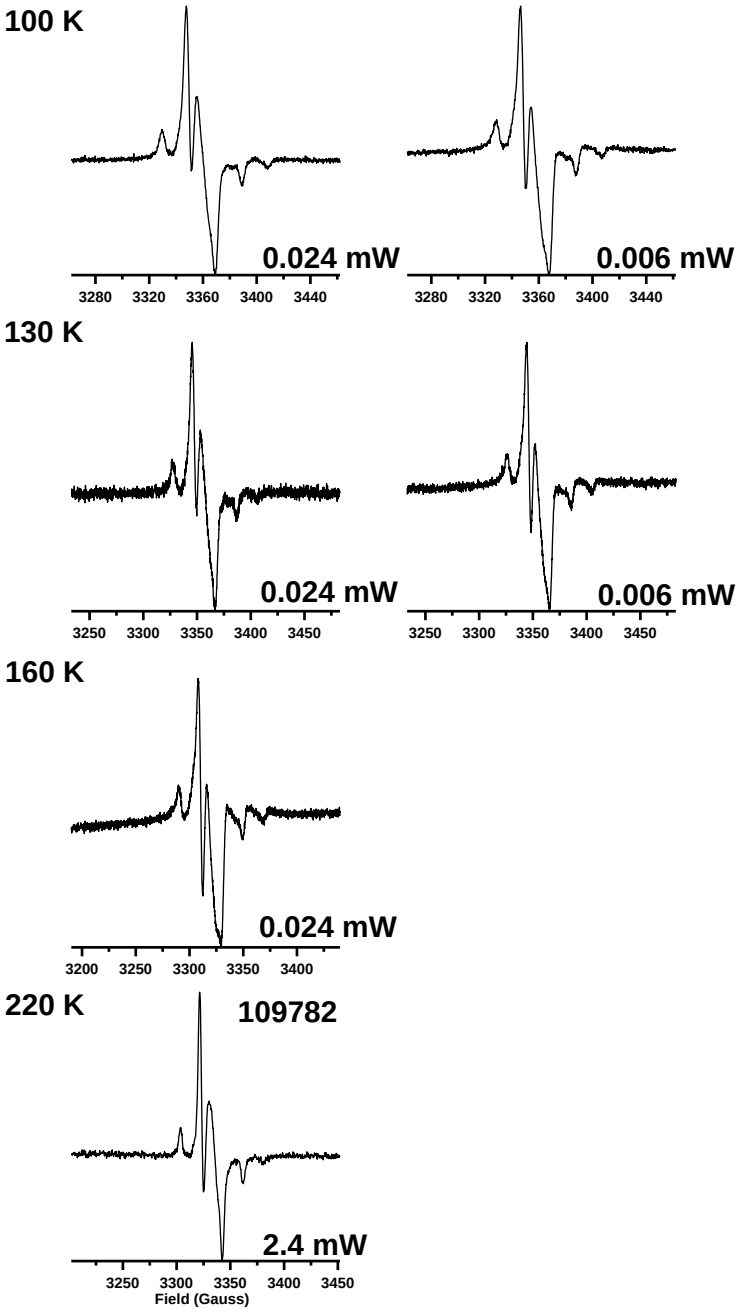

Figure 8.4 CW Spectra for 2 in the presence of lanthanide at X-band. Small amounts of lineshape distortion can still be observed between high power (left) and lower power, (right).

At the time of this dissertation, Dr. Stoll is working on developing a two-nitrogen model for determining tumbling correlation time based on the data collected at the University of Denver.

8.4 The Longest Nitroxide T_1 In The Rapid Tumbling Regime

The models for relaxation mechanisms that contribute to T_1 were tested against T_1 values for a wide range of nitroxide radicals, with different structures and hyperfine values, and in different solvents in chapters 4 and 5. Assuming radicals similar to the *t-butyl*-pyrrolidine radical in chapter 5 (**6)** can be synthesized, Table 8.1 gives an estimate of how T_1 can be increased for τ_R = 20 and 100 ps. The range of τ is an approximation of what may be characteristic of probes in a variety of *in vivo* environments. The modeling suggests an order or magnitude increase in T_1 could be achieved by synthesizing *in vivo* probes to be like **6** rather than radical ^{14}N-PDT (**1a)**. Slowing the tumbling decreases the contribution from spin rotation for both **1a** and **6**, but at longer τ the T_1 of **1a** decreases due to a larger contribution from the END mechanism. For radicals like **6** where the contribution from A-anisotropy is reduced, the contribution from the END mechanism is smaller in comparison to radicals like **1a.** No thermally activated process was included for the modeling of **6** in Table 8.1. Values of T_1 for **6** at frequencies between 34 GHz and 1.5 GHz indicate that it is not impacted by the same thermally-activated process assigned to radicals **1-3** (Chapter 3,4,5). In the absence of a thermally activated process and absent a large contribution from the END mechanism, it's possible some other mechanism, like generalized spin diffusion (GSD), could be observed for radicals like **6**. Further research

is warranted, due to the very large and positive impact this line of work could have on the design and synthesis of spin probes for *in vivo* EPRI.

Table 8.1 Predicted Values of T_1 in μs[a].

Frequency(GHz)	**1a**[b]		**6**[c]	
	20 ps	100 ps	20 ps	100 ps
34.5	2	6.3	2.5	12.5
9.5	0.67	2	2.2	10
2.5-3.0	0.4	0.4	2.2	5.0
1.5	0.4	0.15	2.2	2.0
0.25	0.5	0.13	2.2	1.7

[a] Using g- and A- values for **1a** and **6** from Table 5.1
[b] Assuming contributions from Eq.(3.2),(3.3-3.4),(4.1-4.2)
[c] Assuming contributions from Eq. (3.2), (3.3-3.4), (4.1)

8.5 The Rapid Scan Background

In chapter 7, Figure 7.24 highlights the rapid scan background described in section 7.1.2 induced by the rapidly changing magnetic field. Within the Eaton lab we have made a series of fortunate discoveries that lead to instrumentation changes which decreased the background. The background signal at 250 MHz increases with sweep width, power and magnetic field setting, though not linearly. The causes are likely many and inter-connected. The improvements made in reducing the rapid scan background have already led to the ability to image concentrations of radicals ca. 5-10 μM and allowed full-spectrum data collection of nitroxides and other hyperfine-split spectra for image reconstruction. The systematic characterization of this background signal at wider sweep widths, and mitigation through resonator or coil driver design will be the single largest future improvement to the rapid scan technique. It is hoped that quantitative measures,

such as the mechanical resonance scans described in Section 6.2.3 will aid completion of this goal.

8.6 Final Thoughts

This dissertation is the result of two projects I was introduced to in April of 2009, involving selection of the best probe for EPRI, and extension of the capabilities for the 250 MHz pulse EPR system constructed in the Denver lab.

The first project concerned ^{14}N vs. ^{15}N nitroxides, and determination of which would be better for imaging at frequencies < 1 GHz. Isotopic substitution with ^{15}N and ^{2}H gave a smaller ΔB_{pp} in CW experiments [3] [4], but this was an expensive and time consuming modification. Isotopic substitution was driven by the fact that for CW experiments, only one of two (^{15}N) or three (^{14}N) lines could be used. At the very low frequencies for *in vivo* EPR, it was possible that Breit-Rabi shifts within the ^{14}N and ^{15}N lines would make one of the m_I narrower than the others, and better for imaging. I spent a lot of time taking careful CW measurements and modeling the contribution from unresolved hyperfine to see if we could "eek" out just a little more signal intensity. These studies, along with relaxation time measurements at X-band, became the basis for Chapter 3.

The second project concerned pulse EPR measurement of nitroxide radicals at 250 MHz. This task was difficult, but it forced me to *really* learn how a pulsed experiment works, from a timing and instrument perspective, which is the basis for Sec. 2.6. Pulse EPR capabilities at 250 MHz facilitated the multi-frequency measurements in

Chapters 4 and 5, and opened the door to a completely new understanding of what contributed to the T_1 and T_2 of the nitroxide radicals. There is another set of nitroxides whose relaxation times are being measured in the lab currently by graduate student Laura Buchanan. These nitroxides differ in structure from many of those in Chapter 4 and 5, in the ways that we have suggested would increase T_1. Preliminary measurements do show much longer T_1 values, but I will let you look forward to *how much longer* as part of the story Laura will tell.

The rapid-scan experiments in Chapter 6 showed the superiority of the technique, in comparison to CW, for fast relaxing nitroxide probes. We have further developed the rapid-scan technique in a way that will revolutionize *in vivo* EPRI, which we are currently preparing for publication. Between our new rapid-scan imaging method for nitroxide probes, and the now well-developed pulse methods by the National Cancer Institute (NCI) for trityl probes, EPRI is primed for major contributions in pre-clinical and (eventually) clinical imaging applications.

"Lately it occurs to me,

What a long strange trip it's been"

Robert Hunter

8.6 References

[1] R. Owenius, G. R. Eaton and S. S. Eaton, "Frequency (250 MHz to 9.2 GHz) and viscosity dependence of electron spin relaxation of triarylmethyl radicals at room temperature.," *J. Magn. Reson.*, vol. 172, no. 1, pp. 168-175, 2005.

[2] D. Kivelson, "Theory of EPR [electron paramagnetic resonance] line widths of free radicals," *J. Chem. Phys.*, vol. 33, pp. 1094-1106, 1960.

[3] S. R. Burks, M. Makowsky, Z. A. Yaffe, C. Hoggle, P. Tsai, S. Muralidharan, M. K. Bowman, J. P. Kao and G. M. Rosen, "The Effect of Structure on Nitroxide EPR Spectral Linewidth," *J. Org. Chem.*, vol. 75, no. 14, pp. 4737-4741, 2010.

[4] S. R. Burks, M. A. Bakhshai, M. A. Makowsky, S. Muralidharan, P. Tsai, G. M. Rosen and J. Y. Kao, "2H, 15N-Substituted nitroxides as sensitive probes for electron paramagnetic resonance imaging," *J. Org. Chem.*, vol. 75, pp. 6463-6467, 2010.

BIBLIOGRAPHY

A. Bobko, I. Dhimitruka, T. D. Eubank, C. B. Marsh, J. L. Zweier and V. V. Khramtsov, "Trityl-based EPR probe with enhanced sensitivity to oxygen," *Free Rad. Biol. Med.*, vol. 47, no. 5, pp. 654-658, 2009.

A. Bobko, T. D. Eubank, J. L. Voorhees, O. V. Efimova, J. L. Zweier, I. A. Grigor'ev, A. Samouilov and V. V. Khramtsov, "In vivo monitoring of pH, redox status, and glutathione using L-band EPR of assessment for therapeutic effectiveness in solid tumors," *Magn. Reson. Med.*, vol. 67, no. 6, pp. 1827-1836, 2012.

A. Barbon, M. Brustolon, A. L. Maniero, M. Romanelli and L. C. Brunel, "Dynamics and spin relaxation of tempone in a host crystal. An ENDOR, high field EPR and electron spin echo study," *Phys. Chem. Chem. Phys.*, vol. 1, pp. 4015-4023, 1999.

A. Bobko, I. Dhimitruka, J. L. Zweier and V. V. Khramtsov, "Trityl Radicals as Persistent Dual Function pH and Oxygen Probes for in Vivo Electron Paramagnetic Resonance Spectroscopy and Imaging: Concept and Experiment," *J. Am. Chem. Soc.*, vol. 129, no. 23, pp. 7240-7241, 2007.

A. Collauto, A. Barbon and M. Brustolon, "First determination of the spin relaxation properties of a nitronyl nitroxide in solution by electron spin echo at X-band: a comparison with tempone," *J. Magn. Reson.*, vol. 223, pp. 180-186, 2012.

A. Collauto, M. Mannini, L. Sorace, A. Barbon, M. Brustolon and D. Gatteschi, "A slow relaxaing species for molecular spin devices: EPR characterization of static and dynamic magnetic propertis of a nitronyl nitroxide radical," *J. Mat. Chem.*, vol. 22, pp. 22272-22281, 2012.

A. Friedrich, A. Doelle and M. D. Zeidler, "Reorientational dynamics of glycerol derived from temperature-dependent multi-nuclear magnetic relaxation data," *Magn. Reson. Chem.*, vol. 41, pp. 813-818, 2003.

A. G. Taube, S. Subramanian, R. Murugesan, N. Devasahayam, J. B. Mitchell, M. C. Krishna and J. A. Cook, "An application system for automation of constant-time radio frequency electron paramagnetic resonance imaging," *Computer Methods and Programs in Biomedicine*, vol. 72, no. 2, pp. 127-138, 2003.

A. J. Fielding, P. J. Carl, G. R. Eaton and S. S. Eaton, "Multifrequency EPR of Four Triarylmethyl Radicals," *Appl. Magn. Reson.* , vol. 28, pp. 231-238, 2005.

A. Rockenbauer, L. Korecz and K. Hideg, "Ring pseudorotation of pyrroline N-oxyl radicals: an analysis of carbon-13 hyperfine structure of EPR spectra," *J.C.S. Perkin Trans*, vol. 22, pp. 2149-2156, 1993.

A. Rockenbauer, M. Gyor, K. Hankovszky and K. Hideg, "ESR of the conformation of 5- and 6-membered cyclic nitroxide (aminoxyl) radicals," *Electron Spin Reson.*, vol. 11A, pp. 145-182, 1988.

A. Savitsky, M. Plato and K. Mobius, "Temperature Dependence of Nitroxide Spin-Label Interaction Parameters: a High-Field EPR Study of Intramolecular Motional Contributions," *Appl. Magn. Reson*., vol. 37, pp. 415-434, 2010.

A. Schweiger and G. Jeschke, Principles of pulse electron paramagnetic resonance, Oxford University Press, 2001.

B. B. Williams, H. al Hallaq, G. V. Chandramouli, E. D. Barth, J. N. Rivers, M. Lewis, V. E. Galtsev, G. S. Karczmar and H. J. Halpern, "Imaging spin probe distribution in the tumor of a living mouse with 250 MHz EPR: correlation with BOLD MRI," *Magn. Reson. Med*., vol. 47, no. 4, pp. 634-638, 2002.

B. B. Williams, M. Elas, C. Mailer, A. D. Parasca, E. D. Barth, V. E. Galtsev and H. J. Halpern, "Fast 4D Spectral-Spatial Electron Paramagnetic Resonance Imaging for In Vivo Oxymetry," in Nuclear Science Symposium Conference Record, 2001.

B. B. Williams, X. Pan and H. J. Halpern, "EPR Imaging: The relationship between CW spectra acquired from an extended sample subjected to fixed stepped gradients and the Radon transform of the resonance density," *J. Magn. Reson*., vol. 174, no. 1, pp. 88-96, 2005.

B. B. Williams and H. H. Halpern, "In Vivo EPR imaging," in Biological Magnetic Resonance 23, pp. 283-319, 2005.

B. D. Armstrong and S. Han, "A new model for Overhauser enhanced nuclear magnetic resonance using nitroxide radicals," *J. Chem. Phys*., vol. 127, pp. 104508/1-104507/10, 2007.

B. Epel, C. R. Haney, D. Hleihel, C. Wardrip, E. D. Barth and H. J. Halpern, "Electron paramagnetic resonance oxygen imaging of a rabbit tumor using localized spin probe delivery.," *Med. Phys*., vol. 37, no. 6, pp. 2553-2559, 2010.

B. Epel, C. R. Haney, D. Hleihel, C. Wardrip, E. D. Barth and H. J. Halpern, "Electron paramagnetic resonance oxygen imaging of a rabbit tumor using localized spin probe delivery.," *Med. Phys*., vol. 37, no. 6, pp. 2553-2559, 2010.

B. Epel, M. K. Bowman, C. Mailer and H. J. Halpern, "Absolute oxygen R1e imaging in vivo with pulse electron paramagnetic resonance," *Magn. Reson. Med*., p. DOI: 10.1002/mrm.24926, 2013.

B. Epel, S. V. Sundramoorthy and H. J. Halpern, "Retractable loop-gap resonators for electron paramagnetic resonance imaging with in situ irradiation capabilities," *Concepts Magn. Reson.,* vol. 39B, pp. 167-172, 2011.

B. Epel, S. V. Sundramoorthy, C. Mailer and H. J. Halpern, "A versatile high speed 250-MHz pulse imager for biomedical applications," *Concepts Magn. Reson.*, vol. 33B, pp. 163-176, 2008.

B. Epel, S. V. Sundramoorthy, E. D. Barth, C. Mailer and H. J. Halpern, "Comparison of 250 MHz electron spin echo and continuous wave oxygen EPR imaging methods for in vivo applications," *Med. Phys.*, vol. 38, pp. 2045-2052, 2011.

B. Epel and H. J. Halpern, "Comparison of transverse and spin-lattice relaxation based electron paramagnetic resonance oxygen images," in Biomedical Imaging: From Nano to Macro, 2011 IEEE International Symposium on, Chicago, 2011.

B. Gallez, C. Baudelet and B. F. Jordan, "Assessment of tumor oxygenation by electron paramagnetic resonance: principles and applications," *NMR in Biomedicine*, vol. 17, no. 5, pp. 240-262, 2004.

B. Gallez, K. Mader and H. M. Swartz, "Noninvasive measurements of the pH inside the gut by using pH-sensitive nitroxides. An in vivo ESR study.," *Magn. Reson. Med.*, vol. 36, pp. 694-697, 1996.

B. H. Robinson, A. W. Reese, E. Gibbons and C. Mailer, "A unified descriptionof the spin-spin and spin-lattice relaxation rates applied to nitroxide labels in viscous liquids," *J. Phys. Chem. B*, vol. 103, pp. 5881-5894, 1999.

B. H. Robinson, C. Mailer and A. W. Reese, "Linewidth analysis of spin labels in liquids II. Experimental," *J. Magn. Reson.*, vol. 138, pp. 210-2219, 1999.

B. H. Robinson, C. Mailer and A. W. Reese, "Linewidth analysis of spin labels in liquids I. Theory and data analysis," *J. Magn. Reson.*, vol. 191, pp. 66-77, 1999.

B. H. Robinson, D. A. Haas and C. Mailer, "Molecular dynamics in liquids: spin-lattice relaxation of nitroxide spin labels," *Science*, vol. 263, pp. 490-493, 1994.

B. L. Bales, R. A. Blum, D. Mareno, M. Peric and H. J. Halpern, "Solvent and temperature dependence of the hyperfine coupling constants in CTPO," *J. Magn. Reson.*, vol. 98, pp. 299-307, 1992.

C. A. Popp and J. S. Hyde, "Electron-electron double resonance and saturation recovery studies of nitroxide electron andn nuclear spin-lattice relaxation times and Heisenberg exchange rates: lateral diffusion in dimyristoyl phosphatidylcholine," *Proc. Natl. Acad. Sci. USA*, vol. 79, pp. 2559-2563, 1982.

C. Mailer, B. H. Robinson, B. B. Williams and H. J. Halpern, "Spectral fitting: The extraction of crucial information from a spectrum and a spectral image," *Magn. Reson. Med.*, vol. 49, no. 6, pp. 1175-1180, 2003.

C. Mailer, R. D. Nielsen and B. H. Robinson, "Explanation of spin-lattice relaxation rates of spin labels obtained with multifrequency saturation recovery EPR," *J. Phys. Chem. A*, vol. 109, pp. 4049-4061, 2005.

C. Mailer, S. V. Sundramoorthy, C. P. Pelizzari and H. J. Halpern, "Spin echo spectroscopic electron paramagnetic resonance imaging," *Magn. Reson. Med*., vol. 55, no. 4, pp. 904-912, 2006.

C. R. Haney, A. D. Parasca, K. Ichikawa, B. B. Williams, M. Elas, C. A. Pelizzari and H. J. Halpern, "Reduction of Image Artifacts in Mice by Bladder Flushing with a Novel Double-Lumen Urethral Catheter," *Mol. Imaging*, vol. 5, no. 3, pp. 175-179, 2006.

C. R. Haney, A. D. Parasca, X. Fan, R. M. Bell, M. A. Zamora, G. S. Karczmar, H. J. Maucen, H. J. Halpern, R. R. Weichselbaum and C. A. Pelizzari, "Characterization of response to radiation mediated gene therapy by means of multimodality imaging," *Magn. Reson. Med.*, vol. 62, no. 2, pp. 348-356, 2009.

C. R. Haney, X. Fan, A. D. Parasca, G. S. Karczmar, H. J. Halpern and C. A. Pelizzari, "Immobilization using dental material casts facilitates accurate serial and multimodality small animal imaging," *Concepts Magn. Reson*., vol. 33B, pp. 138-144, 2008.

D. A. Morozov, I. A. Kirilyuk, D. A. Komarov, A. Goti, I. Y. Bagryanskaya, N. V. Kuratieva and I. A. Grigor'ev, "Synthesis of a Chiral C2 Symmetric Sterically Hindered Pyrrolidine Nitroxide Radical via Combined Iterative Nucleophilic Additions and Intramolecular 1,3-Dipolar Cycoadditions to Cyclic Nitrones," *J. Org. Chem*., vol. 77, pp. 10688-10698, 2012.

D. E. Budil, S. Lee, S. Saxena and J. H. Freed, "Nonlinear least-squares analysis of slow-motion EPR spectra in one and two dimensions using a modified Levenberg-Marquardt algorithm," *J. Magn. Reson*. A, vol. 120, pp. 155-189, 1996.

D. J. Greenslade, A. V. Koptyug and M. R. Symons, "Aspects of low-frequency low-field electron spin resonance," *Annu. Rep. Prog. Chem., Sect. C: Phys. Chem*., vol. 92, pp. 3-21, 1995.

D. J. Schneider and J. H. Freed, "Calculating slow motional magnetic resonance spectra: a user's guide," in Biol. Magn. Reson. Vol. 8, L. J. Berliner and J. Reuben, Eds., 1989, pp. 1-76.

D. Kivelson, "Theory of EPR [electron paramagnetic resonance] line widths of free radicals," *J. Chem. Phys*., vol. 33, pp. 1094-1106, 1960.

D. P. Dalal, R. Damoder, C. Benner, G. R. Eaton and S. S. Eaton, "Metal-nitroxyl interactions 44. Collision interactions between transition metal complexes and nitroxyl radicals in aqueous solution," *J. Magn. Reson*., vol. 63, pp. 125-132, 1985.

D. Sezer, M. Gafurov, M. J. Prondolini, V. P. Denysenkov and T. F. Prisner, "Dynamic nuclear polarization of water by a nitroxide radical: rigorous treatment of the electron spin saturation and comparison with experiments at 9.3 Tesla," *Phys. Chem. Chem. Phys.,* vol. 11, pp. 6638-6653, 2009.

D. Siri, A. Guadel-Siri and P. Tordo, "Conformational Analysis of five-membered rings by molecular mechanics: applications to nitroxides," *J. Mol. Struct*. (Theochem.), vol. 582, pp. 171-185, 2002.

D.G. Mitchell, G.M. Rosen, M. Tseitlin, B. Symmes, S.S. Eaton, and G.R. Eaton, "Use of Rapid-Scan EPR to Improve Detection Sensitivity for Spin-Trapped Radicals", *Biophys. J., vol. 105, pp. 338 - 342, 2013.*

D.G. Mitchell, M. Tseitlin, R.W. Quine, V. Meyer, M.E. Newton, A. Schnegg, B. George, S.S. Eaton, and G.R. Eaton, "X-Band Rapid-scan EPR of Samples with Long Electron Relaxation Times: A Comparison of Continuous Wave, Pulse, and Rapid-scan EPR", *Mol. Phys*., vol. 111, pp.2664 - 2673, 2013.

D.G. Mitchell, R.W. Quine, M. Tseitlin, S.S. Eaton, and G.R. Eaton, "X-band Rapid-Scan EPR of Nitroxyl Radicals", *J. Magn. Reson*., vol. 214, pp.221-226, 2012

E. F. Ullman, J. H. Osiecki, D. B. Boocock and R. Darcy, "Studies of stable free radicals. X. Nitronyl nitroxide monoradicals and biradicals as possible small molecule spin labels," *J. Am. Chem. Soc*., vol. 94, pp. 7049-7059, 19972.

E. van der Drift, B. C. Rousseeuw and J. Smidt, "EPR and ELDOR studies on spin relaxation in perdeuterated 2,2,6,6-tetramethyl-4-piperidone-N-oxyl in liquid solutions: The slowly relaxing local structure mechanism," *J. Phys*. *Chem*., vol. 88, pp. 2275-2284, 1984.

F. Gerson and W. Huber, Electron Spin Resonance Spectroscopy of Organic Radicals, Wiley-VCH,Weinheim, 2003.

F. Hyodo, R. Murugesan, K. Matsumoto, E. Hyodo, S. Subramanian, J. B. Mitchell and M. C. Krishna, "Monitoring redox-sensitive paramagnetic contrast agent by EPRI, OMRI and MRI," *J. Magn. Reson*., vol. 190, no. 1, pp. 105-112, 2008.

F. Hyodo, S. Matsumoto, N. Devasahayam, C. Dharmaraj, S. Subramanian, J. B. Mitchell and M. C. Krishna, "Pulsed EPR imaging of nitroxides in mice," *J. Magn. Reson*., vol. 197, pp. 181-185, 2009.

G. A. Rinard, R. W. Quine and G. R. Eaton, "An L-band Crossed Loop (Bimodal) EPR Resonator," *J. Magn. Reson.,* vol. 144, pp. 85-88, 2000.

G. A. Rinard, R. W. Quine, B. T. Ghim, S. S. Eaton and G. R. Eaton, "Easily tuneable crossed-loop (bimodal) EPR resonator," *J Magn. Reson*. A, vol. 122, pp. 50-57, 1996.

G. A. Rinard, R. W. Quine, G. R. Eaton and S. S. Eaton , "Adapting a hall probe controller for current control of an air-core magnet," *Concepts Magn. Reson*., vol. 15, pp. 47-50, 2002.

G. A. Rinard, R. W. Quine, G. R. Eaton and S. S. Eaton, "250 MHz Crossed-Loop Resonator for Pulsed Electron Paramagnetic Resonance," *Concepts Magn. Reson*., vol. 15, no. 1, pp. 37-46, 2002.

G. A. Rinard, R. W. Quine, G. R. Eaton, S. S. Eaton, E. D. Barth, C. A. Pelizzari and H. J. Halpern, "Magnet and gradient coil system for low-field EPR imaging," *Concepts Magn. Reson.*, vol. 15, pp. 51-58, 2002.

G. A. Rinard, R. W. Quine, J. R. Biller and G. R. Eaton, "A Wire Crossed-Loop-Resonator for Rapid Scan EPR," *Concepts Magn. Reson*., vol. 37B, pp. 86-91, 2010.

G. A. Rinard, R. W. Quine, J. R. Harbridge, R. Song, G. R. Eaton and S. S. Eaton, "Frequency Dependence of EPR Signal-to-Noise," *J. Magn. Reson*., vol. 140, pp. 218-227, 1999.

G. A. Rinard, R. W. Quine, R. Song, G. R. Eaton and S. S. Eaton, "Absolute EPR Spin Echo and Noise Intensities," *J. Magn. Reson*., vol. 140, pp. 69-83, 1999.

G. A. Rinard, R. W. Quine, S. S. Eaton and G. R. Eaton, "Dispersion and superheterodyne EPR using a bomodal resonator," *J. Magn. Reson*., vol. 122, pp. 58-63, 1996.

G. A. Rinard, R. W. Quine, S. S. Eaton and G. R. Eaton, "Frequency dependence of EPR signal intensity, 248 MHz to 1.4 GHz.," *J. Magn. Reson.*, vol. 154, no. 1, pp. 80-84, 2002.

G. A. Rinard, R. W. Quine, S. S. Eaton, G. R. Eaton and W. Froncisz, "Relative benefits of overcoupled resonators vs. inherently low-Q resonators for pulsed magnetic resonance," *J. Magn. Reson*., vol. 108, pp. 71-81, 1994.

G. C. Borgia, R. S. Brown and P. Fantazzini, "Uniform-penalty inversion of multiexponential decay data II. Data spacing, T2 data, systematic errors, and diagnostics," *J. Magn. Reson.*, vol. 147, pp. 273-285, 2000.

G. C. Borgia, R. S. Brown and P. Fantazzini, "Uniform-penalty inversion of multiexponential decay data," *J. Magn. Reson*., vol. 132, pp. 65-77, 1998.

G. He, "Electron Paramagnetic Resonance Oximetry and Redoximetry," Advanced Protocols in Oxidative Stresss II: Methods in Molecular Biology, vol. 594, pp. 85-105, 2010.

G. Ilangovan, A. Bratasz, H. Li, P. Schmalbrock, J. L. Zweier and P. Kuppusamy, "In vivo measurement and imaging of tumor oxygenation using coembedded paramagnetic particulates," *Magn. Reson. Med*., vol. 52, no. 3, pp. 650-657, 2004.

G. Ilangovan, H. Li, J. L. Zweier and P. Kuppusamy, "Electrochemical Preparation and EPR Studies of Lithium Phthalocyanine. 3. Measurements of Oxygen Concentration in Tissues and Biochemical Reactions," *J. Phys. Chem. B*, vol. 105, no. 22, pp. 5323-5330, 2001.

G. Ilangovan, H. Li, J. L. Zweier, M. C. Krishna, J. B. Mitchell and P. Kuppusamy, "In vivo measurement of regional oxygenation and imaging of redox status in RIF-1 murine tumor: Effect of carbogen breathing," *Magn. Reson. Med*., vol. 48, no. 4, pp. 723-730, 2002.

G. M. Rosen, A. Beselman, P. Tsai, S. Pou, C. Mailer, K. Ichikawa, B. H. Robinson, R. Nielsen, H. J. Halpern and A. D. MacKerell, "Influence of conformation on the EPR spectrum of 5,5-dimethyl-1-hydroperoxy-1-pyrrolidinyloxyl: a spin trapped adduct of superoxide.," *J. Org. Chem*., vol. 69, no. 4, pp. 1321-1330, 2004.

G. M. Rosen, B. E. Britigan, H. J. Halpern and S. Pou, Free Radicals: Biology and Detection by Spin Trapping, Oxford: Oxford University Press, 1999, pp. 225-226.

G. M. Rosen, S. R. Burks, M. J. Kohr and J. P. Kao, "Synthesis and biological testing of aminoxyls designed for long-term retention by living cells," *Org. Biomol. Chem*., vol. 3, no. 4, pp. 645-648, 2005.

G. R. Eaton , S. S. Eaton , D. P. Barr and R. T. Weber, Quantitative EPR, New York: Springer-Verlag/Wien, 2010.

G. Redler, E. D. Barth, K. S. Bauer, J. Y. Kao, G. M. Rosen and H. J. Halpern, "In vivo electron paramagnetic resonance imaging of differential tumor targeting using cis-3,4-di(acetoxymethoxycarbonyl)-2,2,5,5-tetramethyl-1-pyrrolidinyloxyl," *Magn. Reson. Med.*, vol. 71, no. 4, pp. 1650-1656, 2013.

G.A. Rinard, R.A. Quine, J.R. Biller, and G.R. Eaton, "A Wire Crossed-Loop-Resonator for Rapid Scan EPR", *Concepts Magn. Reson*., vol. 37B, pp. 86-91, 2010.

G.A. Rinard, R.W. Quine, and G.R. Eaton, "An L-Band crossed-loop (bimodal) EPR resonator", *J. Magn. Reson*., vol. 144, pp.85-88, 2000.

G.A. Rinard, R.W. Quine, G.R. Eaton, and S.S. Eaton, "250 MHz crossed loop resonator for pulsed electron paramagnetic resonance", *Magn. Reson. Engineer*., vol. 15, pp. 37-46, 2002.

G.A. Rinard, R.W. Quine, S.S. Eaton, G.R. Eaton, E.D. Barth, C.A. Pelizzari, and H.J. Halpern, “Magnet and Gradient Coil System for Low-Field EPR Imaging”, *Magn. Reson. Engineer.*, vol. 15, pp.51-58, 2002.

G.R. Eaton and S.S. Eaton, “Introduction to EPR imaging using magnetic-field gradients”, *Concepts Magn. Reson*., vol 7, pp. 49-67, 1997.

H. J. Halpern, "Applications of In Vivo EPR Spectroscopy and Imaging in Cancer Research," in In Vivo EPR (ESR): Biological Magnetic Resonance vol. 18, L. Berliner, Ed., Springer, 2003, pp. 469-482.

H. J. Halpern, "Stable Soluble Paramagnetic Compounds," in Biological Magnetic Resonance (18) In Vivo EPR (ESR), vol. 18, Springer, 2003, pp. 201-232.

H. J. Halpern, C. Yu, M. Peric, E. D. Barth, D. J. Grdina and B. A. Teicher, "Oxymetry deep in tissues with low-frequency electron paramagnetic resonance," *Proc. Natl. Acad. Sci. U.S.A.*, vol. 91, pp. 13047-13051, 1994.

H. J. Halpern, G. R. Chandramouli, E. D. Barth, C. Yu, M. Peric, D. J. Grdina and B. A. Teicher, "Diminished Aqueous Microviscosity of Tumors in Murine Models Measured with in Vivo Radiofrequency Electron Paramagnetic Resonance," *Cancer Research*, vol. 15, pp. 5836-5841, 1999.

H. J. Halpern, M. Elas, D. Bell, E. D. Hleihel, E. D. Barth, C. R. Chaney, K. Ahn, C. A. Pelizzari, M. Kocherginsky and R. R. Weichselbaum, "Electron Paramagnetic Resonance Oxygen Images Correlates Spatially and Quantitatively with Increased Vascular Endothelial Growth Factor Concentrations," *International Journal of Radiation Oncology * Biology * Physics* , vol. 75, no. 3, 2009.

H. J. Halpern, M. Peric, C. Yu and B. L. Bales, "Rapid quantitation of parameters from inhomogeneously broadened EPR spectra," *J. Magn. Reson*., vol. 103, pp. 13-22, 1993.

H. J. Halpern, M. Peric, T. D. Nguyen, D. P. Spencer, B. A. Teicher, Y. J. Lin and M. K. Bowman, "Selective isotopic labeling of a nitroxide spin label to enhance sensitivity for T2 oxymetry," *J. Magn. Reson*., vol. 90, pp. 40-51, 1990.

H. J. Halpern, Y. Cheng, M. Peric, E. D. Barth, G. S. Karczmar, J. N. River, D. J. Grdina and B. A. Teicher, "Measurement of Differences in pO2 in Response to Perfuorocarbon/Carbogen in FSa and NFSa Murine Fibrosarcomas with Low-Frequency Electron Paramagnetic Resonance Oximetry," *Radiation Research*, vol. 145, no. 5, pp. 610-618, 1996.

H. Jang, S. Subramanian, N. Devasahayam, K. Saito, S. Matsumoto, M. C. Krishna and A. B. McMillan, "Single Acquisition Quantitative Single-Point Electron Paramagnetic Resonance Imaging," *Magn. Reson. Med*., vol. 70, no. 4, pp. 1173-1181, 2013.

H. M. Swartz, J. Dunn, O. Grinberg, J. O'Hara and T. Walczak, "What Does EPR Oximetry with Solid Particles Measure- and How Does this Relate to Other Measures of PO?," *Oxygen Transport to Tissue XIX*, vol. 428, pp. 663-670, 1997.

H. M. Swartz and J. F. Dunn, "Measurements of Oxygen in Tissues: Overview and Perspectives on Methods," *Oxygen Transport to Tissue XXIV: Advances in Experimental Medicine and Biology*, vol. 530, pp. 1-12, 2003.

H. M. Swartz and R. B. Clarkson, "The measurement of oxygen in vivo using EPR techniques," *Phys. Med. Biol.* , vol. 43, p. 1957, 1998.

H. Sato, S. E. Bottle, J. P. Blinco, A. S. Micallef, G. R. Eaton and S. S. Eaton, "Electron spin-lattice relaxation of nitroxyl radicals in temperature ranges that span glassy solutions to low-viscosity liquids," *J. Magn. Reson.*, vol. 191, no. 1, pp. 66-77, 2008.

H. Sato, V. Kathirvelu, A. Fielding, J. P. Blinco, A. Micallef, S. E. Bottle, S. S. Eaton and G. R. Eaton, "Impact of molecular size on electron spin relaxation rates of nitroxyl radicals in glassy solvents between 100 and 300 K," *Mol. Phys.*, vol. 105, pp. 2137-2151, 2007.

H. Utsumi, K. I. Yamada, K. Ichikawa, K. Sakai, Y. Kinoshita and S. Matsumoto, "Simultaneous molecular imaging of redox reactions monitored by Overhauser-enhanced MRI with 14N and 15N labeled nitroxyl radicals," *Proc. Nat. Acad. Sci. U.S.A.*, vol. 103, pp. 1463-1468, 2006.

I. Bertini, G. Martini and C. Luchinat, "Relaxation,Background and Theory," in Handbook of Electron Spin Resonance, C. P. Poole and H. A. Farach, Eds., *American Institute of Physics Press*, 1994, pp. 51-77.

I. Dhimitruka, A. A. Bobko, C. M. Hadad, J. L. Zweier and V. V. Khramtsov, "Synthesis and Characterization of Amino Derivatives of Persistent Trityl Radicals as Dual Function pH and Oxygen Paramagnetic Probes," J. Am. Chem. Soc., vol. 130, no. 32, pp. 10780-10787, 2008.

I. Dhimitruka, O. Grigorieva, J. L. Zweier and V. V. Khramtsov, "Synthesis, structure, and EPR characterization of deuterated derivatives of Finland trityl radical," *Bioorg. Med. Chem. Let.*, vol. 20, no. 13, pp. 3946-3949, 2010.

I. Panagiotelis, I. Nicholson and J. S. Hutchison, "Electron Spin Relaxation Time Measurements Using Radiofrequency Longitudinally Detected ESR and Application in Oximetry," *J. Magn. Reson.*, vol. 149, no. 1, pp. 74-84, 2001.

I. Ratera and J. Veciana, "Playing with organic radicals as building blocks for functional materials," *Chem. Soc. Rev.*, vol. 41, pp. 303-349, 2012.

J. Cirujeda, J. Vidal-Gancedo, O. Jurgens, F. Monta, J. J. Novoa, C. Rovira and J. Veciana, "Spin Density Distribution of alpha-Nitronyl Aminoxyl Radicals from Experimental and ab Initio Calculated ESR Isotropic Hyperfine Coupling Constants," *J. Am. Chem. Soc.*, vol. 122, pp. 11393-11405, 2000.

J. D. Beckmann, M. C. McKean and F. E. Frerman, "Inhibition of general acyl-CoA dehydrogenase by electron transfer flavoprotein semiquinone," Biochem. Biophys. *Res. Comm.*, vol. 102, pp. 1290-1294, 1981.

J. D. Roberts, Nuclear Magnetic Resonance: Applications to Organic Chemistry, New York Toronto London: McGraw-Hill Book Company Inc., 1959.

J. Goldman, T. E. Petersen, K. Torssell and J. Becher, "19F and 1H NMR and ESR investigations of aryl-t-butyl nitroxides and nitronyl nitroxides," *Tetrahedron, vol. 29, pp. 3833-3843, 1973.*

J. H. Ardenkjaer-Larsen, I. Laursen, I. Leunback, G. Ehnhom, L. G. Wistrand, J. S. Petersson and K. Golman, "EPR and DNP properties of certain novel single electron contrast agents intended for oximetric imaging," *J. Magn. Reson*., vol. 133, no. 1, pp. 1-12, 1998.

J. H. Freed, "ESR and molecular dynamics," in *Biol. Magn. Reson*. Vol. 24, 2005, pp. 239-268.

J. H. Freed, "Theory of multiple resonance and ESR saturation liquids and related media," in Multiple Electron Resonance Spectroscopy, New York, Plenum, 1979, p. 100.

J. H. Freed, "Theory of slow tumbling ESR spectra of nitroxides," in Spin Labeling: Theory and Applications, New York, Academic Press, 1976, pp. 53-132.

J. Huisjen and J. S. Hyde, "A pulsed EPR spectrometer," *Rev. Sci. Instrum*., vol. 45, pp. 669-675, 1974.

J. J. Yin, M. Pasenkiewicz-Gierula and J. S. Hyde, "Lateral diffusion of lipids in membranes by pulse saturation recovery electron spin resonance," *Proc. Natl. Acad. Sci.* , vol. 84, pp. 964-968, 1987.

J. J. Yin and J. S. Hyde, "Spin-label saturation-recovery electron spin resonance measurements of oxygen transport in membranes," *Zeitschrift fuer Physikalische Chemie*, vol. 153, pp. 57-65, 1987.

J. Labsky, J. Pilar and J. Lovy, "Magnetic resonance study of 4-amino -2,2,6,6-tetramethylpiperidine-N-oxyl and its deuterated derivatives," *J. Magn. Reson*., vol. 37, pp. 515-522, 1980.

J. M. Brown and W. R. Wilson, "Exploiting tumor hypoxia in cancer treatment," *Nat. Rev*., vol. 4, pp. 437-447, 2004.

J. P. Joshi, J. R. Ballard, G. A. Rinard, R. W. Quine, S. S. Eaton and G. R. Eaton, "Rapid-scan EPR with triangular scans and Fourier deconvolution to recover the slow scan spectrum," *J. Magn. Reson*., vol. 175, pp. 44-51, 2005.

J. P. Kao, E. D. Barth, S. R. Burks, P. Smithback, C. Mailer, K. Ahn, H. J. Halpern and G. M. Rosen, "Very-Low-Frequency Electron Paramagnetic Resonance (EPR) Imaging of Nitroxide-Loaded Cells," *Magn. Reson. Med*., vol. 58, no. 4, pp. 850-854, 2007.

J. P. Kao and G. M. Rosen, "Esterase-assisted accumulation of 3-carboxy-2,2,5,5-tetramethyl-1-pyrrolidinyloxyl into lymphocytes.," *Org. Biomol*. Chem., vol. 2, no. 1, pp. 99-102, 2004.

J. P. Lloyd and G. E. Pake, "Spin relaxation in free radical solutions exhibiting hyperfine structure," *Phys. Rev*., vol. 94, pp. 579-591, 1954.

J. R. Biller, H. Elajaili, V. Meyer, G. M. Rosen, S. S. Eaton and G. R. Eaton, "Electron spin-lattice relaxation mechanisms of rapidly-tumbling nitroxide radicals," *J. Magn. Reson.*, vol. 236, pp. 47-56, 2013.

J. R. Biller, M. Tseitlin, R. Q. Quine, G. A. Rinard, H. A. Weismiller, H. Elajaili, G. M. Rosen, J. Y. Kao, S. S. Eaton and G. R. Eaton, "Imaging of Nitroxides at 250 MHz using Rapid-Scan Electron Paramagnetic Resonance," *J. Magn. Reson*., vol. 242, pp. 162-168, 2014.

J. R. Biller, V. M. Meyer, H. Elajaili, G. M. Rosen, S. S. Eaton and G. R. Eaton, "Frequency dependence of electron spin relaxation times in aqueous solution for a nitronyl nitroxide radical and perdeuterated-tempone between 250 MHz and 34 GHz," *J. Magn. Reson*., vol. 225, pp. 52-57, 2012.

J. R. Biller, V. Meyer, H. Elajaili, G. M. Rosen, J. P. Kao, S. S. Eaton and G. R. Eaton, "Relaxation times and line widths of isotopically-substituted nitroxides in aqueous solution at X-band," *J. Magn. Reson*., vol. 212, no. 2, pp. 370-377, 2011.

J. R. Harbridge, S. S. Eaton and G. R. Eaton, "Electron spin-lattice relaxation in radicals containing two methyl groups, generated by g-irradiation of polycrystalline solids," *J. Magn. Reson.*, vol. 159, pp. 195-206, 2002.

J. R. Harbridge, S. S. Eaton and G. R. Eaton, "Electron Spin-Lattice Relaxation Processes of Radicals in Irradiated Crystalline Organic Compounds," *J. Phys. Chem. A*, vol. 107, pp. 598-610, 2003.

J. R. Harbridge, S. S. Eaton and G. R. Eaton, "Spin Relaxation of Radicals in g-irradiated Malonic Acid and Methyl Malonic Acid," *Appl. Magn. Reson.*, vol. 24, pp. 261-276, 2003.

J. S. Hwang, R. P. Mason, L. P. Hwang and J. H. Freed, "Electron spin resonance studies of anisotropic rotational reorientation and slow tumbling in liquid and frozen media. III. Perdeuterated 2,2,6,6-tetramethyl-4-piperidone-N-oxide and an analysis of fluctuating torques," *J. Phys. Chem*., vol. 79, pp. 489-511, 1975.

J. S. Hwang and Y. T. Al-Janavi, "Frequency dependent study of the correlation functions in EPR spectroscopy - the Cole Davidson Approach 1. Perdeuterated 2,2,6,6-tetramethyl-4-piperidone N-oxide in toluene," *Spect. Chim. Acta.A*, vol. 56, pp. 273-284, 2000.

J. S. Hyde , J. J. Yin, J. B. Feix and W. L. Hubbell, "Advances in spin label oximetry," *Pure Appl. Chem*., vol. 62, pp. 255-260, 1990.

J. S. Hyde, J. J. Yin, W. K. Subczynski, T. G. Camenisch, J. J. Ratke and W. Froncisz, "Spin-labeled EPR T1 values using saturation recovery from 2 to 35 GHz," *J. Phys. Chem. B*, vol. 108, pp. 9524-9529, 2004.

J. Shen, R. Sood, J. Weaver, G. S. Timmins, A. Schnell, M. Miyake, J. P. Kao, G. M. Rosen and K. J. Liu, "Direct visualization of mouse brain oxygen distribution by electron paramagnetic resonance imaging: application to focal cerebral ischemia.," *J. Cereb. Blood Flow Metab*., vol. 29, no. 10, pp. 1695-1703, 2009.

J. Shen, S. Bottle, N. Khan, O. Grinsberg, D. Reid, A. Micallef and H. M. Swartz, "Development of Isoindoline Nitroxides for EPR Oximietry in Viable Systems," *Appl. Magn. Reson.*, vol. 22, pp. 357-368, 2002.

J. Shen, S. Liu, M. Miyake, W. Liu, A. Pritchard, J. P. Kao, G. M. Rosen, Y. Tong and K. J. Liu, "Use of 3-acetoxymethoxycarbonyl-2,2,5,5-tetramethyl-1-pyrrolidinyloxyl as an EPR oximetry probe: potential for in vivo measurement of tissue oxygenation in mouse brain," *Magn. Reson. Med*., vol. 55, no. 6, pp. 1433-1440, 2006.

J. W. Stoner, D. Szymanski, S. S. Eaton, R. W. Quine, G. A. Rinard and G. R. Eaton , "Direct-detected rapid-scan EPR at 250 MHz," *J. Magn. Reson*., vol. 170, pp. 127-135, 2004.

J. Yamauchi and C. A. McDowell, "NMR Study of molecular motion in some molecules containing t-butyl groups," *J. Chem. Phys*., vol. 75, pp. 1051-1058, 1981.

J.P. Joshi, J.R. Ballard, G.A. Rinard, R.W. Quine, S.S. Eaton, and G.R. Eaton, "Rapid-Scan EPR with Triangular Scans and Fourier Deconvolution to Recover the Slow-Scan Spectrum", *J. Magn. Reson*., vol. 175, pp. 44-51, 2005.

K. A. Earle, D. E. Budil and J. H. Freed, "250 GHz EPR of Nitroxides in the Slow-Motional Regime: Models of Rotational Diffusion," *J. Phys. Chem.*, vol. 97, pp. 13289-13297, 1993.

K. H. Ahn and H. J. Halpern, "Comparison of local and global angular interpolation applied to spectral-spatial EPR image reconstruction," *Med. Phys.*, vol. 34, no. 3, pp. 1047-1052, 2007.

K. H. Ahn and H. J. Halpern, "Object dependent sweep width reduction with spectral-spatial EPR imaging," *J. Magn. Reson.*, vol. 186, no. 1, pp. 105-111, 2007.

K. H. Ahn and H. J. Halpern, "Simulation of 4D spectral-spatial EPR images," *J. Magn. Reson.*, vol. 187, no. 1, pp. 1-9, 2007.

K. H. Ahn and H. J. Halpern, "Spatially Uniform Sampling in 4-D EPR spectral-spatial imaging," *J. Magn. Reson.*, vol. 185, no. 1, pp. 152-158, 2007.

K. I. Matsumoto, F. Hyodo, A. Matsumoto, A. P. Koretsky, A. L. Sowers, J. B. Mitchell and M. Krishna, "High-resolution Mapping of Tumor Redox Status by Magnetic Resonance Imaging Using Nitroxides as Redox-Sensitive Contrast Agents," *Clin. Cancer Res.*, vol. 12, pp. 2455-2462, 2006.

K. Matsumoto, B. Chandrika, J. B. Lohman, J. B. Mitchell, M. C. Krishna and S. Subramanian, "Application of continuous-wave EPR spectral-spatial image reconstruction techniques for in vivo oxymetry: Comparison of projection reconstruction and constant-time modalities," *Magn. Reson. Med.*, vol. 50, no. 4, pp. 865-874, 2003.

K. Matsumoto, S. English, J. Yoo, K. Yamada, N. Devasahayam, J. A. Cook, J. B. Mitchell, S. Subramanian and M. C. Krishna, "Pharmacokinetics of a triarylmethyl-type paramagnetic spin probe used in EPR oximetry," *Magn. Reson. Med.*, vol. 52, pp. 885-892, 2004.

K. Matsumoto, S. Subramanian, N. Devasahayam, T. Aravalluvan, R. Murugesan, J. A. Cook, J. B. Mitchell and M. C. Krishna, "Electron paramagnetic resonance imaging of tumor hypoxia: Enhanced spatial and temporal resolution for in vivo pO2 determination," *Mag. Reson. Med.* , vol. 55, no. 5, pp. 1157-1163, 2006.

K. Matsumoto, S. Subramanian, R. Murugesan, J. B. Mitchell and M. C. Krishna, "Spatially Resolved Biologic Information from In Vivo EPRI, OMRI, and MRI," *Antioxidant and Redox Signaling*, vol. 9, no. 8, pp. 1125-1142, 2007.

K. Matsumoto, T. Yahiro, K. Yamada and H. Utsumi, "In vivo EPR spectroscopic imaging for a liposomal drug delivery system," *Magn. Reson. Med.*, vol. 53, no. 5, pp. 1158-1165, 2005.

L. B. Volodarsky, Imidazoline Nitroxides, Synthesis and Properties, vol I., Boca Raton: CRC Press, 1988.

L. Banci, I. Bertini and C. Luchinat, Electron relaxation in Dilute Systems, Nuclear and Electron Relaxation, VCH Wienheim, 1991, pp. 71-90.

L. Berliner, Ed., Spin Labeling II, New York: Academic Press, 1979.

L. Columbus and W. L. Hubbell, "A new spin on protein dynamics," *Trends Biochem. Sci*., vol. 27, pp. 288-295, 2002.

L. L. Jones and R. N. Schwartz, "An electron paramagnetic resonance study of rotational and translational motion in solution," *Mol. Phys*., vol. 43, pp. 527-555, 1981.

L. Lumata, M. E. Merritt and Z. Kovacs, "Influence of deuteration in the glassing matrix on 13C dynamic nuclear polarization," *Phys. Chem. Chem. Phys*., vol. 15, pp. 7032-7035, 2013.

L. Yong, J. Harbridge, R. W. Quine, G. A. Rinard, S. S. Eaton, G. R. Eaton, C. Mailer, E. Barth and H. J. Halpern, "Electron spin relaxation of triarylmethyl radicals in fluid solution.," J. Magn. Reson., vol. 152, no. 1, pp. 156-161, 2001.

M. Afeworki, G. M. van Dam, N. Devasahayam, R. Murugesan, J. Cook, D. Coffin, J. H. A-Larsen, J. B. Mitchell, S. Subramanian and M. C. Krishna, "Three-dimensional whole body imaging of spin probes in mice by time-domain radiofrequency electron paramagnetic resonance," *Magn. Reson. Med*., vol. 43, no. 3, pp. 375-382, 2000.

M. Afeworki, N. R. Miller, N. Devasahayam, J. Cook, J. B. Mitchell, S. Subramanian and M. C. Krishna, "Preparation and EPR Studies of Lithium Phthalocyanine Radical as an Oxymetric Probe," *Free Rad. Bio. Med*., vol. 25, no. 1, pp. 72-78, 1998.

M. Brustalon and E. Giamello, Eds., Electron Paramagnetic Resonance: A Practicioner's Toolkit, Wiley, 2009.

M. C. Krishna, N. Devasahayam, J. A. Cook, S. Subramanian, P. Kuppusamy and J. B. Mitchell, "Electron Paramagnetic Resonance for Small Animal Imaging Applications," *ILAR J*, vol. 42, no. 3, pp. 209-218, 2001.

M. C. Krishna, S. English, K. Yamada, J. Yoo, R. Murugesan, N. Devasahayam, J. A. Cook, K. Golman, J. H. Ardenkjaer-Larsen, S. Subramanian and J. B. Mitchell, "Overhauser enhanced magnetic resonance imaging for tumor oximetry: Coregistration of tumor anatomy and tissue oxygen concentration," *Proc. Natl. Acad. Sci. U.S.A*., vol. 99, no. 4, pp. 2216-2221, 2002.

M. C. Krishna, S. Matsumoto, H. Yasui, K. Saito, N. Devasahayam, S. Subramanian and J. B. Mitchell, "Electron Paramagnetic Resonance Imaging of Tumor pO2," *Radiation Research,* vol. 177, no. 4, pp. 376-386, 2012.

M. Elas, A. Parasca, D. J. Grdina and H. J. Halpern, "Oral administration is as effective as intraperitoneal administration of amifostine in decreasing nitroxide EPR signal decay in vivo," *Biochim. Biophys. Acta,* vol. 1637, no. 2, pp. 151-155, 2003.

M. Elas, B. B. Williams, A. Parasca, C. Mailer, C. A. Pelizzari, M. A. Lewis, J. N. River, G. S. Karczmar, E. D. Barth and H. J. Halpern, "Quantitative tumor oxymetric images from 4D electron paramagnetic resonance imaging (EPRI): Methodology and comparison with bood oxygen level-dependent (BOLD) MRI," *Magn. Reson. Med.* , vol. 49, no. 4, pp. 682-691, 2003.

M. Elas, D. Hleihel, E. D. Barth, C. R. Haney, K. H. Ahn, C. A. Pelizzari, B. Epel, R. R. Weichselbaum and H. J. Halpern, "Where it's at really matters: in situ in vivo vascular endothelial growth factor spatially correlates with electron paramagnetic resonance pO2 images in tumors of living mice.," *Mol .Imag. Biol*., vol. 13, no. 6, pp. 1107-1113, 2011.

M. Elas, J. M. Magwood, B. Butler, C. Li, R. Wardak, R. DeVries, E. D. Barth, B. Epel, S. Rubinstein, C. A. Pelizzari, R. R. Weichselbaum and H. J. Halpern, "EPR Oxygen Images Predict Tumor Control by a 50% Tumor Control Radiation Dose," *Cancer Research*., vol. 73, pp. 5328-5335, 2013.

M. Elas, K. H. Ahn, A. Parasca, E. D. Barth, D. Lee, C. Haney and H. J. Halpern, "Electron paramagnetic resonance oxygen images correlate spatially and quantitatively with Oxylite oxygen measurements," *Clinical Cancer Research*, vol. 12, no. 14 (Pt. 1), pp. 4209-4217, 2006.

M. Elas, K. Ichikawa and H. J. Halpern, "Oxidative Stress Imaging in Live Animals with Techniques Based on Electron Paramagnetic Resonance," *Radiation Research,* vol. 177, no. 4, pp. 514-523, 2012.

M. Elas, R. Bell, D. Hleihel, E. D. Barth, C. McFaul, C. R. Haney , J. Bielanska, K. Pustelny, K. Ahn, C. A. Pelizzari, M. Kocherginsky and H. J. Halpern, "Electron Paramagnetic Resonance Oxygen Image Hypoxic Fraction Plus Radiation Dose Strongly Correlates With Tumor Cure in FSa Fibrosarcomas," *International Journal of Radiation Oncology Biology Physics,* vol. 71, no. 2, pp. 542-549, 2008.

M. H. Levitt, Spin Dynamics: Basics of Nuclear Magnetic Resonance, Wiley, 2008.

M. K. Bowman, C. Mailer and H. J. Halpern, "The solution conformation of triarylmethyl radicals," *J. Magn. Reson*., vol. 172, no. 2, pp. 254-267, 2005.

M. K. Bowman, T. J. Michalski, M. Peric and H. J. Halpern, "Fourier transform EPR and low frequency EPR studies of nitroxide radicals," *Pure Appl. Chem*., vol. 62, pp. 271-274, 1990.

M. M. Kundalika, G. R. Eaton and S. S. Eaton, "Determination of T1 and T2 by Simulation of EPR Power Saturation Curves and Saturated Spectra. Application to Spin-Labeled Iron Porphyrins," *J. Magn. Reson*., vol. 60, pp. 54-65, 1984.

M. M. Mossoba, K. Makino, P. Riesz and R. C. Perkins, "Long-range proton hyperfine coupling in alicyclic nitroxide radicals by resolution-enhanced electron paramagnetic resonance," *J. Phys. Chem*., vol. 88, pp. 4717-4723, 1984.

M. Miyake, J. Shen, S. Liu, H. Shi, W. Liu, Z. Yuan, A. Pritchard, J. P. Kao, K. J. Liu and G. M. Rosen, "Acetoxymethoxycarbonyl nitroxides as electron paramagnetic resonance proimaging agents to measure O2 levels in mouse brain: a pharmacokinetic and pharmacodynamic study.," *J. Pharmacol. Exp. Ther*., vol. 318, no. 3, pp. 1187-1193, 2006.

M. Miyake, S. R. Burks, J. Weaver , P. Tsai, W. Liu, D. Bigio, K. S. Bauer, K. J. Liu, G. M. Rosen and J. P. Kao, "Comparison of two nitroxide labile esters for delivering electron paramagnetic resonance probes into mouse brain.," *J. Pharm. Sci*., vol. 99, no. 8, pp. 3594-3600, 2010.

M. P. Eastman, G. V. Bruno and J. H. Freed, "ESR studies of Heisenberg spin exchange II. Effects of radical charge and size," J. *Chem. Phys*., vol. 52, pp. 2511-2522, 1970.

M. Pavone, M. Biczysko, N. Rega and V. Barone, "Magnetic Properties of Nitroxide Spin Probes: Reliable Account of Molecular Motions and Nonspecific Solvent Effects by Time-Dependent and Time-Independent Approaches," *J. Phys. Chem. B*, vol. 114, pp. 11509-11514, 2010.

M. T. Turke and M. Bennati, "Saturation factor of nitroxide radicals in liquid DNP by pulsed ELDOR experiments," *Phys. Chem. Chem. Phys*. , vol. 13, pp. 3630-3633, 2011.

M. Tseitlin, A. Dhami, R. W. Quine, G. A. Rinard, S. S. Eaton and G. R. Eaton, "Electron spin T2 of a nitroxyl radical at 250 MHz measured by rapid scan EPR," *Appl. Magn. Reson*., vol. 30, pp. 651-656, 2006.

M. Tseitlin, A. Dhami, S. S. Eaton and G. R. Eaton, "Comparison of maximum entropy and filtered back-projection methods to reconstruct rapid-scan EPR images," *J. Magn. Reson*., vol. 184, no. 1, pp. 157-168, 2007.

M. Tseitlin, D.G. Mitchell, S.S. Eaton, and G.R. Eaton, "Corrections for sinusoidal background and non-orthogonality of signal channels in sinusoidal rapid magnetic field scans", *J. Magn. Res*., vol. 223, pp.80 - 84, 2012.

M. Tseitlin, G. A. Rinard, R. W. Quine, S. S. Eaton and G. R. Eaton, "Deconvolution of Sinusoidal Rapid EPR Scans," *J. Magn. Reson.*, vol. 208, no. 2, pp. 279-283, 2011.

M. Tseitlin, R. W. Quine, G. A. Rinard, S. S. Eaton and G. R. Eaton, "Combining Absorption and Dispersion Signals to Improve Signal-to-noise for Rapid Scan EPR Imaging," *J. Magn. Reson.*, vol. 203, no. 2, pp. 305-310, 2010.

M. Tseitlin, R. W. Quine, G. A. Rinard, S. S. Eaton and G. R. Eaton, "Digital EPR with an arbitrary waveform generator and direct detection at the carrier frequency," *J. Magn. Reson.*, vol. 213, no. 1, pp. 119-125, 2011.

M. Tseitlin, R. W. Quine, S. S. Eaton and G. R. Eaton, "Use of polyphase continuous excitation based on the Frank sequence in EPR," *J. Magn. Reson.* , vol. 211, no. 2, pp. 221-227, 2011.

M. Tseitlin, R. W. Quine, S. S. Eaton, G. R. Eaton, H. J. Halpern and J. H. Ardenkjaer-Larsen, "Use of the Frank sequence in pulsed EPR.," *J. Magn. Reson.*, vol. 209, no. 2, pp. 306-309, 2011.

M. Tseitlin, S.S. Eaton, and G.R. Eaton, "Uncertainty analysis for absorption and first-derivative EPR spectra", Conc. *Magn. Reson.*, vol. 40A, pp. 295 - 305, 2012.

M. Tseitlin, T. Czechowski, R. W. Quine, S. S. Eaton and G. R. Eaton, "Background Removal Procedure for Rapid Scan EPR," *J. Magn. Reson.*, vol. 196, no. 1, pp. 48-53, 2009.

M. Tseitlin, T. Czechowski, S. S. Eaton and G. R. Eaton, "Regularized Optimization (RO) Reconstruction for Oximetric EPR Imaging," *J. Magn. Reson.*, vol. 194, no. 2, pp. 212-221, 2008.

M.P. Klein and B.W. Barton, "Enhancement of signal-to-noise ratio by continuous averaging: application to magnetic resonance", *Rev. Sci. Instrum.*, vol. 34, pp. 754 - 759, 1963.

M.R. Dreher, M. Elas, K. Ichickawa, E.D. Barth, A. Chilkoti, G.M. Rosen, H.J. Halpern, and M. Dewhirst, Nitroxide conjugate of a thermally responsive elastin-like polypeptide for noninvasive thermometry, *Med. Phys.*, vol. 31, pp. 2755 - 2762, 2004.

N. Bloembergen, E. M. Purcell and R. V. Pound, "Relaxation effects in nuclear resonance absorption," *Phys. Rev.*, vol. 73, pp. 679-712, 1948.

N. D. Chasteen and M. W. Hanna, "Electron paramagnetic resonance line widths of vanadyl (IV) a-hydroxycarboxylates," *J. Phys. Chem.*, vol. 76, pp. 3951-3958, 1972.

N. Davidson and R. H. Cole, "Dielectric relaxation in glycerol, propylene glycol, and n-propanol," *J. Chem. Phys.*, vol. 19, pp. 1484-1490, 1951.

N. Devasahayam, S. Subramanian and M. C. Krishna, "A novel programmable pulse generator with nanosecond resolution for pulsed electron paramagnetic resonance applications," *Rev. Sci. Instrum*., vol. 79, no. 2, pp. 026106-1 to 026106-4, 2008.

N. Devasahayam, S. Subramanian, R. Murugesan, J. Cook, M. Afeworki, R. G. Tschudin, J. B. Mitchell and M. C. Krishna, "Parallel Coil Resonators for Time-Domain Radiofrequency Electron Paramagnetic Resonance Imaging of Biological Objects," *J. Magn. Reson*., vol. 142, no. 1, pp. 168-176, 2000.

N. Khan, C. M. Wilmot, G. M. Rosen, E. Demidenko, J. Joseph, J. O'Hara, B. Kalyanaraman and M. Swartz, "Spin traps: in vitro toxicity and stability of radical adducts.," *Free Rad. Biol. Med*., vol. 34, no. 11, pp. 1473-1481, 2003.

N. Khan, J. P. Blinco, S. E. Bottle, K. Hosokawa, H. M. Swartz and A. S. Micallef, "The evaluation of new and isotopically labeled isoindoline nitroxides and azaphenalene nitroxides for EPR oximetry," *J. Magn. Reson*., vol. 211, pp. 170-177, 2011.

P. A. Beckmann, H. A. Al-Hallaq, A. M. Fry, A. L. Plofker, B. A. Roe and J. A. Weiss, "Solid state proton spin relaxation and methyl and t-butyl reorientation," *J. Chem. Phys.* , vol. 100, pp. 752-753, 1994.

P. A. Beckmann and E. Schneider, "Methyl group rotation, 1H spin-lattice relaxation in an organic solid and the analysis of nonexponential relaxation," *J. Chem. Phys*., p. 054508, 2012.

P. Kuppusamy, H. Li, G. Ilangovan, A.J. Cardounel, J.L. Zweier, K. Yamanda, M.C. Krishna, and J.B. Mitchell, "Noninvasive imaging of tumor redox status and its modification by tissue glutathione levels", *Cancer Res*., vol. 62, pp.307 - 312, 2002.

P. Kuppusamy, M. Afeworki, R. A. Shankar, D. Coffin, M. C. Krishna, S. M. Hahn, J. B. Mitchell and J. L. Zweier, "In vivo Electron Paramagnetic Resonance Imaging of Tumor Heterogeneity and oxygenation in a murine model," *Cancer Res.*, vol. 58, no. 7, pp. 15662-1568, 1998.

P. Kuppusamy and J. L. Zweier, "Cardiac applications of EPR imaging," *NMR in Biomedicine*, vol. 17, no. 5, pp. 226-239, 2004.

P. Seifi, B. Epel, C. Mailer and H. J. Halpern, "Multiple-stepped Zeeman field offset method applied in acquiring enhanced resolution spin-echo electron paramagnetic resonance images," *Med. Phys*., vol. 37, pp. 5412-5420, 2010.

P. Seifi, B. Epel, S. V. Sundramoorthy, C. Mailer and H. J. Halpern, "Frequency bandwidth extension by use of multiple Zeeman field offsets for electron spin-echo EPR oxygen imaging of large objects," *Med. Phys*., vol. 38, p. 3062, 2011.

P. Tsai, G. L. Cao, T. J. Merkel and G. M. Rosen, "Spin labelling of Bacillus anthracis endospores: a model for in vivo tracking by EPR imaging.," *Free Rad. Res*., vol. 42, no. 1, pp. 49-56, 2008.

P. Tsai, S. Porasuphatana, H. J. Halpern, E. D. Barth and G. M. Rosen, "In vivo in situ detection of nitric oxide using low-frequency EPR spectroscopy," *Methods Mol. Biol.*, vol. 196, pp. 227-237, 2002.

P. Vaupel, M. Hockel and A. Mayer, "Detection and characterization of tumor hypoxia using pO2 histography," *Anitoxidant and Redox Signaling*, vol. 9, pp. 1221-1235, 2007.

P. W. Atkins, "Spin-rotation interaction," in Electron Spin Relaxation in Liquids, L. T. Muus and P. W. Atkins, Eds., New York, Plenum Press, 1972, pp. 279-312.

P. W. Atkins and D. Kivelson, "Linewidths in Solution II. Analysis of Spin-Rotational Relaxation Data," *J. Chem. Phys*., vol. 44, pp. 169-174, 1966.

P. W. Percival and J. S. Hyde, "Saturation-recovery measurements of the spin-lattice relaxation times of some nitroxides in solution," *J. Magn. Reson*., vol. 23, pp. 249-257, 1976.

R. Ahmad, D. S. Vikram, L. C. Potter and P. Kuppusamy, "Estimation of mean and median pO2 values for a composite EPR spectrum," *J. Magn. Reson*., vol. 192, no. 2, pp. 269-275, 2008.

R. Ahmad and P. Kuppusamy, "Theory, Instrumentation and Applications of Electron Paramagnetic Resonance Oximetry," *Chem. Rev.,* vol. 110, pp. 3212-3236, 2010.

R. Avni, B. Cohen and M. Neeman, "Hypoxic stress and cancer: imaging the axis of evil in tumor metastasis," *NMR in Biomedicine*, vol. 24, pp. 569-581, 2010.

R. D. Nielsen, S. Canaan, J. A. Gladden, M. H. Gelb, C. Mailer and B. H. Robinson, "Comparing continuous wave progressive saturation EPR and time domain saturation recovery EPR over the entire motional range of nitroxide spin labels.," *J. Magn. Reson.,* vol. 169, no. 1, pp. 129-163, 2004.

R. G. Kooser, W. V. Volland and J. H. Freed, "E.S.R. relaxation studies on orbitally degenerate free radicals I. Benzene anion and tropenyl," *J. Chem. Phys*., vol. 50, pp. 5243-5257, 1969.

R. H. Pursley, G. Salem, N. Devasahayam, S. Subramanian, J. Koscielniak, M. C. Krishna and T. J. Pohida, "Integration of digital signal processing technologies with pulsed electron paramagnetic resonance imaging," *J. Mag. Reson*. , vol. 178, no. 2, pp. 220-227, 2006.

R. H. Pursley, G. Salem, T. J. Pohida, N. Devashayam, S. Subramanian and M. C. Krishna, "Direct detection and time-locked subsampling applied to pulsed electron paramagnetic resonance imaging," *Rev. Sci. Instrum.*, vol. 76, no. 5, 2005.

R. H. Pursley, J. Kakareka, G. Salem, N. Devasahayam, S. Subramanian, R. G. Tschudin, M. C. Krishna and T. J. Pohida, "Stochastic excitation and Hadamard correlation spectroscopy with bandwidth extension in RF FT-EPR," *J. Mag. Reson.*, vol. 162, no. 1, pp. 35-45, 2003.

R. H. Tomlinson and L. H. Gray, "The histological structure of some human lung cancers and the possible implications for radiotherapy," *British Journal of Cancer*, vol. 9, pp. 539-849, 1955.

R. M. Davis, S. Matsumoto, M. Bernardo, A. Sowers, K. I. Matsumoto, M. Krishna and J. B. Mitchell, "Magnetic resonance imaging of organic contrast agents in mice: capturing the whole-body redox landscape," *Free Rad. Biol. Med.*, vol. 50, pp. 459-468, 2011.

R. Murugesan, J. A. Cook, N. Devasahayam, M. Afeworki, S. Subramanian, R. Tschudin, J. A. Larsen, J. B. Mitchell, A. Russo and M. C. Krishna, "In vivo imaging of a stable paramagnetic probe by pulsed-radiofrequency electron paramagnetic resonance spectroscopy," *Magn. Reson. Med.*, vol. 38, no. 3, pp. 409-414, 1997.

R. Murugesan, M. Afeworki, J. A. Cook, N. Devasahayam, R. Tschudin, J. B. Mitchell, S. Subramanian and M. C. Krishna, "A broadband pulsed radio frequency electron paramagnetic resonance spectrometer for biological applications," *Rev. Sci. Instrum.*, vol. 59, p. 1869, 1998.

R. N. Schwartz, L. L. Jones and M. K. Bowman, "Electron spin echo studies of nitroxide free radicals in liquids," *J. Phys. Chem.*, vol. 83, pp. 3429-3439, 1979.

R. Owenius, G. R. Eaton and S. S. Eaton, "Frequency (250 MHz to 9.2 GHz) and viscosity dependence of electron spin relaxation of triarylmethyl radicals at room temperature," *J. Magn. Reson.*, vol. 172, no. 1, pp. 168-175, 2005.

R. Owenius, G. R. Terry, M. J. Williams, S. S. Eaton and G. R. Eaton, "Frequency Dependence of Electron Spin Relaxation of Nitroxyl Radicals in Fluid Solution," *J. Phys. Chem. B,* vol. 108, pp. 9475-9481, 2004.

R. Ramasseul and A. Rassat, "Nitroxydes XXXIII: radicaux nitroxydes pyrroliques encombres. Un pyrryloxyle stable.," Bulletin de la Societe Chimique de France, pp. 4330-4341, 1970.

R. W. Quine, D. G. Mitchell and G. R. Eaton, "A General Purpose Q-Measuring Circuit Using Pulse Ring-Down," *Concepts Magn. Reson.*, vol. 39B, no. 1, pp. 43-46, 2011

.

R. W. Quine, G. A. Rinard, B. T. Ghim, S. S. Eaton and G. R. Eaton, "A 1-2 GHz pulsed and continuous wave electron paramagnetic resonance spectrometer," *Rev. Sci. Instrum*., vol. 67, pp. 2514-2527, 1996.

R. W. Quine, G. A. Rinard, S. S. Eaton and G. R. Eaton, "A pulsed and continuous wave 250 MHz electron paramagnetic resonance spectrometer," *Concepts Magn. Reson*., vol. 15, no. 1, pp. 59-91, 2002.

R. W. Quine, G. A. Rinard, S. S. Eaton and G. R. Eaton, "Quantitative rapid scan EPR spectroscopy at 258 MHz," *J. Magn. Reson*., vol. 205, no. 1, pp. 23-27, 2010.

R. W. Quine, G. R. Eaton and S. Dillon, "Fast-response VHF pulsed 2 kW power amplifiers," *Concepts Magn. Reson*., vol. 29B, no. 4, pp. 185-190, 2006.

R. W. Quine, G. R. Eaton and S. S. Eaton, "Pulsed EPR spectrometer," *Rev. Sci. Instrum.*, *v*ol. 58, pp. 1709-1723, 1987.

R. W. Quine, G. R. Eaton, S. Dillon and D. Myer, "Fast-response VHF-band pulsed power amplifiers," *Concepts Magn. Reson*., vol. 27B, pp. 1-7, 2005.

R. W. Quine, M. Tseytlin, S. S. Eaton and G. R. Eaton, "A very fast switched-attenuator circuit for microwave and RF applications," *Concepts Magn. Reson*., vol. 37B, pp. 39-44, 2010.

R. W. Quine, S. S. Eaton and G. R. Eaton, "Saturation recovery electron paramagnetic resonance spectrometer," *Rev. Sci. Instrum*., vol. 63, pp. 4251-4262, 1992.

R.W. Quine, D.G. Mitchell, S.S. Eaton, and G.R. Eaton, "A Resonated Coil Driver for Rapid Scan EPR", *Concept. Magn. Reson*., vol. 41B, pp.95 - 110, 2012.

S. A. Goldman, G. V. Bruno and J. H. Freed, "ESR Studies of anisotropic rotational reorientation and slow tumbling in liquid and frozen media II. Saturation and nonsecular effects," *J. Chem. Phys*., vol. 59, pp. 3071-3091, 1973.

S. J. Ellis, M. Velayutham, S. S. Velan , E. F. Petersen, J. L. Zweier, P. Kuppusmay and R. S. Spencer, "EPR oxygen mapping (EPROM) of engineered cartilage grown in a hollow-fiber bioreactor," *Magn. Reson. Med*., vol. 46, no. 4, pp. 819-826, 2001.

S. K. Hoffmann, W. Hilczer, J. Goslar, S. Kiczka and I. Polus, "Resonance-type effects in free radical electron spin-lattice relaxation and electron spin echo dephasing due to dynamics of a homogeneous-chain oligomeric system," *Phys. Chem. Chem. Phys*., vol. 4, pp. 4944-4951, 2002.

S. K. Rengan, M. P. Khakhar, B. S. Prabhananda and B. Venkataraman, "Electron Spin-Lattice Relaxation in Organic Free Radicals in Solutions," *Pure. Appl. Chem*., vol. 32, pp. 287-305, 1972.

S. Matsumoto, F. Hyodo, S. Subramanian, N. Devasahayam, J. Munasinghe, E. Hyodo, C. Gadisetti, J. A. Cook, J. B. Mitchell and M. C. Krishna, "Low-field paramagnetic resonance imaging of tumor oxygenation and glycolytic activity in mice," *J. Clin. Invest.*, vol. 118, pp. 1965-1973, 2008.

S. R. Burks, E. D. Barth, H. J. Halpern, G. M. Rosen and J. Y. Kao, "Cellular Uptake of Electron Paramagnetic Resonance Imaging Probes Through Endocytosis of Liposomes," *Biochim. Biophys. Acta*, vol. 1788, no. 10, pp. 2301-2308, 2009.

S. R. Burks, J. Ni, S. Muralidharan, A. Coop, J. P. Kao and G. M. Rosen, "Optimization of labile esters for esterase-assisted accumulation of nitroxides into cells: a model for in vivo EPR imaging.," *Bioconjug. Chem.*, vol. 19, no. 10, pp. 2068-2071, 2008.

S. R. Burks, L. F. Macedo, E. D. Barth, K. H. Tkaczuk, S. S. Martin, G. M. Rosen, H. J. Halpern, A. M. Brodie and J. P. Kao, "Anti-HER2 immunoliposomes for selective delivery of electron paramagnetic resonance imaging probes to HER2-overexpressing breast tumor cells.," *Breast Cancer Res. Treat.*, vol. 124, no. 1, pp. 121-131, 2010.

S. R. Burks, M. A. Bakhshai, M. A. Makowsky, S. Muralidharan, P. Tsai, G. M. Rosen and J. Y. Kao, "2H, 15N-Substituted nitroxides as sensitive probes for electron paramagnetic resonance imaging," *J. Org. Chem.*, vol. 75, pp. 6463-6467, 2010.

S. R. Burks, M. Makowsky, Z. A. Yaffe, C. Hoggle, P. Tsai, S. Muralidharan, M. K. Bowman, J. P. Kao and G. M. Rosen, "The Effect of Structure on Nitroxide EPR Spectral Linewidth," *J. Org. Chem.*, vol. 75, no. 14, pp. 4737-4741, 2010.

S. S. Eaton, J. Harbridge, G. A. Rinard, G. R. Eaton and R. T. Weber, "Frequency Dependence of Electron Spin Relaxation for Three S=1/2 Species Doped into Diamagnetic Solid Hosts," *Appl. Magn. Reson.*, vol. 20, pp. 151-157, 2001.

S. S. Eaton and G. R. Eaton, "Frequency Dependence of Pulsed EPR Experiments," *Concepts Magn. Reson.* , vol. 34A, no. 6, pp. 315-321, 2009.

S. S. Eaton and G. R. Eaton, "Relaxation times of organic radicals and transition metal ions," in Biological Magnetic Resonance 19, 2000, pp. 29-154.

S. S. Eaton and G. R. Eaton, "Relaxation times of organic radicals and transition metal ions," in Biological Magnetic Resonance 19, 2000, pp. 29-154.

S. S. Velan, R. S. Spencer, J. L. Zweier and P. Kuppusamy, "Electron paramagnetic resonance oxygen mapping (EPROM): Direct visualization of oxygen concentration in tissue," *Magn. Reson. Med.*, vol. 43, no. 6, pp. 804-809, 2000.

S. Sanvito, "Molecular spintronics," *Chem. Soc. Rev.*, vol. 40, pp. 3336-3355, 2011.

S. Som, L. C. Potter, R. Ahmad and P. Kuppusamy, "A parametric approach to spectral-spatial EPR imaging," *J. Magn. Reson*., vol. 186, no. 1, pp. 1-10, 2007.

S. Som, L. C. Potter, R. Ahmad, D. Vikram and P. Kuppusamy, "EPR oximetry in three spatial dimensions using sparse spin distribution," *J. Magn. Reson*., vol. 193, no. 2, pp. 210-217, 2008.

S. Subramanian, J. B. Mitchell and M. C. Krishna, "Time-Domain Radio Frequency EPR Imaging," in In Vivo EPR (ESR) Biological Magnetic Resonance, vol. 18, 2003, pp. 153-197.

S. Subramanian, J. W. Koscielniak, N. Devasahayam, G. Salem, R. H. Pursley, T. J. Pohida and M. C. Krishna, "A novel fast imaging modality for free radicals in vivo: continuous wave (CW) EPR imaging with direct detection and rapid field scan in the presence of rotating gradients," SPIE Proceedings, vol. 7170, 2009.

S. Subramanian, K. Matsumoto, J. B. Mitchell and M. C. Krishna, "Radio frequency continuous-wave and time-domain EPR imaging and Overhauser-enhanced magnetic resonance imaging of small animals: instrumental developments and comparison of relative merits for functional imaging," *NMR in Biomedicine*, vol. 17, no. 5, pp. 263-297, 2004.

S. Subramanian, K. Yamada, A. Irie, R. Murugesan, J. A. Cook, N. Devasahayam, G. M. Van Dam, J. B. Mitchell and M. C. Krishna, "Noninvasive in vivo oximetric imaging by radiofrequency FT EPR," *Magn. Reson. Med*., vol. 47, no. 5, pp. 1001-1008, 2002.

S. Subramanian, N. Devasahayam and M. C. Krishna, "Radiofrequency time-domain EPR imaging: instrumentation development and recent results in functional physiological in vivo imaging," in Imaging, Manipulation, and Analysis of Biomolecules, Cells, and Tissues V, San Jose, 2007.

S. Subramanian, N. Devasahayam, R. Murugesan, K. Yamada, J. Cook, A. Taube, J. B. Mitchell, J. B. Lohman and M. C. Krishna, "Single-point (constant-time) imaging in radiofrequency Fourier transform electron paramagnetic resonance," *Magn. Reson. Med*., vol. 48, no. 2, pp. 370-379, 2002.

S. Subramanian, R. Murugesan, N. Devasahayam, J. A. Cook, M. Afeworki, T. Pohida, R. G. Tschudin, J. B. Mitchell and M. C. Krishna, "High-Speed Data Acquisition System and Receiver Configurations for Time-Domain Radiofrequency Electron Paramagnetic Resonance Spectroscopy and Imaging," *J. Magn. Reson*., vol. 137, no. 2, pp. 379-388, 1999.

S. Subramanian and M. C. Krishna, "Time-Domain Radio Frequency EPR Imaging," in Biological Magnetic Resonance: Biomedical EPR- Part A: Free Radicals, Metals, Medicine and Physiology, vol. 23, 2005, pp. 321-382.

S.R. Burks, J. Bakhshai, M.A. Makowsky, S. Muralidharan, P. Tsai, G.M. Rosen, and J.P.Y. Kao, “2H,15N-Substituted Nitroxides as Sensitive Probes for Electron Paramagnetic Resonance Imaging” *J. Org. Chem.*, vol. 75, pp.6463 - 6467, 2010.

S.S. Eaton, R.W. Quine, M. Tseitlin, D.G. Mitchell, G.A. Rinard, and G.R. Eaton, Rapid Scan Electron Paramagnetic Resonance in Handbook of High Frequency EPR S. K. Misra, Ed., Wiley 2014

S.S. Velan, R.G. Spencer, J.L. Zweier, and P. Kuppusamy, Electron paramagnetic resonance oxygen mapping (EPROM): direct visualization of oxygen concentration in tissue, *Magn. Reson. Med*., vol. 43, pp. 804 - 809, 2000.

T. Akaike, M. Yoshida, Y. Miyamoto, K. Sato, M. Kohno, K. Sasamoto, K. Miyazaki, S. Ueda and H. Maeda, "Antagonistic action of imidazolineoxyl N-oxides against endothelium-derived relaxation factor/NO through a radical reaction," *Biochem*. , vol. 32, pp. 827-832, 1993.

T. Blochowicz, A. Kudik, S. Benkhof, J. Senker, E. Rossler and G. Hinze, "The spectral density in simple organic glass formers: comparison of dielectric and spin-lattice relaxation," *J. Chem. Phys*., vol. 110, pp. 12011-12022, 1999.

T. D. Yager, G. R. Eaton and S. S. Eaton, "[Cr(oxalate)3]3- as a broadening agent in nitroxyl spin probe studies," *J. Chem. Soc. Chem. Comm*., pp. 944-945, 1978.

T. J. Reddy, T. Iwama, H. J. Halpern and V. H. Rawal, "General Synthesis of Persistent Trityl Radicals for EPR Imaging of Biological Systems," *J. Org. Chem*., vol. 67, no. 14, pp. 4635-4639, 2002.

T. Ueda and N. Nakamura, "1H MAS NMR study of local structure and dynamics of water molecule in (+/-) [Co(en)3]Cl3-nD2O," *J. Phys. Chem. B*, vol. 107, pp. 13681-13687, 2003.

V. Barone, M. Brustolon, P. Cimino, A. Polimeno, M. Zerbetto and A. Zoleo, "Development and validation of an integrated computational approach for the modeling of CW-ESR spectra of free radicals in solution: p-(methylthio) phenyl nitronylnitroxide in toluene as a case study," *J. Am. Chem. Soc*., vol. 128, pp. 15685-15873, 2006.

V. Khramtsov, "Functional EPR Spectroscopy and Imaging of Nitroxides," in Supramolecular Structure and Function 9, 2007, pp. 181-208.

V. S. Sastry, A. Polimeno, R. H. Crepeau and J. H. Freed, "Studies of spin relaxation and molecular dynamics in liquid crystals by two-dimensional Fourier transform electron spin resonance II. Perdeuterated-tempone in butoxy benzyidene octylaniline and dynamic cage effects," *J. Chem. Phys*., vol. 105, pp. 5773-5791, 1996.

V. S. Subramanian, B. Epel and H. J. Halpern, "Orthogonal resonators for pulse in vivo electron paramagnetic imaging at 250 MHz," *J. Magn. Reson*., vol. 240, pp. 45-51, 2014.

V. S. Subramanian, B. Epel, C. Mailer and H. J. Halpern, "A passive dual-circulator based transmit/receive switch for use with reflection resonators in pulse EPR," *Concepts Magn. Reson*., vol. 35B, no. 3, pp. 133-138, 2009.

V. V. Khramtsov, "In vivo Spectroscopy and Imaging of Nitroxide Probes," in Nitroxides- Theory, Experiment and Applications, I. A. Kokorin, Ed., 2012.

V. V. Khramtsov, G. L. Caia, K. Shet, E. Kesselring, S. Petryakov, J. L. Zweier and A. Samouilov, "Variable Field Proton–Electron Double-Resonance Imaging: Application to pH mapping of aqueous samples," *J. Magn. Reson*., vol. 202, no. 2, pp. 267-273, 2010.

V. V. Khramtsov, I. A. Grigor'ev, M. A. Foster, D. J. Lurie and I. Nicholson, "Biological Applications of spin pH probes," *Cell. Mol. Biol*., vol. 46, pp. 1361-1374, 2000.

V. V. Khramtsov, L. M. Weiner, I. A. Grigoriev and L. B. Volodarsky, "Proton Exchange in stable nitroxide radicals. EPR study of the pH of aqueous solutions.," *Chem. Phys. Lett.*, vol. 91, pp. 69-72, 1982.

V. V. Khramtsov and J. L. Zweier, "Functional in vivo EPR Spectroscopy and Imaging Using Nitroxide and Trityl Radicals," in Stable Radicals: Fundamentals and Applied Aspects of Odd-Electron Compounds, R. Hicks, Ed., John Wiley & Sons, Ltd, 2010.

V.V. Khramtsov, V.I. Yelinova, Y.I. Glazachev, V.A. Reznikov, and G. Zimmer, “Quantitative determination and reversible modification of thiols using imidazolidine biradical disulfide label”, *J. Biochem. Biophys. Methods*, vol. 35, pp. 115-128, 1997.

W. Froncisz, T. G. Camenisch, J. J. Ratke, J. R. Anderson, W. K. Subczynski, R. A. Strangeway, J. W. Sidabra and J. S. Hyde, "Saturation recovery EPR and ELDOR at W band for spin labels," *J. Magn. Reson*., vol. 193, pp. 297-304, 2008.

W. K. Subczynski, L. Mainali, T. G. Camenisch, W. Froncisz and J. S. Hyde, "Spin-label oximetry at Q- and W-band," *J. Magn. Reson*., vol. 209, pp. 142-148, 2011.

X. Pan, D. Xia and H. J. Halpern, "Targeted-ROI imaging in electron paramagnetic resonance imaging," *J. Magn. Reson*., vol. 187, no. 1, pp. 66-77, 2007.

X. Zhu, L. Zuo, A. J. Cardounel, J. L. Zweier and G. He, "Characterization of In Vivo Tissue Redox Status, Oxygenation, and Formation of Reactive Oxygen Species in Postichemic Myocardium," *Antioxidants and Redox Signaling*, vol. 9, no. 4, pp. 447-455, 2007.

Y. Deng, R. P. Pandian, R. Ahmad, P. Kuppusamy and J. L. Zweier, "Application of magnetic field over-modulation for improved EPR linewidth measurements using probes with Lorentzian lineshape," *J. Magn. Reson*., vol. 181, no. 2, pp. 254-261, 2006.

Y. Hama, K. Matsumoto, R. Murugesan, S. Subramanian, N. Devasahayam, J. W. Koscielniak, F. Hyodo, J. A. Cook, J. B. Mitchell and M. C. Krishna, "Continuous Wave EPR Oximetric Imaging at 300 MHz Using Radiofrequency Power Saturation Effects," *Antioxidants and Redox Signaling*, vol. 9, no. 10, pp. 1709-1716, 2007.

Y. J. Yin and J. S. Hyde, "Use of high observing power in electron spin resonance saturation-recovery experiments in spin-labeled membranes," *J. Chem. Phys*., vol. 91, pp. 6029-6035, 1989.

Y. Kawada, H. Hirata and H. Fujii, "Use of multi-coil parallel-gap resonators for co-registration EPR/NMR imaging," *J. Magn. Reson*., vol. 184, no. 1, pp. 29-38, 2007.

Y. Liu, F. A. Villamena, J. Sun, T. Wang and J. L. Zweier, "Esterified trityl radicals as intracellular oxygen probes," *Free Rad. Biol. Med*., vol. 46, no. 7, pp. 876-883, 2009.

Y. Liu, Y. Song, A. Rockenbauer, J. Sun, C. Hemann, F. A. Villamena and J. L. Zweier, "Synthesis of Trityl Radical-Conjugated Disulfide Biradicals for Measurement of Thiol Concentration," *J. Org. Chem*., vol. 76, no. 10, pp. 3853-3860, 2011.

Y.J. Lin, B.A. Teicher, and H.J. Halpern, “Synthesis of 4-protio-3-carbamoyl-2,2,5,5-tetraperdeuteromethyl-3-pyrrolin-1-yloxy (mHCTPO): a selectively isotopically labeled compound for use in T2 spin label oxymetry”, *J. Labelled Compds. Radiopharm*., vol 28, pp.621-631, 1990.

APPENDIX A

Table A1. Frequency Dependence of T_1.[a,b]

		τ_R (ps)	33.9 GHz			9.4-9.5 GHz			2.5-3.0 GHz		
	Solvent		LF	CF	HF	LF	CF	HF	LF	CF	HF
1a	Toluene	4	0.40	0.37	0.36	0.38	0.36	0.35	0.36	0.37	0.39
	Water	9	1.0	1.1	1.0	0.61	0.58	0.52	0.51	0.50	0.46
	LMO	9	---	1.05	---	0.57	0.51	0.48	0.51	0.50	0.47
	44% Gly	19	2.1	2.0	1.8	1.1	0.85	0.9	0.56	0.54	0.47
	69% Gly	50	3.6	3.8	---	2.2	2.2	1.5	---	0.57	---
1b	Water	9	1.1	---	1.2	0.72	---	0.63	0.59	---	0.57
2a	Water	13	1.3	1.4	1.3	0.64	0.61	0.54	0.47	0.44	0.41
2b	Water	13	1.4	---	1.4	0.84	---	0.72	0.62	---	0.57
3a	Water	19	1.7	1.7	1.7	0.73	0.63	0.59	0.44	0.45	0.41
3b	Water	19	1.9	---	1.9	0.94	---	0.80	0.63	---	0.56
4	Toluene	26	4.2	4.3	4.2	2.2	2.2	1.9	0.57	0.57	0.5
5	NaOH	25	2.1	2.1	2.1	1.0	1.2	0.84	0.64	0.87	0.60
6	Toluene	10	1.2	1.2	1.3	1.3	1.1	1.1	1.2	1.1	1.0

		τ_R (ps)	1.5 GHz			250 MHz		
	Solvent		LF	CF	HF	LF	CF	HF
1a	Toluene	4	0.37	0.37	0.36	---	---	---
	Water	9	0.48	0.48	0.46	0.58	0.60	0.56
	LMO	9	0.45	0.45	0.44	---	0.59	---
	44% Gly	19	0.42	0.50	0.38	---	---	---
	69% Gly	50	0.25	0.39	0.22	---	0.25[c]	---
1b	Water	9	0.58	---	0.55	0.69	---	0.67
2a	Water	13	0.44	0.46	0.41	0.57	0.57	0.53
2b	Water	13	0.61	---	0.56	0.67	---	0.61
3a	Water	19	0.38	0.41	0.35	0.52	0.55	0.48
3b	Water	19	0.58	---	0.52	0.74	---	0.63
4	Toluene	26	0.39	0.48	0.36	0.42	0.47	0.36
5	NaOH	25	0.54	0.76	0.50	0.60	0.90	0.60
6	Toluene	10	0.86	0.79	0.76	---	---	---

[a] Measured in deoxygenated samples at 293 ± 2 K. Values are in μs. The standard deviations for a minimum of three replicate measurements are 3 – 5 % for all frequencies.
[b] For ^{14}N LF, CF, and HF correspond to m_I = +1, 0, and -1 respectively. For ^{15}N LF and HF correspond to m_I = +0.5 and -0.5,
[c] The value for the center field line was measured at 630 MHz, instead of 250 MHz.

Table A2. Frequency Dependence of T_2.[a,b]

		τ_R (ps)	33.9 GHz			9.4-9.5 GHz			2.5-3.0 GHz		
	Solvent		**LF**	**CF**	**HF**	**LF**	**CF**	**HF**	**LF**	**CF**	**HF**
1a	Toluene	4	0.35	0.36	0.25	0.35	0.34	0.32	0.31	0.30	0.31
	Water	9	0.52	0.42	0.31	0.49	0.47	0.38	0.42	0.43	0.38
	LMO	9	0.41	0.34	0.24	0.41	0.41	0.34	0.35	0.39	0.33
	44% Gly	19	0.80	0.39	0.19	0.60	0.60	0.36	0.36	0.41	0.29
	69% Gly	50	0.34	0.13	---	0.34	0.36	0.15	---	0.3	---
1b	Water	9	0.52	---	0.35	0.54	---	0.44	0.47	---	0.45
2a	Water	13	0.48	0.36	0.25	0.41	0.40	0.32	0.36	0.37	0.32
2b	Water	13	0.47	---	0.28	0.53	---	0.42	0.49	---	0.43
3a	Water	19	0.51	0.33	0.19	0.43	0.43	0.29	0.3	0.34	0.28
3b	Water	19	0.63	---	0.25	0.71	---	0.45	0.42	---	0.37
4	Toluene	26	0.63	0.26	0.14	0.61	0.57	0.30	0.37	0.42	0.29
5	NaOH	25	0.46	0.38	0.25	0.61	0.71	0.44	0.46	0.62	0.40
6	Toluene	10	0.43	0.34	0.25	1.1	0.98	0.74	0.86	0.91	0.87

		τ_R (ps)	1.5 GHz			250 MHz		
	Solvent		**LF**	**CF**	**HF**	**LF**	**CF**	**HF**
1a	Toluene	4	0.31	0.35	0.31	---	---	---
	Water	9	0.39	0.41	0.37	0.55	0.58	0.55
	LMO	9	0.34	0.35	0.33	---	0.39	---
	44% Gly	19	0.32	0.34	0.12	---	---	---
	69% Gly	50	0.14	0.21	---	---	0.16[c]	---
1b	Water	9	0.46	---	0.44	0.57	---	0.55
2a	Water	13	0.34	0.36	0.32	0.47	0.50	0.48
2b	Water	13	0.42	---	0.40	0.47	---	0.45
3a	Water	19	0.30	0.32	0.27	0.45	0.47	0.46
3b	Water	19	0.39	---	0.36	0.50	---	0.54
4	Toluene	26	0.39	0.48	0.36	---	---	---
5	NaOH	25	0.45	0.6	0.39	0.56	0.69	0.44
6	Toluene	10	0.71	0.72	0.67	---	---	---

[a] Measured in deoxygenated samples at 293 ± 2 K. Values are in μs. The standard deviations for a minimum of three replicate measurements are 3 – 6 % from 33.9 GHz to 1.5 GHz, and 10% at 250 MHz.
[b] For ^{14}N LF, CF, and HF correspond to m_I = +1, 0, and -1 respectively. For ^{15}N LF and HF correspond to m_I = +0.5 and -0.5, respectively.
[c] The value for the center field line was measured at 630 MHz, instead of 250 MHz.

APPENDIX B

Molecular Modeling of Nitroxides with Gaussian 09

The method used for the structures below is density functional method B1LYP with expanded valence basis set 6-31G*. A prior comparison with B3LYP and UHF methods for MSE2 show B1LYP predicted nitrogen hyperfine coupling (A_I, Fermi Contact Coupling in Gaussian) close to experimental values. The agreement between measured isotropic hyperfine in organic solvent and the model was surprising since no solvent molecules were included in the calculation.

All values listed below are in Gauss. The A_I of natural isotope abundance piperidine tempone was calculated to be 14.9 G, compared to 16.3 G (aqueous) experimentally. This represents a difference ca. 10% between calculation and theory, however A_I is commonly 10% larger in aqueous compared to organic solvents . Analysis of natural isotope abundance nitroxide with pyrrolidine rings, CTPO and the ^{14}N-Proxyl synthesized by Dr. Rosen, gave theoretical ^{14}N A_I 35% less than experiment. Theoretical values for A_I for each "novel" nitroxide considered for synthesis were scaled up by 10% and 35% to develop a qualitative idea of how small structure changes relate to ^{14}N A_I. Fig. B1 shows the geometries for several types of nitroxide base structures. Table B1 compares the calculated A_I with experimentally measured A_I.

Table B1. Comparison of modeled and experimental values of nitrogen isotropic hyperfine for five nitroxides. Radicals are identified in Fig. B1 below.

Nitroxide	Mol. Mod. A_I (G)	Exp. A_I (G)	Exp. Solvent
A	14.9	16.3	Aqueous
B	12.3	16.3	Aqueous
C	11.9	16.3	Aqueous
D	4.8	4.7	Toluene
E	7.3/7.3	8.4	NaOH

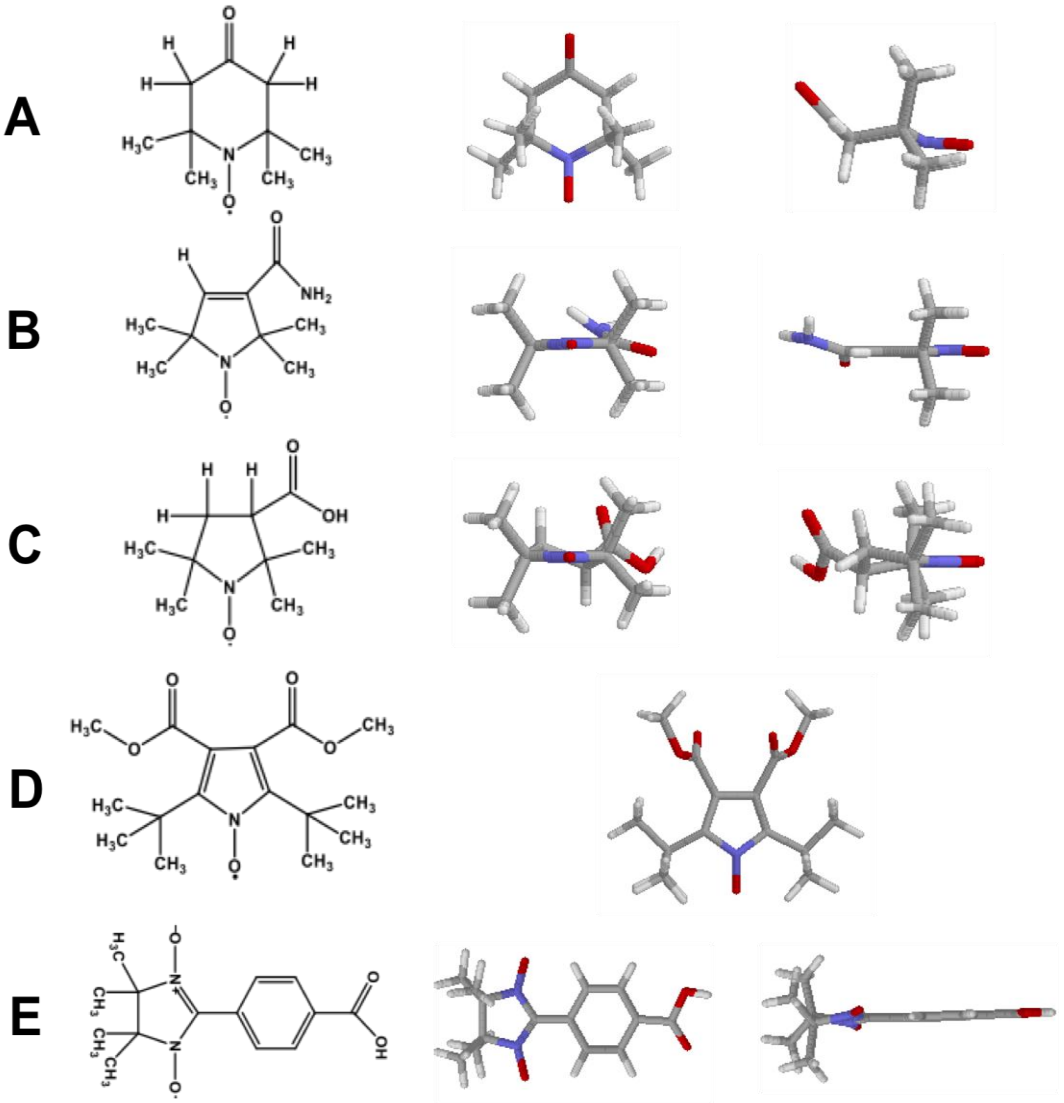

Figure B1 Results of molecular modeling for different nitroxide structures. Modeled above are natural isotope (^{1}H,^{14}N) tempone (A), CTPO (B), Proxyl (C), *t-butyl*-pyrrolidine (D) and a nitronyl radical (E).

APPENDIX C

DATE: 12/18/13

RECORDED BY: JRB, NB#9, pg. 19

EQUIPMENT:

Bruker BLAH300 600 MHz

SAMPLE:

ID: E168

Radical: Trityl, Ox63

Created by/Date: JRB/

Preparation: 0.2 mM, H_2O,de-gassed

Diameter: 16 mm o.d. (15 mm i.d.)

Liquid Column Height: 26 mm

BRIDGE CONFIGURATION:

Pre-Amp Gain:low

Video Gain: 200

Power: 74 W (10 dB), 181 W (4 dB)

Carrier Frequency: 590 MHz

(VHF Console, L-band Field Control)

RESONATOR:

Type:16 mm variable frequency (585-900 MHz) solid copper bi-modal.

Coupling: Critically Coupled w/Q-spoil

Excitation: Q = 311, 400 V bias

Detection: Q = 168, 9 V bias

Q-spoil Detector Settings:

U1: 1000 ns

U2: 1260 ns

U3: 800 ns

DATA:

$\pi/2$: 80 ns (**blue**), 40 ns (**red**)

d_1:2 µs

d_0: 1.1 µs

pg: 400 ns

Field Sweep: 8G, 256 steps

Program: BsweepQspoil4step

Variable Set: AmplifierCompare

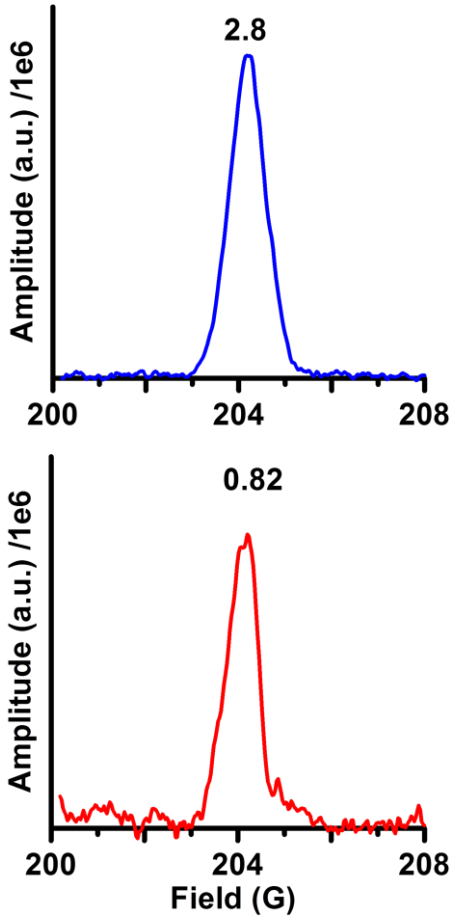

DATE: 03/11/14

RECORDED BY: JRB, NB#9, pg.66

EQUIPMENT:

TOMCO 400 MHz to 1 GHz

SAMPLE:

ID: E168

Radical: Trityl, Ox63

Created by/Date: JRB/

Preparation: 0.2 mM, H_2O,de-gassed

Diameter: 16 mm o.d. (15 mm i.d.)

Liquid Column Height: 26 mm

BRIDGE CONFIGURATION:

Pre-Amp Gain: low

Video Gain: 200

Power: 12 W (16 dB), 48 W (10 dB), 480 W (0 dB)

Carrier Frequency: 589.5 MHz

(VHF Console, L-band Field Control)

RESONATOR:

Type:16 mm variable frequency (585-900 MHz) solid copper bi-modal.

Coupling: Critically Coupled w/Q-spoil

Excitation: Q = 304, 450 V bias

Detection: Q = 172, 9 V bias

Q-spoil Detector Settings:

U1: 1000 ns

U2: 1060 ns

U3: 1000 ns

DATA:

π/2: 80 ns (**black**), 40 ns (**blue**), 20 ns (red)

d_1:2 μs

d_0: 1.4 μs

pg: 500 ns

Field Sweep: 8G, 128 steps

Program: BsweepQspoil4step

Variable Set: AmplifierCompare

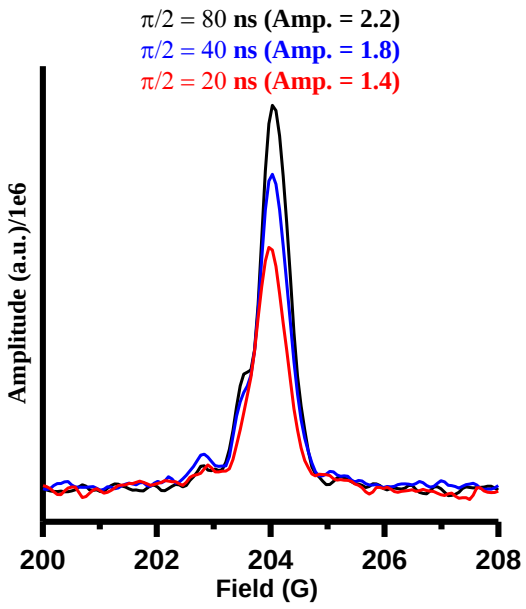

DATE: 03/10/14

RECORDED BY: JRB, NB#9, pg.64-65

EQUIPMENT:

TOMCO 400 MHz to 1 GHz

SAMPLE:

ID: E168

Radical: Trityl, Ox63

Created by/Date: JRB/

Preparation: 0.2 mM, H_2O,de-gassed

Diameter: 16 mm o.d. (15 mm i.d.)

Liquid Column Height: 26 mm

BRIDGE CONFIGURATION:

Pre-Amp Gain:low

Video Gain: 200

Power: 8.7 (17 dB), 54.8 W (9 dB), 435 W (0 dB)

Carrier Frequency: 693.9 MHz

(VHF Console, L-band Field Control)

RESONATOR:

Type:16 mm variable frequency (585-900 MHz) solid copper bi-modal.

Coupling: Critically Coupled w/Q-spoil

Excitation: Q = 242, 450 V bias

Detection: Q = 139, 9 V bias

Q-spoil Detector Settings:

U1: 1000 ns

U2: 1060 ns

U3: 1000 ns

DATA:

π/2: 80 ns (**black**), 40 ns (**blue**), 20 ns (red)

d_1:2 μs

d_0: 1.1 μs

pg: 400 ns

Field Sweep: 8G, 128 steps

Program: BsweepQspoil4step

Variable Set: AmplifierCompare

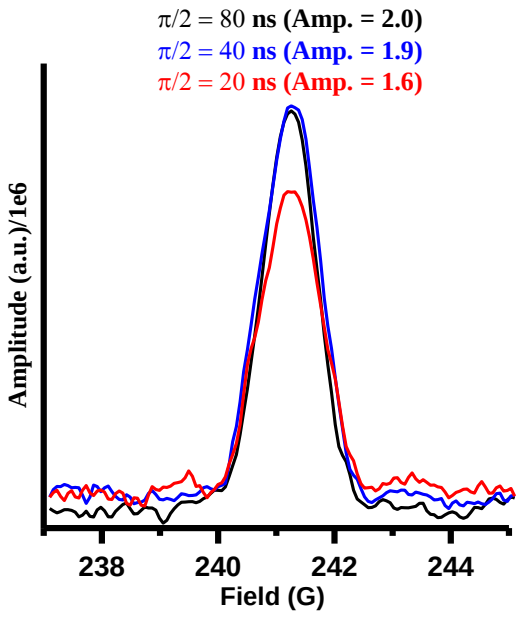

DATE: **π/2**:

RECORDED BY: **d_1:**

EQUIPMENT: **d_0:**

SAMPLE: **pg:**

ID: **Field Sweep:**

Radical: **Program:**

Created by/Date: **Variable Set:**

Preparation:

Diameter:

Liquid Column Height:

BRIDGE CONFIGURATION:

Pre-Amp Gain:

Video Gain:

Power:

Carrier Frequency:

RESONATOR:

Type:

Coupling:

Excitation: Q =

Detection: Q =

Q-spoil Detector Settings:

U1:

U2:

U3:

DATA:

APPENDIX D

LIST OF PUBLICATIONS

1. **Biller, J.R.**, Tseitlin, M., Quine, R.W., Rinard, G.A., Weismiller, H.A., Elajaili, H., Rosen, G.M., Kao, J.P.Y., Eaton, S.S., Eaton, G.R., Imaging of Nitroxides at 250 MHz using Rapid-Scan Electron Paramagnetic Resonance *J. Magn. Reson.*, vol. 242, pp. 162-168, 2014.

2. **Biller, J.R**., Elajaili, H., Meyer, V., Rosen, G.M., Eaton, S.S., & Eaton, G.R. Electron spin-lattice relaxation mechanisms of rapidly-tumbling nitroxide radicals. *J. Magn. Reson.*,vol. 236,pp. 47–56, 2013.

3. **Biller, J.R.**, Meyer, M., Elajaili, H. Rosen, G.M., Eaton, S.S., & Eaton, G.R. Frequency Dependence of Spin Relaxation Times in Aqueous Solution for a Nitronyl Nitroxide Radical and Per-deuterated-Tempone between 250 MHz and 34 GHz. *J. Magn. Reson*, vol. 225,pp. 52-57, 2012.

4. **Biller, J.R.**, Meyer, M., Elajaili, H, Rosen, G.M., Kao, Joseph P. Y., Eaton, S.S., & Eaton, G.R. Relaxation times and line widths of Isotopically-substituted nitroxides in aqueous solution at X-band *J. Magn. Reson.*, vol. 212, pp. 370-377, 2011.

5. Rinard, G.A., Quine, R.W., **Biller, J.R**., & Eaton, G.R. A wire-crossed-loop resonator for rapid scan EPR *Concepts Magn. Reson.*, vol. 37B(2), pp. 86-91, 2010